



UNIVERSITÀ  
DEGLI STUDI  
DI PADOVA

Sede Amministrativa: Università degli Studi di Padova

Dipartimento di Ingegneria Industriale

CORSO DI DOTTORATO DI RICERCA IN:   INGEGNERIA INDUSTRIALE  
CURRICOLO:                               INGEGNERIA ENERGETICA  
CICLO:                                       XXXI

## **INVESTIGATION OF DROPWISE CONDENSATION ON ENGINEERED SURFACES**

**Coordinatore:** Ch.mo Prof. Paolo Colombo

**Supervisore:** Ch.mo Prof. Davide Del Col

**Dottorando :** Dott. Riccardo Parin



“It’s a dangerous business, Frodo, going out your door. You step onto the road, and if you don’t keep your feet, there’s no knowing where you might be swept off to.”

—**J.R.R. Tolkien**

# Index

Abstract.....	1
Chapter 1 – Introduction .....	3
Chapter 2 – Heat transfer during condensation.....	9
2.1 Wettability.....	9
2.2 Filmwise condensation.....	16
2.2.1 Gravity controlled condensation .....	16
2.2.2 Shear controlled condensation .....	21
2.2.3 Condensation under combined gravity and shear control .....	23
2.3 Dropwise condensation .....	25
2.3.1 DWC model history .....	26
2.3.2 Phenomenology.....	27
2.3.3 Predicting models.....	35
2.3.4 Comparison among models.....	56
2.4 Conduction through thin film.....	64
2.4.1 Phonon processes .....	64
2.4.2 Fourier’s law boundaries.....	67
2.4.3 Nanoscale thermal transport models .....	70
Chapter 3 - Tested surfaces.....	73
3.1 Hydrophilic surfaces .....	73
3.1.1 Mirror-polished aluminum surface .....	73
3.1.2 Mirror-polished copper surface.....	74
3.2 Hydrophobic surfaces .....	76
3.2.1 Sol-gel silica-based coatings .....	76
3.2.2 Graphene coatings.....	93

3.3 Superhydrophobic surfaces .....	97
3.3.1 Wet-chemical etching .....	97
3.3.2 Aerogel.....	101
3.4 The bouncing tests .....	105
3.4.1 Experimental procedure .....	106
3.4.2 Droplet bouncing results .....	107
Chapter 4 - Experimental apparatus.....	111
4.1 Components of the experimental apparatus .....	111
4.2 Measurement system.....	115
4.3 Data reduction technique .....	115
2.3.1 Wall temperatures .....	115
4.3.2 Heat flux.....	116
4.3.3 Heat transfer coefficient.....	117
4.3.4 Specific vapor mass flow rate .....	118
4.4 Experimental apparatus uncertainty.....	118
Chapter 5 - Experimental Results .....	123
5.1 Condensation tests description.....	123
5.1.1 Durability tests .....	123
5.1.2 Heat flux tests.....	124
5.1.3 Effect of vapor velocity tests .....	125
5.2 Durability tests .....	126
5.2.1 FWC tests.....	126
5.2.2 DWC tests .....	127
5.3 Heat flux tests.....	160
5.3.1 FWC tests.....	160
5.3.2 DWC tests .....	165
5.4 Effect of vapor velocity tests .....	169
Chapter 6 - Data analysis of DWC .....	173

6.1 Heat transfer measurement analysis.....	173
6.1.1 On the coating life.....	173
6.1.2 On the coating performance.....	176
6.1.3 Heat flux from video analysis.....	177
6.1.4 Droplets dynamic at different vapor velocities.....	179
6.2 Experimental data compared to the theory.....	184
6.2.1 Droplet departing radius.....	184
6.2.2 Droplet population.....	185
6.2.3 Model comparison.....	187
Conclusions.....	191
Nomenclature.....	197
Bibliography.....	203



# Abstract

The scientific objective of the present thesis is to investigate dropwise condensation (DWC) over water repellant surfaces. Creation of surfaces which can promote dropwise condensation is one of the main issues. This type of surfaces, in presence of phase change, vapour-liquid or liquid-solid, can bring significant benefits to various applications, for example in thermoelectric power plant condensers, in the production of drinking water, or in applications that require defrosting for their correct operation (e.g. air source heat pumps). The research activity is focused on metallic surfaces such as aluminum and copper, as they are widely used in industry. The advantage of dropwise condensation of steam is related to the promotion of liquid droplets, which leads to higher heat transfer coefficients by one order of magnitude compared to film condensation. The development and characterization (pre and post experimental condensation tests) of several surfaces with different wettability, from hydrophilic to superhydrophobic, is presented. In particular, hydrophobic surfaces obtained via sol-gel method using hybrid organic-inorganic sol-gel silica coatings functionalized with methyl and phenyl groups are analyzed. This type of surfaces paves the way to a cheap and green route to promote stable DWC on metal substrates without using fluorocarbons or controlled roughness patterns. Indeed, the hydrophobic behavior due to methyl/phenyl groups allows to promote DWC and at the same time  $\text{SiO}_2$  represents a good barrier to chemical agents and provides resistance to mechanical stress. Condensation tests proved that, while these coatings are barely hydrophobic, exhibiting contact angles similar to untreated aluminum, condensation of steam occurs in dropwise mode reaching values of heat transfer coefficient (HTC) up to  $250 \text{ kW m}^{-2} \text{ K}^{-1}$ , among the highest obtained during DWC on metallic substrates, and duration of more than 100 hours with heat flux of  $400 \text{ kW m}^{-2}$ . Furthermore, the robustness and performances of such coating at different vapor velocities, from  $2.7 \text{ m s}^{-1}$  to  $11 \text{ m s}^{-1}$ , is assessed. The experimental data are compared against DWC models proposed in the past 50 years by different research groups. Such models describe the phenomena that take place during dropwise condensation: the nucleation of a droplet until its departure, the heat exchanged by the drop during its lifetime and the droplets population on the surface. The conduction through thin film ( $\approx 200 \text{ nm} - 300 \text{ nm}$ ) is also discussed for its importance to the process.

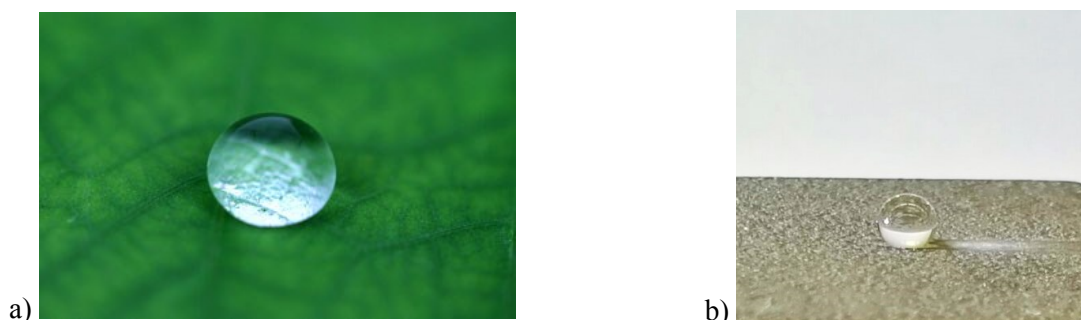
The experimental campaign is conducted at the Two-phase Heat Transfer Laboratory of the University of Padova with the collaboration of the Material Science Engineering laboratory for the surfaces development.





# Chapter 1 – Introduction

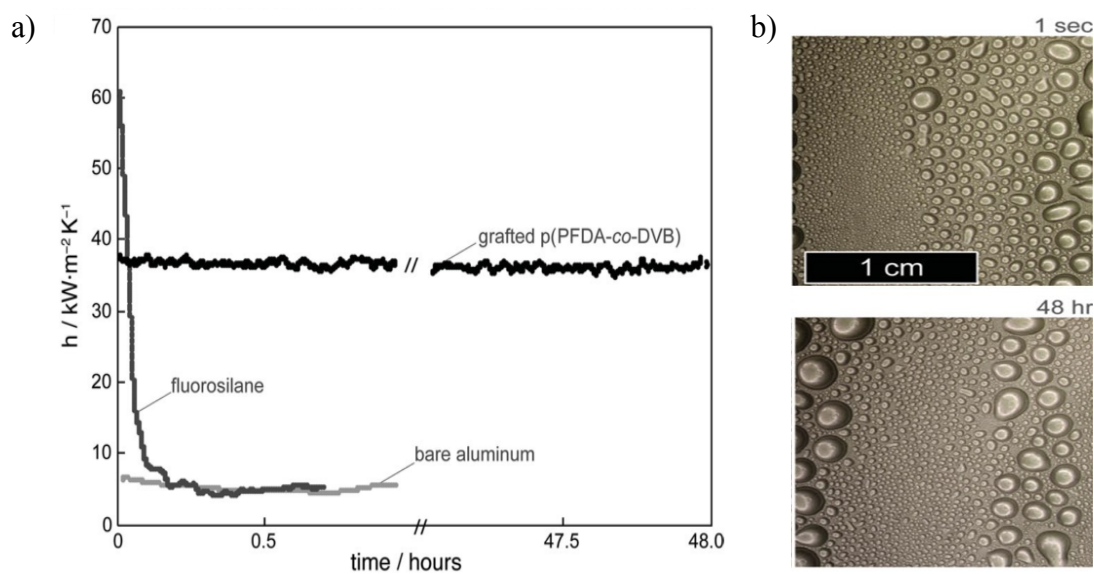
The condensation of steam occurs in many applications. For example, it is essential for production of electrical energy<sup>1</sup> (the condenser is one of the main components in a thermal power plant) and for production of freshwater in desalination plants<sup>2</sup> or in dew water harvesting<sup>3</sup>. A solution to enhance the condensation heat transfer process is to promote and maintain dropwise condensation (DWC)<sup>4-6</sup> instead of the classic filmwise condensation (FWC), in fact it is well established that the DWC mode can lead up to several times higher heat transfer coefficients as compared to FWC<sup>5,7</sup>. The DWC needs, however, surfaces that repel water<sup>8-12</sup>. These "smart" surfaces can find application in real processes, both condensation (vapor/liquid) and solidification (liquid/solid), increasing the efficiency of current industrial processes and bringing huge benefits for different applications. Hydrophobic/superhydrophobic surfaces are often related to the “Lotus effect” of the famous leaf on which water droplets sit over it quasi-spherically. In Figure 1.1 a comparison between a water droplet on a lotus leaf and on an aluminium treated superhydrophobic surface obtained in our laboratories<sup>5</sup> is shown.



**Figure 1.1 - Water drop on a lotus leaf (left) and on a superhydrophobic-treated aluminium surface<sup>5</sup> (right). The picture on the right is taken at the Two Phase Heat Transfer Lab of the University of Padova**

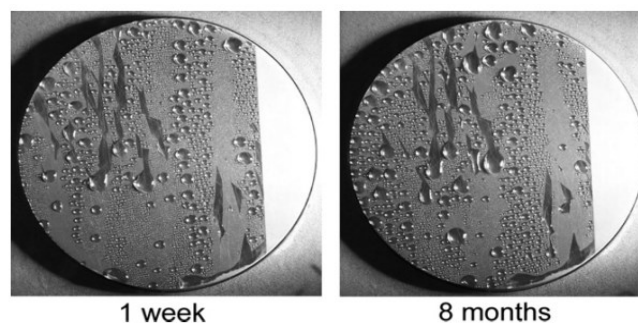
So far, in industrial applications, condensation occurs in filmwise mode, without exploiting the potentiality of the dropwise mode. The key problem is to devise reliable treatments that are able to promote long-lived dropwise condensation under industrial conditions<sup>13</sup>. Metals are still the family of materials most used in the heat transfer applications, from steel<sup>14-17</sup> to copper<sup>6,18,19</sup>. Since clean solid metal surfaces are hydrophilic<sup>20</sup>, one solution to achieve DWC is to apply a low-surface-energy coating. The degradation of the hydrophobic treatments is the main issue at which looking for, and a proper surface characterization before and after the tests is important for a better understanding of the phenomena. Thanks to the developments in the material science, new techniques for constructing both hydrophobic and superhydrophobic surfaces have been discovered in the recent years. Although great successes have been achieved in the fabrication of functional surfaces, most of these techniques

are subjected to certain limitations, such as severe conditions, expensive materials, poor durability, leaving the robustness of those treatments an open issue. A complete overview of the principal hydrophobic treatments is presented by Enright et al.<sup>4</sup> with their drawbacks. While on copper substrates satisfactory results in terms of lifetime have been obtained<sup>21,22</sup>, treatments on aluminum have yet to reach sufficiently long lives for an industrial use<sup>23,24</sup>. Paxson et al.<sup>23</sup> report the sustained dropwise condensation of steam on a thin film of poly-(1 H ,1 H ,2 H ,2 H-perfluorodecyl acrylate)-co -divinyl benzene p(PFDA- co -DVB) grafted to an aluminum substrate by initiated chemical vapor deposition (iCVD). The coating was tested for 48 hours and it did not show clear signs of deterioration. The HTC measured during DWC remained around  $35 \text{ kW m}^{-2} \text{ K}^{-1}$ ; value 7 times higher than the coefficient obtained during FWC on the uncoated sample (Figure 1.2).



**Figure 1.2 - a) HTC of aluminum substrates with no coating, with a fluorosilane coating, and with a grafted p(PFDA-co-DVB) coating, plotted vs. time<sup>23</sup>. b) Photographs during condensation of saturated steam at  $100^\circ\text{C}$  and  $101 \text{ kPa}$  of prolonged dropwise condensation on grafted coating over a period of 48 hours.**

Rausch and co-workers<sup>24</sup> also achieved impressive results regarding sustained DWC on aluminum substrate (Figure 1.3). The surface is treated with ion selective ion beam implantation technology with an ion dose of  $10^{16} \text{ N}^+ \text{ cm}^{-2}$  at an implantation energy of  $20 \text{ keV}$ . However, the HTC enhancement compared to FWC was limited to less than 100%.



**Figure 1.3 - Time behavior of DWC after one week and after 8 months from the test begin<sup>24</sup>.**

As regards copper substrate, interesting results have been obtained by Vemuri *et al.*<sup>21</sup> and by June *et al.*<sup>25</sup> where the surfaces have been treated with self-assembled monolayer (SAM). Both the research group obtained prolonged DWC, 2600 hours and 500 hours, with HTC around  $50 \text{ kW m}^{-2} \text{ K}^{-1}$  and  $20 \text{ kW m}^{-2} \text{ K}^{-1}$ , respectively. The hydrophobic treatment then has to be properly designed and optimized. From the heat transfer point of view, minimizing the thickness of the layer is essential, in fact, usually the thermal conductivity of these layers ( $0.2 \text{ W m}^{-1} \text{ K}^{-1}$ )<sup>26,27</sup> is very low compared to the thermal conductivity of the metallic substrate ( $200 \text{ W m}^{-1} \text{ K}^{-1}$  as regards aluminum). A wide range of HTC can be found in literature for DWC of pure steam at atmospheric pressure: during DWC on metallic substrate, the HTC ranges from  $1\text{-}2 \text{ kW m}^{-2} \text{ K}^{-1}$ <sup>16,28-30</sup> up to tens of  $\text{kW m}^{-2} \text{ K}^{-1}$ <sup>5,6,21-23,31</sup>; the high dispersion of HTC values is related to the high variety of DWC promoters. Often, the thermal resistance of the hydrophobic layer can be the main resistance in the heat transfer process, greatly influencing the overall HTC during the condensation process<sup>26,27</sup>. If the conductivity and the thickness of the hydrophobic layer are known, the HTC of the DWC phenomenon itself can be calculated: an evaluation is reported in Rose<sup>13</sup>. On the other hand, in industrial and energy applications the fundamental parameter is the overall HTC, accounting also for the thermal resistance of the hydrophobic layer. To the best of the authors' knowledge, when comparing results in terms of overall HTC (thermal resistance between steam and metallic substrate) the highest value measured with pure steam is obtained on a copper substrate plated with gold<sup>32</sup> which, due to its high thermal conductivity, does not add any significant thermal resistance to the heat transfer (about  $250 \text{ kW m}^{-2} \text{ K}^{-1}$ ).

A wide experimental campaign has been conducted on the optimization of the surface morphology (imparting a controlled roughness) for further enhance the HTC during DWC. In this case, a drop may assume different states described by the equations of Wenzel<sup>33</sup> and Cassie-Baxter<sup>34</sup>. The mobility of a droplet is described by the advancing contact angle, the maximum angle which takes the drop while expanding, and the receding contact angle, the minimum angle that the drop has while withdrawing<sup>35,36</sup>. The difference between the advancing and receding contact angle is called contact angle hysteresis which is related to the adhesion energy of the liquid to the surface, thus the droplet mobility<sup>37,38</sup>. The maximum mobility for a droplet will be obtained on superhydrophobic surfaces, where the Cassie-Baxter state is reached, thanks to the role of roughness<sup>39-41</sup>. Theoretically, to increase the performance of the condensation, the number of the nucleation sites and the mobility of the droplets should be increased, thus, surfaces with low surface energy and high roughness should be required. Actually, the mechanism is highly affected by the fluid. In presence of non-condensable or low thermal flux the Cassie-Baxter regime can be obtained<sup>4,42</sup>. In presence of pure saturated vapor or at high thermal flux<sup>43</sup>, the Wenzel state or even the flooding of the surface may occur<sup>44</sup>. In the

Wenzel state the mobility of the droplets is limited since they are retained within the roughness and, moreover, this leads to an additional thermal resistance proportional to the amplitude of the roughness. Thus, the surfaces with the highest droplet mobility in atmospheric conditions does not guarantee the highest performance during condensation of steam. In fact, several authors measured higher heat transfer coefficients (HTCs) on smooth hydrophobic surfaces than those measured on superhydrophobic surfaces<sup>31,42,45</sup>. The jumping droplets condition represents a separate case: this mechanism is typical of low values of heat transfer (below of  $100 \text{ kW m}^{-2}$ ) and produces very high HTC on superhydrophobic surfaces<sup>42,46-48</sup>.

Moreover, water repellent surfaces are required not only for enhancing the condensation performance but also for the delay of ice and frost formation<sup>49-52</sup>. Ice accumulation can cause problems to power lines and hazardous conditions on aerodynamic wing structures. Frost formation can reduce the performance of HVAC systems. Thus, de-icing and defrosting are periodically required in most applications. Frosting process over a surface generally began with the condensation of the moisture in the air, which forms condensate droplets that freeze. The ice formation is, then, not instantaneous, a certain amount of time is required for the phase transition<sup>53</sup>. Then, frost crystals grow on the surface of the droplets and gradually form a frost layer; the frost layer continues to grow and when the frost layer stops growing in thickness, the diffusion of water vapor into the porous medium leads to the increase of the frost layer density<sup>54</sup>. Since the operating conditions of ice-phobic surfaces can vary significantly, from the case of evaporators in HVAC systems, where humid air is in contact with a subcooled surface, to the case of airplane wings, where subcooled liquid (clouds) impact at high velocities into a surface, several tests have been identified in order to determine the icephobicity of surfaces. For example, the bouncing of water droplets over the surface can be studied<sup>50</sup>. Some preliminary tests of water jumping droplets have been conducted on different coatings, for further characterize such treatments for assessing their capability as water-repellant surfaces.

The present work reports a study of DWC on smooth and roughened metallic substrates in saturated vapor conditions. Aiming at a low environmental impact of the fabrication process, for example the fluorine element should be preferably avoided although it has very good water repellent characteristic<sup>55-57</sup>, a viable “green” alternative to the hydrophobic treatments is presented. The hydrophobicity has been studied on machined surface to eliminate as much as possible the effect of roughness and to promote homogeneity of the coating. The objective is to obtain a more compact and dense film, more resistant both to mechanical and chemical stresses, through an acidic sol gel

reaction. A mild hydrophobic behavior is achieved, instead of using fluorinated compounds, using silica precursors with hydrophobic groups and graphene. Both thermal and fluid dynamics analyses will be presented on more than 10 coatings which promoted DWC. An extended theoretical analysis about the DWC phenomenon is, also, reported. Five different models, developed in more than 50 years, have been compared to the experimental data.



# Chapter 2 – Heat transfer during condensation

In this Chapter, the theory beyond the condensation heat transfer process is presented. Condensation on a surface is a nucleation process, starting from cluster of molecules bonded to the surface at the nucleation sites ( $N_s$ ), evolving with the passing time in two modes: filmwise and dropwise mode. The condensation evolution, which then reaches a steady state, is controlled by the interaction between the surface and the liquid and the vapor phases of the substance which has to be cooled. The interaction between the three phases is called wettability, which means that controlling the surface wettability the condensation mode can be determined. To the author's knowledge, there is no a common definition for the identification of the condensation regime from the wettability of a certain surface. However, it is commonly accepted that in order to obtain DWC, hydrophobicity has to be pursued. The first paragraph of this Chapter, then, is focused on describing the wettability. As already reported in Chapter 1, since DWC discovery in 1930 by Schmidt *et al.*<sup>58</sup>, it has attracted significant attention due to its superior heat transfer performance compared with filmwise condensation. This is due to from the fact that the absence of condensate film and the continuous surface renewal by falling large drops drastically reduce the global thermal resistance improving the heat transfer. Unlike filmwise condensation where the liquid condensate forms a continuous film over the surface, dropwise condensation can be described as a combination of time-spatial random processes such as initial drop formation, drop growth, and departure of large drops. The film formation during FWC and the droplet population during DWC heat transfer performance are discussed below from a theoretical point of view. At the end of this Chapter, a brief discussion about the heat transfer process through thin film ( $\approx 200$  nm) is presented. In fact, changing the surface energy means, most of the time, adding a hydrophobic layer to the surface. The thickness of these layers is such low that the Fourier's law is not valid.

## 2.1 Wettability

The wettability phenomenon is fully analyzed in the book of de Gennes<sup>12</sup> and co-workers, here a brief summary is reported concerning the fundamental parameters for the DWC<sup>59-61</sup>. During DWC, the condensate assumes spherical cap shape until the gravity effect can be neglected (capillarity length<sup>12</sup>), then droplets start to slide with an elongated form when they reach their departing diameter. All the shapes assumed by droplets are the result of the interaction of surface energy of the liquid and the solid matter. The wettability of a surface describes the interaction between the solid and a liquid in



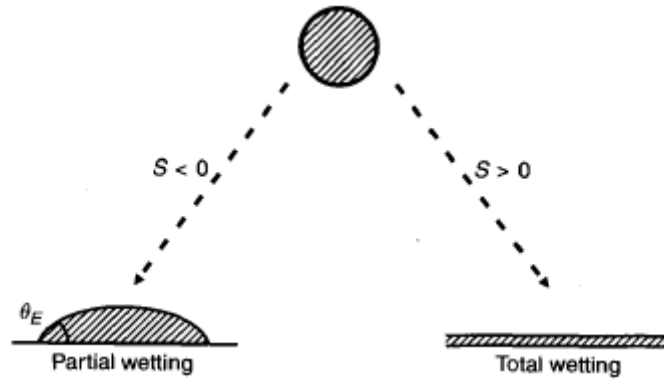
presence of a gaseous phase, the condensation case the gas is saturated vapor. The wettability is fully described by the contact angle ( $\theta$ ), defined as the angle formed by the tangent to the liquid-gas interface, and by the tangent to the solid-liquid interface<sup>11</sup>. The point of solid-liquid-gas interfaces is called contact line or contact triple line. For simplicity, the gas phase is neglected from now on. The liquid can assume different shapes on the surface, if the surface is considered ideal the liquid assumes a spherical cap with different heights depending on how strong the bonds between the phases. The phenomenon is due to the combination of complex processes, of which some originate at the nano-microscale<sup>37,62</sup> and can be explained in terms of chemical-physical properties of the surface and of the fluid and of long-range Van der Waals interactions<sup>63</sup>. Among the various properties of the surface certainly the most interesting is its free energy, which related to the surface tension of a liquid, can be used to estimate  $\theta$ <sup>64</sup>. The interaction between molecules of the same material is governed by attractive forces, defined as cohesion forces, while between different material adhesion forces are originated<sup>65</sup>. Molecules, which are disposed at the material boundary, loses half of its cohesive interactions. In liquids, surface molecules tend to move towards the bulk where all the bonds will be fulfilled and consequently liquids tend to expose the minimum surface area reached through a spherical shape. The work  $dW$  required to distort a liquid to increase its surface area by an amount  $dA$  is proportional to the number of molecules that must be brought up to the surface and it can be written as

$$dW = \gamma \cdot dA \quad (2.1)$$

where  $\gamma$  is the surface tension, which is the energy (or work) which must be supplied to increase the liquid by one unit area and it can be expressed as  $\text{J m}^{-2}$  or  $\text{N m}^{-1}$ . Regarding solids, the surface free energy is the excess energy that is on the surface similarly to the liquids case. For solids in general it is possible to distinguish two types of surfaces:

- high energy surfaces: the bonds that hold atoms together are chemical (covalent, ionic or metallic bonds) and are very strong. Most liquids can completely wet a high-energy surface;
- low energy surfaces: the molecules are constrained by physical forces (Van der Waals bonds or hydrogen bridge bonds). Such surfaces are wettable only by low surface tension liquids such as hydrocarbons or molecular liquids.

The combined effect of the surface energy of the liquid and of the solid on the wettability can be observed in the following:

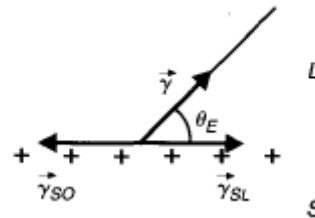


**Figure 2.1 - The two wetting regime for sessile drop<sup>12</sup>**

In Figure 2.1 the spreading parameter<sup>65,66</sup> is introduced, which measures the difference between the surface energy (per unit area) of the substrate when dry and wet

$$S = \gamma_s - (\gamma_{sl} - \gamma) \quad (2.2)$$

where  $s$  is solid and  $l$  liquid,  $\gamma$  alone is related to the liquid surface tension. When  $S > 0$  the liquid partially wets the surface, the limit case is when the droplet assumes a perfect spherical shape, whereas  $S < 0$  the interaction between the solid-liquid is very strong and total wetting is reached. When  $S > 0$  the droplet can displays different angle with the solid as can be inferred from Figure 2.2.



**Figure 2.2 - Surface tensions balance at the triple line<sup>12</sup>.**

The surface tensions balance lead to the Young<sup>67</sup> formulation for the equilibrium contact angle  $\theta$  or  $\theta_E$

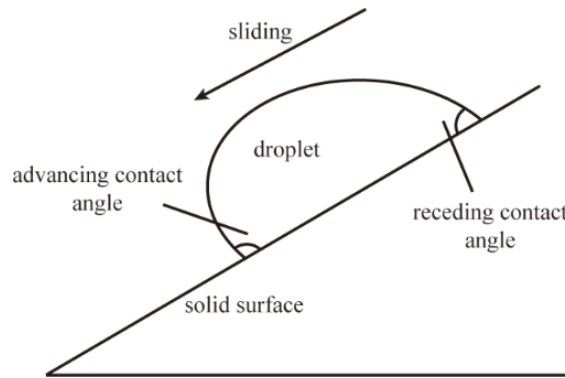
$$\gamma_l \cdot \cos \vartheta = \gamma_s - \gamma_{sl} \quad (2.3)$$

However, Equation 2.3 is exclusively applicable to a perfectly smooth and chemically homogeneous surface<sup>10</sup>. In reality, solid surfaces are never perfectly smooth and always present small local variations of the composition, also due to a possible absorption of atoms, molecules or ions. These superficial imperfections lead to another characteristic parameter of DWC process, i.e. the formation of an angle of hysteresis. It is in fact known that when a drop is made to expand on a surface and then it is slowly withdrawn, or it is slowly put into motion, two distinct contact angles are shown: the

advancing contact angle ( $\theta_a$ ) and the receding contact angle ( $\theta_r$ )<sup>68</sup>, the difference between these two angles is called hysteresis<sup>35,36</sup> ( $\Delta\theta$ ) and is caused by three different factors:

- inhomogeneity of the surface composition;
- surface roughness;
- impurities on the surface.

Hysteresis plays a very important role in the shape of a drop in an inclined substrate, high hysteresis deforms the droplet shape in gravity field direction assuming a stable position at the equilibrium between the gravity force and the deformation force (Figure 2.3). If the gravity force is higher than the adhesion force of the droplet, which is proportional to the solid-liquid surface tension, the droplet starts to move in the direction of the resulting force. The angle assumed at the contact line in the moving direction is  $\theta_a$ , at the opposite is  $\theta_r$ . All along the contact line, the droplet assumes angles in between the two. In a sense, the  $\theta_a$  is the angle assumed by the liquid moving toward dry solid, whereas the  $\theta_r$  is the angle assumed by the liquid moving toward the wet surface.



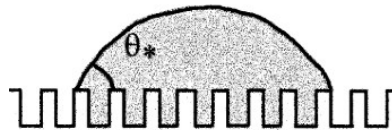
**Figure 2.3 - Droplet dynamic on inclined surface. Advancing and receding contact angle are highlighted.**

Higher the value of hysteresis, lower will be the mobility of the droplet, the surface presents several defects at the nano-micro scale which prevent the drop motion. During DWC the optimum scenario is, then, having zero hysteresis in order to promote droplet mobility and to prevent the liquid stagnation on the surface which adds a thermal resistance. The main cause for the hysteresis is the surface roughness. The first who gave an explanation of the effect of the roughness on the contact angle was Wenzel<sup>69</sup> in 1936 [5], who proposed the following equation to determine the apparent contact angle:

$$\cos \vartheta_w = r \cdot \cos \vartheta \quad (2.4)$$

where  $r$  is the degree of roughness ( $r = 1$  in the case of completely smooth surface, while  $r > 1$  for rough surfaces) and  $\theta$  is the angle calculated according to the Young equation. The degree of

roughness is obtained by the ratio between the true and projected surface area, defining as true surface area the area actually wet by the drop, while it is defined projected surface area (or apparent, or geometric) the projection of the drop on the geometric plane of the surface. On surfaces with  $\theta < 90^\circ$  the roughness will decrease the angle between the liquid and solid, vice versa where  $\theta > 90^\circ$  is valid, the roughness will increase that angle. The surface roughness amplifies hydrophilicity or hydrophobicity of the surface. From a physical point of view, since a liquid tends to spread more on a hydrophilic media, the droplet advancing encounters air pockets<sup>11</sup> due to the roughness (see Figure 2.4) and it assumes an angle higher than the angle assumed on a dry surface (the contact angle of a liquid in air is  $180^\circ$ ) because the movement becomes not thermodynamically favorable, the droplet has to change its shape according to the surface tensions balance. It is remembered that the most thermodynamic preferred shape is the spherical shape. On the contrary, while receding, the droplet is entrapped within the surface roughness (hydrophilic) and it needs a higher shape deformation for moving. This is why the contact angle varies compared to a smooth surface.

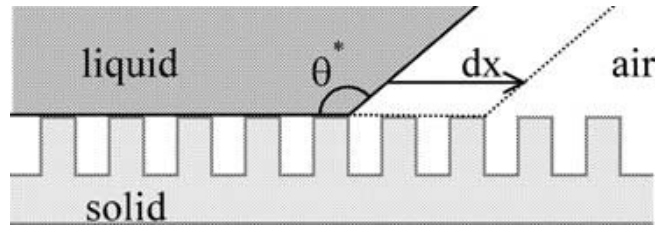


**Figure 2.4 - Wenzel regime: the surface is dry ahead the contact line<sup>70</sup>.**

A similar reasoning can be applied to a drop on a chemically heterogeneous surface, in which case the apparent contact angle ( $\vartheta_c$ ) can be calculated using the relation proposed by Cassie-Baxter<sup>34</sup>, which for two different components can be written in the form:

$$\cos \vartheta_c = f_1 \cdot \cos \vartheta_1 + f_2 \cdot \cos \vartheta_2 \quad (2.5)$$

where  $\vartheta_1$  and  $\vartheta_2$  are the contact angles according to the Young equation for component 1 and component 2 respectively, while  $f_1$  and  $f_2$  are the area fractions occupied by component 1 and component 2 ( $f_1 + f_2 = 1$ ). The value of  $\vartheta_c$  will therefore be restricted in the interval  $[\vartheta_1, \vartheta_2]$ . The cosine of the apparent angle is therefore an average of the cosines of the Young contact angles proportional to the occupied area of each component. It should be pointed out that area factors are related to flat surfaces<sup>71</sup>. If one of the components is air<sup>72</sup>, the configuration of the droplet is displayed in Figure 2.5.

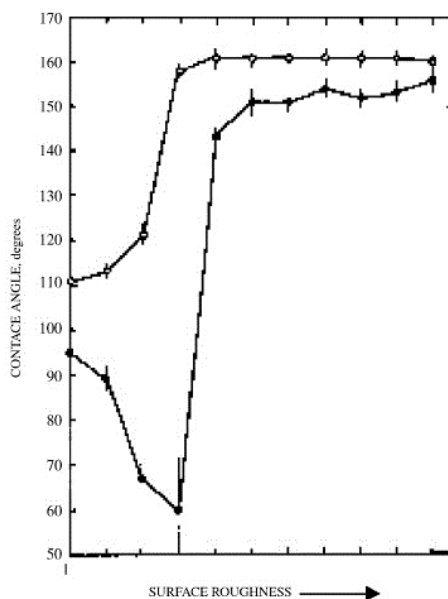


**Figure 2.5 - Cassie-Baxter regime: air is trapped below the liquid, inducing a composite interface between the solid and the drop.**

In this case, the drop does not wet the entire underlying surface, but only lies on the peaks of the surface roughness, leaving air trapped between them. The result is a heterogeneous surface consisting of the substrate material and air. This situation allows to considerably increase the hydrophobicity of a surface, because the contact angle between air and water is  $180^\circ$ . Remember that the model presented above can also be extended to surfaces without roughness and composed of more than two materials. In this case, by extension of the formula 2.5 the equation is as follows:

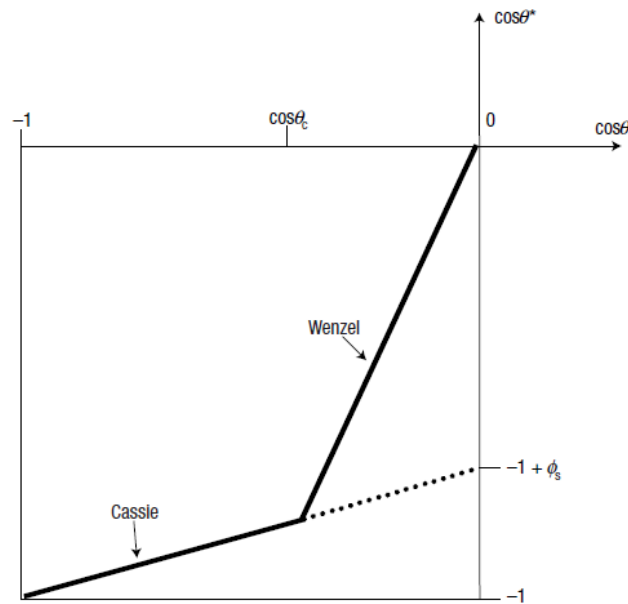
$$\cos \vartheta_c = \sum_i^n f_i \cdot \cos \vartheta_i \quad (2.6)$$

where  $n$  is the number of components present on the surface. It must be pointed out that both Wenzel and Cassie-Baxter Equations are applied to the contact line<sup>9</sup>. Both Wenzel and Cassie-Baxter wetting regime can be achieved for enhancing hydrophobicity of the surface aiming at obtaining perfectly spherical droplet. Experimentally, the two states cannot survive at the same surface roughness (besides some metastable state<sup>8</sup>) an interesting experiment is reported in Figure 2.6<sup>73</sup>.



**Figure 2.6 - Advancing (empty dot) and receding (full dot) contact angle in function of surface roughness<sup>73</sup>.**

There is a certain value of roughness<sup>70,74</sup>, which can be obtained imposing an optimized double-scale roughness<sup>38,39,75-77</sup>, which permits to entrap air inside the roughness and consequently to increase the receding contact angle. Likewise, a critical angle is possible to identify as boundary between the two regimes<sup>8</sup> as reported in Figure 2.7. In Figure 2.7,  $\phi_s$  is the solid fraction ( $f_l$  in Equation 2.6) and  $\theta_c$  is the critical angle.



**Figure 2.7 - Wenzel and Cassie-Baxter regimes<sup>8</sup>.**

Now, it is possible to fully describe the solid-liquid interaction by determining the dynamic ( $\theta_a$  and  $\theta_r$ ) and static contact angles ( $\theta$ ), in the case where the liquid perfectly wets the surface the angle is zero, whereas when the drop is perfectly spherical,  $\theta = 180^\circ$ , there is a perfect situation of non-wettability. In the middle of the two ideal conditions there are intermediate situations for which the contact angle is  $0^\circ < \theta < 180^\circ$ . In these intermediate situations it is possible to carry out a further classification based on angles. In literature different definitions can be found<sup>78</sup>, here it is reported the most common shared:

- $0^\circ < \theta \leq 90^\circ$ : hydrophilic surface;
- $90^\circ < \theta \leq 140^\circ$ : hydrophobic surface;
- $\theta_a > 150^\circ$  and  $\Delta\theta < 10^\circ$ : superhydrophobic surface.

Law<sup>79</sup> suggests to use  $\theta_r$  instead of  $\theta$  for the threshold of phobicity and philicity. The maximum mobility for a droplet is then obtained on so-called superhydrophobic surfaces, where the Cassie-Baxter state is reached, thanks to the role of roughness<sup>39-41</sup>. The classification of a surface is not particularly important though, instead, the idea should be to relate the phenomenon with the field of existence of the phenomenon itself. In the present case an open question remains: what is the

relationship between contact angles and condensation mode? Or, what is the fundamental contact angle for the dropwise condensation? There are several authors<sup>7,80</sup> that try to answer to those questions, but a full comprehensive study is not reported yet.

## **2.2 Filmwise condensation**

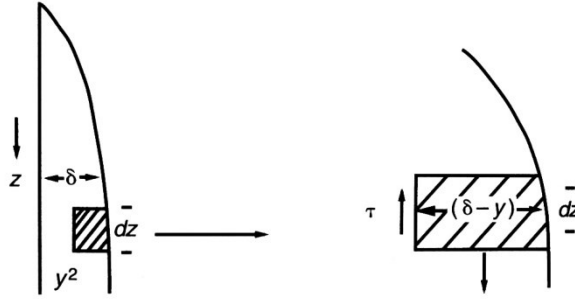
During FWC on vertical surfaces the condensing steam forms a continuous film of liquid over the surface where heat exchange occurs. In this mechanism of condensation there are various thermal resistances, among these, however, is worth considering only the resistance given by the condensate layer of surface liquid, being this much greater than the other. If the film of liquid moves in a laminar state, heat is transferred by conduction. Therefore, a thin condensate film presents less thermal resistance and thus higher heat transfer coefficient compared to a thicker film. The vapor can condense on a vertical surface in static or dynamic conditions. In the first case, the liquid film is influenced only by the force of gravity, in the second case even by the tangential forces due to the steam velocity. Other factors that affect the HTC, besides the speed of the steam, the thickness of the film and to the turbulence of the motion, are the presence of waves on the film, the drag and the deposition of the droplets, the presence of splashing of condensate and the degree of subcooling of the liquid. For the readers' convenience, the theory beyond the filmwise condensation is briefly reported here from my previous works<sup>44,81</sup>.

### **2.2.1 Gravity controlled condensation**

Hence the theory of Nusselt<sup>82,83</sup> (1916) for the calculation of the heat transfer coefficient  $\bar{\alpha}_{grav}$  during laminar film condensation in stagnant condition on vertical surfaces is presented. This theory is valid under following hypothesis:

- the condensate forms a continuous film that flows under the effect of gravity;
- the steam has zero velocity;
- the fluid is in laminar regime;
- pure fluid at constant pressure;
- the temperature difference through the film of liquid is constant;
- the fluid is a Newtonian one;
- the properties of the film are constant.

The treated situation is illustrated in Figure 2.1, which points out how the condensate film thickness  $\delta$  increases along the plate.



**Figure 2.8 – Gravity controlled condensation on a vertical surface.**

At a distance  $z$ , we may write a force balance for a unit width of condensate film between the shear force  $\tau$  and the gravitational force on the element highlighted in Figure 2.8:

$$\tau dz = (\rho_l - \rho_v)g(\delta - y)dz \quad (2.7)$$

where  $\rho_l$  is the liquid density,  $\rho_v$  is the vapor density,  $g$  is the gravity acceleration and  $y$  is the coordinate in the direction of the liquid. The shear force is related to the velocity gradient within the liquid film

$$\tau = \mu_l \frac{du}{dy} \quad (2.8)$$

where  $\mu_l$  is the liquid viscosity. Combing Eq. (2.7) and Eq. (2.8) it is obtained

$$\frac{du}{dy} = \frac{(\rho_l - \rho_v)g}{\mu_l}(\delta - y) \quad (2.9)$$

which may be integrated to give

$$u = \frac{(\rho_l - \rho_v)g}{\mu_l} \left( \delta y - \frac{y^2}{2} \right) + C \quad (2.10)$$

since  $u=0$  at  $y=0$ , it is  $C=0$ . The mean velocity in the liquid film  $\bar{u}$  is given by

$$\bar{u} = \frac{1}{\delta} \int_0^\delta u dy = \frac{(\rho_l - \rho_v)g}{\mu_l \delta} \int_0^\delta \left( \frac{\delta y - y^2}{2} \right) dy = \frac{(\rho_l - \rho_v)g \delta^2}{3\mu_l} \quad (2.11)$$



defining  $\Gamma$  as the mass flow in the film per unit width, then it follows that

$$\Gamma = \rho_l \bar{u} \delta = \frac{\rho_l (\rho_l - \rho_v) g \delta^3}{3 \mu_l} \quad (2.12)$$

and the local liquid film thickness is thus given by

$$\delta = \left[ \frac{3 \mu_l \Gamma}{\rho_l (\rho_l - \rho_v) g} \right]^{1/3} \quad (2.13)$$

$\Gamma$  increases down the surface as a result of the condensation process. If the local condensation rate per unit surface area of the liquid film is  $\dot{m}$ , then we can write

$$\frac{d\Gamma}{dz} = \dot{m} = \frac{\dot{q}}{r'} = \frac{\rho_l (\rho_l - \rho_v) g \delta^2}{\mu_l} \frac{d\delta}{dz} \quad (2.14)$$

where  $\dot{q}$  is the heat flux. The parameter  $r'$  is the heat transferred to the surface and includes both latent and sensible heat transferred in the liquid phase per unit width between  $T_{SAT}$ , the temperature of saturation, and  $T_{WALL}$ , the temperature of the wall. If the surface is maintained at a constant temperature  $T_{WALL}$  and the film is in laminar flow, then  $\dot{q}$  is calculated by considering the conduction process through the film, i.e.

$$\dot{q} = \frac{(T_{SAT} - T_{WALL}) \lambda_l}{\delta} \quad (2.15)$$

where  $\lambda_l$  is the liquid thermal conductivity. Combining Eq. (2.14) and Eq. (2.15)

$$\delta^3 \frac{d\delta}{dz} = \frac{\mu_l \lambda_l (T_{SAT} - T_{WALL})}{\rho_l (\rho_l - \rho_v) g r'} \quad (2.16)$$

and integrating with the boundary condition that  $\delta=0$  at  $z=0$ ,

$$\delta^4 = \frac{4 \mu_l \lambda_l (T_{SAT} - T_{WALL}) z}{\rho_l (\rho_l - \rho_v) g r'} \quad (2.17)$$

The local liquid film heat transfer coefficient  $\alpha_{Nu}$  is defined as

$$\alpha_{Nu} = \frac{\dot{q}}{T_{SAT} - T_{WALL}} \quad (2.18)$$

and from foregoing equations it follows

$$\alpha_{Nu} = \frac{\lambda_l}{\delta} = \left[ \frac{\lambda_l^3 \rho_l (\rho_l - \rho_v) g r'}{4 \mu_l (T_{SAT} - T_{WALL}) z} \right]^{1/4} \quad (2.19)$$

It's often convenient to define a mean heat transfer coefficient  $\bar{\alpha}_{Nu}$  over the plate length  $L$

$$\bar{\alpha}_{Nu} = \frac{1}{L} \int_0^L \alpha_{Nu} dz = 0.943 \left[ \frac{\lambda_l^3 \rho_l (\rho_l - \rho_v) g r'}{\mu_l (T_{SAT} - T_{WALL}) L} \right]^{1/4} \quad (2.20)$$

By considering the liquid flow rate  $\Gamma_L$  at a specific coordinate  $L$  from the top

$$\Gamma = \frac{\bar{\alpha}_{Nu} (T_{SAT} - T_{WALL}) L}{r'} \quad (2.21)$$

$\bar{\alpha}_{Nu}$  becomes

$$\bar{\alpha}_{Nu} = 0,925 \left[ \frac{\lambda_l^3 \rho_l (\rho_l - \rho_v) g}{\mu_l \Gamma} \right]^{1/3} \quad (2.22)$$

It is also convenient to rewrite  $\bar{\alpha}_{Nu}$  in terms of Reynolds number  $Re$

$$Re = \frac{D_h \Gamma}{\mu_l \delta} = \frac{4\Gamma}{\mu_l} \quad (2.23)$$

where  $D_H$  is the hydraulic diameter

$$D_h = \frac{4P\delta}{P} = 4\delta \quad (2.24)$$

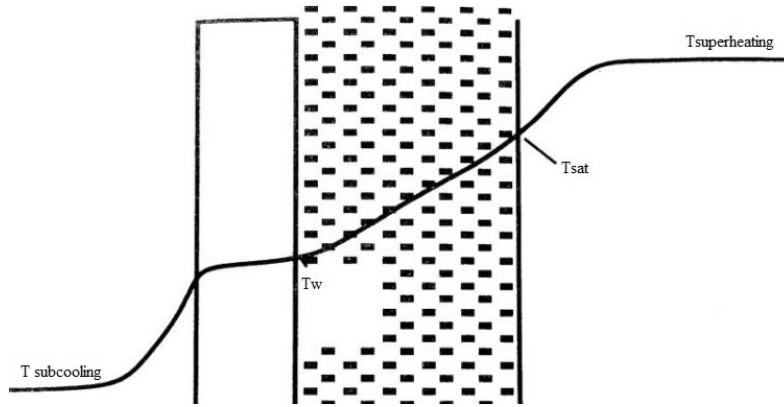
thus it is

$$\bar{\alpha}_{Nu} = 1,47 \left[ \frac{\lambda_l^3 \rho_l (\rho_l - \rho_v) g}{\mu_l^2} \right]^{1/3} Re^{-1/3} \quad (2.25)$$

The Nusselt theory is a simplified theory of condensation, thus for comparison with experimental processes, therefore a number of additional effects should be considered<sup>83,84</sup>:

- Subcooling. Since there is a temperature gradient in the film of liquid, the liquid near the wall is subcooled and the mean temperature  $T_L$  of liquid is lower than the saturation one.
- Inertia. Vapor condensing over the liquid film should not be assumed to be static, because it has to accelerate to the film velocity leading to inertia effects, as studied by Chen (1961)<sup>85</sup>.
- Vapor superheat. If vapor is superheated it has to be cooled from his bulk temperature to the interface saturation temperature, adding to the process a thermal resistance.
- Interfacial waves. Falling liquid film forms waves that grow along the surface. Some experiments by Van de Walt and Kroger (1974)<sup>84</sup> showed that experimental heat fluxes were 5 to 10% greater, because of waves presence, than those predicted from the Nusselt theory.

The profile temperature accounting for all previous effects is shown in Figure 2.9.



**Figure 2.9 – Condensation of a superheated vapor.**

The heat transfer coefficient in gravity controlled condensation is thus calculated

$$\bar{\alpha}_{grav} = 1.15 \left[ 0.0206 \left( \frac{r' \mu_l}{\lambda_l (T_{SAT} - T_{WALL})} \right)^{0.5} + 0.79 \right] \bar{\alpha}_{Nu} \quad (2.26)$$

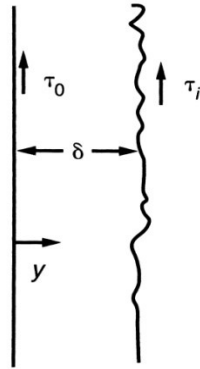
The multiplicative factor 1.15 was introduced by Baehr and Stephan<sup>84</sup> (2004) to consider the enhancement of  $\bar{\alpha}_{grav}$  due to film waves. The term between square parenthesis is used to consider the inertia effect and was added by Depew and Reisbig<sup>86</sup> (1964). The liquid subcooling is finally accounted by calculating the thermodynamic proprieties of the condensate at the mean temperature

$$T_l = 0.75T_{WALL} + 0.25T_{SAT} \quad (2.27)$$

meanwhile only vapor properties are calculated at  $T_{SAT}$ <sup>87</sup>.

### 2.2.2 Shear controlled condensation

When there are high vapor velocities, the heat transfer coefficient  $\alpha_{ss}$  is controlled by the shear of the vapor, indeed the interfacial shear becomes significant compared to the gravitational force on the liquid phase. The first aspect for the calculation of  $\alpha_{ss}$  is the regime of motion of the liquid film. Laminar flow of the condensate is the most common situation. If the speed of vapor is high enough the effect of gravity on the two-phase process could be ignored, leading to the shear controlled condensation mode. A scheme of the process is illustrated in Figure 2.10.



**Figure 2.10 – Shear forces on a liquid film in laminar regime.**

The film thickness is  $\delta$ , the interfacial shear stress is  $\tau_i$  and the wall shear stress is  $\tau_0$ . If the interfacial shear stress dominates, then  $\tau_i \approx \tau_0$  and we can write

$$\mu_l \frac{du}{dy} = \tau_0 = \tau_i \quad (2.28)$$

Where  $u$  is the liquid velocity within the film at a distance  $y$  from the wall. Integrating with the condition  $u=0$  at  $y=0$ , we have

$$u = \frac{\tau_0 y}{\mu_l} \quad (2.29)$$

thus, the mean velocity in the liquid film is given by

$$\bar{u} = \frac{1}{\delta} \int_0^\delta u dy = \frac{\tau_0 \delta}{2\mu_l} \quad (2.30)$$

The mass flow per unit periphery  $\Gamma$  and the liquid film thickness  $\delta$  are given by

$$\Gamma = \rho_l \bar{u} \delta = \frac{\rho_l \tau_0 \delta^2}{2\mu_l} \quad (2.31)$$

$$\delta = \sqrt{\frac{2\Gamma\mu_l}{\tau_0\rho_l}} \quad (2.32)$$

and the local liquid film heat transfer coefficient, deduced from Eq. 2.19 is given by

$$\alpha_{ss} = \frac{\lambda_l}{\delta} = \sqrt{\frac{\lambda_l^2 \tau_0 \rho_l}{2\Gamma\mu_l}} \quad (2.33)$$

A well detailed analysis of this phenomenon was formulated by Carpenter and Colburn<sup>88</sup> (1951). If the vapor density is small and the condensation rate is low, then the shear stress is given by

$$\tau_0 = -\frac{D_h}{4} \left( \frac{dp}{dz} \right)_F \quad (2.34)$$

where  $\left( \frac{dp}{dz} \right)_F$  is the gradient of pressure along the channel, which can be evaluated with the model by Friedel<sup>89</sup> (1979). The Friedel model uses a two-phase multiplier to correlate the two-phase pressure gradient with the one which would occur during single-phase liquid flow

$$\Phi_{LO}^2 = \frac{\left( \frac{dp}{dz} \right)_f}{\left( \frac{dp}{dz} \right)_{LO}} \quad (2.35)$$

with the liquid-only pressure gradient defined as

$$\left( \frac{dp}{dz} \right)_{LO} = \frac{2f_{LO}G^2}{D_h\rho_l} \quad (2.36)$$

where  $G$  is the moisture specific mass flow rate. The two-phase multiplier is calculated as

$$\Phi_{LO}^2 = E + \frac{3.24 F H}{Fr^{0.045} We^{0.035}} \quad (2.37)$$

Where

$$E = (1 - x)^2 + x^2 \frac{\rho_l f_{VO}}{\rho_v f_{LO}} \quad (2.38)$$

$$F = x^{0.78} (1 - x)^{0.224} \quad (2.39)$$

$$H = \left(\frac{\rho_l}{\rho_v}\right)^{0.91} \left(\frac{\mu_v}{\mu_l}\right)^{0.19} \left(1 - \frac{\mu_v}{\mu_l}\right)^{0.7} \quad (2.40)$$

$$Fr = \frac{G^2}{g D_h \rho_H^2} \quad (2.41)$$

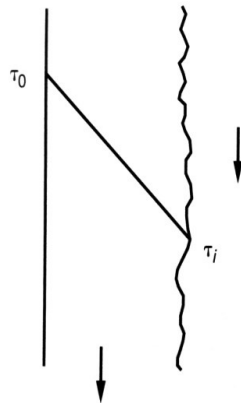
$$We = \frac{G^2 D_h}{\gamma \rho_H} \quad (2.42)$$

where  $\gamma$  is the surface tension of the liquid and  $f_{LO}$  and  $f_{VO}$  liquid only and vapor only are friction coefficients calculated by Hagen-Poiseuille and Blasius<sup>90</sup>. The element  $\rho_H$  is the homogenous density defined by

$$\rho_H = \left(\frac{x}{\rho_v} + \frac{1-x}{\rho_l}\right)^{-1} \quad (2.43)$$

### 2.2.3 Condensation under combined gravity and shear control

For intermediate vapor velocities, gravity begins to have a significant effect on the shear stress phenomena. Thus, in downflow conditions,  $\tau_i$  is lower than  $\tau_0$  as illustrated in Figure 2.11.



**Figure 2.11 – Shear stress profiles in downflow.**

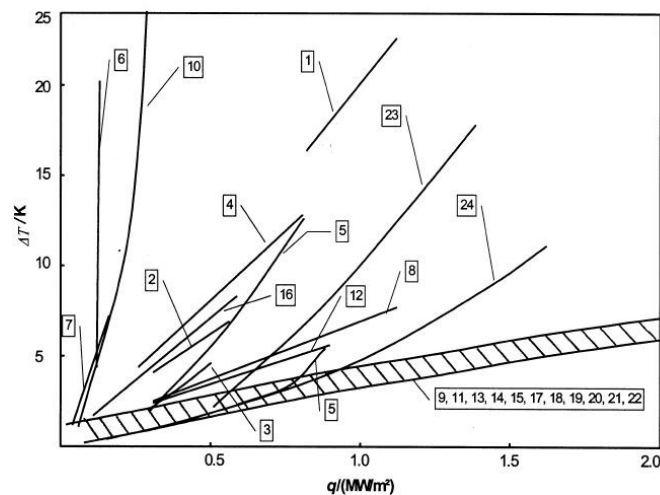
Using the simplified approach of Butterworth<sup>91</sup> (1983), the heat transfer coefficient in the presence of both gravity and shear stress forces is evaluated as

$$\overline{HTC}_{th} = \sqrt{\alpha_{ss}^2 + \bar{\alpha}_{grav}^2} \quad (2.44)$$

The calculation of  $\overline{HTC}_{th}$  concludes the theoretical model of filmwise condensation.

## 2.3 Dropwise condensation

The dropwise condensation starts at molecular level, with the formation of small clusters of molecules (minimum radius  $r_{min}$ ) in a number of preferential nucleation sites ( $N_s$ ), which grow by direct condensation of steam on them. Subsequently, due to the proximity of the nucleation sites, the drops come into contact with each other, they coalesce (effective radius  $r_e$ ) and, when maximum radius  $r_{max}$  is reached (the external forces, gravity force/vapor shear stress/wettability gradient exceed the adhesion force which allows them to remain attached to the surface), the drops begin to slip away. While slipping, the droplets continue to grow for coalescing with other droplets that they encounter along their path leaving the surface clean and available for the formation of new nuclei<sup>92</sup>. Although discovered by Schmidt *et al.*<sup>93</sup>, Rose should be mentioned for his contribution on the DWC phenomenon analysis<sup>4,80,94-98</sup>. Interesting his reflections<sup>99</sup> on data gathered during DWC where the iconic graph (Figure 2.12) on very different heat fluxes measured during DWC is analyzed. The wide span of measurements which can be obtained during DWC is peculiar of this phenomenon and some explanations are provided by Rose with several experiments during the years.



**Figure 2.12 - Heat transfer measurements for dropwise condensation of steam at near-atmospheric pressure: 1, Schmidt et al. (1930); 2, Nagle et al. (1935); 3, Gnam (1937); 4, Fitzpatrick et al. (1939); 5, Shea and Krase (1940); 6, Fatica and Katz (1949); 7, Kirschbaum et al. (1951); 8, Hampson and Ozisik (1952); 9, Wenzel (1957); 10, Welch and Westwater (1961); 11, Le Fevre and Rose (1964); 12, Kast (1963); 13, Le Fevre and Rose (1965); 14, Tanner et al. (1965a); 15, Citakoglu (1966); 16, Griffith and Lee (1967); 17, Citakoglu and Rose (1968); 18, Graham (1969); 19, Wilmshurst and Rose (1970); 20, Tanasawa and Ochiai (1973); 21, Aksan and Rose (1973); 22, Stylianou and Rose (1980); 23, Ma et al. (1994); 24, Leipertz and Koch (1998). Image taken from Rose (2002)<sup>80</sup>.**

Two of the major problems encountered are related to the presence of non-condensable gas (NCG) within the experimental apparatus and to the insufficient accuracy of the surface temperature measurements. In particular, it has been proved that even small quantities of NCG (in the order of some ppm) can negatively influence the heat exchange coefficient, thus demonstrating that the DWC is extremely sensitive to this problem<sup>4,80</sup>. Other secondary factors are the different geometrical characteristics of the experimental apparatus and the condensation rate<sup>100</sup>. Having an accordance on



the experimental data is necessary for developing the models. The present work mainly deals with dropwise condensation on flat surfaces and thus without considering the presence of artificial roughness. Several heat transfer models that can be used during DWC on flat surfaces have been proposed in the literature and in this dissertation five different studies have been selected: Le Fevre and Rose (1966) as reported in Rose<sup>13</sup>, Abu-Orabi<sup>101</sup> (1998), Kim *et al.*<sup>27</sup> (2011), Miljkovic *et al.*<sup>26</sup> (2013) and Chavan *et al.*<sup>102</sup> (2016). The models are discussed in a chronological order so the evolution on the understanding of the phenomenon can be appreciated. For further model analyses and considerations please see other my personal works<sup>103,104</sup>. The dissertation about the historical part is based on the work of Sameer *et al.*<sup>105</sup>.

### 2.3.1 DWC model history

The phenomenon of DWC was reported for the first time in a scientific article in the 30s of the last century by the Schmidt<sup>58</sup>. The author measured HTC 10 times higher than the HTC measured during FWC, which paved the way for the interest of promoting this new mode of condensation. The study of the DWC aroused a discontinuous interest from the heat transfer community, and the first semi-empirical models were developed only starting from the second half of the 60s<sup>13</sup> and the early 70s<sup>80,95,96,106,107</sup>. After this period, to find other publications about this topic, it has to be waited until the end of 90s and particularly until the beginning of new millennium<sup>26,27,101,108</sup>. Indeed, in recent years, the material science has made major progress in the development of new surfaces that could favor dropwise condensation<sup>4</sup>. Moreover, researchers have focused their attention on micro- and nanostructured surfaces displaying superhydrophobic characteristics which may lead to even higher heat transfer coefficients promoting the phenomenon of “jumping droplets”<sup>18,42,109,110</sup>. Actually, the very first model of DWC was proposed by Fatica and Katz<sup>111</sup> in 1949, but its predictions were very rough compared to the later models. The first model worth mentioning is the model developed by Le Fevre and Rose model<sup>80</sup> (1966). In this model, a calculation for heat transfer through a single drop was combined with that of the drop size distribution to obtain the average heat flux. Gose *et al.*<sup>112</sup> (1967) developed a model for heat transfer during dropwise condensation on randomly distributed nucleation sites. The authors proposed that small drops grow by vapor condensation, and that larger drops grow by coalescence. The HTC resulted to be strongly influenced by nucleation sites and drop removal from substrate. Rose and Glicksman<sup>113</sup> (1973) proposed a formula for the distribution of “large” drops population which grow primarily by coalescence. Wu and Maa<sup>107</sup> (1976) introduced the drop size distribution of “small” drops using the population balance method. Maa<sup>114</sup> (1978) combined the “small” and “large” droplet population, considering both drop growth due to direct condensation and coalescence between drops, to obtain the resulting drop size distributions. Abu-Orabi<sup>101</sup> (1998) proposed a model with different thermal resistance in series: resistances to heat

transfer due to the drop (conduction through the drop, vapor–liquid interfacial resistance, and drop curvature) and the promoter layer. The total heat flux was calculated from the drop size distributions and the heat transfer rate through a single drop. Liu *et al.*<sup>115</sup> (2007) experimentally proved that the condensation is a nucleation phenomenon and a liquid nanofilm is not formed in between droplets as supported by other researchers<sup>116</sup>. Kim and Kim<sup>27</sup> (2011) modeled dropwise condensation considering the contact angle of droplets. The formulation is similar to those described earlier, but results showed that the single droplet heat transfer and drop distribution are significantly affected by the contact angle. Although the Kim and Kim model considers superhydrophobic surfaces, the surface morphology is neglected. With the model of Miljkovic *et al.*<sup>26</sup> (2013), the surface structure is taken into account, furthermore different scenarios are described based on the geometry. The phenomenon of the “jumping droplets” is also modeled. The last step, to the best of the author’s knowledge, on DWC modeling is the work of Chavan *et al.*<sup>102</sup>, where the heat transfer through the droplet is numerically simulated. The work reveals that the majority of heat transfer occurs at the three phase contact line. Droplet distribution theory is incorporated to show that previous modeling approaches underestimate the overall heat transfer. However, before the detailed analysis of the models, the phenomenon itself has to be properly described, from the droplet born to its departure. Different aspects of the droplet life are described in the same manner by all the models and this will be underlined.

### 2.3.2 Phenomenology

As already reported, the DWC is a nucleation phenomenon, where molecule clusters interact with the solid at specific points, called nucleation sites, and they start to grow by direct condensation. Once these small droplets reach adjacent droplets the phenomenon of coalescence begins. A drop, grown by direct condensation and coalescence, falls down (on a vertical surface) when it assumes the departing radius. The falling drop cleans its path, allowing the formation of new droplets and thus removing the drops which lessen the heat flow process<sup>105</sup>. In this case, a condensate film between the vapor and the cold surface is not formed as for FWC, which can be modeled as an equivalent thermal resistance, but a high number of drops are displaced, modeled as thermal resistances in parallel<sup>117</sup>. In this case, unlike the FWC, the problem is treated by the most of authors on two dimensions. This is still a simplification compared to a more detailed analysis of the phenomenon, for example through CFD<sup>105</sup> or Lattice-Boltzman<sup>118</sup>. There are several aspects that are in common in between all the models and are reported in the following. All the models hereafter reported are developed with the same hypothesis:

- The vapor temperature is uniform and it is the saturation temperature;

- The vapor is in quiescent conditions, there is not a convective contribution in the heat exchanged;
- The substrate is assumed as a semi-infinite body since its thickness is greater than most of the drops present.

The idea of all the models is to estimate the droplet population, which includes droplets from the nucleation dimensions to the departing diameter, and to model a droplet as a series of thermal resistances. Once estimated the thermal flow of a single drop ( $q_d$ ) and the number of drops present per unit area with respect to the single drop radius ( $N(r)$ ), the specific heat flux ( $q$ ) can be calculated integrating  $q_d$  between the minimum and the maximum radius:

$$q = \int_{r_{min}}^{r_{max}} q_d(r) \cdot N(r) dr \quad (2.45)$$

This formulation assumes a uniform distribution of drops between the maximum and minimum radius. Actually, as already reported<sup>114,119</sup>, there are two different droplet population depending on the dimensions. So, naming  $n(r)$  the "small" droplets population ( $r < r_e$ ) and  $N(r)$  the population of "large" droplets ( $r > r_e$ ), it follows that:

$$q = \int_{r_{min}}^{r_e} q_d(r) \cdot n(r) dr + \int_{r_e}^{r_{max}} q_d(r) \cdot N(r) dr \quad (2.46)$$

Dividing the heat flux by the temperature difference between the surface and the steam, the HTC is obtained

$$HTC = q / \Delta T \quad (2.47)$$

Finding the temperature distribution within the single drop it is not an easy task, it is necessary to find the solution of a system of partial differential equations<sup>117</sup>. Reason why the droplet is represented by a series of equivalent thermal resistance<sup>13,26,27,101</sup>, besides in the work of Chavan *et al.*<sup>102</sup>. The different assumption will provide a big difference in the results. Other authors simulate every single drop on the condensing surface from the "birth" starting from the nucleation site to its "departure", thus carrying out a spatial and temporal investigation<sup>120,121</sup>. However, this different approach requires important resources from the computational point of view, and, at least at the present state, it has not received great attention in the scientific community.

### 2.3.2.1 Minimum droplet radius

The minimum radius of drop  $r_{min}$  is the minimum radius that a drop can assume at equilibrium with the saturated vapor in order not to maintain its shape. Consider a system containing a droplet surrounded by saturated steam at constant temperature  $T_w$  and pressure  $p_v$ . The vapor temperature is equal to the condensing wall temperature and the saturation temperature ( $T_s$ ) corresponding to vapor pressure is higher than  $T_w$ . At equilibrium, the temperature and chemical potential of the vapor and the chemical potential of the liquid must be the same:

$$\varphi_{ve} = \varphi_{le} \quad (2.48)$$

The chemical potentials can be calculate by the Gibbs' law for constant temperature process:

$$\varphi - \varphi_{sat} = \int_{p_{sat}}^p v dp \quad (2.49)$$

The specific volume can be evaluated by the ideal gas law as follow:

$$v = \frac{R_g T_w}{p} \quad (2.50)$$

Therefore, the chemical potential of the vapor phase is:

$$\varphi_{ve} = \varphi_{v sat} + R_g T_w \ln \left[ \frac{p_v}{p_{sat}(T_w)} \right] \quad (2.51)$$

For the liquid phase, the specific volume is constant. Then

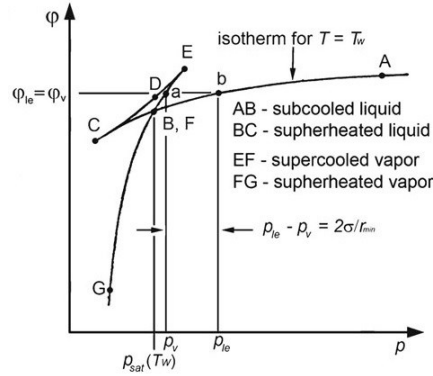
$$\varphi_{le} = \varphi_{l sat} + v_l [p_{le} - p_{sat}(T_w)] \quad (2.52)$$

Remembering Equation 2.48:

$$p_v = p_{sat}(T_w) \exp \left( \frac{v_l [p_{le} - p_{sat}(T_w)]}{R_g T_w} \right) \quad (2.53)$$

Equation 2.53 indicates that if  $p_v$  is greater than  $p_{sat}(T_w)$ , then  $p_{le}$  must also be greater than  $p_{sat}(T_w)$ . Thus, for the liquid droplet with finite radius, equilibrium can be achieved only if the liquid is

subcooled and the vapor is supersaturated relative to its normal saturation state for a flat interface (Figure 2.13).



**Figure 2.13 -  $\phi$  -  $p$  diagram. Liquid is in equilibrium with the surrounding vapor<sup>105</sup>.**

The droplet pressure at the curvature is given by the Laplace equation:

$$p_{le} = p_v + \frac{2\sigma}{r_{min}} \quad (2.54)$$

Which can be substituted in Equation 2.53:

$$p_v = p_{sat}(T_w) \exp\left(\frac{v_l[p_v - p_{sat}(T_w) + 2\sigma/r_{min}]}{R_g T_w}\right) \quad (2.55)$$

Assuming  $p_v - p_{sat}(T_w) \ll 2\sigma/r_{min}$  (Figure 2.13),  $r_{min}$  can be evaluated as:

$$r_{min} = \frac{2\sigma v_l}{R_g T \ln[p_v/p_{sat}(T)]} \quad (2.56)$$

The Clapeyron equation is combined with the ideal gas law of vapor to obtain:

$$\frac{dp}{dT} = \frac{h_{lv} p}{R_g T^2} \quad (2.57)$$

Integrated between  $p_v$  and  $p_{sat}$ :

$$\ln\left(\frac{p_v}{p_{sat}}\right) = -\frac{h_{lv}}{R_g} \left(\frac{1}{T_w} - \frac{1}{T_v}\right) \quad (2.58)$$

Substituting Equation 2.56 in Equation 2.58,

$$r_{min} = \frac{2\sigma T v_l}{h_{lv}(T_v - T_w)} \quad (2.59)$$

the minimum droplet radius is obtained. Equation 2.59 is used in all the models here presented. It has to be underlined that this expression depends only on the thermodynamic properties of the fluid without considering the geometric characteristics of the specimen such as roughness and wettability which may change the chemical potential in Equation 2.48. For more details please refer to Khandekar and Muralidhar<sup>92</sup>. Liu and Cheng<sup>122,123</sup> recently proposed a new approach for calculating the nucleation radius considering the presence of a promoting layer which tends to increase the minimum radius, however their result are not taken into account by the here proposed models. Rose<sup>95</sup> proposed a relation between the minimum radius and the nucleation site deducible from an equation for the distribution of drop sizes.

$$N_s = \frac{0.037}{r_{min}^2} \quad (2.60)$$

Equation 2.60 is not commonly used, since it should overestimate  $N_s$ <sup>123</sup>. The range used in models span in between  $10^9 - 10^{15} \text{ m}^{-2}$ , values experimentally determined by several authors<sup>18,95</sup>. Effect of  $N_s$  on heat transfer will be discussed later. However, a nucleation sites heat flux dependent (in Equation 2.59 there is the  $T_v - T_w$ ) should be more accurate than a fixed nucleation site value, since it was experimentally observed that the nucleation sites are driven by the heat flux<sup>95,124</sup>. Equation 2.60 has been further developed for rough surfaces by Rose<sup>95</sup> and Mu *et al.*<sup>125</sup>. Nucleation density depends on changes in surface energy induced by a chemical species (chemical texturing) and varying roughness morphology of the substrate (physical texturing). The modified expression for the nucleation density is not established yet and it is a topic of research.

### 2.3.2.2 Maximum droplet radius

The maximum droplet radius  $r_{max}$  is obtained from a balance force between the adhesion force<sup>126</sup>, which is applied to the contact area between the droplet and the solid, and the gravity force, which is applied to the volume of the droplet<sup>26,27</sup>. Other forces can interact with this system, as the shear stress induced by the vapor velocity<sup>6,127</sup>, but, to the best of the author's knowledge, this effect is not taken into account so far. The force balance can be written as follow

$$F_{adhesion} = F_{gravity} \quad (2.61)$$

Substituting:

$$2\gamma r_{max} \sin(\vartheta) (\cos(\vartheta_r) - \cos(\vartheta_a)) = \frac{2-3 \cos(\vartheta)+\cos^2(\vartheta)}{3} r_{max}^3 \pi \rho_l g \quad (2.62)$$

The maximum radius can be obtained

$$r_{max} = \sqrt{\frac{6(\cos(\vartheta_r)-\cos(\vartheta_a)) \sin(\vartheta) \gamma}{\pi(2-3 \cos(\vartheta)+\cos^2(\vartheta)) \rho_l g}} \quad (2.63)$$

The maximum radius is strongly influenced by the contact angles measured between the three phases. The first models<sup>13,101</sup> which do not consider the contact angle use a different expression for the departing radius:

$$r_{max} = K_3 \left[ \frac{\sigma}{\rho g} \right]^{\frac{1}{2}} \quad (2.64)$$

where  $K_3$  is a constant equal to 0.4 determined experimentally. For uniformity in models, a measured maximum radius has been imposed.

### 2.3.2.3 Droplet population

LeFevre and Rose<sup>13</sup> introduced for the first time a relationship regarding the droplet population, while Maa and coworkers<sup>114,119</sup> and Tanaka<sup>128</sup> proposed an evolution of this concept with the introduction of the droplet population balance. Before going into the theoretical discussion it is necessary to define "small" and "big" drops. The main difference between the two entities is related to the process by which they increase their size. The "small" droplet population grows due to direct condensation of vapor on them, whereas the "big" droplet population grows primarily by coalescence. The distribution of the "big" and "small" drops will be indicated respectively with the symbols  $N(r)$  and  $n(r)$ . The radius which separates the two population is named critical radius and is defined as

$$r_e = \frac{1}{\sqrt{4N_s}} \quad (2.65)$$

or

$$r_e = \frac{1}{4\sqrt{N_s}} \quad (2.66)$$

depending on the nucleation sites distribution: square array or random Poisson distribution, respectively. One aspect that can be confusing, which is hardly clarified in the literature, is the unit measurement for the droplet distribution, which is usually indicated with  $[m^{-3}]$ . It represents the number of drops present [#] per unit of surface  $[m^{-2}]$  and per unit of radius  $[m^{-1}]$ . The "large" droplet population, the empirical expression proposed by LeFevre and Rose<sup>13</sup>, is obtained by direct observations and it is equal to:

$$N(r) = \frac{1}{3\pi r^2} \left( \frac{r}{r_{max}} \right)^{-\frac{2}{3}} \quad (2.67)$$

which is dependent by the maximum droplet radius. In order to introduce the formulation for the "small" droplet population, the growth rate for a drop  $G [m/s]$  should be defined.

$$G = \frac{dr}{dt} \quad (2.68)$$

Assuming that in a given surface area  $A$ , the number of entering droplets is equal to the number of leaving droplets plus the droplets swept and assuming the growth the droplet balance in that area will be:

$$An_1G_1\Delta t = An_2G_2\Delta t + S\bar{n}\Delta r\Delta t \quad (2.69)$$

where  $n$  is the number of drops per unit area per unit drop radius,  $S$  is the rate at which the substrate surface is renewed due to sweeping,  $\bar{n}$  is the average population density in the size range  $r_1$  to  $r_2$ ,  $\Delta r = r_2 - r_1$ , and  $\Delta t$  is an increment of time. For  $\Delta r \rightarrow 0$ , the Equation (2.69) becomes

$$G \frac{dn}{dr} + n \frac{dG}{dr} + \frac{n}{\tau} = 0 \quad (2.70)$$

where  $\tau = A/S$  is the sweeping period. As a boundary condition, the authors impose that the population of "small" droplets equals that of "large" droplets at  $r_e$ :

$$n(r_e) = N(r_e) \quad (2.71)$$

The Equation 2.70 can be integrated with respect to  $r$ , obtaining:



$$n(r) = N(r_e) \frac{r(r_e - r_{min})(A_2 r + A_3)}{r_e(r - r_{min})(A_2 r_e + A_3)} e^{B_1 + B_2} \quad (2.72)$$

where

$$B_1 = \frac{A_2}{A_1 \tau} \left[ \frac{r_e^2 - r^2}{2} + r_{min}(r_e - r_{min}) - r_{min}^2 \ln \left( \frac{r - r_{min}}{r_e - r_{min}} \right) \right] \quad (2.73)$$

$$B_2 = \frac{A_3}{A_1 \tau} \left[ (r_e - r) - r_{min} \ln \left( \frac{r - r_{min}}{r_e - r_{min}} \right) \right] \quad (2.74)$$

$$\tau = \frac{3r_e^2 (A_2 r + A_3)^2}{A_1 [8A_3 r_e - 14A_2 r_e r_{min} + 11A_2 r_e^2 - 11A_3 r_{min}]} \quad (2.75)$$

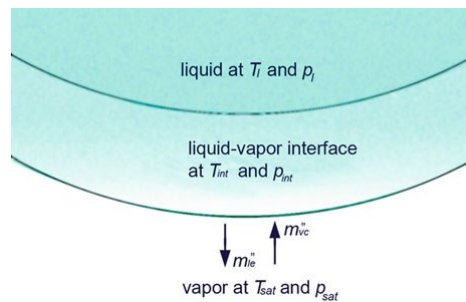
The three parameters ( $A_1$ ,  $A_2$ , and  $A_3$ ) in Eqs. 2.72-2.75 are derived from the heat flow exchanged by a droplet (it is different for each model) by means of Eq. (2.68) and Eq. (2.76)

$$q_d(r) = \rho_l h_{lv} \left( 2\pi r \frac{dr}{dt} \right) \quad (2.76)$$

thus each model has different coefficient based on the own formulation for the single droplet heat flow rate. This procedure was proposed for the first time by Maa<sup>114</sup> and Tanaka<sup>128</sup> but readapted by Abu-Orabi<sup>101</sup>.

#### 2.3.2.4 Interfacial condensation heat transfer coefficient

The interfacial resistance between the drop and the vapor takes into account the transport of mass from the steam to the condensate and from the condensate to the steam (Figure 2.14), with a certain quantity of vapor molecules that coming in contact with the single drop will increase its size. The interfacial HTC is then related to the direct condensation of steam on the condensate, its influence is stronger on the “small” droplet population since it is the only mechanism with which they grow.



**Figure 2.14 - Liquid–vapor interface and mass fluxes at the liquid–vapor interface<sup>92</sup>.**

The formulation is taken by the work of Shrage<sup>129</sup> and it can be considered constant along the liquid-vapor interface<sup>102,130</sup>.

$$h_i = \frac{2\alpha}{2-\alpha} \frac{1}{\sqrt{2\pi R_g T_{sat}}} \frac{h_{lg}^2}{v_g T_{sat}} \quad (2.77)$$

where  $0 < \alpha \leq 1$ . The accommodation coefficient ( $\alpha$ ) defines the fraction of the striking vapor molecules that actually gets condensed on the vapor–liquid interface. A low  $\alpha$  (close to 0), therefore, will indicate a high presence of NCG; while for  $\alpha$  close to 1 an absence of NCG<sup>130</sup>. There is a wide range of the accommodation coefficient suggested by literature. Very low values are suggested for liquid ethanol, methanol, alcohol, and water, ranging from 0.02 to 0.04, whereas for benzene and carbon tetrachloride are closer to 1<sup>92</sup>. Abu-Orabi<sup>101</sup>, instead, fixes this parameter equal to 1, while Kim and Kim<sup>27</sup> hypothesize that the whole coefficient of interfacial resistance is constant and equal to  $15.7 \text{ MW}/(\text{m}^2\text{K})$ . In the present work, the accommodation coefficient is assumed equal to 1 since the experimental tests are performed without (as much as possible) the presence of NCG.

### 2.3.3 Predicting models

Henceforth the chosen models for DWC on vertical flat surface are described in detail. In Table 2.1, all the values used for the graphs, which are the same used for the comparison with experimental data are reported.

**Table 2.1 - List of input variables considered in the models.**

Variable	Value
$t_{SAT}$ [°C]	108
$\Delta T$ [°C]	5
$\delta$ [μm]	0.2
$\lambda_{COAT}$ [W m <sup>-1</sup> K <sup>-1</sup> ]	0.2
$\alpha$ [-]	1
$\theta$ [°]	90
$\theta_a$ [°]	88.6
$\theta_r$ [°]	63.4
$R_{max}$ [mm]	0.93

The dissertation is taken by the original models. For further parametric analyses please refer to my other works<sup>103,104</sup>.

### 2.3.3.1 Le Fevre and Rose model (1966)

The very first model of Rose is an empirical equation obtained from a series of experiments carried out by the same author, which was based only on the vapor temperature, in degrees Celsius, and on the temperature difference  $\Delta T$  between the surface and the vapor

$$Q = t^{0.8} [5 \Delta T + 0.3 \Delta T^2] \quad \left[ \frac{kW}{m^2} \right] \quad (2.78)$$

The first empirical equation was developed by Le Fevre and Rose in 1966. The heat flow rate through a single drop is obtained with a semi-empirical relationship:

$$q_d(r) = \frac{\Delta T - \frac{2\sigma T_{SAT}}{r \rho_l h_{lv}}}{K_1 \frac{r}{\lambda_l} + K_2 \left( \frac{0.627}{0.664} \right) \frac{T_{SAT}}{h_{lv}^2 \rho_l} \frac{\gamma+1}{\gamma-1} \left[ \frac{RT_{SAT}}{2\pi} \right]^{0.5}} \quad (2.79)$$

where  $K_1$  and  $K_2$  are constants imposed by the authors and they are equal to 2/3 and 1/2 respectively<sup>95</sup>,  $\lambda_l$  is the liquid conductivity,  $\rho_l$  is the liquid density,  $\gamma$  is the ratio of the specific heat capacities and  $R$  is the ideal-gas constant. At the numerator, in addition to the temperature difference  $\Delta T$ , the effect of the droplet curvature is taken into account. At the denominator, the first term represents the resistance to the heat conduction through the condensate, meanwhile, the second term represents the resistance to the mass transport at the interface between vapor and liquid. All the resistance are accounted as temperature drop and are summarized in Figure 2.15 and Figure 2.16. In Figure 2.15 the thermal resistances are plotted varying the total temperature drop from 0°C to 5°C. In Figure 2.16, the total temperature drop is fixed equal to 5°C.

Figure 2.15 shows the relation between the thermal resistances varying the saturation-wall temperature difference. All resistances maintain the same behavior besides the  $\Delta T$ . The temperature drop due to the curvature depends only on the saturation temperature, which is fixed (Table 2.1). The constant  $K_2$  can include the promoter layer resistance, however if it is assumed equal to 1/2 it represents only the ratio of the base area to the area of the curved surface<sup>95</sup>. The present model, then, predict the heat transfer coefficient of DWC itself. Unlike the next models, Rose calculates the specific heat flux,  $\left[ \frac{W}{m^2} \right]$ , instead of the heat flow.

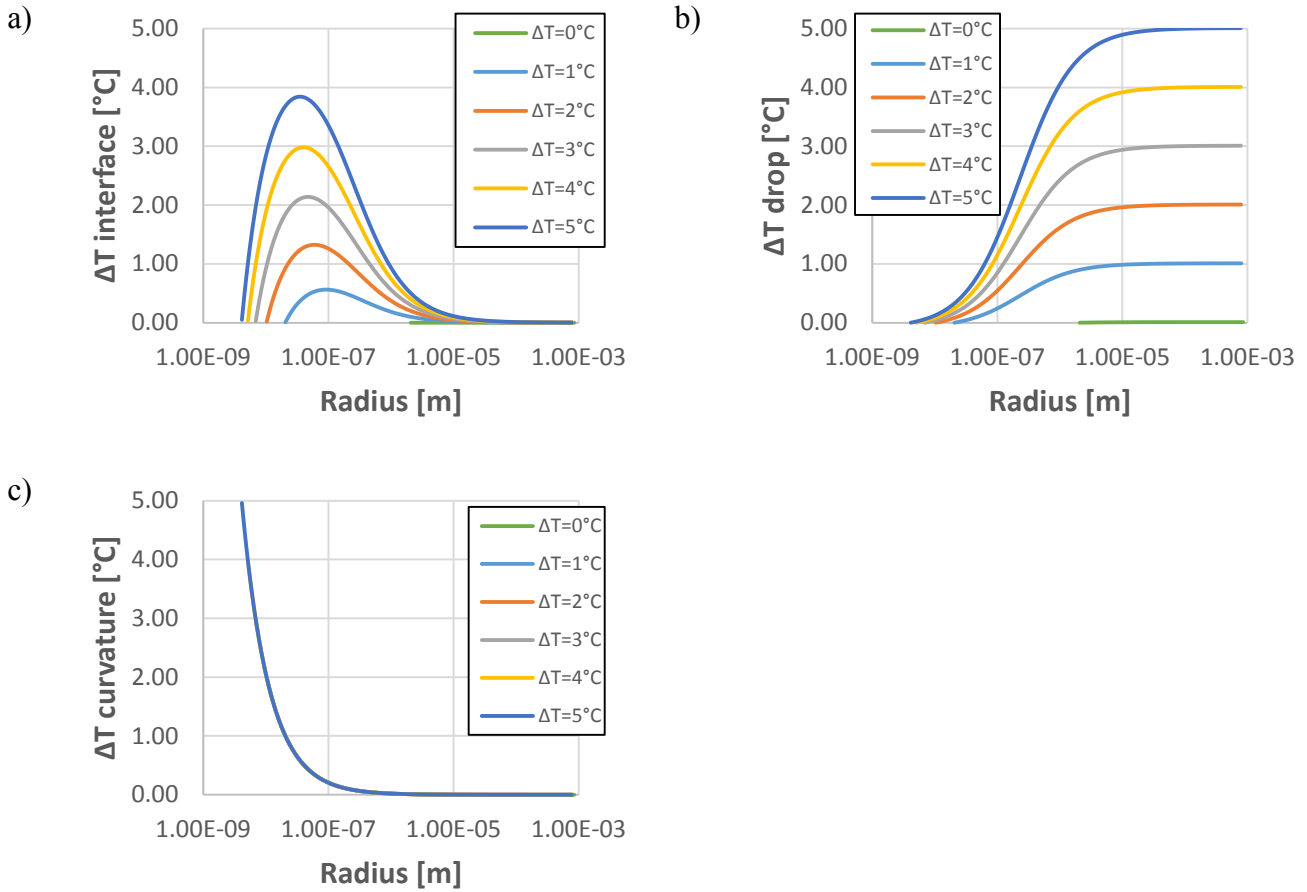


Figure 2.15 - a), b) and c)  $\Delta T$  due to the interface, to the drop and curvature versus droplet radius, respectively. The difference between the saturation and wall is varied.

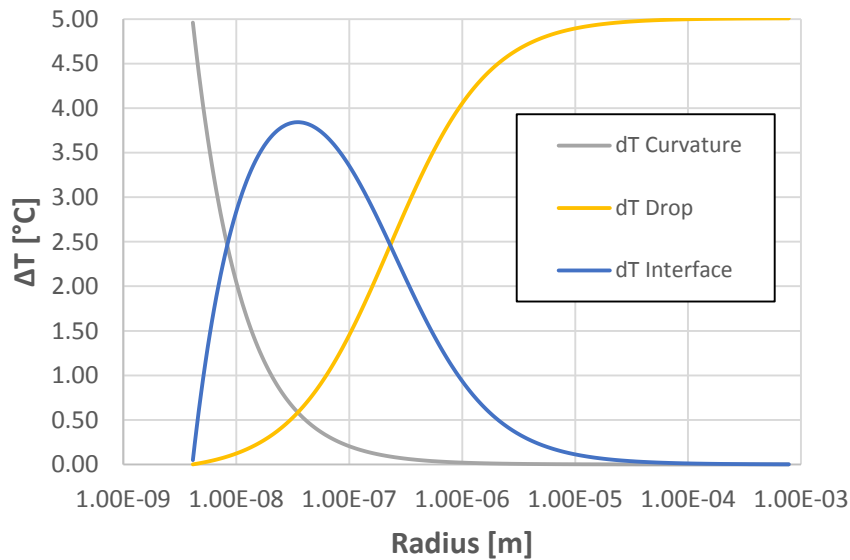
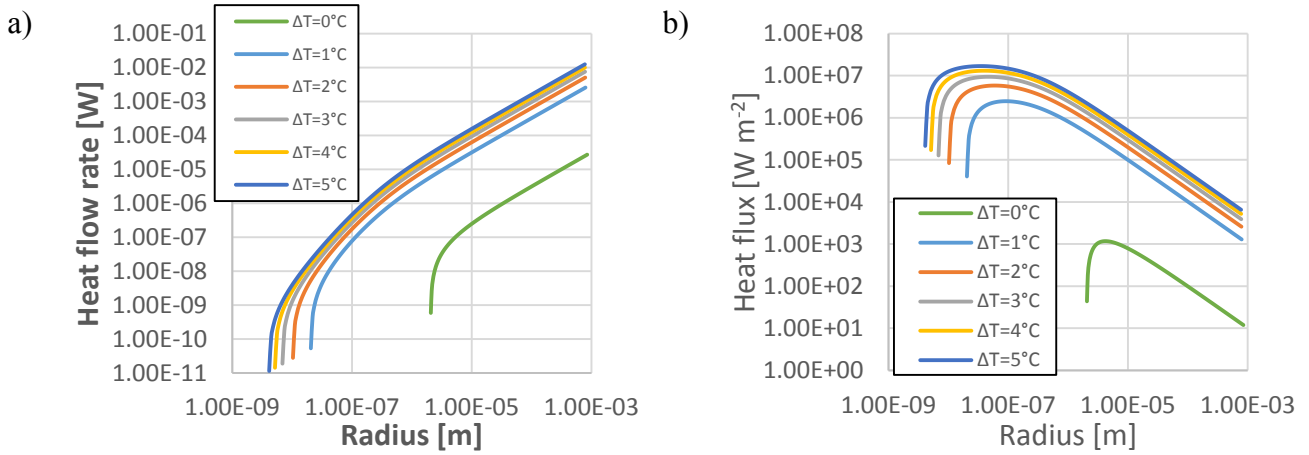


Figure 2.16 - Temperature drop at the interface, through the droplet and due to the curvature versus radius. The total temperature drop is fixed at  $5^\circ\text{C}$ .



**Figure 2.17 - Heat flow rate a) and heat flux b) vs droplet radius for different  $\Delta T$  predicted by LeFevre and Rose.**

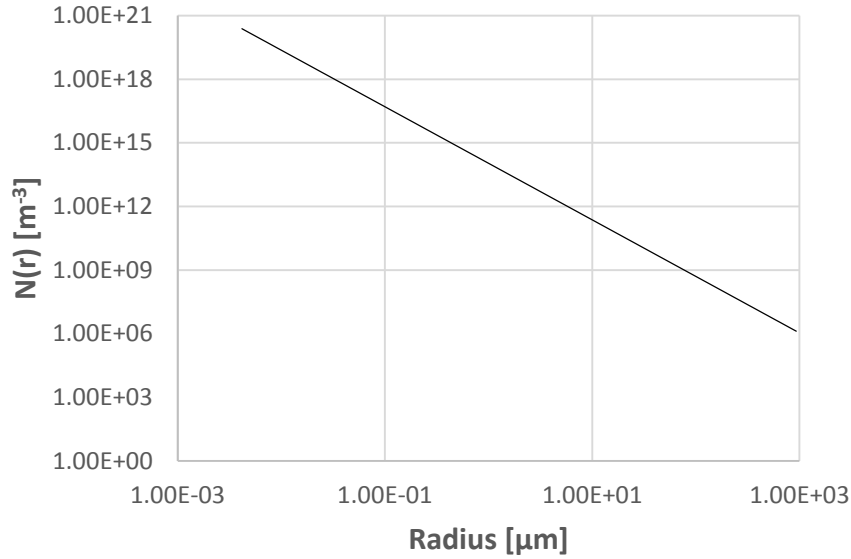
Both the heat flow rate and the heat flux seem to asymptotically approach to a determined value, in fact the distance between the curves decreases as the  $\Delta T$  increases. All the curves start at different  $r_{min}$ , as suggested by Equation 2.59. The heat flow rate is obtained multiplying the heat flux by the droplet area. Figure 2.17 shows a very different trend for  $\Delta T = 0^\circ\text{C}$ . Actually, all the models, approaching to  $\Delta T = 0^\circ\text{C}$  are not well defined tending asymptotically to  $-\infty$ . Some models predict total heat flux lower than zero, which is impossible. The simulation, then, are done with  $\Delta T = 0.01^\circ\text{C}$ . From Figure 2.17b, it is interesting to notice that the heat flux presents a maximum for a value of the radius very close to the minimum radius and it increases with the increasing of  $\Delta T$ . In fact, from Equation 2.79, the heat flux exchanged by a droplet with the minimum radius tends to zero. In the model, the droplet population covers only the “large” droplets with the expression:

$$N(r) = \frac{1}{3\pi r^2 r_{max}} \left( \frac{r}{r_{max}} \right)^{-\frac{2}{3}} \quad (2.80)$$

where the maximum radius is defined as:

$$r_{max} = K_3 \left[ \frac{\sigma}{\rho g} \right]^{\frac{1}{2}} \quad (2.81)$$

$K_3$  is a constant already reported in paragraph 2.3.2.2 and  $g$  is the gravity acceleration. It should be noticed that  $N(r)$  does not depend on the  $\Delta T$ .

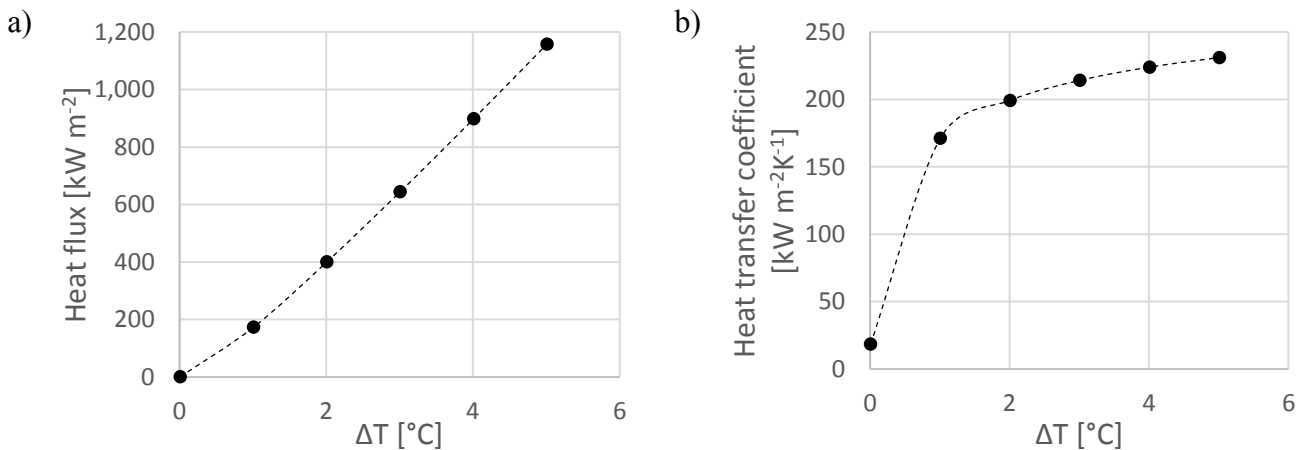


**Figure 2.18 - Droplet population vs droplet radius predicted by LeFevre and Rose.**

Combining Equations 2.79 and 2.80 and remembering Equation 2.45 the global heat flux is determined as

$$q' = \frac{1}{3r_{max}^{\frac{1}{3}}} \int_{r_{min}}^{r_{max}} \frac{\Delta T - \frac{2\sigma T_{sat}}{r} \rho_f h_{fg}}{K_1 \frac{r}{\lambda} + K_2 \left( \frac{0.627}{0.664} \right) \frac{T_{sat}}{h_{fg}} \frac{\gamma + 1}{\rho_g \gamma - 1} \left[ \frac{RT_{sat}}{2\pi} \right]^{\frac{1}{2}}} r^{-\frac{2}{3}} dr \quad (2.82)$$

The value of this integral can be obtained both numerically and analytically<sup>106</sup> through a symbolic analysis, here the numerical approach is used.



**Figure 2.19 - Total heat flux a) and HTC b) vs ΔT predicted by LeFevre and Rose.**

Figure 2.19 show the heat flux and the HTC versus ΔT predicted by the model. The HTC trend is very different from the FWC one (Equation 2.26), which tends to  $+\infty$  for  $\Delta T \rightarrow 0$  and it decreases with the increasing of the ΔT.

### 2.3.3.2 Abu-Orabi model

The model developed in 1998 by Abu-Orabi<sup>101</sup> was the first that computes the heat transfer through a single drop by incorporating the various thermal resistances from the vapor to the surface and considers both the populations of “small” and “large” droplets<sup>107,128</sup>. The model assumes a constant contact angle equal to 90°, as reported in the previous models<sup>80,111</sup>. The thermal resistances can be evaluated as the ratio between temperature drop and heat flow rate  $q_d$ ; in particular the temperature drop due to the interfacial resistance is:

$$\Delta T_i = \frac{q_d}{h_i 2\pi r^2} \quad (2.83)$$

where  $h_i$  is the interfacial heat transfer coefficient, which includes the accommodation coefficient ( $\alpha$ ). For further consideration about the value of  $\alpha$  please refer to paragraph 2.3.2.4. The thermal resistance due to heat conduction through the drop can be estimated from Eq. (8)

$$\Delta T_d = \frac{q_d r}{4\pi r^2 \lambda_l} \quad (2.84)$$

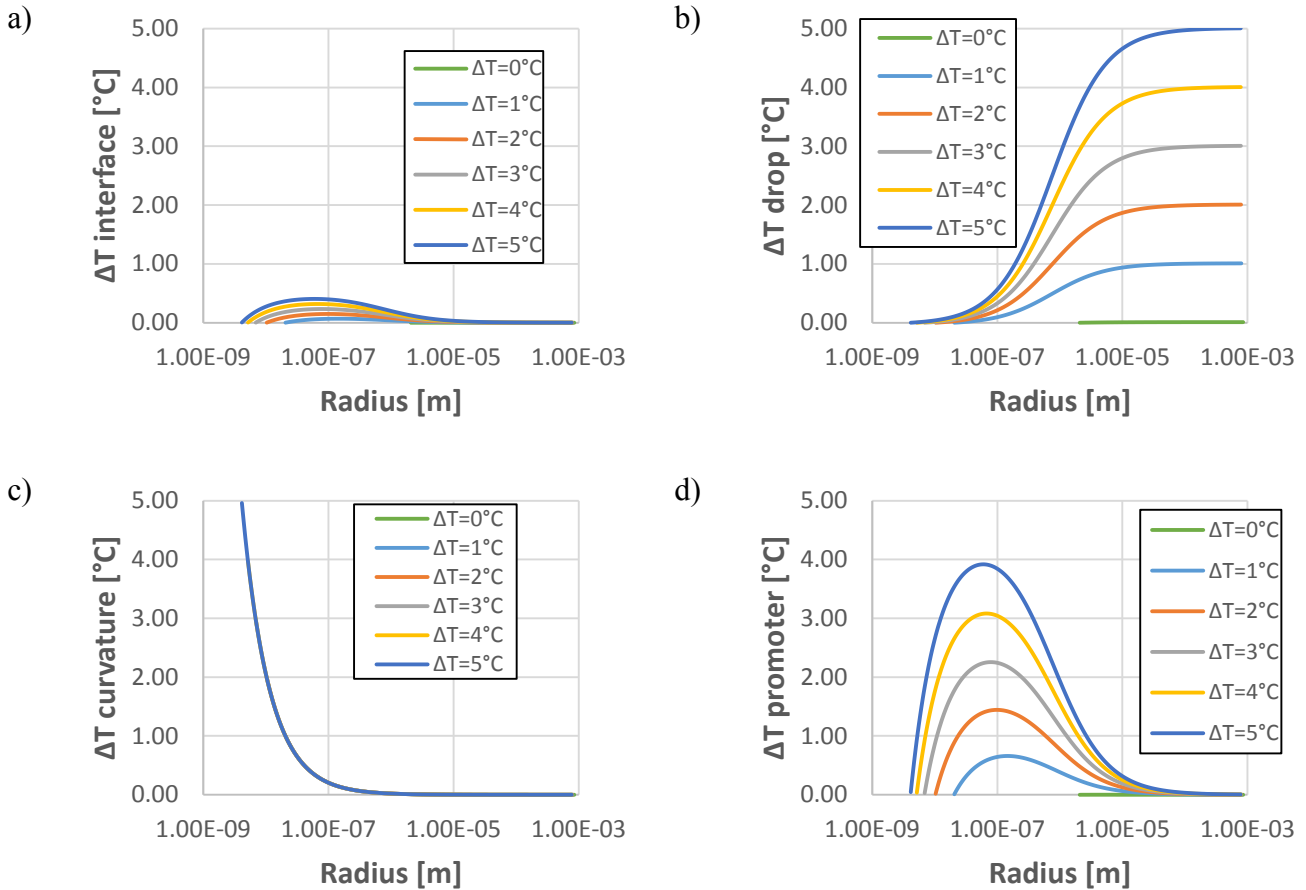
The promoting layer on the substrate adds a temperature drop equal to:

$$\Delta T_{coat} = \frac{q_d \delta}{4\pi r^2 \lambda_{coat}} \quad (2.85)$$

where  $\delta$  is the layer thickness. The  $\Delta T_{coat}$  is applied to  $4\pi r^2$  which can be the surface area of the droplet. This resistance should be applied, instead, to the base area of the droplet since the heat flux is passing through the interface coating-liquid. The following models fix this discrepancy. Finally, the droplet curvature gives a temperature variation

$$\Delta T_c = \frac{2T_{SAT}\sigma}{h_{lv} r \rho_l} \quad (2.86)$$

In Figure 2.20 and Figure 2.21, a parametric analysis of the different temperature drops is reported. Comparing Figure 2.15 with Figure 2.22, it can be noticed the different weights of the resistances in the two models. In Abu-Orabi, the  $\Delta T_i$  is smaller as compared to the Rose models, however the  $\Delta T_{coat}$  comes into play and for a considerable amount of radiuses is the higher temperature drop.

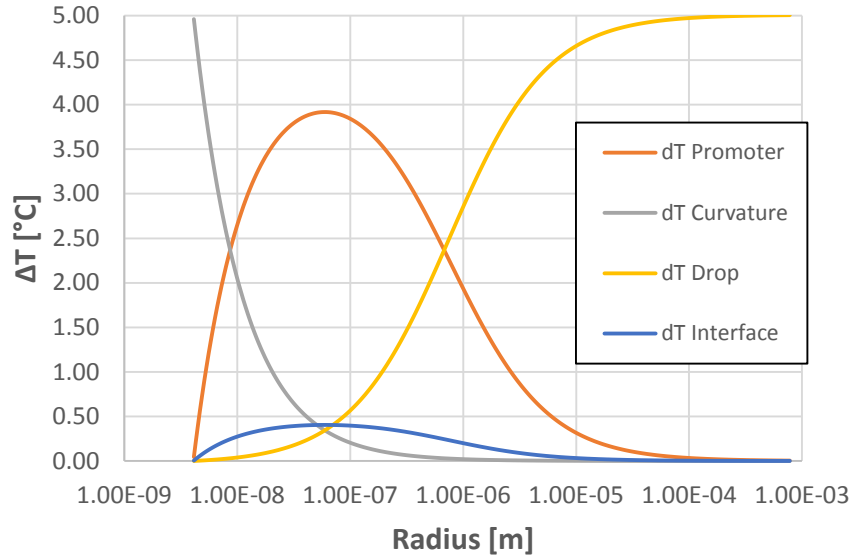


**Figure 2.20 - a), b) c) and d)  $\Delta T$  due to the interface, to the drop, curvature and promoter versus droplet radius, respectively. The difference between the saturation and wall is varied.**

In Figure 2.21, the total temperature drop is fixed equal to  $5^{\circ}\text{C}$  and the droplet radius is varied from the minimum radius to the maximum radius. The plot can be divided in three zones:

- $R_{\min} < r < 9 \cdot 10^9$  . The bigger temperature drop is due to the curvature of the droplet.
- $9 \cdot 10^9 < r < 6 \cdot 10^7$  . The promoter is the dominant resistance, hence the importance of choosing the most conductive/thin coating.
- $6 \cdot 10^7 < r < R_{\max}$  . The droplet growing in dimensions becomes the biggest barrier to the thermal exchange.

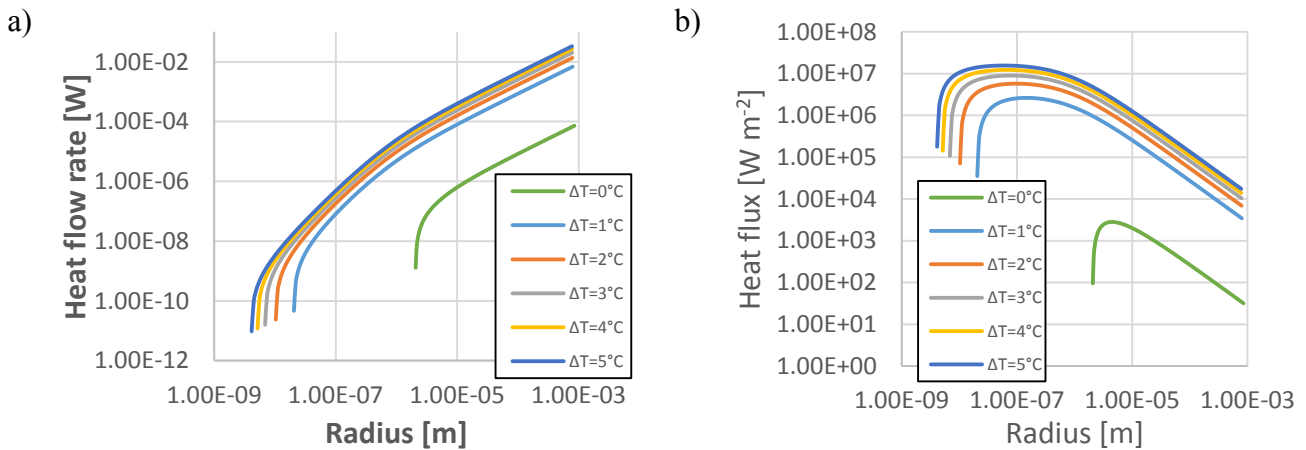




**Figure 2.21 - Temperature drop at the interface, through the droplet and due to the curvature versus radius. The total temperature drop is fixed at 5°C.**

From Equations (2.83-2.86) and considering Equation (2.59), the heat flow rate through a single drop of radius  $r$  can be calculated as:

$$q_d(r) = \frac{4\pi r^2 \left(1 - \frac{r_{min}}{r}\right) \Delta T}{\left(\frac{\delta}{\lambda_{coat}} + \frac{r}{\lambda_l} + \frac{2}{h_i}\right)} \quad (2.87)$$



**Figure 2.22 - Heat flow rate a) and heat flux b) vs droplet radius for different  $\Delta T$  predicted by Abu-Orabi.**

Figure 2.22, where the heat flow rate and the heat flux are presented, shows the same behavior predicted by Le Fevre and Rose (Figure 2.17), the values are quite different, though. With regard to the droplet population, the author extends the Le Fevre and Rose analysis (Eq. 2.80) in order to add the "small" droplet population. The derivation of the small droplet population is reported in paragraph 2.3.2.3, only the main Eqs. are reported in the following. As a boundary condition, the authors impose that the population of "small" droplets equals that of "large" droplets at  $r_e$ :

$$n(r_e) = N(r_e) \quad (2.88)$$

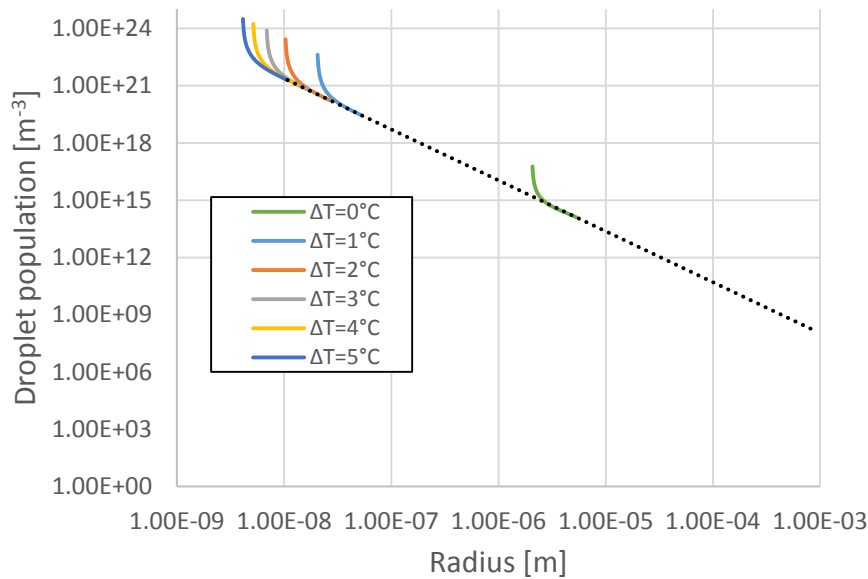
where  $r_e$  is calculated assuming that the nucleation sites form a square array,  $r_e = 1/\sqrt{4N_s}$ ; the Equation for the small droplet population is:

$$n(r) = N(r_e) \frac{r(r_e - r_{min})(A_2 r + A_3)}{r_e(r - r_{min})(A_2 r_e + A_3)} e^{B_1 + B_2} \quad (2.89)$$

Where the three parameters ( $A_1$ ,  $A_2$ , and  $A_3$ ) in Equation 2.89 are defined as:

$$A_1 = \frac{2\Delta T}{\rho_l h_{lv}}; \quad A_2 = \frac{1}{\lambda_l}; \quad A_3 = \frac{2}{h_i} + \frac{\delta}{\lambda_{coat}} \quad (2.90)$$

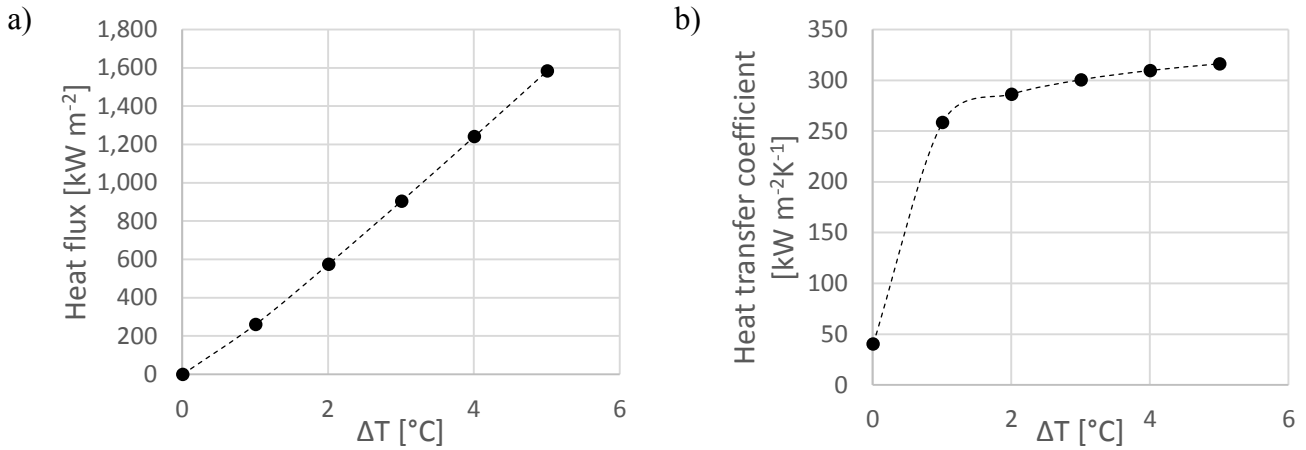
which are derived as reported in paragraph 3.2.3.2. In Figure 2.23, the  $n(r)$  is plotted versus droplet radius for different  $\Delta T$ .



**Figure 2.23 - Droplet population vs droplet radius predicted by Abu-Orabi.**

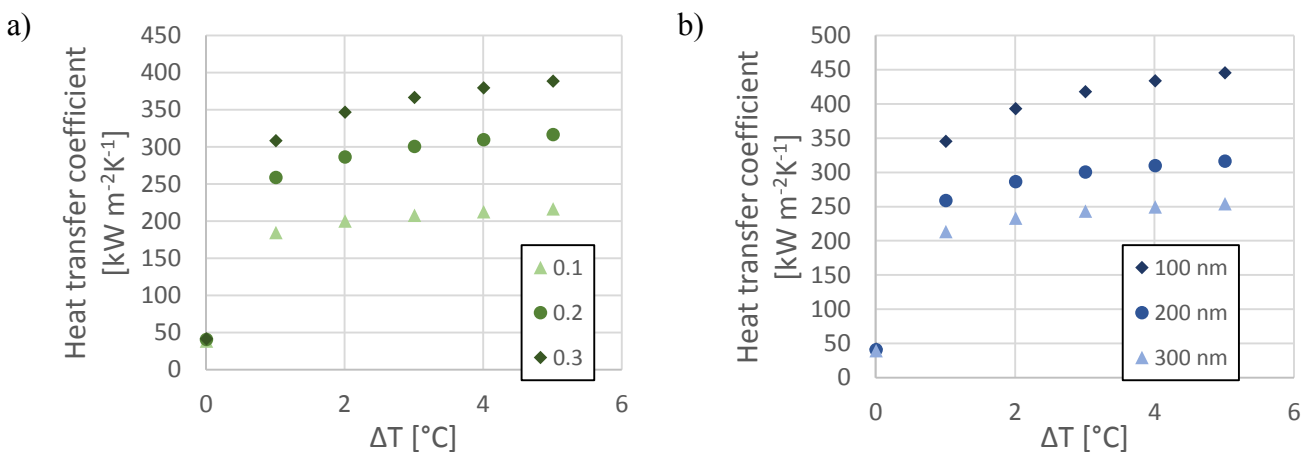
The  $\Delta T$  strongly influences the “small” droplet population, on the contrary of the “big” droplet population. Changing the  $\Delta T$  means change the minimum droplet radius (Equation 2.59), which changes the nucleation sites (Equation 2.60). The effective radius is, then, varied (Equation 2.65). It should be noticed that the “big” droplet population always starts at the end of the related “big” droplet population, in the graph  $N(r)$  is the dotted black line and for simplicity only the  $\Delta T = 5^\circ\text{C}$  is reported. Usually in the literature, the nucleation sites are fixed and varied from  $10^{10}$  to  $10^{15}$  and the influence of the “small” droplet population is more appreciable. Relating the minimum droplet radius to the nucleation density is, in my opinion, reasonable (and experimentally proved) as already reported in

paragraph 2.3.2.1. However, it is necessary to investigate further this relationship. Looking at Figure 2.22b, now it is evident how the heat flux peak is around the effective radius, as the droplet grows, the heat flux decreases as can be expected (by three orders magnitude!). Remembering Equations 2.46 and 2.47, the total heat exchanged and the HTC can be obtained.



**Figure 2.24 - Total heat flux a) and HTC b) vs  $\Delta T$  predicted by Abu-Orabi.**

The behaviours in Figure 2.24 are the same found for the model Le Fevre and Rose, but, for the same input parameters, the  $q$  and HTC are much bigger. The total heat flux is the sum of the heat flux exchanged by the “small” and “big” droplets and it is interesting to notice that the ratio between the two is around 2-3%, meaning that the “small” droplet population has very little importance in the total process, although the peak of the heat flux is obtained by radiuses inside the “small” droplet population.



**Figure 2.25 - HTC versus  $\Delta T$  with a) different coating thermal conductivities [W m<sup>-1</sup> K<sup>-1</sup>] and b) different coating thicknesses.**

In Figure 2.25, the influence of coating thermal conductivity and thickness is reported. The HTC increases with the increasing of the thermal conductivity and with the decreasing of the coating thickness, as expected. However, it is interesting of notice that these values are not easily measured experimentally. The coating conductivity (for such low thicknesses) is really a challenge, in literature

several values are shown in the order of  $0.2 \text{ W m}^{-1} \text{ K}^{-1}$  but each hydrophobic layer should have its measurement. Plus, such coatings are very porous (please refer to Chapter 3) thus a proper measurement relating the coating thickness and the conductivity should be done. About the thickness of the hydrophobic layer, the measurement is easier and there are several methods to get this value, but the values is measured in a single point. Depending on the deposition technique of the coating, the homogeneity is not always guaranteed, the thickness can easily vary of  $\pm 50 \text{ nm}$ .

### 2.3.3.3 Kim *et al.* model

Both the previous models assume that the droplets grow during dropwise condensation with a hemispherical shape, i.e. a contact angle ( $\theta$ ) between solid and liquid equal to  $90^\circ$ . However, liquids wet the surface with different contact angles depending on the surface tension balance at the triple line<sup>4</sup>. The model of Kim *et al.*<sup>27</sup> introduces the contact angle as a variable in order to fill this gap. The authors studied how the contact angle influences the dropwise condensation performances in the range from  $90^\circ$  to  $150^\circ$ . Since the roughness is not considered, using water as a working fluid, the analysis should stop at about  $120^\circ$ . A similar approach to the one proposed by Abu-Orabi is considered: the thermal resistances from the vapor to the surface are considered and, in this case, the droplet growing angle is also accounted for. In particular, the resistance due to conduction in the drop can be obtained from:

$$\Delta T_d = \frac{q_d \theta}{4\pi r \lambda_l \sin \theta} \quad (2.91)$$

Eq. (22) changes dramatically the conduction through a single droplet, giving to the droplets their natural spherical shape instead of a flat layer as in the previous models. It should be mentioned that Le Fevre and Rose takes into account the spherical shape of droplets with the coefficient  $K_1$  lower than 1 (Equation 2.79). The interfacial resistance becomes

$$\Delta T_i = \frac{q_d}{h_i 2\pi r^2 (1 - \cos \theta)} \quad (2.92)$$

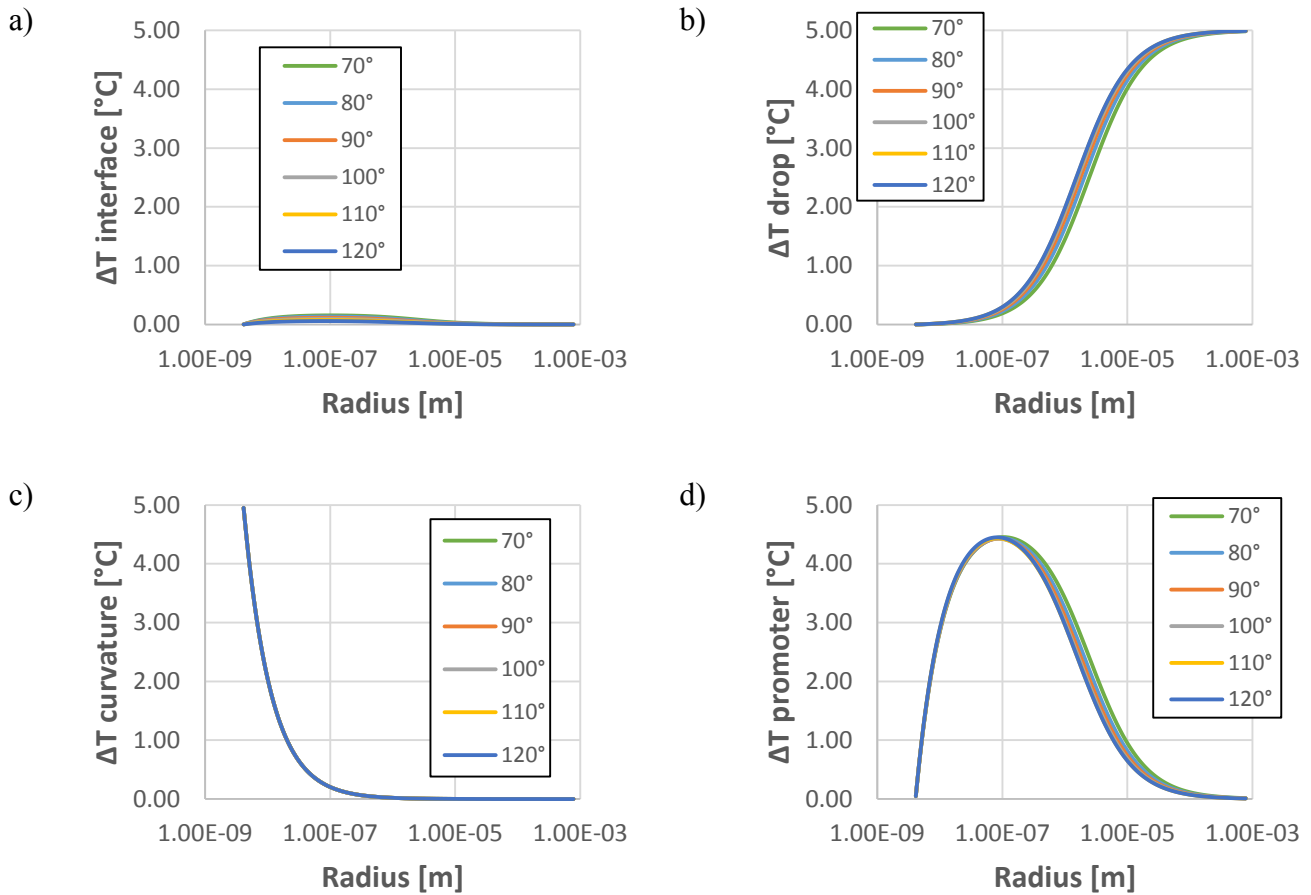
The thermal resistance through the promoter is calculated on the wetted area, resolving the discrepancy made by Abu-Orabi, as

$$\Delta T_{coat} = \frac{q_d \delta}{\lambda_{coat} \pi r^2 \sin^2 \theta} \quad (2.93)$$

and the temperature drop due to the droplet curvature is the same used in the previous models. Adding all the temperature drops and gathering the terms in common in the expression you get:

$$\Delta T = \Delta T_i + \Delta T_{drop} + \Delta T_{coat} + \Delta T_c = q_d \frac{1}{\pi r^2} \frac{1}{1 - \frac{r_{min}}{r}} \left( \frac{\delta}{\lambda_{coat} \sin \theta^2} + \frac{r\theta}{4\lambda_c \sin \theta} + \frac{1}{2h_i(1 - \cos \theta)} \right) \quad (2.94)$$

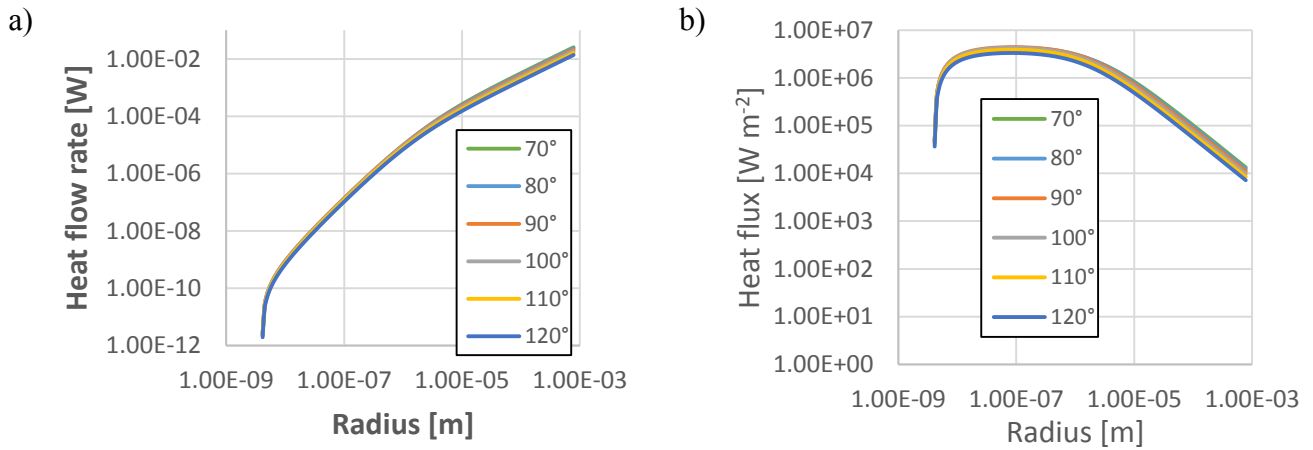
The temperatures drops trend is the same of other models, but it is interesting to investigate how the contact angle influences them. In Figure 2.26, the contact angle is varied from 70° to 120°, values experimentally obtained on the tested surfaces (see Chapter 3).



**Figure 2.26 - a), b) c) and d)  $\Delta T$  due to the interface, to the drop, curvature and promoter versus droplet radius, respectively. The contact angle is varied.**

As reported in Figure 2.26, the parameters do not change significantly with the contact angle in this range. Having surfaces with lower wettability implies higher temperature drop due to the conduction through the droplet, but lower temperature drop at the promoter. The heat flow through the single drop is calculated as:

$$q_d(r) = \frac{\Delta T \pi r^2 \left(1 - \frac{r_{min}}{r}\right)}{\left(\frac{\delta}{\lambda_{coat} \sin \theta^2} + \frac{r\theta}{4\lambda_l \sin \theta} + \frac{1}{2h_i(1 - \cos \theta)}\right)} \quad (2.95)$$

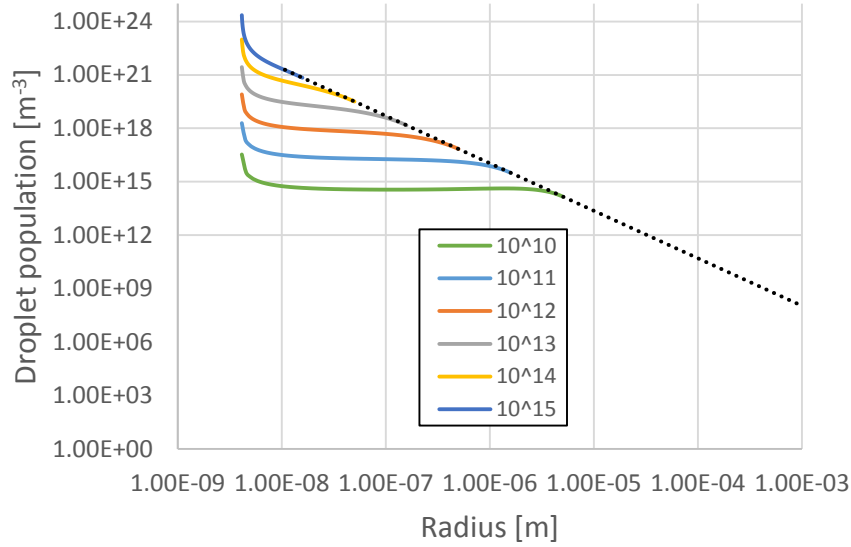


**Figure 2.27 - Heat flow rate a) and heat flux b) vs droplet radius for different contact angle predicted by Kim *et al.*.**

Both the heat flow rate and the heat flux are not significantly affected by the contact angle, which is reasonable considering that the temperature drops are related to the droplet base area which does not change with such contact angle values. It is interesting to notice that the case  $120^\circ$  does not assure higher DWC performances, both the heat flow rate and the heat flux assume the lowest value for the whole range of radius. Also this model considers a division between "large" and "small" droplets. The coefficients for "small" droplets population (Equation 2.72) are:

$$A_1 = \frac{2\Delta T}{\rho_l h_{lv}}; A_2 = \frac{\vartheta(1-\cos(\vartheta))}{4\lambda_l \sin(\vartheta)}; A_3 = \frac{1}{2h_i} + \frac{\delta(1-\cos(\vartheta))}{\lambda_{coat} \sin(\vartheta)^2} \quad (2.96)$$

Imposing  $\theta = 90^\circ$  the coefficients are the same used by Abu-Orabi. Since the influence of  $\Delta T$  is already reported in Figure 2.23, in the following the nucleation site density is varied (and not calculated from the minimum radius). The "small" droplet population with  $10^{15} \text{ m}^{-2}$  is very similar to the populations obtained with Equation 2.60; decreasing the nucleation density  $r_e$  increases and also the "small" droplet population range.

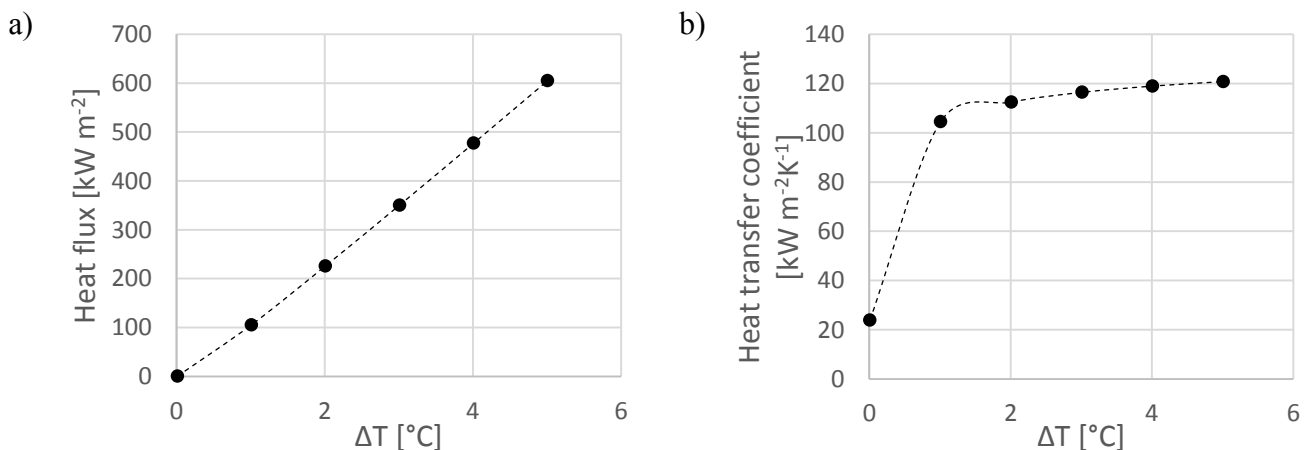


**Figure 2.28 - Droplet population vs droplet radius predicted by Kim *et al.*. The nucleation density is varied.**

In the original model, the maximum droplet radius reached during dropwise condensation on a vertical surface is obtained from the balance between the capillary force and the gravity force:

$$r_{max} = \sqrt{\frac{6(\cos(\vartheta_r) - \cos(\vartheta_a)) \sin(\vartheta) \sigma}{\pi(2 - 3 \cos(\vartheta) + \cos^2(\vartheta)) \rho_l g}} \quad (2.97)$$

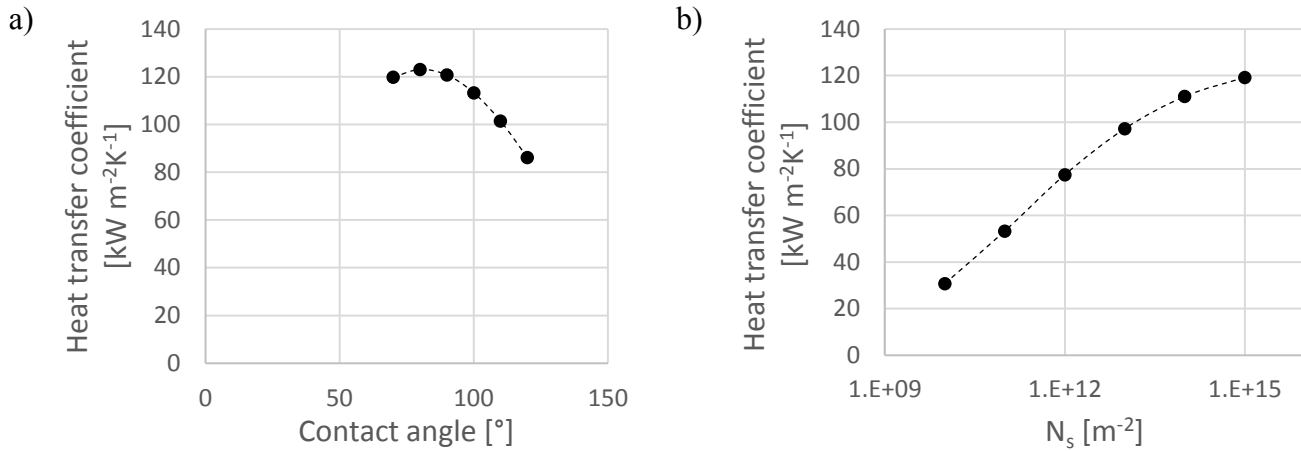
where  $\theta_a$  and  $\theta_r$  are the advancing and receding contact angles, respectively. In the following graphs, however, the maximum radius is imposed at the measured value (Table 2.1). The total heat flux and the HTC are reported in Figure 2.29.



**Figure 2.29 - Total heat flux a) and HTC b) vs  $\Delta T$  predicted by Kim *et al.*.**

From the previous observations, it is clear why the total thermal flux (or HTC) calculated with the present model is lower than those calculated with the previous models. Since it has been shown the

dependence of Kim *et al.* model on contact angles and nucleation sites, in Figure 2.30 the HTC has been varied with these two parameters.



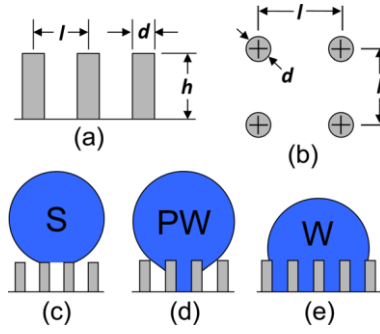
**Figure 2.30 - HTC at fixed  $\Delta T = 5^\circ\text{C}$  with a) different contact angles and b) different nucleation sites.**

The model predicts a maximum HTC at around  $80^\circ$ , which can be unexpected. Decreasing the surface wettability seems to not be a good solution for improving the DWC performances, for the present model. On the other hand, the HTC increases with the increasing of the nucleation site density as expected. Values of nucleation sites ranging from  $10^{10}$  to  $10^{15}$  is commonly used in literature, the problem arises when the  $N_s$  is unknown (as always) and it has to be chosen. As reported in Figure 2.30, the HTC can be easily fixed.

#### 2.3.3.4 Miljkovic *et al.* model

The model described by Miljkovic *et al.* introduces the variable of surface morphology. Dropwise condensation has recently been studied on structured surfaces, thus surfaces with a controlled or randomly distributed roughness. The model supposes pillars built in arrays along a generic surface with heights  $h$ , diameters  $d$ , and pillar-to-pillar spacings  $l$ , which is the case of imposed roughness on silicon substrates<sup>46,47,131,132</sup>; it can be applied also to generic random roughened surface but with less accurate. The authors, then, modified the Kim *et al.* model to account for the pillar geometry and emergent droplet morphology<sup>133</sup> with the scheme reported in Figure 2.31. During DWC on a structured surface, droplets can assume different wetting regime based on the surface morphology (Figure 2.31): **S** (suspended) where condensed droplets sit on top of the micro/nanostructure<sup>34</sup>, **PW** (partially wetted) where the droplets form a liquid bridge connecting the base of the droplet<sup>133</sup>, or **W** (wetted) where droplets are in the Wenzel state<sup>69</sup>. It has to be underlined that droplets in S regime can depart by coalescence-induced droplet jumping if morphology parameters are satisfied<sup>26</sup>.





**Figure 2.31 - Schematics of the modeled structured surface showing a) side view and (b) top view of the characteristic structure dimensions  $h$ ,  $d$ , and  $l$  representing the pillar height, diameter and center-to-center spacing, respectively. Schematics showing the (c) S, (d) PW, and (e) W morphologies.**

The authors suggest two criteria to accurately predict the wetting morphology of a single droplet. The first is a nonequilibrium thermodynamic energy criterion<sup>43</sup> which compares the dimensionless energy of the advancing Wenzel<sup>69</sup> ( $\cos \theta^W$ ) and Cassie<sup>134</sup> ( $\cos \theta^{CB}$ ) droplet morphologies and it results

$$E^* = \frac{\cos \theta^{CB}}{\cos \theta^W} = \frac{-1}{\cos \theta_a} \quad (2.98)$$

When  $E^* > 1$  the contact line can overcome the energy barrier to depin and a W droplet is formed (Figure 2.31e). If  $E^* < 1$  complete depinning is not possible and the droplet grows upward over the top of the pillar array forming a PW Cassie droplet (Figure 2.31c and Figure 2.31d). The second criterion is related to the spacing between the pillars  $l$  and the average condensing droplet spacing ( $l_c$ ). If  $l_c \geq 2l$  the distance between the pillars is sufficient for avoid the flooding of the surface. The mean condensing droplet spacing can be related to the nucleation density  $N_s$  by

$$l_c = \frac{1}{\sqrt{4N_s}} \quad (2.99)$$

For the purposes of this model, condensation on the structured surface is assumed to be spatially random. These two wetting criteria (Eqs. 2.98 and 2.99) have been validated experimentally for a wide variety of structured surfaces with a range of length scales and surface energies<sup>18,43,133</sup>. This is the starting point for the incorporation of roughness on the heat transfer model. While the previous models assume a constant droplet contact angle, which is appropriate for dropwise condensation on flat hydrophobic surfaces<sup>27,101,135</sup>; it does not apply for structured superhydrophobic surfaces, since droplets have been observed to have variable contact angles during growth<sup>136,137</sup>. To resolve this discrepancy, a model was developed to predict the droplet contact angle as a function of the droplet radius  $R$ . Depending on the wetting regime

$$\theta_{PW}(R) = \begin{cases} \theta_a & \text{if } R \leq l \\ \frac{\pi}{2} + \frac{(\theta_a^{CB} - \pi/2)}{(R_{max} - l)}(R - l) & \text{if } l < R < R_{max} \\ \theta_a^{CB} & \text{if } R > R_{max} \end{cases} \quad (2.100)$$

$$\theta_W(R) = \begin{cases} \theta_a & \text{if } R \leq l \\ \theta_a^w & \text{if } R > l \end{cases} \quad (2.101)$$

$$\theta_s(R) = \theta_a^{CB} \quad (2.102)$$

where

$$\cos(\theta_a^{CB}) = \varphi(\cos(\theta_a) + 1) - 1 \quad (2.103)$$

$$\theta_a^w = r \cos(\theta_a) \quad (2.104)$$

where  $r = 1 + \frac{\pi dh}{l^2}$  is the roughness and  $\varphi = \frac{\pi d^2}{4l^2}$  the surface solid fraction. Remembering Figure 2.31 and Equations 2.91-2.94, the considerations on the droplet heat flow rate are the same of the previous models, then

$$q(R, \vartheta) = \frac{\pi R^2 \left( \Delta T - \frac{2T_{sat}\sigma}{Rh_{fg}\rho_w} \right)}{\frac{1}{2h_i(1-\cos(\vartheta))} + \frac{R\vartheta}{4k_w \sin(\vartheta)} + \frac{1}{k_{HC} \sin(\vartheta)^2} \left[ \frac{k_p \varphi}{\delta_{HC} k_p + h k_{HC}} + \frac{k_w(1-\varphi)}{\delta_{HC} k_w + h k_{HC}} \right]^{-1}} \quad (2.105)$$

The droplet in S wetting morphology is not affected by the liquid bridge between the pillars (Figure 2.31), however this volume would be occupied by saturated steam or uncondensable gases which have a lower thermal conductivity than the condensate and this would correspond to a higher thermal resistance for the heat flux. The best scenario is, then, when the droplet removal is due to the coalescence-induced jumping phenomenon (microscale droplet dimension) which eliminates the condensate thermal resistance. The droplet population is modified with the following coefficients:

$$A_1 = \frac{2\Delta T}{\rho_c h_{fg} (1-\cos\vartheta)^2 (2+\cos\vartheta)} \quad (2.106)$$

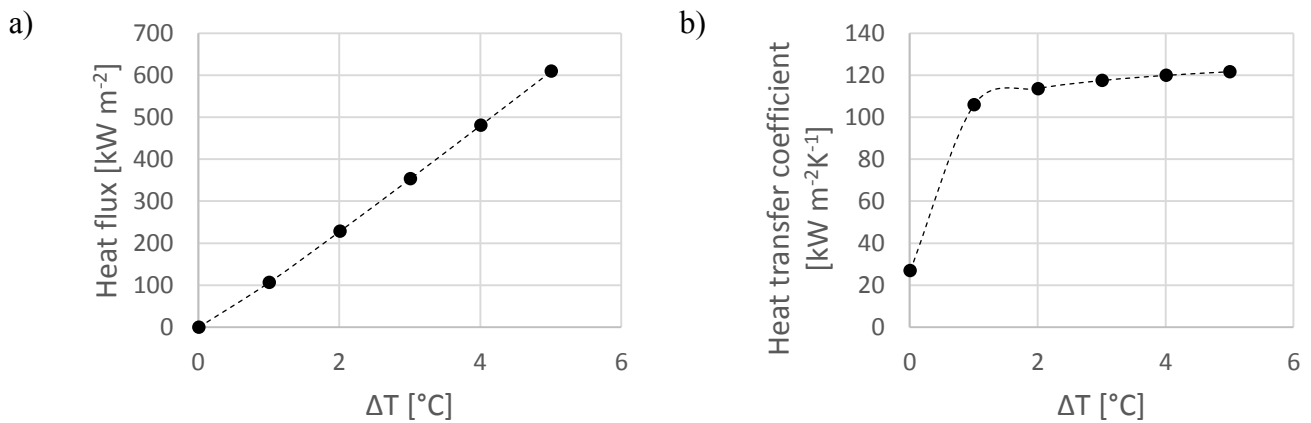
$$A_2 = \frac{\vartheta}{4 \lambda_c \sin(\vartheta)} \quad (2.107)$$

$$A_3 = \frac{1}{2 h_i (1-\cos\vartheta)} + \frac{1}{k_{HC} \sin(\vartheta)^2} \left[ \frac{k_p \varphi}{\delta_{HC} k_p + h k_{HC}} + \frac{k_w(1-\varphi)}{\delta_{HC} k_w + h k_{HC}} \right]^{-1} \quad (2.108)$$

The model adds the substrate inclination to the calculation of the maximum droplet radius as follows

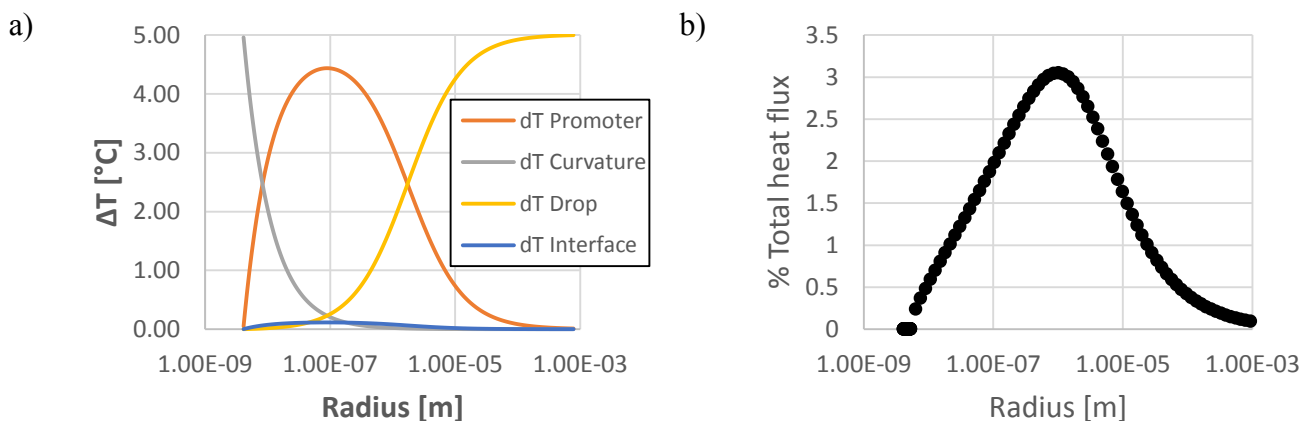
$$r_{max} = \sqrt{\frac{6(\cos(\vartheta_r) - \cos(\vartheta_a)) \sin(\vartheta)}{\pi(2 - 3 \cos(\vartheta) + \cos^2(\vartheta))} \frac{\gamma}{\rho_l g \cos\beta}} \quad (2.109)$$

Decreasing the inclination of the plate, the thermal flow will decrease, since the maximum radius tends to increase more and more. For a perfectly horizontal surface, in fact, it will be impossible for the phenomenon of sweeping to take place, since the action of gravity on the drops will be zero. As already reported, the maximum radius is imposed fixed to the measured one. Furthermore, since the HTC are measured on flat surfaces, the model is compiled with  $h=0$  and  $\varphi=1$ . The total heat flux and HTC are presented in Figure 2.32.



**Figure 2.32 - Total heat flux a) and HTC b) vs ΔT predicted by Miljkovic *et al.*.**

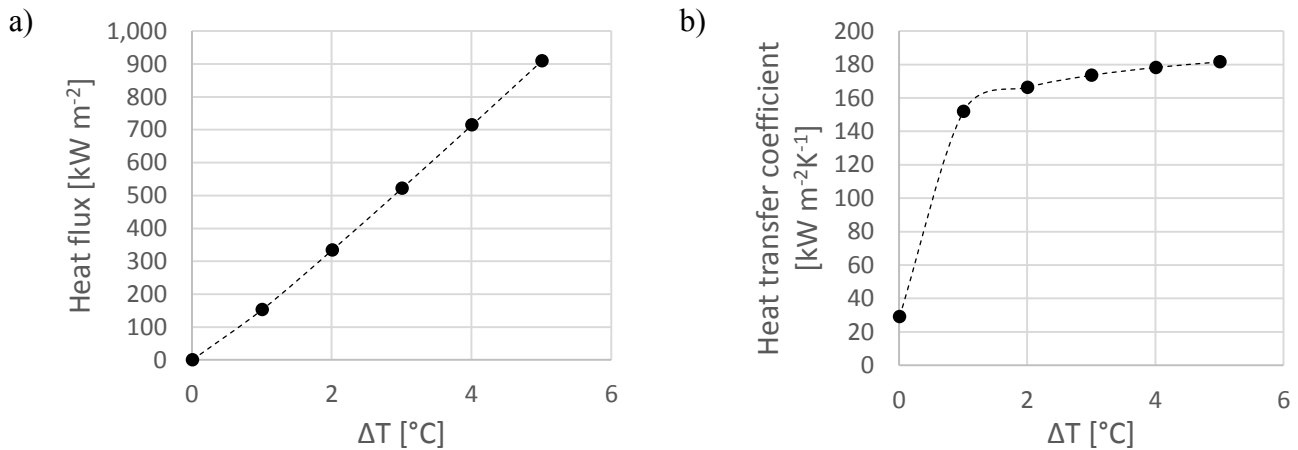
In Figure 2.33a, the thermal resistances are plotted against the radius, from the minimum to the departing radius. It is interesting to compare this graph to the percentage of heat exchanged by a certain droplet dimension (Figure 2.33b). In this case, the droplet radii interval is 20 nm.



**Figure 2.33 - a) Temperature drop at the interface, through the droplet, through the promoter and due to the curvature versus radius. b) Percentage of heat flux exchanged by a droplet radius interval respect to the total heat flux versus droplet radius. The total temperature drop is fixed at 5°C.**

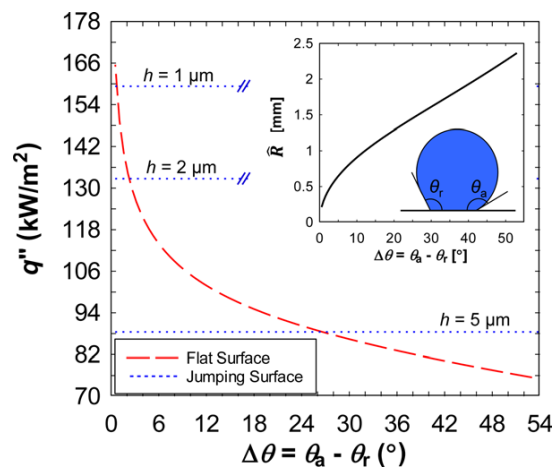
In Figure 2.33b, a heat flux peak appears at radii around 1 μm and it is equal to 3%. Considering the interval where the promoter is the main resistance (Figure 2.33a), it is interesting to notice that the

65% of the heat flux is exchanged in this area (Figure 2.33b). It is, then, stressed the importance of the coating thermal resistance on the total heat exchanged even if the coating thickness is within the nanometric scale. Knowing the coating parameters becomes, moreover, fundamental in order to properly develop a heat exchange model and, also, how the heat is exchanged in such low scales. This topic is discussed theoretically in paragraph 2.4. For instance, Figure 2.34 shows the total heat flux and HTC with a 100 nm coating thickness, which is the half as compared to the usual imposed thickness.



**Figure 2.34 - Total heat flux a) and HTC b) vs ΔT predicted by Miljkovic *et al.* for a coating thickness of 100 nm instead of 200 nm.**

The HTC is increased by 50% compared to the obtained with 200 nm, highlighting how the models (and DWC performances) are really sensitive by this parameter. Although surface structures are not considered in the present model analysis, some interesting information can be extrapolated for the surface optimization.



**Figure 2.35 - Structured (jumping) and flat (gravity shedding) surface steady-state heat flux as a function of intrinsic promoter coating contact angle hysteresis for three structured surfaces coated with the same promoter. Inset: droplet departure diameter, as a function of intrinsic flat surface contact angle hysteresis. Image taken in Miljkovic *et al.*<sup>26</sup>.**

In Figure 2.35 the comparison between a flat and a structure surface, which induces the jumping droplets, is presented. Firstly, rough surfaces show lower HTC compared to flat surface, except of

the surface promotes jumping droplets<sup>42</sup>. Secondly, HTC on flat surfaces is strongly influenced by contact angle hysteresis which influences the departing diameter, thus the condensate thermal resistance<sup>31,138</sup>. Figure 2.35 shows the potential of inducing jumping droplets for the HTC enhancement during DWC, but experimentally it was demonstrated that the phenomenon has some limitations in terms of heat flux. Since increasing the heat flux means increases the nucleation sites, there is a critical heat flux<sup>42,46-48</sup> where the nucleation sites are so close to flood the surface and the jumping droplet phenomenon is suppressed.

### 2.3.3.5 Chavan *et al.* model

All the previous models assume for the conduction resistance through the single droplet constant temperature boundary conditions on the droplet base (solid–liquid interface) and on droplet surface (liquid–vapor interface)<sup>130</sup>. During the 70ies, detailed three-dimensional simulations of droplets has been solved on hydrophilic surfaces ( $15^\circ < \theta_a < 90^\circ$ ) by assuming a convective boundary condition with a finite HTC on the free surface<sup>139,140</sup>. The work of Chavan *et al.* fill the gap for droplets growing on hydrophobic or superhydrophobic surfaces. A constant heat transfer coefficient boundary condition at the liquid–vapor interface (Equation 2.77), and a constant temperature ( $T_{wall}$ ) boundary condition at the solid–liquid interface have been imposed in order to avoid sudden temperature jump across the three phase contact line, and the temperature will change gradually along the liquid–vapor interface. The authors use two-dimensional axisymmetric numerical simulations to study individual droplet heat transfer on surfaces with  $90^\circ < \theta_a < 170^\circ$ , showing that previous models underpredict the overall heat transfer by as much as 300% for DWC. The three phase contact line resulted to be the location where the local heat flux can be up to 4 orders of magnitude higher than at the droplet top, which is the phenomenon not considered by the previous formulations. The present model is based on three dimensionless groups governing the droplet heat transfer behavior: the droplet Nusselt number ( $Nu$ ), the Biot number ( $Bi$ ) and apparent advancing contact angle ( $\theta_a$ ); that is,  $Nu = f(Bi, \theta_a)$ . The Nusselt and Biot numbers are defined in terms of the droplet base radius ( $R_b$ ) as

$$Bi = \frac{h_i r_b}{\lambda_l} \quad (2.110)$$

$$Nu = \frac{q}{\lambda_l r_b (T_{sat} - T_{wall})} \quad (2.111)$$

The authors provide analytical result that can more easily be integrated into droplet growth and phase change heat transfer models. The least-squares method leads to the following expressions ( $\theta_a$  is in radians):

$$Nu = 3\theta_a^{0.65} Bi^{0.83} + 0.007\theta_a^{5.1} Bi^{-0.23} \quad Bi \leq 0.5 \quad (2.112)$$

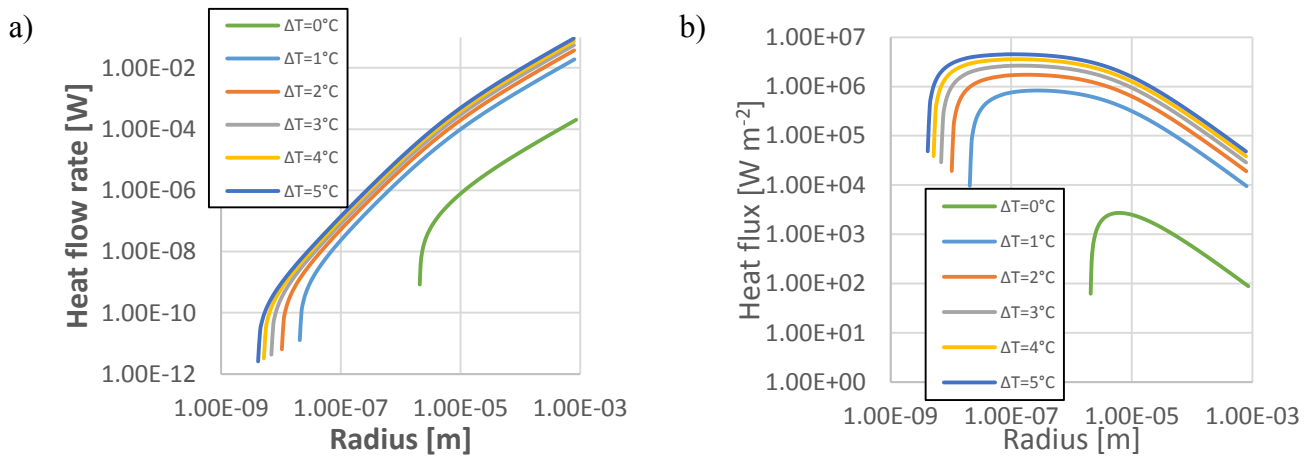
$$Nu = 0.29\theta_a^{2.24} Bi^{-0.17} + 3.33\theta_a^{-0.3} Bi^{0.72} \quad 0.5 < Bi \leq 2 \quad (2.113)$$

$$Nu = 5.76e^{-0.28\theta_a^{0.68}} + \ln(1 + 5Bi^{0.82} - 2.79Bi^{0.83}) \quad 2 < Bi \leq 10^5 \quad (2.114)$$

The heat flow rate through the single droplet is then

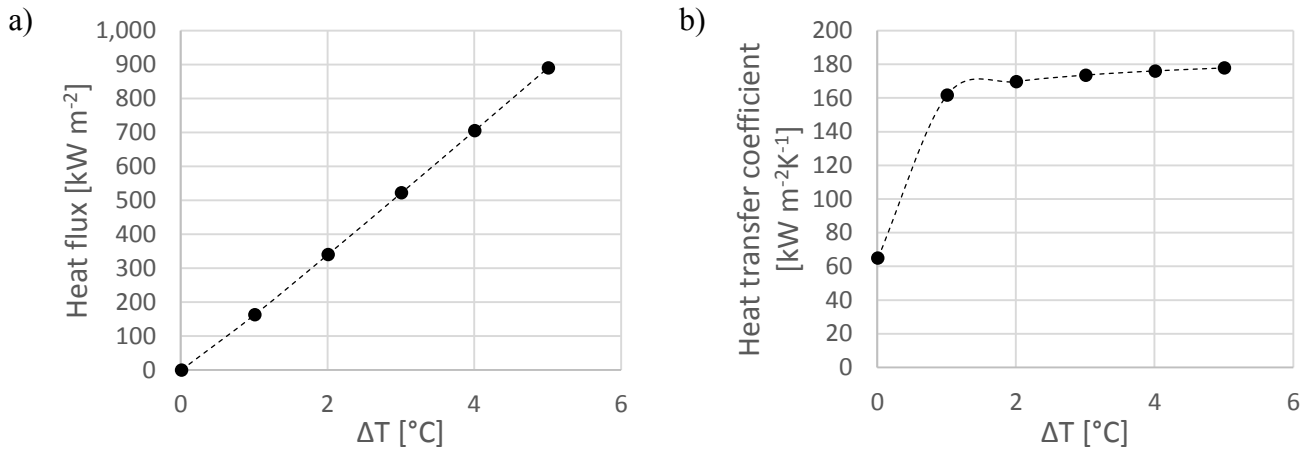
$$q(R, \vartheta) = \frac{\Delta T \left(1 - \frac{r_{min}}{R}\right)}{\frac{1}{Nu\lambda_l R \sin(\theta)} + \frac{\delta_{coat}}{\lambda_{coat} \pi R^2 \sin(\theta)^2}} \quad (2.115)$$

Where at the denominator the Nu number is calculated with Equations 2.112-2.114 and takes into account the conduction through the droplet and the interface resistance; the promoter thermal resistance is in parallel with the previous one. It has to be specified that Equation 2.115 is not reported in the article, but it was chosen from the reasoning reported in it, in particular the part for the coating resistance which is not mentioned in the article. In Figure 2.36a and Figure 2.36b, the single droplet heat flow rate and heat flux are reported, respectively.



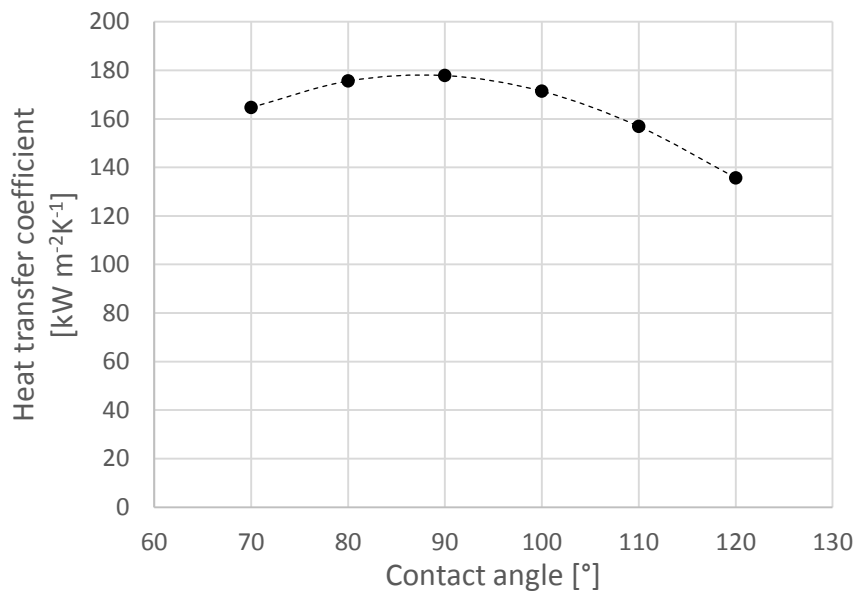
**Figure 2.36 - Heat flow rate a) and heat flux b) vs droplet radius for different  $\Delta T$  predicted by Chavan *et al.***

The model, although it uses a different formulation for the heat flow rate for a single droplet, it considers the droplet population proposed by Miljkovic *et al.*<sup>26</sup>, in particular the coefficients in the “small” droplet population. Remembering paragraph 2.3.2.3, the coefficients are obtained imposing the heat exchanged from the single droplet, thus in this case they should be obtained from Equation 2.115. However, the total heat flux and the HTC are reported in Figure 2.37.



**Figure 2.37 - Total heat flux a) and HTC b) vs  $\Delta T$  predicted by Chavan *et al.*.**

In Figure 2.38 the HTC versus the growing contact angle of droplet during DWC is plotted. All the other conditions are fixed, in particular  $\Delta T = 5^\circ\text{C}$ .



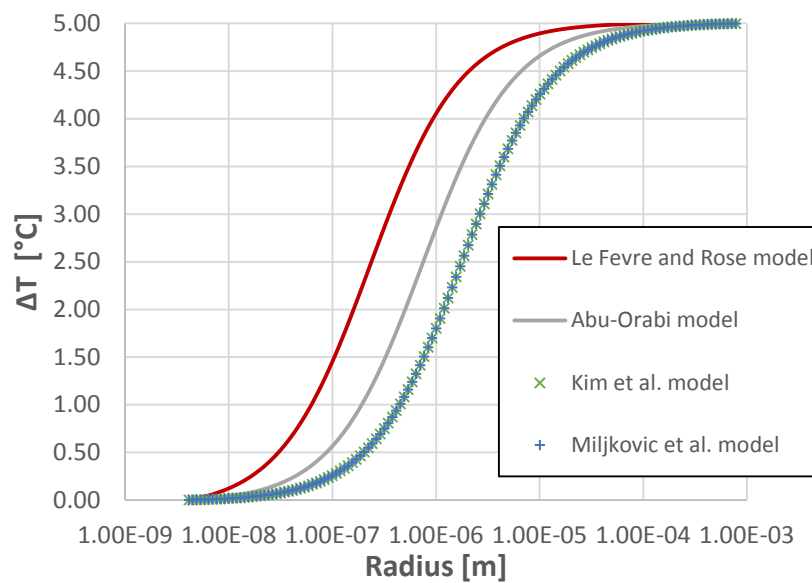
**Figure 2.38 - HTC at fixed  $\Delta T = 5^\circ\text{C}$  with different contact angles.**

In the paper, the influence of  $\theta_a$  is discussed in terms of  $Nu$  number, where  $Nu$  decreases with increasing  $\theta_a$  due to the elevated conduction resistance associated with higher  $\theta_a$ . Here, it was preferable to show the dependency of  $\theta_a$  on the HTC as in Kim *et al.* (Figure 2.30) and it is interesting to notice a HTC peak around  $90^\circ$ . Again, having very low wettable surfaces could not be preferable from a theoretical point of view, even for flat surfaces.

### 2.3.4 Comparison among models

In the following, a comparison between the models is presented. As reported in the previous paragraph, all the models chosen are very similar besides the Le Fevre and Rose one, where the thermal resistances for the schematization of the single droplet are different and it does not consider the “small” droplet population. Actually, using Equation 2.60 for the nucleation sites density value,

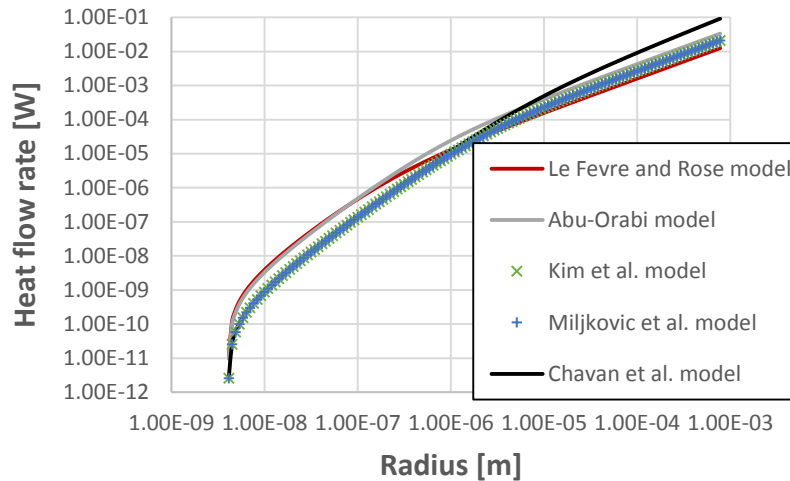
the influence of “small” droplet population is negligible (see Figure 2.23 and Figure 2.28). The main difference becomes, then, the thermal resistance due to the promoter which is “not” (see paragraph 2.3.3.1) taken into account by Le Fevre and Rose. The droplet growing contact angle should play a key role in the HTC formulation (see Figure 2.38), but, again, imposing  $90^\circ$  the differences are not appreciable. Hence the starting point for a model comparison is the conduction thermal resistance through the droplet, which is the distinguishing parameter for understanding why the different HTCs as output. In Figure 2.39, the temperature drop along the condensing droplet as function of droplet radius is shown. In the Figure, the Chavan *et al.* model is not reported since with its numerical simulation incorporates both interfacial and droplet conduction resistance.



**Figure 2.39 - Temperature drop along the condensing droplet versus droplet radius. The total temperature drop is imposed at 5°C. For the full description of the theoretical models please refer to paragraph 2.3.3.**

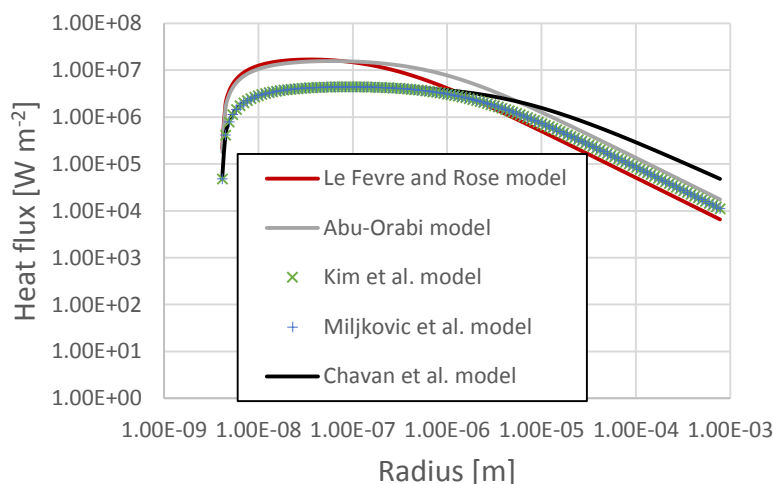
At a fixed droplet radius the temperature drop is always higher for the Le Fevre and Rose model, since it does not consider the temperature drop due to the promoter (the total temperature drop is fixed). Kim *et al.* and Miljkovic *et al.* models are equal, whereas Abu-Orabi model predicts always a higher  $\Delta T$ . Abu-Orabi, likewise Le Fevre and Rose, represents the  $\Delta T$  along the droplet as  $r/\lambda_l$ , as an infinite plane with  $r$  as thickness. Kim and co-authors, instead, introduce in the analysis the real droplet shape, which leads to a lower volume of condensate. The heat flow rate for the different models are presented in Figure 2.40.





**Figure 2.40 - Heat flow rate vs droplet radius. For the full description of the theoretical models please refer to paragraph 2.3.3.**

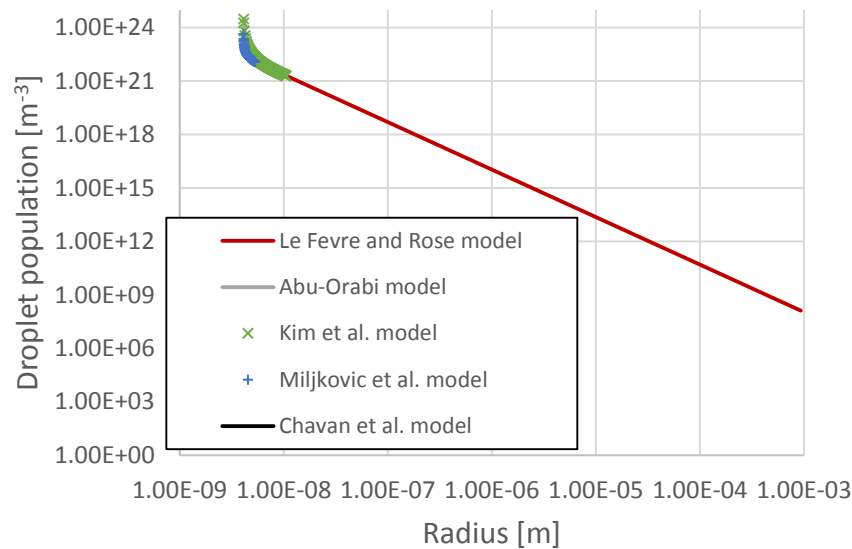
The trend of heat flow rate of a condensing droplet is very different for all the models, besides Kim *et al.* and Miljkovic and co-workers. It is interesting to notice that at around 1  $\mu\text{m}$  of droplet radius, Chavan *et al.* and Miljkovic *et al.* start to diverge, with Chavan *et al.* predicting a higher heat flow. The model of Le Fevre and Rose, instead, predicts a higher heat exchanged for droplets with radius lower (again) than 1  $\mu\text{m}$  and after this radius vice-versa. The model of Abu-Orabi predicts always a higher heat flow rate than Kim *et al.* and Miljkovic and co-workers, not only for the different definition of the conduction resistance through the droplet, but also for the different definition of the resistance of the hydrophobic coating (see paragraph 2.3.3.2). The heat flux though the base area of a single droplet is, instead, shown in Figure 2.41.



**Figure 2.41 - Heat flux vs droplet radius. For the full description of the theoretical models please refer to paragraph 2.3.3.**

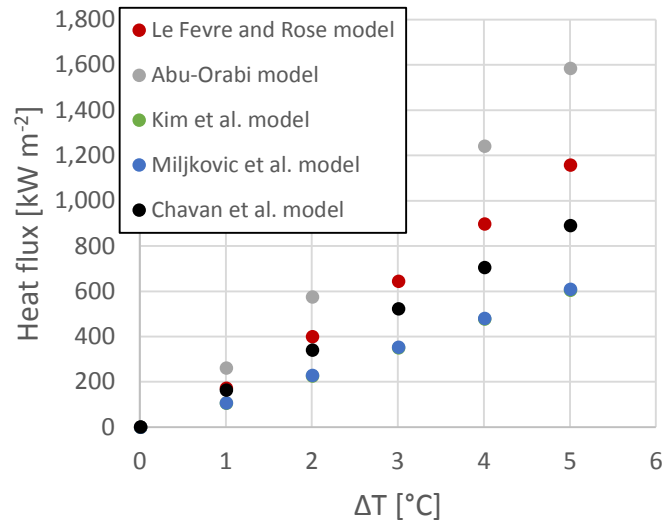
The considerations are similar to those exposed previously for the heat flow rate. Figure 2.41 adds that the peak of the heat flux is similar for Kim *et al.*, Chavan *et al.* and Miljkovic *et al.*, while it is

similar for Le Fevre and Rose and Abu-Orabi. The trend are quite similar though, with a maximum at around  $0.01 \mu\text{m}$  and the heat flux which decreases until the departing radius. In order to calculate the total heat flux during DWC, the droplet population has to be considered (paragraph 2.3.2.3). In Figure X, “small” and “big” droplet population have been displayed for all the models. Le Fevre and Rose considers only the “big” droplet population from the minimum to the maximum radius and its formulation has been used by the other ones.

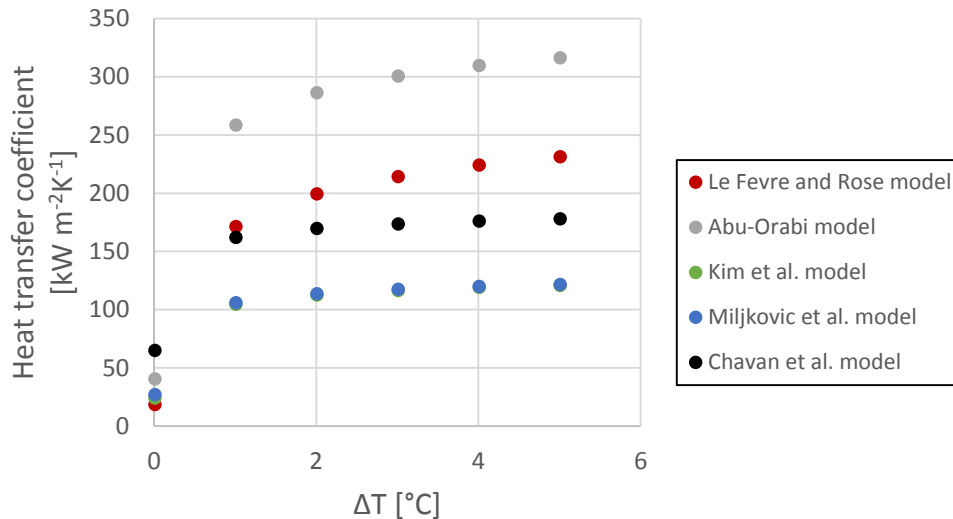


**Figure 2.42 - Droplet population vs droplet radius. For the full description of the theoretical models please refer to paragraph 2.3.3.**

In Figure 2.42, all models share the “big” droplet population from the maximum radius to the effective radius, besides Le Fevre and Rose. The “small” droplet population overlaps for Abu-Orabi and Kim *et al.* and for Chavan *et al.* and Miljkovic *et al.*. The definition of the effective radius is the reason for this discrepancy, which strongly influences  $n(r)$  (Equation 2.72). However, being  $n(r)$  negligible compared to  $N(r)$ , the total heat flux depends more on the single droplet heat flow rate formulation as reported in Figure 2.43 and Figure 2.44, where the total heat flux and the HTC are reported. At a fixed  $\Delta T$  in descending order there is the model of Abu-Orabi, Le Fevre and Rose, Chavan *et al.*, Kim *et al.* and Miljkovic *et al.*. Actually, Kim *et al.* and Miljkovic *et al.* have basically the same values for the total heat flux. Besides Abu-Orabi which underestimates the promoter thermal resistance, the order is reasonable. Le Fevre and Rose do not consider the promoter at all so the HTC is higher, then Chavan *et al.* states that the previous model underestimate the heat flux at the contact triple line and Kim *et al.* and Miljkovic *et al.* have the same formulation.

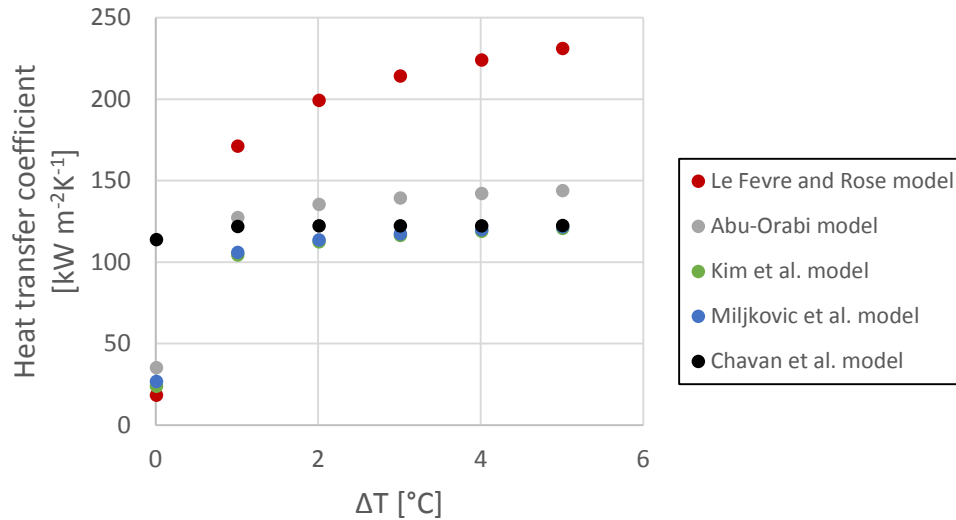


**Figure 2.43 - Total heat flux vs  $\Delta T$ . For the full description of the theoretical models please refer to paragraph 2.3.3.**



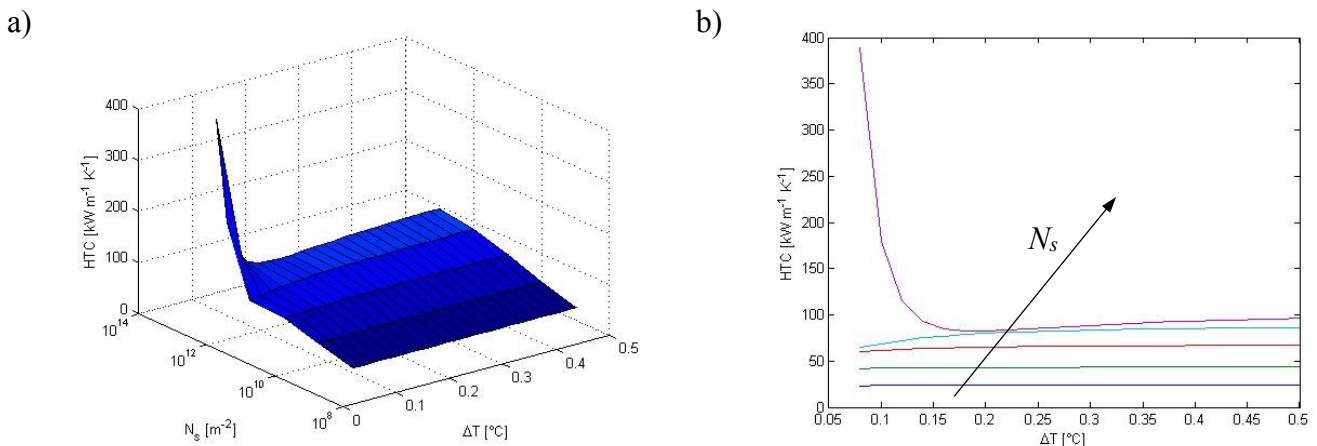
**Figure 2.44 - HTC vs  $\Delta T$ . For the full description of the theoretical models please refer to paragraph 2.3.3.**

In Figure 2.45 the HTC formulation have been modified for the model of Abu-Orabi, applying the promoter thermal resistance to the base area of the droplet. Now, the model shows HTC comparable to the others with the same input parameters (see Table 2.1), to the best of author's knowledge it is not clear if it was a mistake in the article and ex-post corrected or just a mistake. In Figure 2.45, the value of nucleation site density for the Chavan model has been modified in order to obtain HTC in the range of the other model and it was fixed equal to  $10^{11} \text{ m}^{-2}$ . In this case, the formulation of  $N_s$  depending on the minimum radius cannot be used.



**Figure 2.45 - HTC vs  $\Delta T$ . Abu-Orabi is modified as reported in the text. The nucleation site density is fixed equal to  $10^{11} \text{ m}^{-2}$  in Chavan *et al.*. For the full description of the theoretical models please refer to paragraph 2.3.3.**

In Figure 2.45 the nucleation site density is imposed and this can be dangerous for the model stability, in Figure 2.46 Miljkovic and co-workers model is used as example.



**Figure 2.46 - a) and b) different graphs for HTC versus  $\Delta T$  and  $N_s$ .**

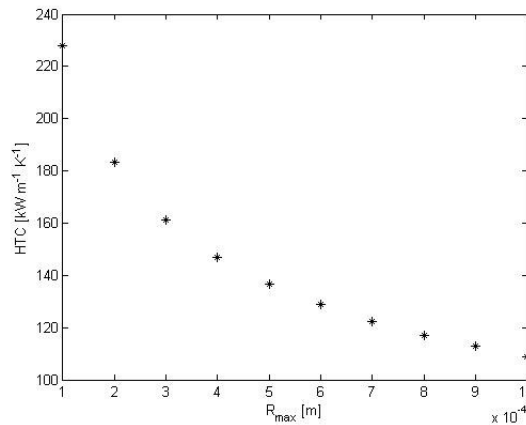
Without imposing a relationship between  $r_{min}$  and  $r_e$  (Equation 2.60),  $r_e$  can be lower than  $r_{min}$  in some cases (Equations 2.59 and 2.66). Looking at Figure 2.46a, the HTC starts to asymptotically tend to  $+\infty$  at low  $\Delta T$  and at high  $N_s$ . In Figure 2.46b, it is more evident how increasing  $N_s$  the shape of HTC curves changes drastically near  $\Delta T = 0^\circ\text{C}$ .

Henceforth some comments on models are reported.

- A very important parameter is the contact angle, the problem arises in which angle must be chosen. As reported in paragraph 2.1, a surface can be characterized by a static contact angle or by two dynamic contact angles: advancing and receding. What value should be used? In other words, what is the angle assumed by droplets while growing? In literature, static contact angle is suggested, even though the advancing contact angle is identified as droplet growing

contact angle. However, those angles are measured in different conditions from the condensing environment, in particular for saturated vapor environments. A droplet while growing (after  $r_e$ ) is growing on a wetted surface (smaller droplets) thus it cannot assume the advancing contact angle measured in open air, but it assumes lower values. Please refer to Chapter 6 for further details.

- As reported in paragraph 2.3.2.2 the droplet departing radius is imposed equal to 0.93 mm, the value measured during DWC on a specific treatment. Different authors suggest different formulas for the  $r_{max}$ , but this choice permits to avoid to introduce another parameter in the models, thus comparisons can be done based on a real experiment. Furthermore, the experimental apparatus does not allow to perform experiment with a negligible vapor velocity which modify  $r_{max}$ . Thus, formulations cannot be used since they do not consider the influence of the vapor shear stress. To the best of the author's knowledge, the presence of a vapor speed should influence only  $r_{max}$  since it is the output of a force balance. Figure 2.47 shows that in order to have significant increasing on HTC the droplet departing radius should increase highly.



**Figure 2.47 - HTC during DWC versus droplet maximum radius. The model of Miljkovic *et al.* has been used.**

- The thermal resistance associated to the promoter is simply the thickness divided by the thermal conductivity of the coating and applied to the droplet base area. The only significant parameter which is supposed in models is the thermal conductivity, which resulted to be a complex measurement. As showed in Figure 2.25, the model of Abu-Orabi (the reasoning can be extended to all models) asserts a strong relationship between HTC and  $\lambda_{coat}$  and a detailed explanation is reported in paragraph 2.3.3.4.
- In the filmwise model, the HTC approaching  $\Delta T = 0^\circ\text{C}$  tends to  $+\infty$ , whereas in DWC models tend to 0. DWC models are based on the single droplet heat flux and the droplet population which starts from the minimum droplet radius. For  $\Delta T \rightarrow 0$   $r_{min}$  tends to  $+\infty$ ; empirically the

droplet nucleation is not promoted. Remembering the relation between  $r_{min}$  and  $N_s$ , it gives that  $N_s \rightarrow 0$  which means that condensation is not happening ( $HTC \rightarrow 0$ ). The limit for which HTC starts to decrease are practically unknown and needs further investigation.

## 2.4 Conduction through thin film

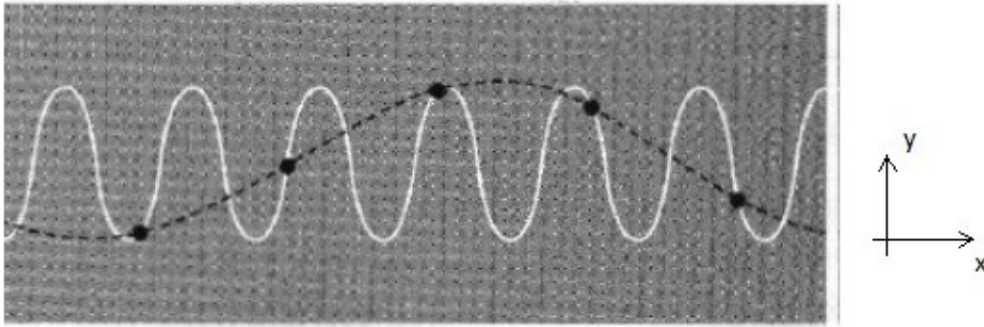
In this paragraph, the process of thermal exchange in a thin film is briefly analyzed<sup>141</sup>. Phonons, that are waves generated by the vibrations of lattice's atoms, affect mostly the process<sup>142,143</sup>. Firstly, phonons nature and the scattering processes are studied<sup>144,145</sup>: the presence of scattering processes, Umklapp process and scattering at the lattice imperfections, permits the definition of a temperature distribution in the material. Thus, the definition of a thermal gradient and of a thermal conductivity. An expression of the thermal conductivity is provided outside the limits of the Fourier's law<sup>142</sup>: this expression shows the dependence of the thermal conductivity on the mean free path, heat capacity and sound's speed of the material. Two models are, then, presented for the solution of the thermal conductivity outside the Fourier's law boundaries: the Gray Model<sup>146</sup> (GM) and the Extended Irreversible Thermodynamics theory<sup>144,147</sup> (EIT). As reported in paragraph 2.3, the thermal conductivity remains the biggest question mark for the use of DWC models. In the range of thicknesses (hundreds of nanometers) associated to the hydrophobic coatings, Fourier's law can not be applied and it was not possible to do some experimental measurements. Having a relationship between the thermal conduction of the bulk material and the material thickness can help in imposing a sensate value in the theoretical models.

### 2.4.1 Phonon processes

A general solid material can be:

- characterized by a regular lattice; in this case a crystal-cell can be identified, where the atoms occupy specific positions, that is repeated along the three space's dimensions;
- an amorphous solid, characterized by a not-regular lattice; atoms are randomly distributed inside the material.

Supposing to have a solid material with a regular lattice, it can be observed that an atom is not fixed in a singular point of the lattice, but it vibrates maintaining an equilibrium point, along all the three axis  $x$ ,  $y$ ,  $z$  of the space. This condition valid for one atom can be extended to all the atoms of the lattice. Considering now a chain of  $N$ -atoms inside the lattice, vibrating only in the  $y$ -direction and orthogonally to  $x$ -axis, a wave propagating along the  $x$ -axis is created (Figure 2.48).



**Figure 2.48 - N-atoms chain in the lattice; atoms are vibrating in y-direction, and orthogonally to x direction, thus a wave propagating along x direction is created. The figure is taken from Kittel<sup>142</sup>.**

Such wave, known as phonon, has:

- a propagation's direction;
- a velocity of propagation: this velocity is the sound's speed of the material. It depends also on the material temperature;
- a wavelength  $\lambda$  [m] and frequency  $f$  [Hz], that are linked together by the correlation  $v_{sound} = f \lambda$ ;
- a pulsance [rad s<sup>-1</sup>],  $\omega = 2 \pi f$ .

The propagation of a phonon inside the lattice in terms of space and time can be described by<sup>142</sup>:

$$u(x, t) = u_0 \cos(kx + \varphi_k) \cos(\omega t + \varphi_\omega) \quad (2.116)$$

The quantized energy associated to a phonon, which can be associated for analogy to the photon, is

$$\epsilon = \left(n + \frac{1}{2}\right) \hbar \omega \quad (2.117)$$

where  $n$  is the quantic number and  $\hbar = 1,055 \cdot 10^{-34}$  [J s] is the reduced Planck constant. One or more phonons can interact with each other or with defects in the lattice generating scattering phenomena. Firstly, a scattering process between two phonons is considered. The two phonons, 1 and 2, are propagating along the direction  $x_1$  and  $x_2$  respectively, with

$$u_1(x_1, t) = U_{0,1} \cos(k_1 x_1 + \varphi_{k,1}) \cos(\omega_1 t + \varphi_{\omega,1}) \quad (2.118)$$

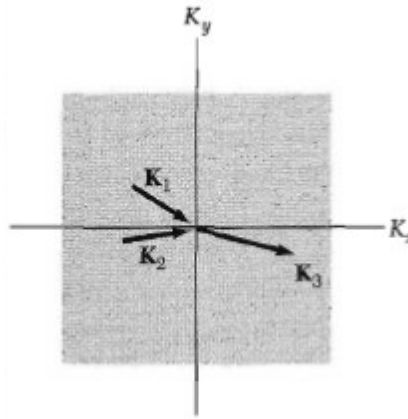
$$u_2(x_2, t) = U_{0,2} \cos(k_2 x_2 + \varphi_{k,2}) \cos(\omega_2 t + \varphi_{\omega,2}) \quad (2.119)$$



After the collision, the energy and the momentum are conserved: this kind of scattering process is called N(normal)-process. If the momentum is conserved,

$$\sum_i \hbar_{in,i} \vec{k}_{in,i} = \sum_j \hbar_{out,j} \vec{k}_{out,j} \quad (2.120)$$

Consequently, a new phonon is born (Figure 2.49), as result of the interference between the two phonons, with a wavevector of  $\vec{k}_3 = \vec{k}_1 + \vec{k}_2$ .



**Figure 2.49 - N(normal) scattering process between phonon 1 and phonon 2<sup>142</sup>.**

If the energy after collision is conserved, but not the momentum,

$$\sum_i \hbar_{in,i} \vec{k}_{in,i} \neq \sum_j \hbar_{out,j} \vec{k}_{out,j} \quad (2.121)$$

and

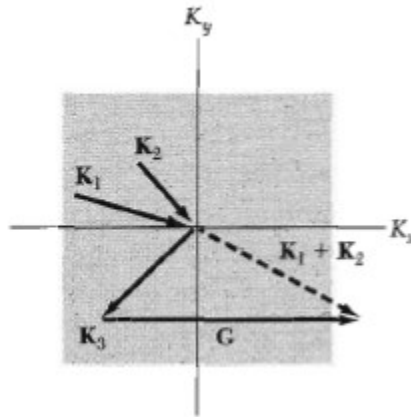
$$\vec{k}_1 + \vec{k}_2 \neq \vec{k}_3 \quad (2.122)$$

This kind of scattering process is called U (Umklapp) process. The crystal reacts with a response phonon in the impact point, with a wavevector  $\vec{G}$  that establishes the conservation of momentum (Figure 2.50). The result come from the requirement that the phonon wavelength cannot be smaller than the lattice constant<sup>143</sup>, and

$$\vec{k}_1 + \vec{k}_2 = \vec{k}_3 + \vec{G} \quad (2.123)$$

The new phonon, leaving from the scattering point, has a wavevector  $\vec{k}_3'$  ( $\vec{k}_1 + \vec{k}_2$  in Figure 2.50) with a modulus lower than  $k_3$ , so a pulsatace lower than  $\omega_3$ . Therefore, it's tolerable by the material

and it can continue its propagation. Without the Umklapp process, the thermal conductivity of a crystal would still be infinite because in a normal scattering process, the generated third phonon preserves both energy and the direction of the two original phonons. The extra reciprocal lattice wavevector in the Umklapp process changes the direction of phonon propagation and thus creates resistance to the heat flow<sup>143</sup>.



**Figure 2.50 - Umklapp scattering process between phonon 1 and phonon 2<sup>142</sup>.**

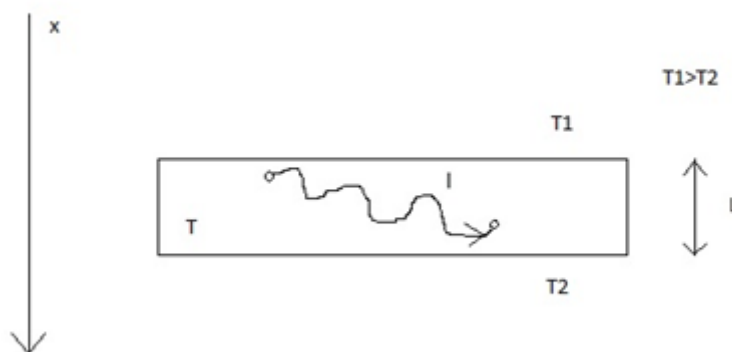
The scattering process can be triggered also by a defect in the material, such as

- point defects, as absence of atoms or presence of foreign atoms in the lattice;
- dislocations;
- grain boundaries.

After a phonon have met an imperfection, it splits into two or more phonons. The scattering obeys the Rayleigh law<sup>143</sup>, the concept is similar to the Umklapp process.

### 2.4.2 Fourier's law boundaries

A general material is considered in Figure 2.51 of thickness  $L$ : and with a surface at a temperature  $T_1$  and the other at  $T_2$  with  $T_1 > T_2$ . The temperature gradient is established in the  $x$  direction as the heat flux.



**Figure 2.51 - General material, with a temperature gradient along the  $x$  direction.**

The mean free path  $l_m$  for phonons is the mean distance that a phonon covers from the point where it is created, until the point where it stops propagating into the material and it is associated to the relaxation time  $\tau$ . The mean free path is usually expressed in [ $\mu\text{m}$ ] or [ $\text{nm}$ ], and it depends on:

- the pulsance of the phonon  $\omega$ : high frequency phonon has a major probability of being scattered;
- the temperature of the material; increasing the temperature increases the number of scattering points and the probability to have a scattering process.

The Knudsen number  $Kn$  related to the material is defined as

$$Kn(\omega, T) = \frac{l_m(\omega, T)}{L} \quad (2.124)$$

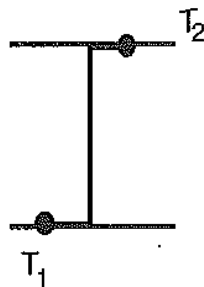
and the acoustical thickness  $\xi_L$

$$\xi_L(T) = \frac{1}{Kn(T)} = \frac{L}{l(T)} \quad (2.125)$$

Depending on the material thickness different scenarios can be discussed for the case reported in Figure 2.51.

1)  $L \ll l(T)$ , so  $\xi_L(T) \ll 1$

In this case, a general phonon does not find a scattering point inside the material, it is born at a surface and it ends at the other. Without scattering points (Figure 2.52), a thermal equilibrium is not established and a temperature distribution  $T(x, y, z)$  can not be defined inside the material. Without a temperature gradient, the thermal conductivity can not be defined based on Fourier's law.



**Figure 2.52 - Temperature's distribution in a very thin semiconductor ( $L \ll l_m$ ), where we have a ballistic thermal transport. As we can see, a singular point in the temperature's function is present, and it does not permit the continuity of the function. A temperature's gradient is not definable.**

A ballistic thermal transport is established, each surface emits an amount of phonons that arrives undisturbed at the opposite boundary. The surface with higher temperature emits more phonons than

the other in the same direction of the temperature gradient and of the thermal flux. For the phonons thermal flux is valid:

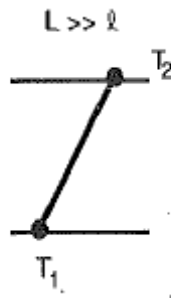
$$q = \sigma (T_1^4 - T_2^4) = 4 \sigma T^3 (T_1 - T_2) \quad (2.126)$$

where  $\sigma$  is the Stefan-Boltzmann constant for phonons, expressed in  $[\text{W m}^{-2} \text{K}^{-4}]$  and given by

$$\sigma(T) = \frac{\pi^2}{40} \frac{k_B^4}{\hbar^3 v(T)^2} \quad (2.127)$$

2)  $L \gg l(T)$ , so  $\xi_L(T) \gg 1$  ( $> 10^2$ )

The thermal transport inside the material is completely diffusive. In this case, having internal scattering points, where a thermal equilibrium is established and where a temperature is definable, a temperature's distribution  $T(x,y,z)$  can be defined inside the material. In this case the thermal conductivity can be defined based on the Fourier's Law.



**Figure 2.53 - Temperature's distribution in a bulk semiconductor ( $L \gg l_m$ ), where we have a diffusive thermal transport. A continuous temperature function is present, and a temperature's gradient is definable.**

The phonons have the same direction of the temperature's gradient and of the thermal flux. The Fourier's Law is valid, and  $q$  is

$$q = \lambda \frac{T_1 - T_2}{L} \quad (2.128)$$

$\lambda$  is the cross thermal conductivity of the material.

3)  $L \approx l(T)$ , so  $\xi_L(T) \approx 1$

In this case, the thermal transport is governed by both the ballistic and diffusive process: there are phonons emitted by a surface that arrive at the other, without meeting internal scattering points

(ballistic behavior), or phonons which are scattered (diffusive behavior). In this case, applying the Fourier's law can lead to big mistake in the evaluation of the thermal conductivity.

Models that try to define a thermal conductivity in the cases  $L \ll l$  and  $L \approx l$  have been developed. These models are valid for  $L \gg l$  (Fourier's field), too. In particular, the models analyzed are:

- the gray model, proposed by Majumdar<sup>144</sup>;
- the EIT model (Extended Irreversible Theory) proposed by Alvarez and Jou<sup>146,147</sup>.

### 2.4.3 Nanoscale thermal transport models

Models that define the thermal conductivity outside the Fourier's field are presented and applied to estimate the thermal conductivity of a thin film of SiO<sub>2</sub> at the temperature of 100 °C. In order to validate the mathematical results, a comparison with experimental results measured by Griffin *et al.*<sup>148</sup> have been made.

#### *2.4.3.1 The gray model*

The gray model for the estimation of thermal conductivity in semiconductors is proposed by Majumdar<sup>144</sup>. Based on the Boltzmann transport theory, the author developed an equation of phonon radiative transport (the EPRT equation). This equation describes the thermal transport governed by phonons in a general semiconductor (in terms of thermal flux and temperature's distribution), considering a parallelism with the phonon's transport inside semitransparent materials. Then, EPRT has been solved in order to find an expression of the cross thermal flux in a semiconductor, valid for all the possible values of the thickness  $L$ . For a general semiconductor, the cross thermal flux  $q$  predicted by the EPRT is given by:

$$q = \frac{4\sigma T^3(T_1 - T_2)}{\frac{3}{4}\left(\frac{L}{l_m}\right) + 1} \quad (2.129)$$

For  $L \ll l$  (T), Equation (2.129) yields to

$$q = \sigma (T_1^4 - T_2^4) = 4 \sigma T^3 (T_1 - T_2) \quad (2.130)$$

The equation for the ballistic thermal transport. For  $L \gg l$ (T), the resulting thermal flux  $q$  is given by the Fourier's law

$$q = k_{Fourier} \frac{T_1 - T_2}{L} \quad (2.131)$$

In the intermediate case, so for a thickness  $L \approx l_m$ , Equation 2.129 can be written as

$$q = \frac{4\sigma T^3 (T_1 - T_2)}{\frac{3}{4} \left(\frac{L}{l_m}\right) + 1} = \left[ \frac{4\sigma T^3}{\frac{3}{4} \left(\frac{L}{l_m}\right) + 1} \right] (T_1 - T_2) \quad (2.132)$$

Using now the typical definition of thermal conductivity, an expression of an equivalent thermal conductivity can be obtained.

$$k_{eff}(T) = \frac{4\sigma T^3}{\frac{3}{4} \left(\frac{L}{l_m(T)}\right) + 1} \quad (2.133)$$

#### 2.4.3.2 The EIT model

The Extended Irreversible Thermodynamics theory has been developed by Alvarez and Jou<sup>147</sup>. In nanosystems, the phonon wave package is assumed to form a series of standing waves with the wavelength the fraction of characteristic size of systems. If all the phonons have the same relaxation time regardless of their frequencies, the effective thermal conductivity of nanofilms is expressed as:

$$\frac{k_{eff}(T)}{k_{Fourier}(T)} = \frac{1}{2\pi^2 Kn(T)^2} (\sqrt{1 + 4\pi^2 Kn(T)^2} - 1) \quad (2.134)$$

In Equation (2.134), the Knudsen number  $Kn(T)$  is defined as

$$Kn(T) = \frac{l_m(T)}{L_{eq}} \quad (2.135)$$

with

$$\frac{1}{L_{eq}^2} = \frac{1}{L_x^2} + \frac{1}{L_y^2} + \frac{1}{L_z^2} \quad (2.136)$$

$L_x, L_y, L_z$  can be the characteristic lengths of nanowires along the three dimensions of the space, expressed in [m]. For the infinite plane case

$$\frac{1}{L_{eq}^2} \approx \frac{1}{L_x^2} \rightarrow L_{eq} \approx L_x \approx L \quad (2.137)$$

and the Knudsen number keeps its original definition, already presented in Equation (2.124).

### 2.4.3.3 Models comparison

In order to calculate the thermal conductivity both gray model and EIT model require the mean free path for phonons. The mean free path in SiO<sub>2</sub> is experimentally evaluated and it ranges from 1 μm to 2 μm<sup>149</sup>. The models are applied under hypothesis reported in Table 2.2.

**Table 2.2 - Hypothesis at the base of the applied models**

<b>Material</b>	SiO <sub>2</sub>
<b>Temperature T [K]</b>	393
<b>Thickness L [nm]</b>	10-100-200-500-1000

The results are summarized in Table 2.3 and compared with the values measured by Griffin et al.<sup>148</sup>.

**Table 2.3 - Effective thermal conductivity of polycrystalline-SiO<sub>2</sub>, at 373 K and at different thicknesses. Gray and EIT model are compared versus experimental values.**

		<b>Gray model</b>	<b>EIT model</b>	<b>Griffin et al.<sup>148</sup></b>
<i>L</i> [nm]	$\zeta_L$	$k_{eff}(373 K)$ [W m <sup>-1</sup> K <sup>-1</sup> ]	$k_{eff}(373 K)$ [W m <sup>-1</sup> K <sup>-1</sup> ]	$k_{eff}(373 K)$ [W m <sup>-1</sup> K <sup>-1</sup> ]
10	0,010	0,011	0,005	0,005
100	0,104	0,100	0,045	0,05
200	0,207	0,186	0,088	0,1
500	0,518	0,388	0,210	0,2
1000	1,036	0,606	0,388	0,4

However, in literature very different values can be found for SiO<sub>2</sub> thin film around 200 nm of thickness. Different authors<sup>150,151</sup> measure 100 W m<sup>-2</sup> K<sup>-1</sup> which differs three order magnitudes from the Griffin e co-workers values. They considered that a substantial thermal resistance may develop at the film/substrate interface; this interfacial thermal resistance would affect the overall thermal resistance of the film<sup>147,152,153</sup>. All DWC model proposed in this work suggest to use values around 0.2 W m<sup>-2</sup> K<sup>-1</sup> as thermal conductivity of hydrophobic coatings. Probably being the contact resistance between the metal surface and the layer the main resistance to the passing heat, that value can be applicable to different coatings assuming a Fourier process with an artificial λ\* applied to the coating thickness.

# Chapter 3 - Tested surfaces

Achieving filmwise or dropwise condensation mode is a question of surface wettability as reported in the previous chapters. In this chapter, the surfaces tested in the experimental apparatus are described and characterized. Different chemical approaches are applied for changing the surface wettability of the bulk material, i.e. aluminum and copper. The wetting states obtained are: hydrophilicity, hydrophobicity and superhydrophobicity. It should be stressed the importance of a proper characterization of the tested surface, since the high number of parameters involved in the condensation test. The fundamental parameters measured on the treatments are listed below with the related technique, not all the analyses are applied to each treatment and the description of the techniques is reported in my other personal work<sup>154,155</sup>.

- Wettability measurement. Technique: sessile drop method;
- Surface morphology. Technique: SEM (*Scanning Electron Microscopy*) analysis, optical microscope, BET (*Brunauer-Emmet-Teller*) analysis;
- Surface roughness. Technique: AFM (*Atomic Force Microscopy*) analysis, 2D profilometer;
- Surface composition. Technique: IR (*Infrared Spectroscopy*) analysis, Raman spectroscopy, EDX (*Energy Dispersive X-ray Analysis*) analysis, XRD (*X-Ray Diffraction*) analysis;
- Surface energy. Technique: sessile drop method;
- Treatment thickness. Technique: Ellipsometry, 2D profilometer;

## 3.1 Hydrophilic surfaces

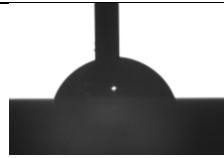
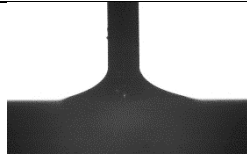

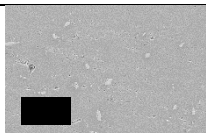
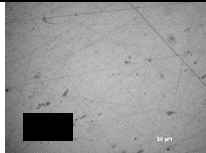
The hydrophilic surfaces consist in polished copper and aluminum and, as well-known, metal surfaces are intrinsically hydrophilic. The samples are mirror polished, cleaned and characterized before condensation tests. The detailed procedure is also reported elsewhere<sup>154,155</sup>.

### 3.1.1 Mirror-polished aluminum surface

The characterization done on the mirror-polished aluminum surface is summarized in Table 3.1.



**Table 3.1 - Mirror-polished aluminum surface characterization.**

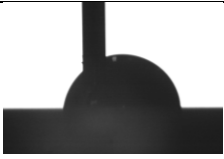
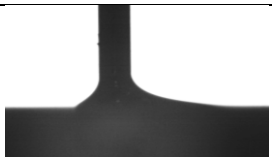
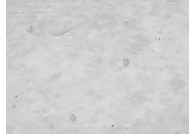
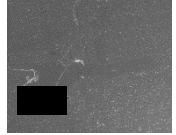
Parameter	Technique	Measurement	Value
$\theta_a$	Sessile drop method		$65^\circ \pm 3^\circ$
$\theta_r$	Sessile drop method		$10^\circ \pm 3^\circ$
Ra	2D Profilometer		$21.1 \text{ nm} \pm 4.2 \text{ nm}$
Surface morphology	SEM		\
Surface morphology	Optical microscope		
Surface free energy	Sessile drop method		$28 \text{ mN m}^{-1} \pm 5 \text{ mN m}^{-1}$

The surface morphology analyses confirm the uniformity of the mirror-polishing procedure which leads to roughness values (Ra) of few nanometers even though some scratches are still visible on the surface. Some impurities on the surface can be observed, dark gray spots in the optical microscope image, which seem to be some iron leftovers from the finishing operation of the surface (EDX analysis). The wettability measurements assess the hydrophilicity of aluminum, in particular the  $\theta_r$  is very low ( $\sim 10^\circ$ ), meaning that a liquid drop wets the surface while sliding. The surface free energy measurement is carried measuring the static contact angle of a water and diiodomethane droplet on the substrate. The global surface free energy,  $28 \text{ mN m}^{-1} \pm 5 \text{ mN m}^{-1}$ , resulted to be in accordance with the literature<sup>155</sup>, where the polar component is equal to  $6 \text{ mN m}^{-1} \pm 4 \text{ mN m}^{-1}$  and the apolar component is equal to  $22 \text{ mN m}^{-1} \pm 2 \text{ mN m}^{-1}$ .

### 3.1.2 Mirror-polished copper surface

The characterization done on the mirror-polished copper surface is summarized in Table 3.2.

**Table 3.2 - Mirror-polished copper surface characterization.**

Parameter	Technique	Measurement	Value
$\theta_a$	Sessile drop method		$84^\circ \pm 3^\circ$
$\theta_r$	Sessile drop method		$11^\circ \pm 3^\circ$
Ra	2D Profilometer		$26.1 \text{ nm} \pm 4.1 \text{ nm}$
Surface morphology	SEM		\

As reported for the aluminum substrate, the copper substrate presents a hydrophilic behavior with very low receding contact angle. The profilometry leads to very low and uniform values of roughness, confirming the successfulness of the process.

## 3.2 Hydrophobic surfaces

Based on the literature (as reported in paragraph 2.1), a surface is defined hydrophobic if the static contact angle is higher than  $90^\circ$ . In this work, it is preferred to report the dynamics contact angles in order to describe the surface wettability, since the advancing and receding contact angles are strongly related to the condensation mode. The surfaces reported in this paragraph have  $\theta_a$  and  $\theta_r$  in between  $90^\circ$  and  $60^\circ$  showing barely hydrophobic properties. Since DWC is obtained on those surfaces, thus they are not fully wetted by the condensate, the hydrophobicity definition, here, is related mostly to the receding contact angle. With such high  $\theta_r$  the droplet sliding on a surface do not leave the surface wetted, meaning that the surface is hydrophobic. Several treatments have been applied to both aluminum and copper substrates, the properties of the specific layer are substrate-independent indeed. The difference in choosing different material is on the strength of the bond between substrate and treatment due to the affinity of the compounds. The bonding energy may influence the duration of such layer during condensation test conditions. The macro areas of surface treatment are the following:

- Sol-gel silica-based coatings;
- Graphene coatings.

### 3.2.1 Sol-gel silica-based coatings

<sup>156,157</sup>The sol-gel process involves the synthesis of a colloidal solution (called sol) of solid particles in a liquid phase. The solution is produced through the introduction into the dispersing phase of one or more precursors that develop into a continuous organic lattice through a series of hydrolysis and condensation reactions (called gel). A colloid is a suspension in which the dispersed phase is so fine (about 1-1000nm) that the gravitational force is negligible and the interaction between the particles is dominated by short-range forces, such as the Van der Waals attraction forces or superficial charges. The inertia of the dispersed phase is so low that it exhibits a Brownian motion, which depends on the momentum transferred through the collision with molecules of the dispersing phase. The sol-gel method is a process that has been greatly studied for its versatility and simplicity (Figure 3.1). It allows obtaining high quality ceramic and glass coatings through a series of polymerization reactions that occur at relatively low temperatures. The great versatility is based on the possibility of conducting most of the synthesis steps at room temperature, to easily control the composition of the coating, to obtain extremely homogeneous coatings and a very high final purity. The sol-gel process can be divided into four main stages:

1. preparation of the liquid suspension containing the precursor (Sol);
2. cross-linking phase and transformation of the suspension in gel (hydrolysis and condensation reactions);

3. gel deposition;
4. heat treatment of the gel to stabilize the coating.

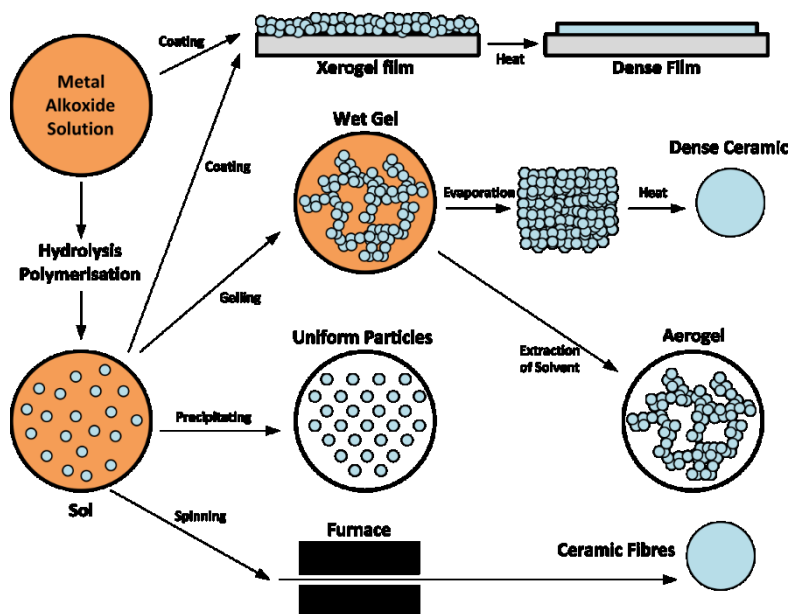


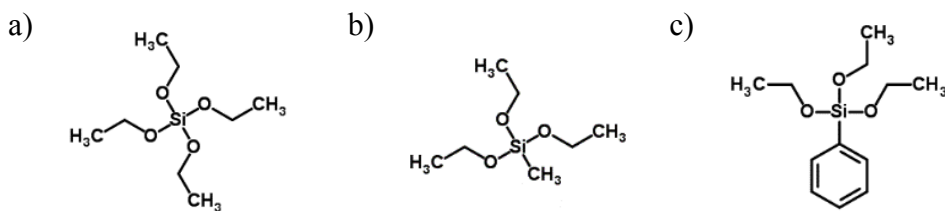
Figure 3.1 - Scheme of the sol-gel process <sup>158</sup>.

The chemical ways of obtaining sol-gel synthesis are very different from each other involving different types of precursors, i.e. reagents in which a metal or a metalloid is bound to multiple ligands. The ligands may be inorganic (i.e. do not contain carbon atoms, for example  $\text{NO}_3^-$ ,  $\text{SO}_4^{2-}$ , ...) or organic compounds. The organometallic compounds consist of reagents with only carbon and hydrogen atoms (such as  $\cdot\text{CH}_3$ ,  $\cdot\text{CH}_2\text{CH}_3$ ,  $\text{H}_3\text{C}(\cdot\text{C})\text{HCH}_3$ , ...), whereas if heteroatoms (e.g. oxygen) are present there is the formation of metal-hetero-atom-carbon bond, which is the basis for the alkoxides family<sup>159</sup>: the most used compounds in this research. Among the alkoxides, the silicon-based are those more thoroughly studied from the point of view of chemical reactivity and synthesis methods, the first attempts to produce this category of alkoxides date back to 1842 <sup>160,161</sup> while the first techniques genuinely definable sol-gel utilizing these precursors can be dated around 1970<sup>162</sup>.

In this work, three silica-based reagents have been used for obtaining hydrophobic layer:

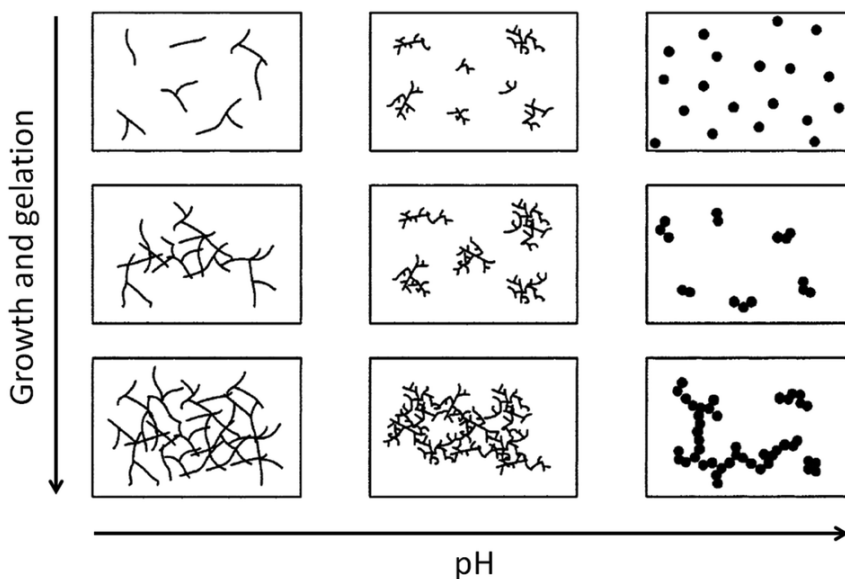
- Tetraethylorthosilicate (TEOS),  $\text{Si}(\text{OC}_2\text{H}_5)_4$ ;
- Methyltriethoxysilane (MTES),  $\text{CH}_3\text{Si}(\text{OC}_2\text{H}_5)_3$ ;
- Phenyltriethoxysilane (PhTES),  $\text{C}_6\text{H}_5\text{Si}(\text{OC}_2\text{H}_5)_3$ .

TEOS is one of the most popular and most used organometallic precursors for the production of vitreous products through sol-gel technique<sup>161,163</sup>. This molecule is insoluble in water and requires the presence of other solvents such as ethanol to obtain complete dissociation in solution<sup>164-166</sup>. MTES and PhTES have been chosen for their hydrophobic elements, the methyl and the phenyl group, respectively.



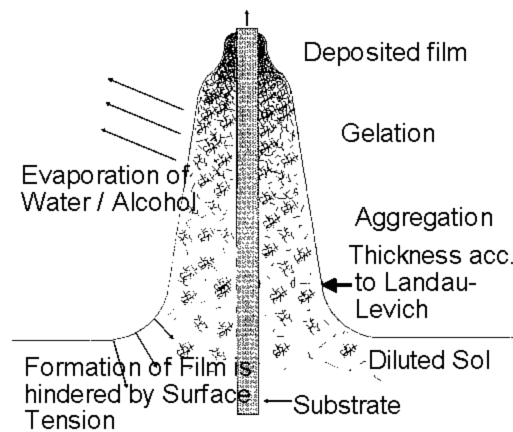
**Figure 3.2 - Schematic representation of TEOS, MTES and PhTES compounds.**

Once the reagents are mixed with the sol, hydrolysis and condensation processes start. The pH of the solution, adjusted by an acid/base (e.g. hydrochloric acid, ammonia), has important consequences for the structure of the resulting gel network<sup>156</sup>. During acid catalysis, an oxygen from the alkoxide group is protonated making the silicon more electrophilic and thus favoring a nucleophilic attack by the water. As the reaction proceeds, the insertion of electron-attractor groups such as OH- and SiO- on the molecule in place of electron-donor groups such as the alkoxide group tends to destabilize the formation of positive charges in the transition state, making the remaining -OR groups less available to a nucleophilic attack and thus slowing down the rate of hydrolysis. The condensation can therefore begin before the monomer is completely hydrolyzed and lead to the formation of linear or slightly branched polymers which become entangled with each other giving rise to new ramifications through aging and leading to gelling. In a basic environment, the hydrolysis of silicon alkoxides proceeds with a lower speed than the acid hydrolysis with a similar mechanism. Following the replacement of the -OR with the less cumbersome hydroxyls and with less tendency to behave as electron-donors, the attack on the silicon is facilitated and therefore the hydrolysis reaches completion before the condensation starts. As a result, very branched bunches, but not interconnected, are obtained before the gelling phase. The differences between acid and base catalyzed reactions and the consequences for particle morphology are conceptually represented in Figure 3.3.



**Figure 3.3 - Effects of pH on particle morphology in sol-gel reactions.**

There are several deposition methods applicable to the present substrates, such as drop casting, dip coating, CVD (chemical vapor deposition), etc., and the dip coating technique was selected. The dip coating, vertical withdrawal of a substrate from reservoir, in fact, is an inexpensive and very reliable method of depositing a thin layer of material in the liquid state onto a substrate <sup>167</sup>. Despite the simplicity of the method, the process is extremely complex <sup>168</sup>, during the deposition there is in fact a continuous polymerization of the precursors, which is accelerated by the evaporation of the solvent since it increases the concentration of the oligomers. A scheme is shown in Figure 3.4.

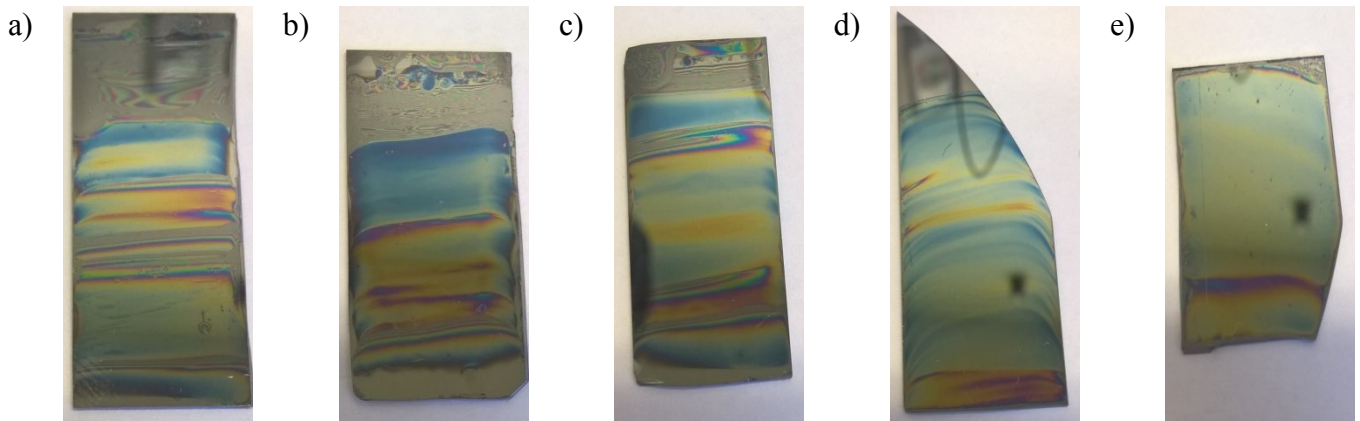


**Figure 3.4 - Dip coating process.**

Using the classical lubrication equations together with the hydrostatic differential equation, a matching condition is applied for the film entrainment and the static meniscus regions. For vertical withdrawal, the Landau-Levich approach provides an expression for the film thickness ( $h$ ) when the coating velocity is very small <sup>169</sup>

$$h = 0,944 \cdot \frac{(\eta \cdot U_0)^{2/3}}{\gamma_{LV}^{1/6} \cdot \sqrt{(\rho \cdot g)}} \quad (3.1)$$

0.944 is valid for Newtonian liquids,  $\eta$  is the liquid viscosity,  $\gamma_{LV}$  liquid vapor surface tension,  $U_0$  is the coating velocity,  $\rho$  (defined as fluid density and gravitational acceleration is  $g$ ). The most important parameter is the sample coating velocity, the faster the extraction takes place the greater the deposited thickness. Secondly, the characteristics of the solution are important, in particular its viscosity and density; an increase in viscosity creates an increase in the viscous forces and the thickness of the film. Preliminary tests have been performed on silicon substrate in order to verify the homogeneity of the deposition process, knowing that to a thickness change corresponds a variation of the refractive index which leads to the formation of streaks of different color. An example is presented in Figure 3.5.



**Figure 3.5 - Dip coating deposition test at different extraction velocities: a) 0.6 cm min<sup>-1</sup>, b) 1.2 cm min<sup>-1</sup>, c) 1.8 cm min<sup>-1</sup>, d) 2.4 cm min<sup>-1</sup>, e) 4.8 cm min<sup>-1</sup>.**

The 4.8 cm min<sup>-1</sup> velocity resulted to be the best for the coating homogeneity, hence it has been chosen as extraction velocity for all the samples. The last phase of the coating deposition is the heat treatment of the gel to stabilize the coating. This phase allows the elimination of the residual solvent, inducing possible crystallization of the compounds and modifying their properties of porosity and homogeneity, affecting the characteristics of the final product. Since the films are made up of slightly ramified macromolecules, they tend to create dense structures and when the pores start to empty out of the solvent during the heat treatment phase, liquid gas interfaces are generated with different curvatures. As a consequence, different curvature radii are created which lead to different capillary pressures and therefore to different tensile stresses. The magnitude of these forces can be calculated from the Laplace equation

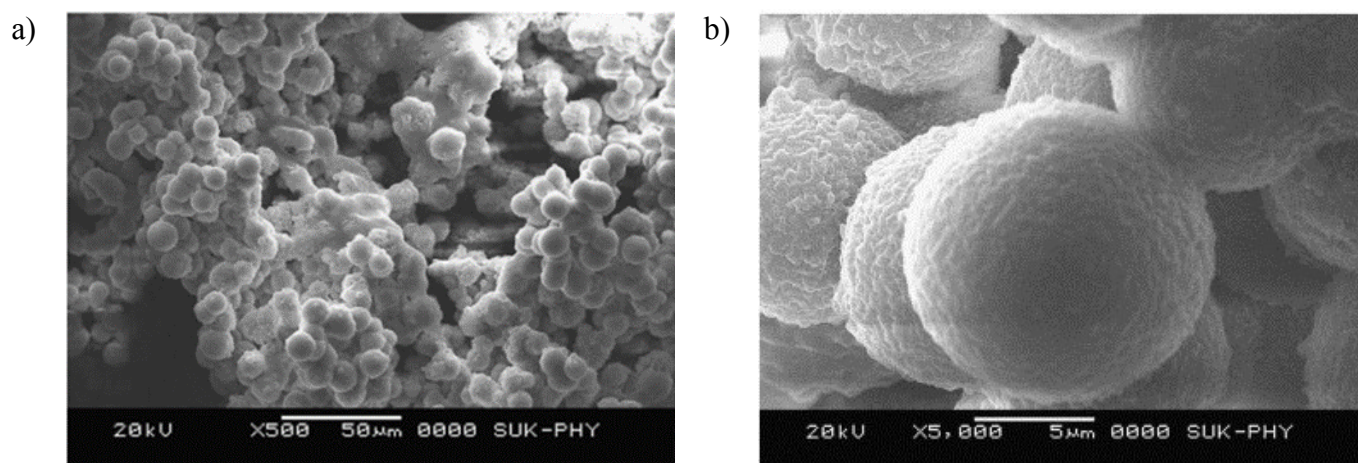
$$P = \frac{2\gamma_{LV} \cos \theta}{r} \quad (3.2)$$

where  $\gamma_{LV}$  is the surface tension at the liquid-vapor interface,  $r$  is the pore radius,  $\theta$  is the contact angle between the liquid-solid-air interface. The pressures that are generated can be higher than 1000 bar; if the stress difference locally exceeds a limit value given by the binding force of the gel lattice, the film breaks. Furthermore, if the expansion coefficient of the coating and of the bulk material are very different (compression stress if  $\alpha_{\text{coating}} < \alpha_{\text{bulk}}$  or tensile if  $\alpha_{\text{coating}} > \alpha_{\text{bulk}}$ ), the coating can also break. Hence the importance of performing a gradual heating and cooling of the coating-substrate system.

### 3.2.1.1 Basic sol-gel solution

The first sol-gel solution method tried was with high pH, referring to Figure 3.6, the synthesis should produce silica-based nanoparticles thin film. Several syntheses have been developed in the last decades for the production of nanoparticles<sup>170-173</sup>; among these the most studied technique consists

in the Stöber method <sup>171</sup>, developed in 1968, but still the most used synthesis. Briefly, the original method involved the use of TEOS as a precursor added in a mixture of water, alcohol and ammonia and stirred to form nanoparticles whose size is closely related to the concentration of the reagents and the presence of any additives. Many investigations have been carried out to identify the kinetics of formation of such nanoparticles in order to precisely control their size, shape and uniformity <sup>174,175</sup>. The wettability of nanoparticle films can be modified by using precursors other than TEOS, precursors with alkyl functional groups, therefore apolar and hydrophobic. In this synthesis, the hydrophobic precursor is MTES (see Figure X) which has a methyl group directly linked to silicon in place of a -OCH<sub>2</sub>CH<sub>3</sub> group. The -CH<sub>3</sub> group interrupts the homogeneity of the Si-O-Si lattice in the nanoparticle, yielding to a hydrophobic behavior to the coating. Film of silica nanoparticles functionalized with methyl groups deposited on copper has already been observed <sup>176</sup>, obtaining dimensions of nanoparticles of micrometers and packed structures as showed in Figure 3.6.



**Figure 3.6 - SEM images of silica nanoparticle films functionalized with methyl groups prepared by a molar ratio of methanol / MTES equal to 19.1 at magnification of: (a) 500x; (b) 5000x.** <sup>176</sup>

The reagents used for the synthesis of nanoparticle films are methyl-triethoxy-silane (MTES, 99%, Sigma-Aldrich), methanol (MeOH, 99.8% anhydrous, Sigma-Aldrich), ammonium hydroxide ( $\geq 27\%$  NH<sub>3</sub> in H<sub>2</sub>O, Sigma-Aldrich) and distilled water. All reagents were used as received. The substrate used in this section is aluminum (AW 1050, minimum quantity of aluminum 99.50%), cleaned in acetone for 5 minutes. The aluminum sample is then immersed in the coating solution and left in the sol for 40 minutes. The sample is air-dried for 30 minutes and finally heat-treated for 3 hours with a heating ramp of  $2^{\circ}\text{C min}^{-1}$  to remove any residual reagents from the films and ensure the silica network densification. Different parameters have been varied, from the molar concentration of the reagents, to the dipping speed to the heat treatment temperature. Here only the combination tested in the experimental apparatus is presented, a detailed description of the investigation is found in <sup>155</sup>. The parameters are summarized in Table 3.3.

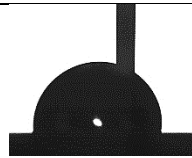
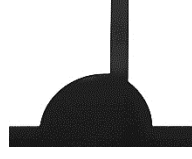
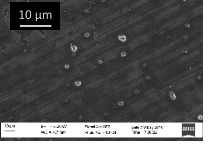


**Table 3.3 - Nanoparticles film parameters.**

<i>Reagents molar ratio</i>	MeOH/MTES = 22.56
	NH <sub>4</sub> OH 7M/MTES = 1.62
	H <sub>2</sub> O/MTES = 11.09
<i>Dipping speed</i>	4.8 cm min <sup>-1</sup>
<i>Baking temperature</i>	250°C

The characterization done on the silica nanoparticles coating is summarized in Table 3.4.

**Table 3.4 - Silica nanoparticles coating surface characterization.**

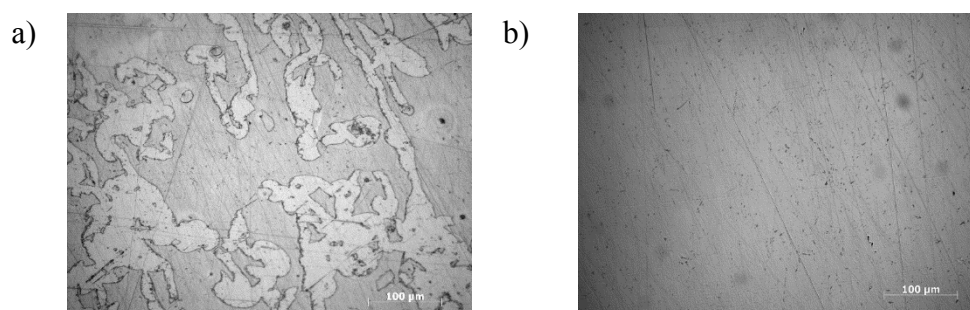
Parameter	Technique	Measurement	Value
$\theta_a$	Sessile drop method		$96^\circ \pm 2^\circ$
$\theta_r$	Sessile drop method		$77^\circ \pm 2^\circ$
Surface morphology	SEM		\

The nanoparticle thin film resulted to be hydrophobic from the sessile drop measurement, but not homogeneous on the aluminum surface. Nanoparticles of almost spherical shape were deposited, isolated from each other, with a wide range of dimensions (from 1  $\mu\text{m}$  to 10  $\mu\text{m}$ ) probably due to a process of non-uniform nucleation and accretion.

### 3.2.1.2 Acid sol-gel solution

As can be seen in the previous paragraph, the basic pH of the sol-gel solution does not allow a continuous film on the metallic substrate and in order to provide a stronger mechanical resistance to the coatings, acid sol-gel solutions have been explored (see Figure 3.3). The acid environment should favor the formation of a three-dimensional continuous hybrid organic-inorganic network on the entire surface in place of the nanoparticles, acting on the equilibrium of hydrolysis and condensation previously presented. In this case, MTES and PhTES are utilized as organic hydrophobic compounds. Indeed, the precursors play a different role in the film properties: TEOS promotes the formation of a

SiO<sub>2</sub> network with a low thickness and greater rigidity than a mixture of precursors<sup>177</sup>. However, during the heat treatment step there is the formation of micro-fractures on the substrate and in addition the film obtained is of hydrophilic properties, which are typical of silica. The MTES and PhTES, vice versa, have hydrophobic properties, thanks to the apolar nature of methyl and phenyl groups. The Si-CH<sub>3</sub> bonds is stable to the hydrolysis mechanism, increasing the porosity of the layer, increasing the final thickness of the coating compared to the use of only TEOS. The hydrophobic groups also interrupt the structural continuity of the SiO<sub>2</sub>, providing greater flexibility to the coating, which is therefore able to relax the tensions due to thermal stress, preventing cracking phenomena (e.g. reported in Figure 3.7)<sup>178</sup>. Furthermore, those molecules, mixed with TEOS, produce coatings with good optical properties, reason why this type of treatments have been explored also on transparent surfaces<sup>179,180</sup> (e.g. glass).



**Figure 3.7 - Optical microscopy image (200x): a) silica film, b) silica film functionalized with methyl groups, both treated at 200 ° C. The lack of homogeneity of the film in the first case is evident.**

The reagents used for those synthesis are methyl-triethoxy-silane (MTES, 99%, Sigma-Aldrich), fenil- triethoxy-silane (PhTES, 98%, Sigma-Aldrich), tetraethyl orthosilicate (TEOS, 98%, Sigma-Aldrich), ethanol (EtOH, ≥99.8% puriss., Fluka Analytical), hydrochloric acid (1N, Labochimica srl) and distilled water. All reagents were used as received. The substrates used in this section are made of aluminum and copper mirror-finished (characterization presented in paragraphs 3.1.1 and 3.1.2) and cleaned by means of sonication procedure in acetone for 5 minutes. Several molar ratio concentrations, baking temperature and substrate have been produced and all the combinations is summarized in Table 3.5. The dipping velocity is maintained 4,8 cm min<sup>-1</sup> for homogeneity reasons (see Par. 3.2.1). An example of nomenclature is reported below

MxTy\_z

The uppercase letters are the initial of the reagents used for producing the coating, thus T, M and P are for TEOS, MTES and PhTES respectively. The x and y represent the molar ratio with which those reagents are mixed in the solution and z is the baking temperature.

**Table 3.5 - Acid silica-based sol-gel treatments list.**

Sample	Name		% TEOS	% MTES	% PhTES	Baking Temp.	Dipping Vel.
Al	M5T5_200		50	50	/	200	4,8 cm min <sup>-1</sup>
Al	M7T3_200		30	70	/	200	4,8 cm min <sup>-1</sup>
Cu	M7T3_200		30	70	/	200	4,8 cm min <sup>-1</sup>
Al	M7T3_300		30	70	/	300	4,8 cm min <sup>-1</sup>
Al	M7T3_300	2 layer	30	70	/	60+300	4,8 cm min <sup>-1</sup>
Al	M7T3_300	2 layer	30	70	/	300+300	4,8 cm min <sup>-1</sup>
Al	M7T3_400		30	70	/	400	4,8 cm min <sup>-1</sup>
Al	P7T3_200		30	/	70	200	4,8 cm min <sup>-1</sup>
Al	P7T3_400		30	/	70	400	4,8 cm min <sup>-1</sup>
Al	P7M3_200		/	30	70	200	4,8 cm min <sup>-1</sup>
Al	M7P3_200		/	70	30	200	4,8 cm min <sup>-1</sup>

The treatments' procedure will be explained in the following sections.

### 3.2.1.2.1 MxTy series

The MTES/TEOS mixtures are the most widely explored. The idea is to study the effect of the reagents concentration from high to low concentrations of TEOS. Since too high values of TEOS lead to hydrophilic surfaces and too low values of it leads to not uniform coatings, the mixture here presented are M5T5 and M7T3. With those combinations, DWC is obtained, a detailed description of other combinations can be found in other works<sup>155,181</sup>. In the following Table, the recipe for M7T3 series is presented.

**Table 3.6 - M7T3 recipe.**

	Density (g cm <sup>-3</sup> )	Volume (ml)	Weight (g)	MM (uma)	Mole
TEOS	0,933	6,00	5,60	208,33	0,03
MTES	0,895	12,50	11,19	178,30	0,06
EtOH	0,789	10,46	8,26	46,07	0,18
H <sub>2</sub> O	1,000	5,56	5,56	18,02	0,31
HCl	1,187	0,90	1,07	36,46	0,03
Dilution after 30 min					
EtOH	0,789	33,16	26,17	46,07	0,57

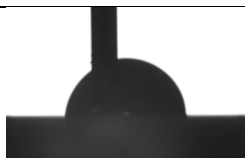
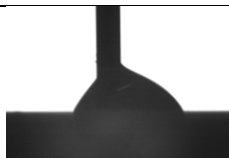
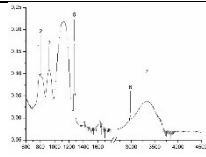
The procedure is performed by first mixing the alcohol with, in order, TEOS, MTES, distilled water and the hydrochloric acid. The obtained solution is stirred by means of a magnetic stir bar for 30

minutes, providing sufficient time for the hydrolysis and condensation reactions to take place. Subsequently, keeping the solution stirring active, the dilution alcohol is added. The sol is then filtered, using a filter with a grid size of 5 $\mu$ m to remove the silica agglomerates that could form in suspension during the condensation process. The aluminum sample is immersed in the solution with an insertion speed of 12 cm min<sup>-1</sup> and immediately extracted at a speed of 4.8 cm min<sup>-1</sup>. After a brief drying to the air, the film is stabilized through a 30-minute heat treatment with a heating ramp at 10 $^{\circ}$  C min<sup>-1</sup>. Three different temperature have been tested for M7T3 series: 200 $^{\circ}$ C, 300 $^{\circ}$ C and 400 $^{\circ}$ C. Higher temperatures lead to the loosing of the hydrophobic molecules, lower temperatures do not allow a full stabilization of the layers <sup>179</sup>.

### M5T5\_200

The characterization done on the M5T5\_200 coating is summarized in Table 3.7.

**Table 3.7 - M5T5\_200 surface characterization.**

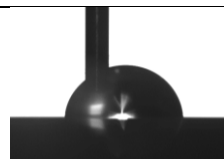
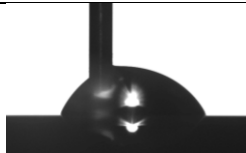
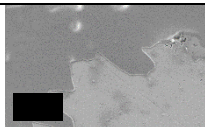
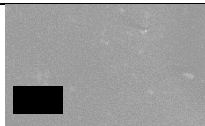
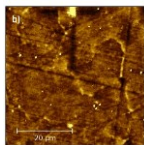
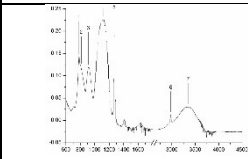
Parameter	Technique	Measurement	Value
$\theta_a$	Sessile drop method		84 $^{\circ}$ $\pm$ 3 $^{\circ}$
$\theta_r$	Sessile drop method		61 $^{\circ}$ $\pm$ 4 $^{\circ}$
Coating thickness	Ellipsometry		$\approx$ 198 nm
Coating composition	FT-IR		\

The coating M5T5\_200 presents mild hydrophobic behavior and thicknesses around 200 nm. The FT-IR analysis is useful to indirectly check if the hydrophobic elements are successfully bonded in the coating. The IR absorption spectra of sol-gel films is one of the most widely used techniques for the study of silica-based coatings <sup>182,183</sup> functionalized with methyl groups <sup>179,184</sup>. The presence of the organic phase of this coating is appreciable at about 1270 cm<sup>-1</sup> with an intense peak, which represents the deformation in the plane of the CH bond of the methyl group of MTES and about 2980 cm<sup>-1</sup> due instead to the symmetrical stretching of the bond.

### M7T3\_200

The characterization done on the M7T3\_200 coating is summarized in Table 3.8.

**Table 3.8 - M7T3\_200 surface characterization.**

Parameter	Technique	Measurement	Value
$\theta_a$	Sessile drop method		$83^\circ \pm 3^\circ$
$\theta_r$	Sessile drop method		$64^\circ \pm 2^\circ$
Coating thickness	Ellipsometry \ Etching method		$\approx 210$ nm
Surface morphology	SEM		\
Surface roughness	AFM		$\approx 10$ nm
Coating composition	FT-IR		
Surface free energy	Sessile drop method		$29.1 \text{ mN m}^{-1} \pm 0.6 \text{ mN m}^{-1}$

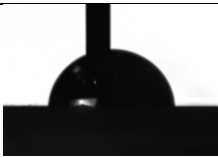
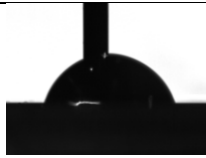
From the contact angles measurement can be noticed that the main difference between the treated and the untreated sample is the receding angle indeed, which assumes a values close to zero on the mirror-polished surface before the treatment <sup>20</sup>. SEM images after sol-gel film deposition, confirm the coating uniformity and the absence of imposed roughness patterns. From AFM images, different profiles were extracted and analyzed. The sample coated with silica showed lower roughness (few nanometers) as compared aluminum substrate, consistent with a dipped thin film covering aluminum asperity due to machining. Two different techniques were used to estimate the silica layer thickness (around 210 nm). FTIR spectrum of hybrid silica coating shows absorbance peaks due to Si-O-Si bonds ( $1100 \text{ cm}^{-1}$ ) and Si-CH<sub>3</sub> ( $1270 \text{ cm}^{-1}$ ), confirming the presence of methyl groups. Moreover, it is evident a peak at  $920 \text{ cm}^{-1}$  related to Si-OH stretching vibration, indicating that the heat treatment at  $200^\circ\text{C}$  is not enough to promote complete silica condensation. The FTIR spectrum is very similar to M5T5\_200 one. The static contact angle of water is equal to  $83^\circ$ , while the one obtained with

diiodomethane is measured equal to  $61^\circ$ , both very similar to those relating to the aluminum surface. Therefore the total free energy (IFT (s)) was also comparable with that of aluminum and equal to  $29.1 \pm 0.6 \text{ mN m}^{-1}$ , similarly distributed between the polar component (IFT (s, P) =  $7.1 \pm 0.1 \text{ mN m}^{-1}$ ) and the apolar component (IFT (s, D) =  $22.0 \pm 0.4 \text{ mN m}^{-1}$ ). Detailed information can be found in Parin *et al.*.

### M7T3\_300

The characterization done on the M7T3\_300 coating is summarized in Table 3.9.

**Table 3.9 - M7T3\_300 surface characterization.**

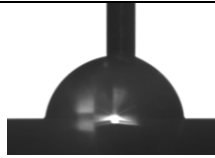
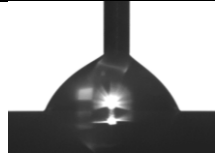
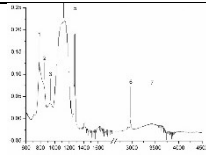
Parameter	Technique	Measurement	Value
$\theta_a$	Sessile drop method		$81^\circ \pm 3^\circ$
$\theta_r$	Sessile drop method		$67^\circ \pm 2^\circ$
Coating thickness	Etching method	\	$\approx 216 \text{ nm}$

The coating presents similar characteristics to the M7T3\_200 sample. With this synthesis three samples were made: the first with a single layer, the second with two layers in which after the first deposition a heat treatment of  $60^\circ\text{C}$  was performed and the third with two layers but with an intermediate heat treatment of  $300^\circ\text{C}$ . In the latter case, the coating thickness is about 300 nm. For further details, refer to <sup>154</sup>.

## M7T3\_400

The characterization done on the M7T3\_400 coating is summarized in Table 3.10.

**Table 3.10 - M7T3\_400 surface characterization.**

Parameter	Technique	Measurement	Value
$\theta_a$	Sessile drop method		$81^\circ \pm 2^\circ$
$\theta_r$	Sessile drop method		$65^\circ \pm 2^\circ$
Coating thickness	Ellipsometry		$\approx 200$ nm
Coating composition	FT-IR		
Surface free energy	Sessile drop method		$29.1 \text{ mN m}^{-1} \pm$ $0.6 \text{ mN m}^{-1}$

Regarding wettability and coating thickness, the temperature has not a real influence on the layer characteristics. Studying the peaks referred to the methyl groups, a decrease in the absorption intensity with respect to the sample M7T3\_200 is not evident, so it is possible to conclude that the methyl groups are certainly present also in the coating obtained at 400°C, but the relative decrease due to thermal degradation is not quantifiable. The water static contact angle has a value equal to 79° while diiodomethane 61°. The total free surface energy (IFT (s)) equal to  $30, 6 \pm 0.5 \text{ mN m}^{-1}$ , still comparable to that determined for the previous samples, and distributed equally between the polar component (IFT (s, P) =  $8.9 \pm 0.2 \text{ N m}^{-1}$ ) and the apolar component (IFT (s, D) =  $21.7 \pm 0.3 \text{ mN m}^{-1}$ ).

### 3.2.1.2.2 PxTy series

As reported for the MxTy series, acid silica-based sol-gel solutions lead to homogenous thin film (around 200 nm in thickness) on aluminum substrate. As for methyl groups, phenols should increase the flexibility of the coating and increase the resistance to thermal stresses<sup>185</sup>.

The substrates are made by aluminum (AW 1050, minimum quantity of aluminum 99.50%, §D.1), mirror-finished as for the previous paragraph. In the following Table, the recipe for P7T3 series is presented.

**Table 3.11 - P7T3 recipe.**

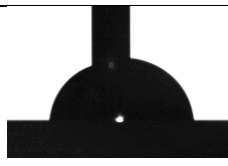
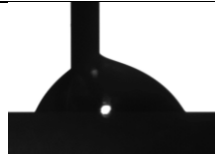
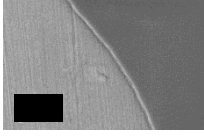
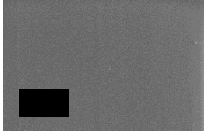
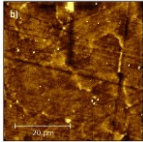
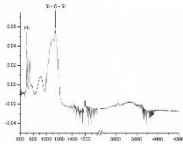
	Density (g cm <sup>-3</sup> )	Volume (ml)	Weight (g)	MM (uma)	Mole
TEOS	0,933	6,00	5,60	208,33	0,03
Ph-TES	0,996	15,15	15,09	240,37	0,06
EtOH	0,789	10,46	8,26	46,07	0,18
H <sub>2</sub> O	1,000	5,56	5,56	18,02	0,31
HCl	1,187	0,90	1,07	36,46	0,03
Dilution after 30 minutes					
EtOH	0,789	33,16	26,17	46,07	0,57

The process beyond the sol-gel formation and treatment deposition is the same reported for the MxTy series. Two different temperature have been tested for P7T3 series: 200°C and 400°C. Further details are reported in <sup>154,155</sup>.

### *P7T3\_200*

The characterization done on the P7T3\_200 coating is summarized in Table 3.12.

**Table 3.12 - P7T3\_200 surface characterization.**

Parameter	Technique	Measurement	Value
$\theta_a$	Sessile drop method		$83^\circ \pm 3^\circ$
$\theta_r$	Sessile drop method		$57^\circ \pm 6^\circ$
Coating thickness	Etching method		$\approx 300$ nm
Surface morphology	SEM		\
Surface roughness	AFM		$\approx 10$ nm
Coating composition	FT-IR		
Surface free energy	Sessile drop method		$35 \text{ mN m}^{-1} \pm 1 \text{ mN m}^{-1}$

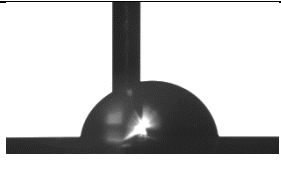
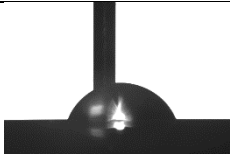
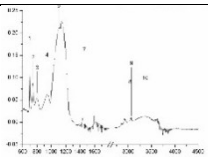


The wetting behavior of P7T3\_200 is very similar to the M7T3\_200, thus it does not introduce an advantage from this point of view. The coating thickness is around 300 nm, 1/3 thicker than the M7T3 series, this comes from the higher steric effect caused by the introduction of a phenyl group into the silica structure, which causes an increase in the average porosity of the film. However, the layer is very homogenous on the aluminum substrate as SEM images show. The FTIR analysis led to the assessment of the phenols presence. The peak at  $698\text{ cm}^{-1}$  is due to bending outside the CC bond plane in the aromatic ring of the PhTES, while the peaks at  $740\text{ cm}^{-1}$  are due to wagging outside the five-plane hydrogen atoms of the CH bond connected to the aromatic ring. Other typical phenyl vibrations produce the evident peaks at  $1430$ ,  $3050$  and  $3070\text{ cm}^{-1}$ . As regards the surface free energy, the static deposition of a drop of water on the coating led to the formation of a contact angle equal to  $85^\circ$ , while that obtained with diiodomethane was measured by  $45^\circ$ . The total free surface energy is (IFT) (s) equal to  $35 \pm 1\text{ mN m}^{-1}$ , higher than that of lapped aluminum and M7T3 coatings presented in the previous paragraph. However, it is of particular interest to observe the distribution between the polar component and the non-polar component, in fact the polar component (IFT (s, P) =  $3.9 \pm 0.3\text{ mN m}^{-1}$ ) is lower than that of the previous cases and its decrease should corresponds to an increase in the contact angle. On the other hand, the dispersed component (IFT (s, D) =  $31 \pm 1\text{ mN m}^{-1}$ ), again due to the introduction of phenyl, increases very significantly and this leads to a greater contact angle in the eventual deposit of apolar liquids on the film.

### P7T3\_400

The characterization done on the P7T3\_400 coating is summarized in Table 3.13.

**Table 3.13 - P7T3\_400 surface characterization.**

Parameter	Technique	Measurement	Value
$\theta_a$	Sessile drop method		$81^\circ \pm 2^\circ$
$\theta_r$	Sessile drop method		$65^\circ \pm 2^\circ$
Coating thickness	Ellipsometry		$\approx 214\text{ nm}$
Coating composition	FT-IR		
Surface free energy	Sessile drop method		$34\text{ mN m}^{-1} \pm 1\text{ mN m}^{-1}$

The baking temperature does not change significantly the properties of the coating (refer to P7T3\_200). The main difference is related to the coating thickness, the increasing of the temperature led to the decreasing of the thickness, probably due to the loosing of phenols groups from the silica network.

### 3.2.1.2.3 PxMy series

This series came after testing MxTy and PxTy series. After the characterization post thermal test, the idea of mixing the MTES and PhTES seemed to be interesting, since the two coatings exhibited two different behaviors during condensation test. Similar recipe with the mix of those compounds can be found also in literature <sup>186,187</sup> for aluminum corrosion protection, but the study of such coatings is lacking from a thermal point of view.

The substrates are made by aluminum (AW 1050, minimum quantity of aluminum 99.50%, §D.1), mirror-finished as for the previous paragraphs. In the following Tables, the recipe for P7M3 and M7P3 are presented.

**Table 3.14 - P7M3 recipe.**

	Density (g cm <sup>-3</sup> )	Volume (ml)	Weight (g)	MM (uma)	Mole
MTES	0,895	4,47	4,00	178,30	0,02
Ph-TES	0,996	12,63	12,58	240,37	0,05
EtOH	0,789	8,73	6,89	46,07	0,15
H <sub>2</sub> O	1,000	4,63	4,63	18,02	0,26
HCl	1,187	0,75	0,89	36,46	0,02
Dilution after 30 minutes					
EtOH	0,789	27,67	21,84	46,07	0,47

**Table 3.15 - M7P3 recipe.**

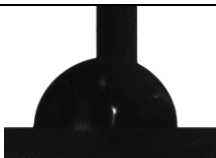
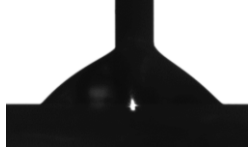


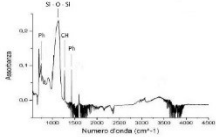
	Density (g cm <sup>-3</sup> )	Volume (ml)	Weight (g)	MM (uma)	Mole
Ph-TES	0,996	5,02	5,00	240,37	0,02
MTES	0,895	9,68	8,67	178,30	0,05
EtOH	0,789	8,09	6,39	46,07	0,14
H <sub>2</sub> O	1,000	4,29	4,29	18,02	0,24
HCl	1,187	0,70	0,83	36,46	0,02
Dilution after 30 minutes					
EtOH	0,789	25,66	20,25	46,07	0,44

The process beyond the sol-gel formation and treatment deposition is the same reported in the previous paragraphs. Only one temperature has been tested for this series: 200°C. Further details are reported in <sup>154</sup>.

P7M3\_200

The characterization done on the P7M3\_200 coating is summarized in Table 3.16.

**Table 3.16 - P7M3\_200 surface characterization.**

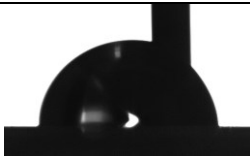

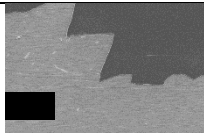
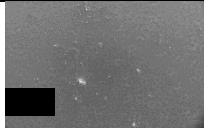
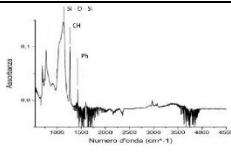
Parameter	Technique	Measurement	Value
$\theta_a$	Sessile drop method		$86^\circ \pm 4^\circ$
$\theta_r$	Sessile drop method		$54^\circ \pm 2^\circ$
Coating thickness	Etching method		$\approx 370$ nm
Surface morphology	SEM		\
Coating composition	FT-IR		

The wetting behavior is still similar to all the silica-based sol-gel coating. The homogeneity of the layer is confirmed by SEM images and the thickness resulted to be the highest. The IR spectrum presents peaks of both  $-CH_3$  groups ( $2976\text{ cm}^{-1}$ ) and phenols ( $999, 740$  and  $1430\text{ cm}^{-1}$ ).

## M7P3\_200

The characterization done on the M7P3\_200 coating is summarized in Table 3.17.

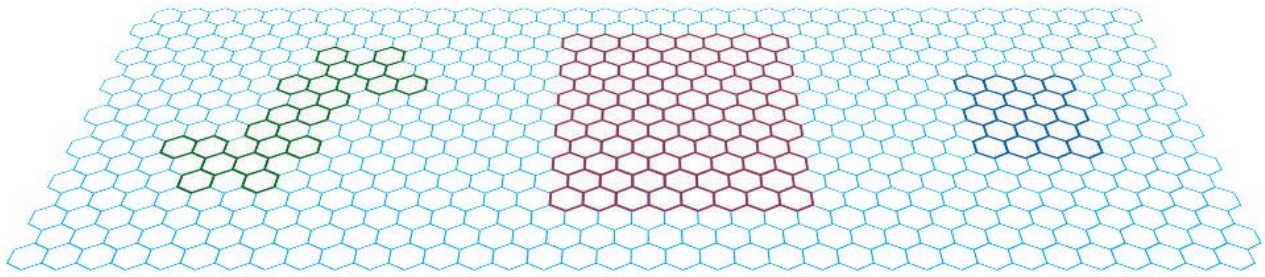
**Table 3.17 - M7P3\_200 surface characterization.**

Parameter	Technique	Measurement	Value
$\theta_a$	Sessile drop method		$89^\circ \pm 2^\circ$
$\theta_r$	Sessile drop method		$61^\circ \pm 4^\circ$
Coating thickness	Etching method		$\approx 190$ nm
Surface morphology	SEM		\
Coating composition	FT-IR		

This sample is the specular of P7M3. It has very similar characteristics to P7M3 (contact angles, FTIR spectrum), but the thickness is the half. Also from SEM images seems less homogenous, since it is characterized by circular dots. The IR spectrum provides indications on the simultaneous presence of both  $-CH_3$  and phenyl groups, but the methyl group has a more intense signal than the phenols, indicating that it is more present in the film.

### 3.2.2 Graphene coatings

Graphene is a new 2D material discovered in 2004 by two physicists Andrej Gejm and Konstantin Novoselov consisting of a single monolayer of  $sp^2$  hybridized carbon atoms<sup>188</sup> (representation of graphene monolayer in Figure 3.8). In the last ten years there has been an incredible interest in this class of 2D materials that has opened up numerous new areas of research and applications<sup>189</sup>.



**Figure 3.8 - Representation of graphene monolayer<sup>189</sup>.**

For the purpose of this thesis the graphene will be used as a protective coating for the metal substrates since its mechanical resistance and it is not oxidized in a wet environment<sup>190</sup>. Other important characteristic of this material is the high in-plane thermal conductivity ( $5000 \text{ W m}^{-1} \text{ K}^{-1}$ )<sup>191,192</sup>, even if it has been demonstrated that has a very anisotropic thermal behavior<sup>193</sup>. Copper samples have already been coated with graphene layers and DWC has been obtained with an increase of HTC of about 200%<sup>190,194</sup>. From the previous, graphene is an attractive solution for promoting DWC, however here a new, industrial scalable, deposition method is proposed<sup>195</sup>. From a synthetic point of view, this material was obtained starting from a solution of Graphene oxide (GO) and was subsequently reduced through a heat treatment in a reducing atmosphere<sup>196–198</sup>. The production of GO mainly occurs through the use of the Hummers<sup>199</sup> synthesis that uses the use of Potassium Permanganate ( $\text{KMnO}_4$ ) and Nitric Acid ( $\text{HNO}_3$ ) to form Manganese Hept Oxide ( $\text{Mn}_2\text{O}_7$ ) which is able to react with the graphite separating the various layers obtaining monolayers. These monolayers, however, are full of defects and functional groups such as: hydroxyls, lactones, carboxylic acids and epoxides which make the material extremely hydrophilic and therefore easily dispersible in water<sup>200</sup>. Once the GO solution has been created, it is necessary to reduce it to obtain graphene (Reduced Graphene Oxide), and there are mainly two ways:

- Deposition of GO and reduction through high temperatures and vacuum or reducing atmospheres;
- Reduction of GO in solution through chemical reactions.

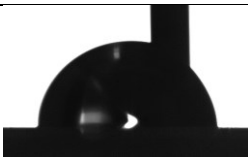
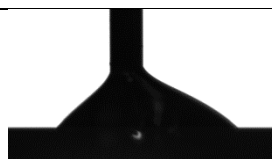
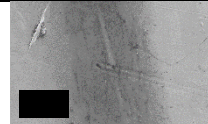
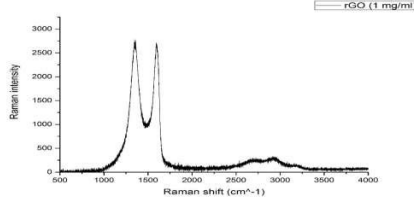
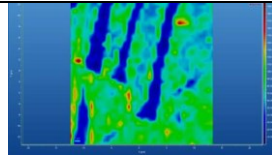
The path chosen in this thesis was the first in which the GO was first deposited on the various copper samples and then it was reduced through high temperatures ( $500^\circ \text{C}$ ) in a hydrogen atmosphere. With this method the undesirable functional groups can be removed, but also the carbon  $\text{sp}^2$  lattice should be restored, at least partially.

**Table 3.18 - Graphene recipe.**

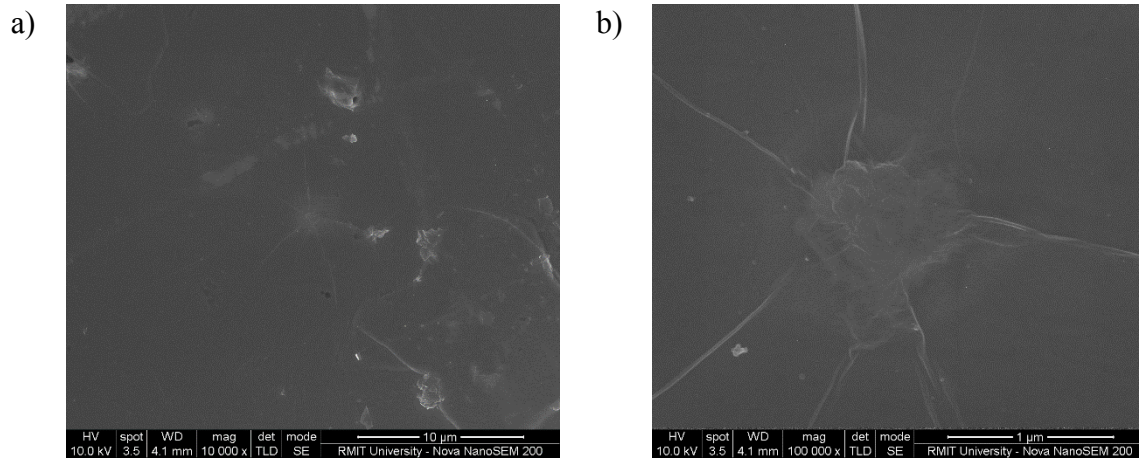
Sample	GO conc.	# Layer	Dipping velocity	Baking temp.	Atm
Copper	$1,0 \text{ mg ml}^{-1}$	1	$4,8 \text{ cm min}^{-1}$	$500^\circ \text{C}$	$\text{H}_2$

The characterization done on the graphene coating is summarized in Table 3.19.

**Table 3.19 - Graphene surface characterization.**

Parameter	Technique	Measurement	Value
$\theta_a$	Sessile drop method		$83^\circ \pm 3^\circ$
$\theta_r$	Sessile drop method		$39^\circ \pm 6^\circ$
Surface morphology	SEM		\
Coating composition	Raman spectroscopy		
Coating composition	Raman map		

Looking at the contact angles, whereas the advancing contact angle is very similar to the one measured on the mirror-polished copper substrate, the receding contact angle is much more higher. Even if the research of Rafiee *et al.*<sup>190</sup> does not consider the dynamic contact angles, seems that the layer cannot be considered as a monolayer. The first analyzes carried out were a Raman spectrum and a Raman map in order to control both the type of deposited material and its homogeneity on the surface. As can be seen, the D band results to have a relative intensity higher than the G band, this is due to a good degree of reduction achieved by the sample<sup>201–204</sup>. A further Raman analysis performed was the realization of a surface map in order to understand if the coating was homogeneous. Looking at the images above, scratches can be seen on the surface where the coating has been removed. These scratches are probably due to the manipulation of the sample since they are not present on the whole surface. In areas outside these defects, in fact, there is a total coverage and a good homogeneity of the film. The coating is barely visible by SEM, in the image above there is the zone transition between pure copper and graphene. In the areas where there is only graphene, some graphene flakes as can be seen in Figure 3.9.



**Figure 3.9 - SEM images of graphene flakes at different magnifications (10kx, 100kx)**

### 3.3 Superhydrophobic surfaces

A surface can be called superhydrophobic if the advancing contact angle is higher than  $150^\circ$  and the contact angle hysteresis is lower than  $10^\circ$  (further explanation can be found in paragraph 2.1). In literature are reported several methods to obtain superhydrophobicity on aluminum surfaces<sup>23,24,57,205–212</sup>: ion implantation<sup>24</sup> and via chemical treatment<sup>23,24,57,206–212</sup>. Unlike ion implantation, which presents some at industrial scale up limitations, the chemical approach has recently received a wide interest. Besides limited reports of methods based on sol-gel and chemical vapor deposition<sup>23,206</sup>, the immersion method appears to be the most viable option<sup>7,57,207–212</sup>. The treatments mainly consist in creating the proper surface roughness by a chemical etching step (e.g. using HCl<sup>207,208</sup>, NaOH<sup>209</sup> or boiling water<sup>210</sup>) before lowering the surface free energy by depositing a proper compound on the substrate (e.g. Teflon<sup>208,210</sup>, hydrocarbons<sup>208</sup> or fluorinated reagents<sup>209</sup>). Several authors studied DWC promotion over superhydrophobic copper<sup>6,22,213</sup> or silicon based surfaces<sup>136,214,215</sup>, while detailed studies of DWC over aluminum substrates are very limited<sup>5,23,216</sup>. Besides, tests have been made on silicon pillars in the literature<sup>214,217–220</sup>, but the influence of the surface morphology, gained via chemical etching methods, has never been evaluated before to the best of our knowledge. Thus the idea is to create a surface roughness, which can be imparted in two ways:

- Etching the surface. In the present work, obtained via wet-chemical method;
- Building structures on the surface<sup>42,221,222</sup>. In the present work, aerogel solutions have been explored.

#### 3.3.1 Wet-chemical etching

The present research starts from the treatment developed by Maitra *et al.*<sup>205</sup> and improved by Bisetto *et al.*<sup>223</sup>, where iron (III) chloride is used to modify the aluminum substrate, and extends the range of etching reagents that were previously tested in order to study the resulting different micro and nano-structures<sup>57,211,212</sup> and the interface connection quality between the substrate and the polymeric coating.

The substrates are made of pure aluminum (AW 1050, Al quantity higher than 99.50%). Iron(III) Chloride (reagent grade 97%), Aluminum(III) Chloride (reagent grade 98%), Copper (II) Chloride (reagent grade XX%), Hydrogen Peroxide (30% w/w solution), Hexane (anhydrous, 95%), Tetrahydrofuran ( $\geq 99.9\%$ ) and Trichloro(1H,1H,2H,2H-perfluorooctyl)silane (FOTS, 97%) were used as provided by Sigma Aldrich. Sodium Hydroxide pellets and triethanolamine (TEA) were purchased from Merck Dow Corning. All the reagents were used as received.

Aluminum substrates were sanded using emery paper #1200, ultrasonically cleaned in isopropanol (IPA) for 15 minutes. The aluminum oxide passivation layer was removed in a NaOH aqueous



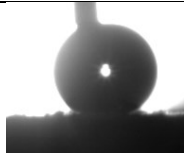
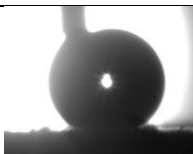
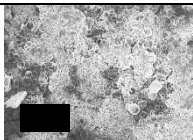
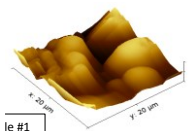
solution (1% by weight) bath. During the process the solution was constantly sonicated with an immersion probe. The resulting substrates were then etched according to three different procedures:

- Sample #1. The sample was immersed in a  $\text{AlCl}_3$  (0.1 M) and triethanolamine (TEA, 0.75 M) aqueous solution in a vial sealed with aluminum foil<sup>212</sup>. The solution was heated on a hot plate at  $90^\circ\text{C}$  for 5 h. Finally, the specimen was rinsed in DI water and dried in a nitrogen stream.
- Sample #2. The sample was immersed in a  $\text{FeCl}_3$  aqueous solution ( $1 \text{ mol L}^{-1}$ ) for 7.5 minutes<sup>205,223</sup>. In order to avoid iron deposition on the surface, this etching process was divided in two periods: after the first period the sample was extracted from the etching solution, it was ultrasonically cleaned in isopropanol for one minute, dried in  $\text{N}_2$  and finally immersed again in the etching solution for the remaining etching time. The cleaning process was also repeated at the end of the etching procedure.
- Sample #3 and Sample #4. The samples are immersed in  $1 \text{ mol L}^{-1}$  aqueous  $\text{CuCl}_2$  solution at ambient temperature for about 8 seconds. In this way, a uniform deposition of a Cu layer can be obtained due to a chemical substitution reaction<sup>57</sup>. After immersion in the etching solution, the Al substrates are rinsed using deionized water to eliminate any residual salt and then dried in  $\text{N}_2$ .

The resulting samples were immersed in a  $\text{H}_2\text{O}_2$  (35% w/w) solution for 30 minutes, transferred in DI water for 15 minutes and dried with nitrogen. A solution of FOTS in hexane (5% by volume) was spin-coated on Sample #1, Sample #2 and Sample #4 at 800 rpm for 30 seconds. The spin coating procedure was repeated twice to ensure a homogenous distribution of FOTS on the surface of the substrate. The Sample #3 is functionalized by means of a different technique in order to improve the connection quality between the substrate and the hydrophobic layer. No spinning of the hydrophobic layer is performed in this case; instead, the substrate is immersed in a FOTS – hexane solution (5% by volume). Functionalization takes place at low temperature ( $7^\circ\text{C}$ ) for 5 hours. After the functionalization, the sample was baked on a hotplate at  $150^\circ\text{C}$  for 30 minutes to remove any solvent residuals and stabilize the silane film.

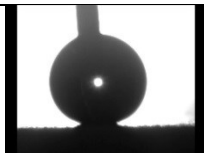
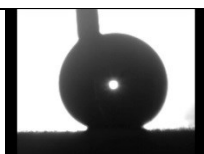
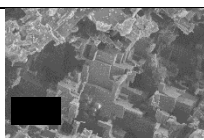
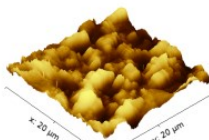
The characterization done on Sample #1 is summarized in Table 3.20.

**Table 3.20 - Sample #1 characterization.**

Parameter	Technique	Measurement	Value
$\theta_a$	Sessile drop method		$156^\circ \pm 2^\circ$
$\theta_r$	Sessile drop method		$152^\circ \pm 1^\circ$
Surface morphology	SEM		\
Surface roughness	AFM		$7,36 \mu\text{m} \pm 0,91 \mu\text{m}$

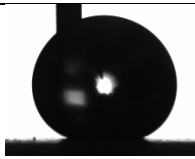
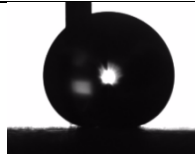
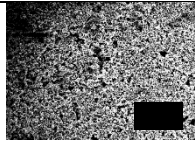
The characterization done on Sample #2 is summarized in Table 3.21.

**Table 3.21 - Sample #2 characterization.**

Parameter	Technique	Measurement	Value
$\theta_a$	Sessile drop method		$155^\circ \pm 3^\circ$
$\theta_r$	Sessile drop method		$149^\circ \pm 6^\circ$
Surface morphology	SEM		\
Surface roughness	AFM		$2,67 \mu\text{m} \pm 0,32 \mu\text{m}$

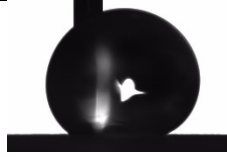

The characterization done on Sample #3 is summarized in Table 3.22.

**Table 3.22 - Sample #3 characterization.**

Parameter	Technique	Measurement	Value
$\theta_a$	Sessile drop method		$158^\circ \pm 1^\circ$
$\theta_r$	Sessile drop method		$149^\circ \pm 5^\circ$
Surface morphology	SEM		\
Surface roughness	2D-profilometer		$3,48 \mu\text{m} \pm 0,30 \mu\text{m}$

The characterization done on Sample #4 is summarized in Table 3.23.

**Table 3.23 - Sample #4 characterization.**

Parameter	Technique	Measurement	Value
$\theta_a$	Sessile drop method		$151^\circ \pm 2^\circ$
$\theta_r$	Sessile drop method		$10^\circ$
Surface roughness	2D-profilometer		$2,22 \mu\text{m} \pm 0,31 \mu\text{m}$

From Table 3.20, Table 3.21 and Table 3.22 it can be seen that Sample #1, #2 and #3 were superhydrophobic after the functionalization step, displaying a Cassie – Baxter<sup>34</sup> wetting regime during contact angle measurements, whereas Sample #4 displays a Wenzel<sup>33</sup> wetting regime, since it presents high advancing contact angle ( $\theta_a=151^\circ$ ) like the other samples, but very low receding contact angle ( $\theta_r \approx 10^\circ$ ). Since the etching step is the same for Sample #3 and Sample #4, the functionalization step must be responsible for the different wetting behavior. A possible explanation is that the spin coating technique (Sample #4) is not sufficient to impart superhydrophobicity for a  $\text{CuCl}_2$  etched

sample. The roughness analysis shows that the roughness imparted from the etching solution is similar for Sample #3 and Sample #4. All the surfaces, although displaying a completely different morphology, are characterized by high erosion which results in a non-homogeneous roughness of the substrate (as can be seen from SEM images). For further details, please see Parin *et al.*<sup>224</sup>.

### 3.3.2 Aerogel

The aerogel is a term coined in 1931 by the scientist Samuel Stephens Kistler to indicate a gelatinous substance in which the liquid media has been replaced by a gas, without causing the collapse of the solid structure. To obtain this new material Kistler used a technique called *Supercritical Drying* which consists in bringing the sample in supercritical conditions, i.e. at a pressure and temperature greater than a determined critical value, for which the formation of the liquid-vapor meniscus is prevented<sup>225</sup>. With this technique, Kistler succeeded in obtaining the removal of the liquid part without causing fractures of the solid network, synthesizing a new material with very particular properties including: high surface area ( $> 900 \text{ m}^2 \text{ g}^{-1}$ ), high porosity ( $> 99\%$ ), very low density ( $< 0.005 \text{ g cm}^{-3}$ ) and low conductivity ( $0.005 \text{ W m}^{-1} \text{ K}^{-1}$ )<sup>226,227</sup>. Despite the incredible properties, this material has long been abandoned due to the high production costs resulting mainly from bringing the sample to supercritical conditions. At the end of the 1990s, however, the chemist Schwertfeger managed to obtain an aerogel sample under ambient pressure conditions, thus overcoming the main problem of this material. In the last twenty years there has therefore been a substantial increase in research to create aerogel with different precursors, different methodologies and innovative properties<sup>228,229</sup>. The objective is to obtain a superhydrophobic material starting from materials with a low cost and using a synthesis that does not require the use of high temperatures and pressures<sup>230-232</sup>. The synthesis of silica aerogels is based on the sol-gel method in which, by means of hydrolysis and water or alcohol condensation reactions, silica nuclei are created, from which a 3D network is obtained by polymerization. In order to obtain superhydrophobic surfaces, the aerogel has to be functionalized with hydrophobic groups. The functionalization of an aerogel is a procedure through which the silanol groups (-Si-OH) are replaced with organic groups (-Si-R) which give the material the hydrophobicity. There are numerous precursors able to perform this task, but they give different effects as described by Rao *et al.*<sup>233</sup>. The functionalization of the surface has other advantages. It helps expel water from the pores and prevents the entry of more water once the sample is formed and during the evaporation there is a narrowing of the volume due to the capillary tensions that are established. Once the liquid has been extracted, the hydrophobic groups begin to repel and return the network to its original size. This mechanism is called spring-back and avoids excessive shrinkage<sup>232,234</sup>.

Before depositing the aerogel on the aluminum substrate, a first deposition of borosilicate was performed at a rate of 4.8 cm min<sup>-1</sup> and a subsequent heat treatment at 500 ° C. The synthesis of this coating is similar to that used for the compounds of TEOS, MTES and PhTES (Table 3.6). After cooling, a dip was made with the aerogel solution (Table 3.24) using the classic method. The silica structure was obtained using sodium silicate (Britesil C335 from PQ Corporation) as a precursor.

**Table 3.24 - Borosilicate recipe.**

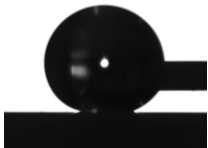
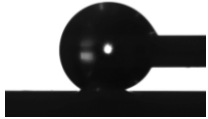
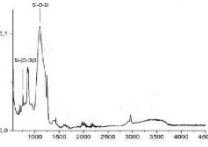
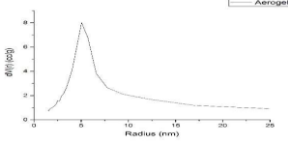
	Density (g cm <sup>-3</sup> )	Volume (ml)	Weight (g)	MM (uma)	Mole
TEOS	0,933	4,40	4,11	208,33	0,02
EtOH	0,789	37,50	29,60	46,07	0,64
H2O	1,000	1,25	1,25	18,02	0,07
HNO3	1,400	0,19	0,27	63,02	0,00
Dopo 2 ore					
TEOB	0,858	6,80	5,83	145,99	0,04

**Table 3.25 - Aerogel recipe.**

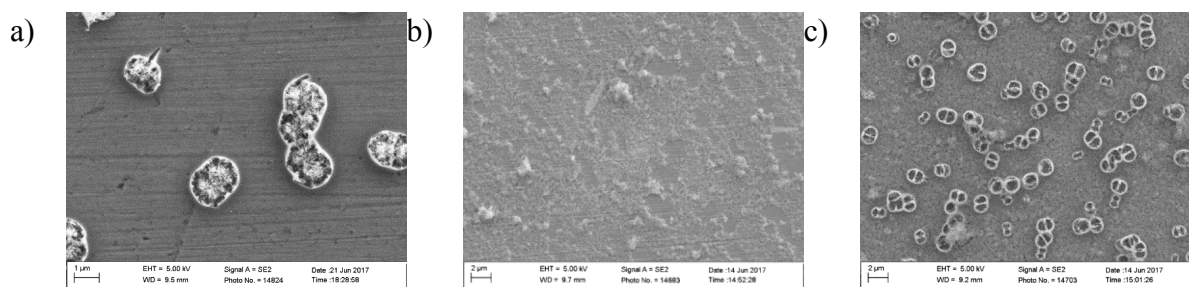
	Density (g cm <sup>-3</sup> )	Volume (ml)	Weight (g)	MM (uma)	Mole
Britesil C335			0,90		
H <sub>2</sub> O	1,000	10	10,00	18,02	0,56
HCl (37%)	1,186	1	1,19	36,46	0,03
2-propanolo	0,786	3	2,36	60,10	0,04
HMDS	0,770	3	2,31	161,39	0,01
Esano	0,660	3	1,98	86,18	0,02
2-propanolo	0,786	50	23,58	60,1	0,39

The characterization done on the aerogel coating is summarized in Table 3.26. From the above IR spectrum, there are some differences compared to the samples seen previously. The appearance of the peaks belonging to the groups -Si(CH<sub>3</sub>)<sub>3</sub> and a decrease of the bands of the -OH group, for instance. Furthermore, there are peaks related to the presence of amines or ammonium. These are probably due to some residues that were trapped in the skeleton of the aerogel during the synthesis.

**Table 3.26 - Aerogel surface characterization.**

Parameter	Technique	Measurement	Value
$\theta_a$	Sessile drop method		$159^\circ \pm 5^\circ$
$\theta_r$	Sessile drop method		$150^\circ \pm 5^\circ$
Coating thickness	Etching method		$\approx 360$ nm
Surface morphology	SEM	\	\
Coating composition	FT-IR		\
Surface morphology	BET		\

In Figure 3.10, several SEM images are presented. In Figure 3.10a the result of the borosilicate deposition is seen, the process did not lead to a continuous layer as for the other depositions (e.g. MxTy series), but it led to randomly distributed conglomerates. The aerogel deposition itself (Figure 3.10b) led to a quasi-uniform layer over the aluminum substrate, though. The combination of both (Figure 3.10c), it permitted to a double-scale roughness, microscale from the borosilicate and nanoscale from the aerogel, on the surface. The double-scale roughness is fundamental to reach good levels of superhydrophobicity<sup>75,76,205,235</sup> (as reported in the wettability measurement in Table 3.26).



**Figure 3.10 - SEM images: a) Borosilicate layer (Table 3.24), b) Aerogel Layer (Table 3.25), c) Borosilicate.**

Through the BET (Table 3.27), both the surface area and the size and distribution of the pores of the aerogel powders were assessed.

**Table 3.27 - BET analysis result.**

Surface area	Porous volume	Porous mean radius
1212 m <sup>2</sup> /g	3,3 cc/g	5,0 nm

### 3.4 The bouncing tests

The bouncing tests are related to the capability of surfaces to retain impacting water droplets, which can further characterize surfaces as a means for avoiding the ice formation or for slowing the formation of frost. Surfaces with extremely low wettability are interesting because droplets bounce remaining on the surface a time lower than the time required to the liquid to freeze (if the thermodynamic requirements are satisfied).











Different surfaces have been tested with different wettability:

- Superhydrophilic surface: SHPHIL. The surface is obtained etching an aluminum substrate with the procedure reported for Sample #3 in paragraph 3.3.1. The surface is not covered with a fluorosilane agent as Sample #3.
- Hydrophilic surface: HPHIL. The surface is mirror-polished aluminum surface. See characterization in Paragraph 3.1.1.
- Hydrophobic surface: HY. The surface is M7T3\_200. For further details see paragraph 3.21.2.1.
- Superhydrophobic surface: SHY\_1. The surface is covered by an aerogel film, obtained following the procedure described in paragraph 3.3.2.
- Superhydrophobic surface: SHY\_2. The surface is the Sample #3 described in paragraph 3.3.1.

The dynamic contact angle measurement is summarized in Table 3.28 for the different samples.



**Table 3.28 - Contact angle measurement done on sample used for the bouncing tests.**

	$\theta_a$ [°]	$\theta_r$ [°]
<b>SHPHIL</b>		
	$23^\circ \pm 5^\circ$	$0^\circ$
<b>HPHIL</b>		
	$65^\circ \pm 3^\circ$	$10^\circ \pm 3^\circ$
<b>HY</b>		
	$83^\circ \pm 3^\circ$	$64^\circ \pm 2^\circ$
<b>SHY_1</b>		
	$159^\circ \pm 3^\circ$	$150^\circ \pm 5^\circ$
<b>SHY_2</b>		
	$158^\circ \pm 1^\circ$	$149^\circ \pm 5^\circ$

### 3.4.1 Experimental procedure

In this experiment, a droplet with a known diameter  $D_0$  (2,6 mm) is released from different highs  $H$  (reported in Table 3.29) over a surface; videos are taken during the bouncing process. For each high, an impact velocity  $V_{imp}$  of the droplet is calculated from the images.

**Table 3.29 - Tested highs and the corresponding impact velocity of a droplet.**

H [mm]	V <sub>impact</sub> [m s <sup>-1</sup> ]
781	4,2
360	2,6
105	1,6
47	1,0
7	0,2

When a droplet interacts with a general surface, different scenarios can occur:

- 1) the droplet does not fragmentize (low V<sub>imp</sub>) (NF)
  - the droplet does not rebound (NF+NR);
  - the droplet rebounds (NF+R);
- 2) the droplet fragmentizes (high V<sub>imp</sub>) (F)
  - the droplet does not rebound (F+NR);
  - the droplet rebounds (F+R).

For further details of the experimental procedure, please refer to Da Re *et al.*<sup>141</sup>.

### 3.4.2 Droplet bouncing results

The observed responses of the surface to the bouncing test are summarized in Table 3.30.

**Table 3.30 - Droplet's behavior after impact. (F) fragmentation; (NF) not fragmentation; (R) rebound; (NR) not rebound.**

V <sub>imp</sub> [m s <sup>-1</sup> ]	SHY_1	SHY_2	HY	HPHIL	SHPHIL
4.2	F+NR	F+NR	NF+NR	F+NR	F+NR
2.6	F+R	F+NR	NF+NR	NF+NR	NF+NR
1.6	NF+R	NF+NR	NF+NR	NF+NR	NF+NR
1.0	NF+R	NF+NR	NF+NR	NF+NR	NF+NR
0.2	NF+R	NF+R	NF+NR	NF+NR	NF+NR

In Figure 3.11 droplet behavior for HY, HPHIL and SHPHIL surface for a fixed velocity is reported.

SURFACE	IMPACT	ADV	MAX SPREAD	REC	REC	EXIT
HY						
HPHIL						
SHPHIL						

Figure 3.11 - Droplet's evolution on not-superhydrophobic surface, at a fixed impact velocity:  $V_{imp} = 1.6 \text{ m s}^{-1}$ . ADV: advancing; REC: receding

A strong bond between the surface and the liquid is shown on high wetting surfaces (HY,SPHIL and SHPHIL). The behavior is similar for all the surfaces, besides the HY surface which exhibits a contracting of the droplet contact line once the maximum spread is reached. In Figure 3.12 and Figure 3.13 the SHY\_1 images are reported for different droplet impact velocities, in Figure 3.14 and Figure 3.15 the same for sample SHY\_2.

$V_{imp}$ [m s <sup>-1</sup> ]	IMPACT	ADV	MAX SPREAD	REC	REC	EXIT
0.2						
1.0						
1.6						

Figure 3.12 - Droplet's behavior on SHY\_1 at different impact velocities. ADV: advancing; REC: receding.

	$V_{imp}=2.6 \text{ m s}^{-1}$	$V_{imp}=4.2 \text{ m s}^{-1}$
IMPACT		
ADVANCING		
MAX SPREAD		
RECEDING		
RECEDING		
EXIT		

Figure 3.13 - Droplet's behavior on SHY\_1 at different impact velocities.

$V_{imp}$ [m s <sup>-1</sup> ]	IMPACT	ADV	MAX SPREAD	REC	REC	EXIT
0.2						
1.0						
1.6						

Figure 3.14 - Droplet's behavior on SHY\_2 at different impact velocities. ADV: advancing; REC: receding

	$V_{imp}=2.6 \text{ m s}^{-1}$	$V_{imp}=4.2 \text{ m s}^{-1}$
IMPACT		
ADVANCING		
MAX SPREAD		
RECEDING		
RECEDING		
EXIT		

Figure 3.15 - Droplet's behavior on SHY\_2 at different impact velocities.

From previous Figures, it can be seen that the rebound of the droplet is showed only by superhydrophobic surfaces ( $\theta_r \approx 150^\circ$ )<sup>253</sup>, highlighting the role of the receding contact angle in governing the drop rebound from a surface. Nevertheless, also the surface structure seems to have a crucial role in the rebound effect. Increasing the droplet velocity, in fact, there is the transition between the rebound and the no-rebound also for the superhydrophobic surfaces. SHY\_2 shows the limit between  $0.2 \text{ m s}^{-1}$  and  $1 \text{ m s}^{-1}$ , whereas SHY\_1 permits the rebound until  $2.6 \text{ m s}^{-1}$ . As it can be seen from SEM images in Chapter 3, the morphology of SHY\_1 and SHY\_2 is completely different, the roughness of SHY\_2 seems to be much higher than the one of SHY\_1. Moreover, the superhydrophobicity is more homogenous on SHY\_1 due to the fabrication process. The rebound/no-rebound is related to the transition between the Cassie and the Wenzel state of a droplet on the surface. Several authors<sup>8,72,224,254,255</sup> show the transition in different ways (increasing the temperature, droplet bouncing, squeezing a droplet between two plane,...) and relating the phenomenon to an energy barrier which has to be overcome by the liquid. In the present case, the energy barrier is overcome by the potential energy associated to the droplet released from a certain high: higher the droplet, higher the impact energy. From Figure 3.13, the SHY\_1 sample is the more robust treatment so far for guaranteeing the rebound of a droplet. Wettability and surface structure have also a role on the fragmentation effect: meanwhile SHY\_1 and SHY\_2 display a fragmentation after  $2.6 \text{ m s}^{-1}$ , the other present fragmentation at  $4.2 \text{ m s}^{-1}$ . Special result has been obtained on the HY sample (Figure 3.16), which do not present fragmentation at all, probably due to the absence of roughness on the surface. The no-fragmentation surfaces can be interesting on the water collection processes.

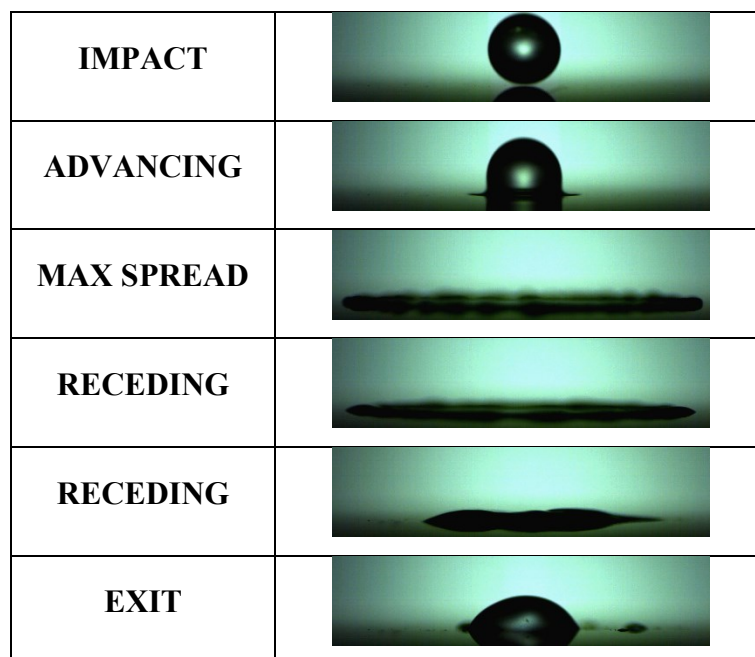


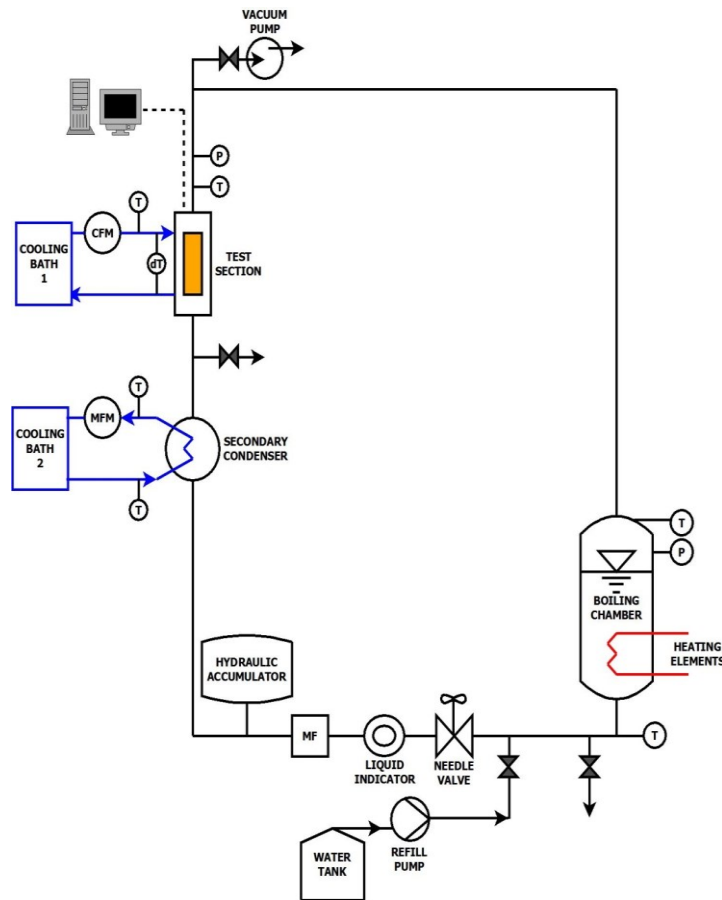
Figure 3.16 - Droplet's behavior on HY at  $4.2 \text{ m s}^{-1}$ .

# Chapter 4 - Experimental apparatus

For the readers' convenience, the experimental apparatus is briefly described as reported in my other works<sup>81,181,236–238</sup>. The data reduction technique and the uncertainty analysis for the experimental results are fully reported.

## 4.1 Components of the experimental apparatus

The experimental setup is schematically shown in Figure 4.1.



**Figure 4.1 – Scheme of the experimental apparatus. P = Pressure transducer, T = Thermocouple, dT = Thermopile, CFM = Coriolis mass Flow Meter, MFM = Magnetic mass Flow Meter, MF = Mechanical Filter.**

A sketch of the thermosiphon loop is reported in Figure 4.1: the steam is generated in the boiling chamber, it is partially condensed inside the test section and then complete condensation is achieved in a home-made heat exchanger (post-condenser). Two thermal baths are used to provide cooling water at the desired temperature conditions in the test section and in the post-condenser. Because non-condensable gases in the vapor can affect the heat transfer coefficient<sup>13,97</sup>, special care was taken to avoid any presence of them<sup>239</sup>. All tests were performed using DI water inside the loop. The steam is

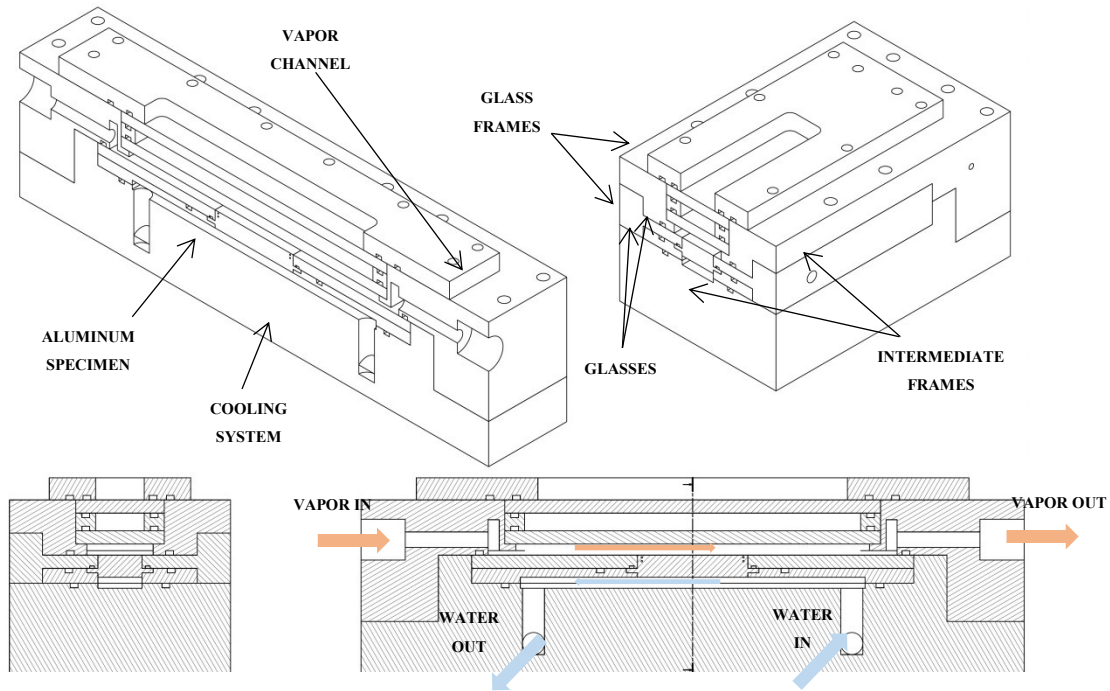
generated in a cylindrical stainless steel evaporator, which can provide a maximum power of 4 kW to the fluid (Figure 4.2).



**Figure 4.2 – Boiling chamber.**

The adjustment of the input power is handled through a separate electrical panel connected to the heating elements, meanwhile the electrical power supplied to vaporize the liquid inside the boiling chamber is measured by a power analyzer NORMA 4000. The subcooled liquid entering the chamber is vaporized in the boiler and then it flows through a stainless steel tube well insulated to ensure that the vapor remains at the saturated state when it reaches the test section. To avoid formation of condensate on the walls of the vapor line the tubes are heated up to saturation temperature by means of an electrical heater installed around the pipe (wall temperature is checked through a T-type thermocouple) for a length of 0.5 m. The condensation phenomenon is analyzed in the test section (Figure 4.3) which consists in a PEEK channel that is fitted with the test surface of a rectangular plain metallic substrate. Vapor pressure and temperature are measured at the inlet of the measuring section by means of a differential pressure transducer (coupled with an absolute one for ambient pressure evaluation) and a T-type thermocouple, respectively. The metallic specimen is cooled on the backside by a water bath, which allows precise control of coolant temperature. Coolant inlet temperature is measured by a T-type thermocouple, while coolant temperature difference between the inlet and the outlet is measured by means of a three-junction copper-constantan thermopile. To assure precise evaluation of heat flux, the coolant mass flow rate is measured by means of a Coriolis effect mass flow meter. A fundamental characteristic of this material is to have a very low thermal conductivity ( $\lambda_{PEEK}=0.25 \text{ W m}^{-1} \text{ K}^{-1}$ ): this means that the dispersions towards the external environment are minimal and ensuring one-dimensionality of heat flux along the specimen. The section consists of a rectangular channel having dimensions equal to 160 mm x 30 mm x 5 mm dug in the block of PEEK (hydraulic

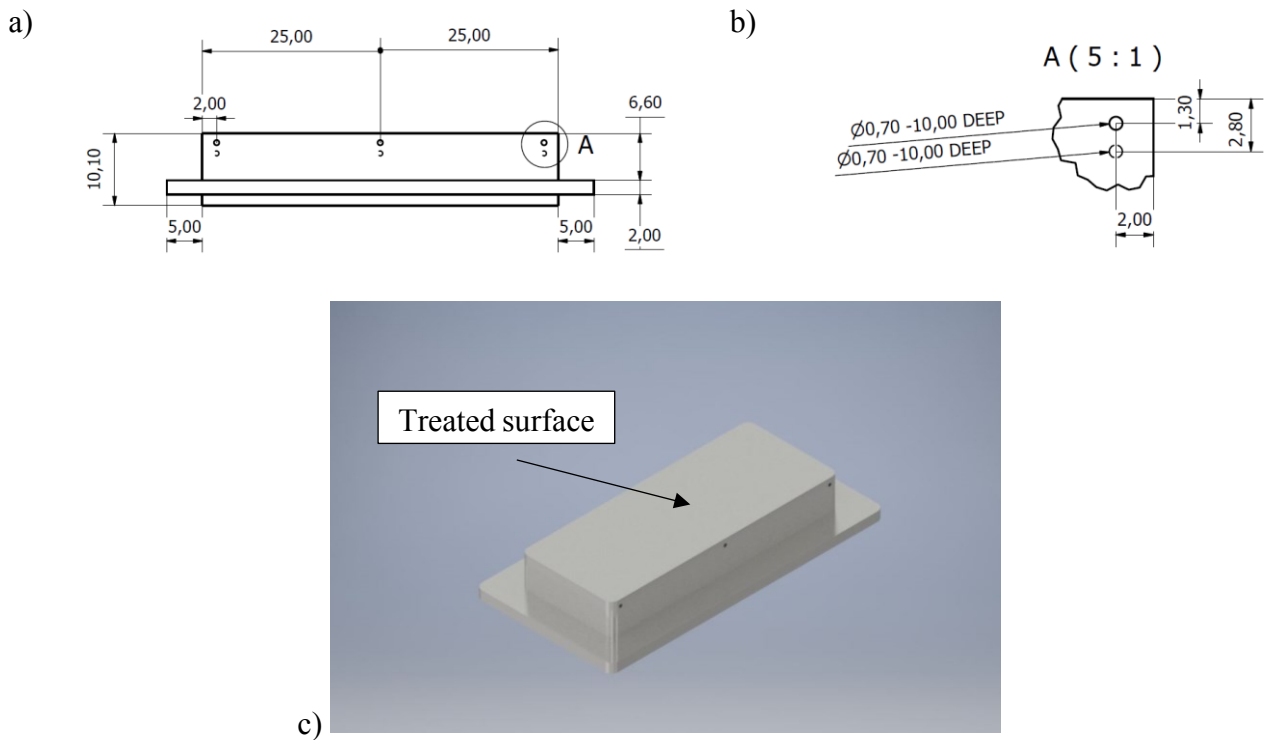
diameter  $d_h=0.0086$  m). One side of the channel is covered by two glass plates that allow the visualization of the process, with an intermediate chamber to increase the thermal insulation. The front glass is equipped with an electric heater to avoid the condensation of the steam on the internal glass and thus to permit to observe the two-phase process. On the opposite side there is a hole where the sample is placed.



**Figure 4.3 – Schematic of the test section.**

The sample (Figure 4.4) is 10 mm thick, condensing surface is 50 mm x 20 mm and for the analysis of the heat exchange it is instrumented with 6 thermocouples. The metal sample is cooled in the backside in order to adjust the surface temperature of the test sample, thus to control the saturation to wall temperature difference. The cooling water flows in countercurrent with respect to the direction of the steam inside the test section. The position of the input and output water channels, as well as the channel length, were determined in order to have a uniform velocity profile of the fluid in the cooling duct<sup>81</sup>.





**Figure 4.4 - a) Side view and b) zoomed image of the metallic substrate with quotes. c) Rendering of the sample.**

Downstream of the test section, the uncondensed vapor and condensed liquid pass through a secondary water condenser which completes the condensation process and returns the subcooled liquid to the boiler through a gravity drain. Inlet and outlet water temperatures are acquired by means of T-type thermocouples while water mass flow rate is measured by a magnetic flow meter. The apparatus is composed by other components that maintain stable and appropriate work conditions, as it is could be seen in Figure 4.1. To regulate the system pressure, a hydraulic accumulator is installed in the liquid line downstream the post-condenser. A precise needle valve is used to regulate the liquid flow at the inlet of the boiling chamber in order to achieve stable conditions during the tests. In between the hydraulic accumulator and the needle valve a mechanical filter and a liquid indicator are installed. Before entering the boiling chamber the temperature of the subcooled liquid is measured by means of a T-type thermocouple. All the components of the test rig, with the exception of the test section, are made by stainless steel in order to avoid contamination of the fluid. Steam components, boiling chamber and the stainless steel line are very well insulated in order to avoid heat losses to the ambient. More details about the test rig can be found elsewhere<sup>44,81,239</sup>.

## 4.2 Measurement system

The aim of the apparatus is to calculate the heat transfer coefficient during pure steam condensation and to pursue this goal it needs different kind of transducers. The different transducers and their uncertainty (Type B) are summarized in the following Table.

**Table 4.1 - List of transducers present in the experimental apparatus with their own uncertainty values.**

Transducer	Uncertainty
T-type thermocouple	$\pm 0.05^\circ \text{C}$
T-type thermopile	$\pm 0.03^\circ \text{C}$
Druck differential pressure	$\pm 0.04\% p_{fullscale}$
Druck absolute pressure	$\pm 0.01\% p_{fullscale}$
Coriolis mass flow meter	$\pm 0.15\% \pm \left(\frac{0.1}{\dot{m}}\right)\%$
Electromagnetic mass flow meter Danfoss MAG 1100	$\pm 0.25\%$ if $v_{fluid} \geq 1.5 \text{ ft/s}$ or $\pm \frac{0.41}{v_{fluid}}\%$ if $v_{fluid} < 1.5 \text{ ft/s}$
Power analyzer Fluke Norma 4000	$\pm 0.1\%$

## 4.3 Data reduction technique

For extrapolating the HTC the following parameters have to be calculated:

- Temperature difference between the wall temperature of the specimen and the saturation temperature of the steam ( $\Delta T$ ).
- Specific heat flux through the specimen ( $q$ ).
- Specific mass flow rate of the vapor flowing in the experimental section.

### 2.3.1 Wall temperatures

The aluminum sample (Figure 4.4) is embedded with 6 thermocouples, two at the inlet, two in the middle and two at the outlet with respect to the vapor flow, located at two different positions along the perpendicular axis of the sample: three are located ( $T'$ ,  $z_1$ ) 1.3 mm from the condensing surface, the other after 2.8 mm ( $T''$ ,  $z_2$ ). The wall temperatures can be measured locally as

$$T_{\text{wall}} = T' + (T' - T'') \frac{z_2}{z_2 - z_1} \quad (4.1)$$

only under the mono dimensional heat flux. The ratio between the longitudinal to the perpendicular heat flux during DWC resulted to be always lower than 1%. From the measure of the saturation pressure the temperature difference is calculated as

$$\Delta T = T_{\text{sat}} - T_{\text{wall}} \quad (4.2)$$

Based on the HTC which is considered, a mean  $\Delta T$  can be evaluated

$$\Delta T_{\text{in-mid}} = \frac{\Delta T_{\text{in}} + \Delta T_{\text{mid}}}{2} \quad (4.3)$$

$$\Delta T_{\text{in-out}} = \frac{\Delta T_{\text{in}} + \Delta T_{\text{out}}}{2} \quad (4.4)$$

$$\Delta T_{\text{mid-out}} = \frac{\Delta T_{\text{mid}} + \Delta T_{\text{out}}}{2} \quad (4.5)$$

$$\Delta T_{\text{in-mid-out}} = \frac{\Delta T_{\text{in}} + \Delta T_{\text{mid}} + \Delta T_{\text{out}}}{3} \quad (4.6)$$

### 4.3.2 Heat flux

There are two different techniques to obtain the specific heat flux through the specimen. The specific heat that is extracted by the cooling water from the condensing vapor, can be calculated as

$$q_{\text{cool}} = \frac{\dot{m}_{\text{coolant}} c_{p,\text{coolant}} \Delta T_{\text{coolant}}}{A} \quad (4.7)$$

where  $c_{p,\text{coolant}}$  is the specific heat of the coolant water, at the average temperature between the inlet and the outlet of the section and  $A$  is the specimen frontal area. The Fourier's law for thermal conduction can be applied to the three different positions of thermocouples in the sample, as follow

$$q = \lambda_{Al} \frac{dT}{dz} = \lambda_{Al} \frac{T_{\text{SAT}} - T_{\text{WALL}}}{Z_2 - Z_1} \quad (4.8)$$

Thus, the average heat flux along the specimen is

$$q_{\text{in-mid}} = \frac{q_{\text{in}} + q_{\text{mid}}}{2} \quad (4.9)$$

$$q_{\text{in-out}} = \frac{q_{\text{in}} + q_{\text{out}}}{2} \quad (4.10)$$

$$q_{\text{mid-out}} = \frac{q_{\text{mid}} + q_{\text{out}}}{2} \quad (4.11)$$

$$q_{\text{in-mid-out}} = \frac{q_{\text{in}} + q_{\text{mid}} + q_{\text{out}}}{3} \quad (4.12)$$

The average heat flux calculated with any Equation from 4.9 to 4.12 can be compared with the Equation 4.7.

### 4.3.3 Heat transfer coefficient

The HTC is calculated from

$$HTC = \frac{q}{\Delta T} \quad (4.13)$$

As reported previously, several heat flux and wall temperatures can be defined: the same for HTC.

The local HTC are

$$HTC_{in} = \frac{q_{in}}{\Delta T_{in}} \quad (4.14)$$

$$HTC_{mid} = \frac{q_{mid}}{\Delta T_{mid}} \quad (4.15)$$

$$HTC_{out} = \frac{q_{out}}{\Delta T_{out}} \quad (4.16)$$

The global HTC calculated with Fourier's law are

$$HTC_{in-mid} = \frac{q_{in-mid}}{\Delta T_{in-mid}} \quad (4.17)$$

$$HTC_{in-out} = \frac{q_{in-out}}{\Delta T_{in-out}} \quad (4.18)$$

$$HTC_{mid-out} = \frac{q_{mid-out}}{\Delta T_{mid-out}} \quad (4.19)$$

$$HTC_{in-mid-out} = \frac{q_{in-mid-out}}{\Delta T_{in-mid-out}} \quad (4.20)$$

Considering a thermal balance at the coolant side

$$HTC_{TP} = \frac{q_{TP}}{\Delta T_{medio}} \quad (4.21)$$

Nel calcolo dei coefficienti di scambio termico, al posto delle termocoppie, si può utilizzare la termopila che rileva la differenza di temperatura a cui è soggetta l'acqua di raffreddamento della sezione di misura. Agli altri *HTC* globali si aggiunge quindi il seguente coefficiente, legato al flusso termico dato dalla termopila e alla differenza di temperatura media:

$$\text{HTC}_{cool} = \frac{q_{cool}}{\Delta T_{in-mid-out}} \quad (4.22)$$

In this paragraph all the approaches for the HTC calculation are summarized. As reported in Chapter 3, the coating deposition is a crucial step for the homogeneity of the treatment and several samples have been found with boundary defects. Inhomogeneity in the coating thickness leads to misleading HTC as seen in Chapter 2, being the HTC very sensitive to this parameter. The majority of the data reported in this thesis are then measured at the middle position where those defects are at the minimum.

#### 4.3.4 Specific vapor mass flow rate

From the temperature and the pressure of the liquid at the entrance of the boiling chamber, it is possible to calculate the enthalpy of the subcooled liquid at the evaporator inlet, as well as the latent heat of vaporization of water using REFPROP version 9.1. Measuring the heat supplied to the boiling chamber for vaporization of the liquid, it is possible to assess the mass flow of the fluid within the system as

$$\dot{m} = \frac{Q_{BC}}{h_v - h_{ls}} \quad (4.23)$$

where  $h_v$  and  $h_{ls}$  are respectively the enthalpies of saturated steam at the exit of the boiling chamber and of the subcooled liquid at the entrance of the boiler. It is then possible to calculate the specific vapor mass flow rate flowing in the test section as

$$G_v = \frac{\dot{m}}{S_c} \quad (4.24)$$

where  $S_c$  is the cross section of the channel, in our case  $S_c = 0.005 \text{ m} * 0.030 \text{ m}$ .

### **4.4 Experimental apparatus uncertainty**

According to ISO Guide<sup>240</sup> (1999) the uncertainty components are grouped into two categories "A" and "B", depending on the method of evaluation. Type A uncertainty obtained from a probability density function derived from the observed frequency distribution. The uncertainty of type B is obtained through a probability density function assumed on the basis of the degree of confidence in the occurrence of an event, and therefore it is estimated a priori on the basis of objective

considerations. The combined uncertainty is used for results obtained from the values of other variables, and is indicated with  $u_c$ : this is the standard deviation associated with the result. Finally, the expanded uncertainty is obtained multiplying the combined uncertainty by a coverage factor. The purpose of it is to provide an interval in the neighborhood of the measurement result, which is expected to include the major portion of the distribution of values attributable to the measured value. As regards the type A uncertainty, the best estimate of the expectation values of a quantity  $q$ , of which were made  $n$  independent observations  $q_k$ , all in the same experimental conditions, is the arithmetic mean or average value  $\bar{q}$  of the  $n$  observations

$$\bar{q} = \frac{1}{n} \sum_{k=1}^n q_k \quad (4.25)$$

Therefore for an input variable estimated by independent repeated observations, the arithmetic mean obtained from Equation (4.25) is used as an estimate of the input. The individual observations differ due to random variations of the quantities of influence. The experimental variance of the observations is given by

$$s^2(q_k) = \frac{1}{n-1} \sum_{k=1}^n (q_k - \bar{q})^2 \quad (4.26)$$

The experimental standard deviation of the mean is

$$\sigma^2(\bar{q}) = \frac{s^2(q_k)}{n} \quad (4.27)$$

And it is used as A type uncertainty of  $\bar{q}$ .

Regarding the type B uncertainty, which has not been obtained from repeated observations, uncertainty or the estimated variance are evaluated by scientific judgment based on all the information available on the variability of the input. These can be obtained from

- Data from previous measurements.
- The manufacturer's specifications.
- Data provided in calibration certificates.
- Uncertainties assigned to reference data taken from handbooks.

If a measurement has both type B uncertainty ( $u_b$ ) and type A uncertainty ( $u_a$ ), the total uncertainty is determined by the formula

$$u_{tot} = \sqrt{u_a^2 + u_b^2} \quad (4.28)$$

Considering the case of input independent variables  $x_i$ , the uncertainty  $u_c(y)$  of a derivate quantity  $y$  is obtained by the following formula

$$u_c(y) = \sqrt{\sum_{i=1}^n \left(\frac{df}{dx_i}\right)^2 u^2(x_i)} \quad (4.29)$$

where  $u(x_i)$  is the uncertainty of the inlet quantity and  $f$  is the relating function

$$y = f(x_1, x_2, \dots, x_n) \quad (4.30)$$

Once the combined uncertainty is calculated, it is possible to calculate the extended uncertainty as

$$U = k u_c(y) \quad (4.31)$$

The coverage factor  $k$  is chosen according to the desired degree of confidence. For example, if we assume a Gaussian configuration,  $k$  refers to the following values:

- With a degree of confidence of 68.3% it is  $k= 1$ .
- With a confidence level of 95.5% it is  $k= 2$ .
- With a confidence level of 99.7% it is  $k= 3$ .

The measures presented in this paper have all been subjected to analysis of the combined uncertainty. Each point reported in this work is the mean of 480 readings at 1 Hz and remembering Equation 4.28, the type A uncertainty assumes a negligible value as compared to the type B. Combined uncertainties calculated with and without type A uncertainty differ about 1%. The uncertainty of a measurement is, then, mostly influenced by the intrinsic uncertainty of instruments (refer to Table 4.1). During FWC typical values of average uncertainty of the  $\Delta T$  between the vapor temperature and the specimen surface temperature are less than 1.3%; while the average uncertainty of the heat transfer coefficient is less than 8.2% referring to a confidence level equal to 95.5%. During DWC, instead, the uncertainty values are higher since very high HTC are measured at low  $\Delta T$ . Referring to paragraph 4.3.3, in the following Tables typical uncertainty values are reported using two thermocouples (local HTC) and all six thermocouples (global HTC).

**Table 4.2 - Local HTC uncertainty.**

	2 Thermocouples			
HTC [ $\text{kW m}^{-2} \text{K}^{-1}$ ]	80		200	
$\Delta T$ [K]	2.8	4.9	1.0	2.7
HTC uncertainty	18 %	8 %	22 %	13 %

**Table 4.3 - Global HTC uncertainty.**

	6 Thermocouples			
HTC [ $\text{kW m}^{-2} \text{K}^{-1}$ ]	80		200	
$\Delta T$ [K]	2.3	5.4	1.1	4.2
HTC uncertainty	12 %	5 %	14 %	6 %

Tables cover from the minimum to the maximum HTC measured during the experimental campaign. It must be underlined that using more thermocouples the values of uncertainty tends to decrease, but as already discussed the values measured at the middle position should be more accurate than the necessity to use only one couple of thermocouples. At very high HTC ( $> 150 \text{ kW m}^{-2} \text{K}^{-1}$ ) the uncertainty reaches around the 22% of the measured value at low  $\Delta T$ . In all the other cases, the uncertainty is acceptable (around 10%).





# Chapter 5 - Experimental Results

In this Chapter, all the experimental results obtained during the PhD research are summarized. The first results consist of pure vapor condensation tests done on several surfaces with different wettability (the experimental apparatus is described in Chapter 4), afterwards some preliminary results about droplet bouncing related to the wetting phenomena are reported. Condensation tests are subdivided in two macro area:

- Type of condensation test;
- Type of condensation mode, FWC or DWC.

Different tests can be performed on a surface, firstly, in order to understand the lifetime of a treatment, duration tests are completed, then the heat flux is varied in order to understand the HTC trend. Another interesting parameter to the comprehension of the physic beyond the condensation phenomenon is the vapor velocity, which has been varied to understand its influence on the HTC. The latter it could be applied to the coatings which showed a good durability under harsh environment. All the typologies of tests have been carried out on the coatings described in Chapter 3. Most of the treatments are applied to several samples in order to confirm the validity of the experimental data, thus the data is related to the treatment not to the sample: more than 40 samples have been tested. During the experimental campaign, some false positives have been discovered and deleted from the data. Here, only the data which resulted to be repeatable is presented. Further details are reported elsewhere<sup>154,155,181</sup>.

## 5.1 Condensation tests description

Hereafter the condensation tests applied to the samples are described. Each data point reported in this Chapter is the mean of 480 readings at 1 Hz. For uncertainty values, for the data reduction technique and for other questions related to the measure chain please refer to Chapter 4. The HTC measured during DWC are calculated with the thermocouples located at the middle of the sample in order to avoid boundary defects, whereas the HTC measured during FWC are shown as mean between the inlet and the outlet position.

### 5.1.1 Durability tests

The duration test is performed maintaining all the input parameters constant during the whole test. This test is fundamental to skim the treatments: if one coating does not sustain DWC for a significant amount of time, the coating should be revised or erased. Besides measuring the thermal parameters and taking videos of the phenomenon, each coating had been undergone to the same characterizations (where it was possible) described in Chapter 3 after the condensation test. This step, most of the time

avoided in the literature, is fundamental for understanding how the surface interact with the vapor flow: which can be etched, eroded, modified in different ways or maintained intact. In the next Table, the different parameters controllable by the User in the experimental apparatus are reported with the related values. Where it is not specifically written, please refer to those values for the thermodynamic conditions of the experimental tests.

**Table 5.1 - Duration test parameters.**

<b>Parameter</b>	<b>Value</b>
<i>Vapor velocity [m s<sup>-1</sup>]</i>	2.7
<i>Saturation temperature [°C]</i>	106
<i>Overheating temperature [°C]</i>	108
<i>Coolant mass flow rate [kg s<sup>-1</sup> m<sup>-2</sup>]</i>	0.11
<i>Coolant temperature [°C]</i>	40

Some words must be spent on Table 5.1. The velocity of the vapor is far from being zero, thus it has an influence on the HTC during condensation, both during FWC and DWC. Since the experimental apparatus is a thermosiphon flow loop, a minimum thermal power supplied to the operating fluid exists in order to win all the flow resistances along the flow. The value 2.7 m s<sup>-1</sup> is the minimum value for the circulation of the fluid and that permits a stable test. The saturation temperature correspond to a pressure just above the atmospheric pressure, which prevents the entrance of non-condensable gasses that strongly influence the DWC measurements<sup>99,224,241</sup>. The overheating temperature can be useful in order to prevent the condensation of vapor before the test section, a couple of degrees more than the saturation temperature resulted to be enough. The cooling mass flow rate is the highest manageable by the thermal bath and it should increment the mixing of the flow, thus the thermopile measurement should be more accurate. The thermal bath can vary the coolant temperature from 10°C to 99°C, the coolant temperature of 40°C was chosen since it is in the middle of the range. Usually, this type of tests are stopped when about the 10% of the surface is covered by a condensate film, meaning that the coating is ruined and it is not able to sustain DWC anymore. The choice of 10% is completely arbitrary, since the transition is related to the degradation of the film and it is irreversible, thus the full covering of the surface of FWC is just question of time (please refer to treatment M5T5\_200 as example).

### 5.1.2 Heat flux tests

The heat flux tests are performed in order to understand the influence of the heat flux on the HTC for a specific coating. Usually, each treatment has a specific thickness as reported in Chapter 3 and, thus,

different thermal resistance (see Chapter 2 for formulas) which means different HTC. Varying the heat flux permits to understand how the HTC is influenced by the heat flux, or in other words, by the temperature difference between the saturation and wall temperatures. Different trends are reported in literature<sup>99</sup>, some authors found constant HTC with different heat fluxes<sup>6,31,242</sup>, others increasing HTC<sup>13</sup>. This becomes a fundamental aspect when models come into play. Furthermore, if the HTC is found to be constant implies that those tests are unnecessary since just one point is needed to know the thermal performance of a coating. In Table 5.2 the thermodynamic conditions imposed during the tests are shown.

**Table 5.2 - Heat flux test parameters.**

<b>Parameter</b>	<b>Value</b>
<i>Vapor velocity [m s<sup>-1</sup>]</i>	2.7
<i>Saturation temperature [°C]</i>	106
<i>Overheating temperature [°C]</i>	108
<i>Coolant mass flow rate [kg s<sup>-1</sup> m<sup>-2</sup>]</i>	0.11
<i>Coolant temperature [°C]</i>	from 10 to 85

As compared to duration tests (see Table 5.1), the only parameter varied is the coolant temperature. The coolant temperature influences the wall temperature of the sample and, maintaining the saturation temperature unvaried, the heat flux changes. The heat flux typically varies from 100 kW m<sup>-2</sup> to 600 kW m<sup>-2</sup> and this is a limit of the present configuration of the experimental apparatus.

### 5.1.3 Effect of vapor velocity tests

The duration tests, but also, the heat flux tests are performed with a constant vapor velocity of 2.7 m s<sup>-1</sup>. The shear stress induced by the vapor on the droplets strongly influence the DWC process, in first instance, changing the droplet departing radius<sup>26,27</sup> (see Chapter 2 for the math). This aspect is very important for the dynamics of the droplets, indeed, and it is partially studied in the literature<sup>6,241</sup>. Controlling the pressure inside the experimental apparatus, being a thermosiphon loop, is quite a challenge, thus this kind of tests are particularly precarious. In fact, in order to rise the vapor speed, the heating power in the boiling chamber must be increased (see Chapter 4 for the experimental apparatus regulation). To an increase of the heating power corresponds to an increase of pressure which has been compensate regulating the needle valve, thus decreasing the pressure drop along the liquid line. Furthermore, the coating has to be robust enough to resist to high value of shear stress<sup>6</sup>. For this reasons, only one vapor velocity test has been performed.

**Table 5.3 - Vapor velocity test parameters.**

<b>Parameter</b>	<b>Value</b>
<i>Vapor velocity [m s<sup>-1</sup>]</i>	from 2.7 to 11
<i>Saturation temperature [°C]</i>	106
<i>Overheating temperature [°C]</i>	108
<i>Coolant mass flow rate [kg s<sup>-1</sup> m<sup>-2</sup>]</i>	0.11
<i>Coolant temperature [°C]</i>	40

From Table 5.3, it can be noticed that the coolant temperature is maintained constant, thus the value of HTC should change only because the variation on the vapor speed.

## **5.2 Durability tests**

Hereafter the duration tests are presented. Firstly, the FWC mode is reported obtained on untreated aluminum and copper surfaces, secondly the more generous group of treatments which promoted DWC.



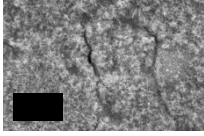
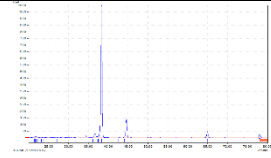
### **5.2.1 FWC tests**

It has to be highlighted that naturally a metal surface, even if it can promote DWC at the initial stage, being condensation a nucleation phenomenon, promote FWC since its intrinsic hydrophilicity<sup>20</sup>. The duration test applied to those surfaces is not particularly interesting since the FWC will endure as long there is material on which vapor can condense. However, some characterizations have been done on aluminum after the testes and it is interesting to see how the surface changes.

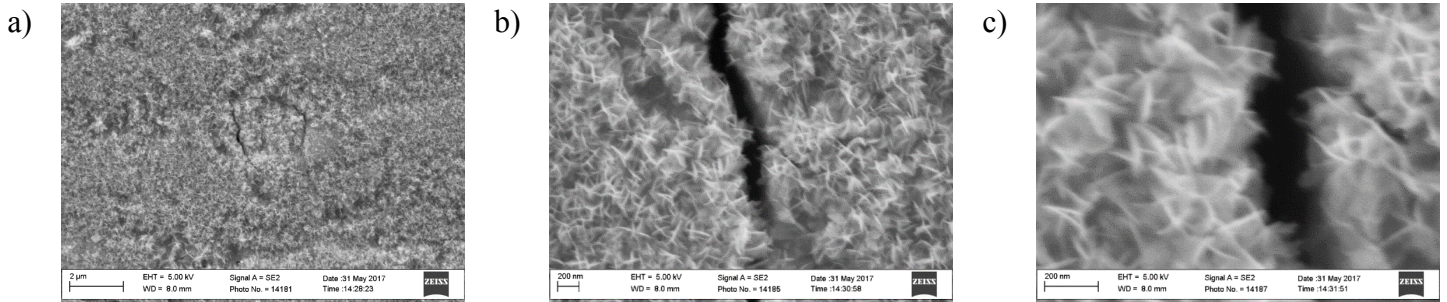
#### **5.2.1.1 Aluminum samples**

The HTC at the conditions reported in Table 5.1 for bare aluminum is around 16 kW m<sup>-2</sup> K<sup>-1</sup> for an exchanged heat flux of about 300 kW m<sup>-2</sup>. Some characterizations have been done after 2 hours of test and they are summarize in Table 5.4.

**Table 5.4 - Mirror-polished aluminum surface characterization after condensation tests.**

Parameter	Technique	Measurement	Value
$\theta_a$	Sessile drop method		$65^\circ \pm 3^\circ$
$\theta_r$	Sessile drop method		$\approx 0^\circ$
Surface morphology	SEM		\
Surface composition	XRD		\

SEM images are further investigated in Figure 5.1.



**Figure 5.1 - SEM images of mirror-polished aluminum after condensation tests at different magnifications.**

The surface is no longer smooth and homogeneous, but it has flower-like structures distributed uniformly throughout the sample. An XRD measurement investigated the nature of these structures that turned out to be Aluminum Hydroxide (JCPDS Card: 04-0787). It is easy to correlate these hydroxide complexes with the nullification of the recession angle (see characterization done before and after the condensation tests). These structures are, in fact, full of -OH groups that interact with water by establishing hydrogen bonds and increasing their adhesion to the substrate.

### 5.2.2 DWC tests

All the treatment proposed in Chapter 3 promoted DWC with different durations. Henceforth, further details can be found.

### 5.2.2.1 Nanoparticle silica-based coating

The experimental data here reported is referred to the treatment reported in paragraph 3.2.1.1. The coating promoted DWC with HTC higher than  $100 \text{ kW m}^{-2} \text{ K}^{-1}$  with heat flux of about  $440 \text{ kW m}^{-2}$ . The thermal measurements are shown in Figure 5.2. The HTC is almost constant for the whole experimental campaign (about 300 minutes), although the condensation mode changes from pure DWC to a mixture of DWC and FWC as shown in Figure 5.3. The degradation of the coating is not homogenous neither, already after 53 minutes a light “foot” is possible to notice on the surface. The nature itself of this kind of treatments can be a possible explanation, as already reported in paragraph 3.2.1.1 from the SEM analysis, the nanoparticles are randomly distributed on the surface.

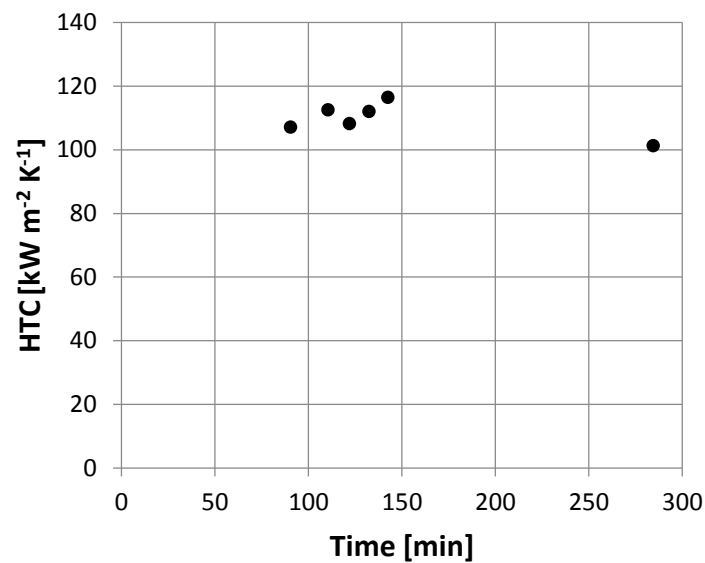


Figure 5.2 - HTC versus time for nanoparticle silica-based coating.

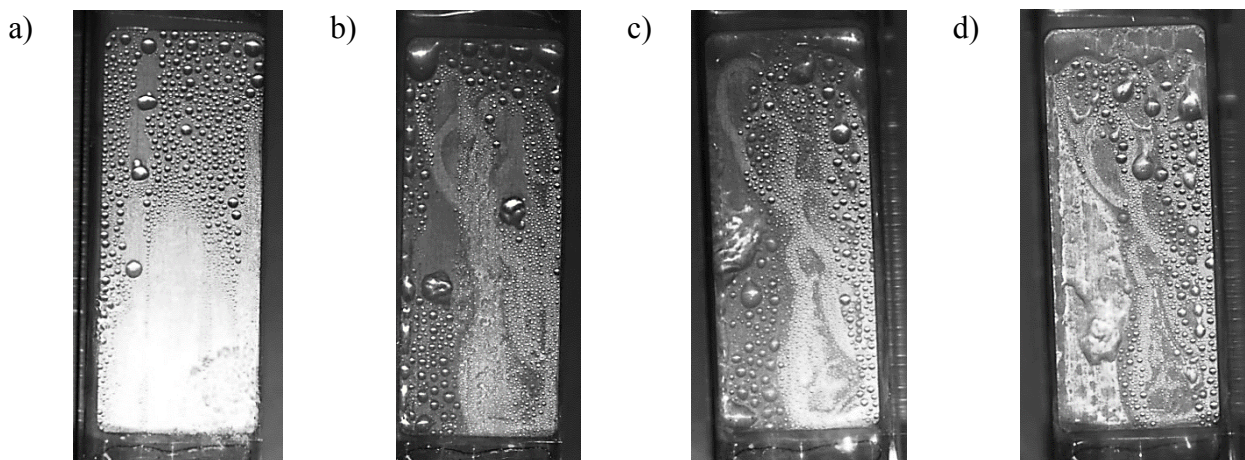
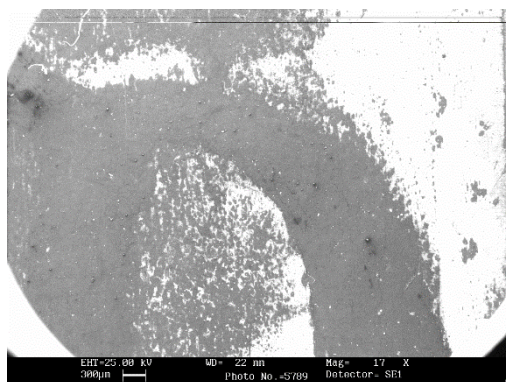


Figure 5.3 - Time evolution of nanoparticle silica-based coating. The images are taken at: a) 0 min, b) 53 min, c) 95 min and d) 276 min.

Contact angle measurement lead to  $\theta_a = 64^\circ \pm 24^\circ$  and  $\theta_r = 13^\circ \pm 3^\circ$ . The receding contact angle dropped from the value before the test, whereas the advancing one is still high but inhomogeneous (high

standard deviation) on the surface. A SEM analysis (Figure 5.4) has been conducted on the surface in order to understand the difference between the lighter and darker zone. Figure 5.4 clearly shows the formation of two different regions having different surface characteristics, one darker and another lighter. The EDX analysis showed that the white region is made of aluminum oxide, while the dark area corresponds to non-oxidized aluminum. This result explains the different gray gradation assumed by the surface, in fact the aluminum oxide is a bad conductor of electrons and therefore when struck by the electrons conveyed by the SEM tends to keep them localized leading to an electrostatic charge of the surface, this phenomenon does not happen instead for aluminum. In the darker zone, the silica coating resisted against the vapor flow, protecting the aluminum from being oxidized.



**Figure 5.4 - SEM images of nanoparticle silica-based coating after condensation tests.**

In this case, replicability of the experimental data has been found difficult since morphologically similar surfaces with similar contact angles have produced great variability on coating duration. In conclusion, these syntheses are not suitable for use on aluminum for heat exchange applications since the replicable films are not obtained and probably the nanoparticle-substrate interaction is too weak to resist the abrasive mechanical action of the steam. For further details are available elsewhere<sup>155,238</sup>.

### 5.2.2.2 MxTy series

The MxTy series includes different combination of precursors MTES and TEOS treated at different temperatures. All the combinations are summarized in Table 5.5.

**Table 5.5 - MxTy series.**

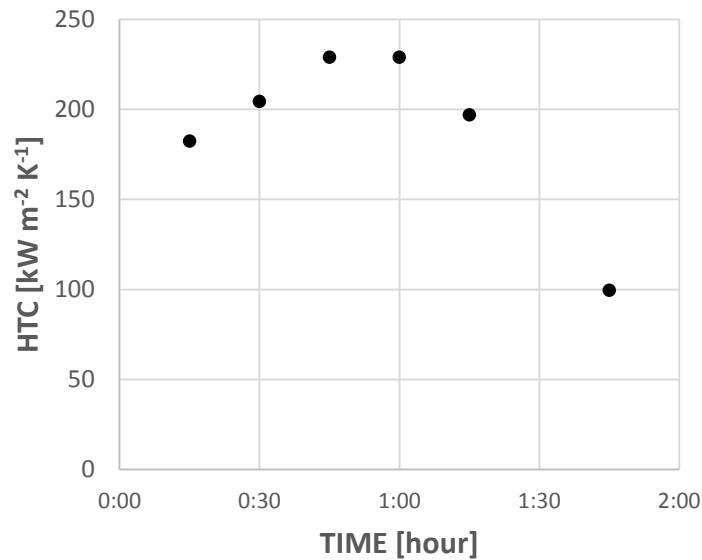
Sample	Name		% TEOS	% MTES	% PhTES	Baking Temp.	Dipping Vel.
Al	M5T5_200		50	50	/	200	4,8 cm min <sup>-1</sup>
Al	M7T3_200		30	70	/	200	4,8 cm min <sup>-1</sup>
Cu	M7T3_200		30	70	/	200	4,8 cm min <sup>-1</sup>
Al	M7T3_300		30	70	/	300	4,8 cm min <sup>-1</sup>
Al	M7T3_300	2 layer	30	70	/	60+300	4,8 cm min <sup>-1</sup>
Al	M7T3_300	2 layer	30	70	/	300+300	4,8 cm min <sup>-1</sup>
Al	M7T3_400		30	70	/	400	4,8 cm min <sup>-1</sup>



Other MTES/TEOS combinations have been tested: pure TEOS and M2T8. These coatings did not lead to DWC, thus here are not discussed<sup>155</sup>.

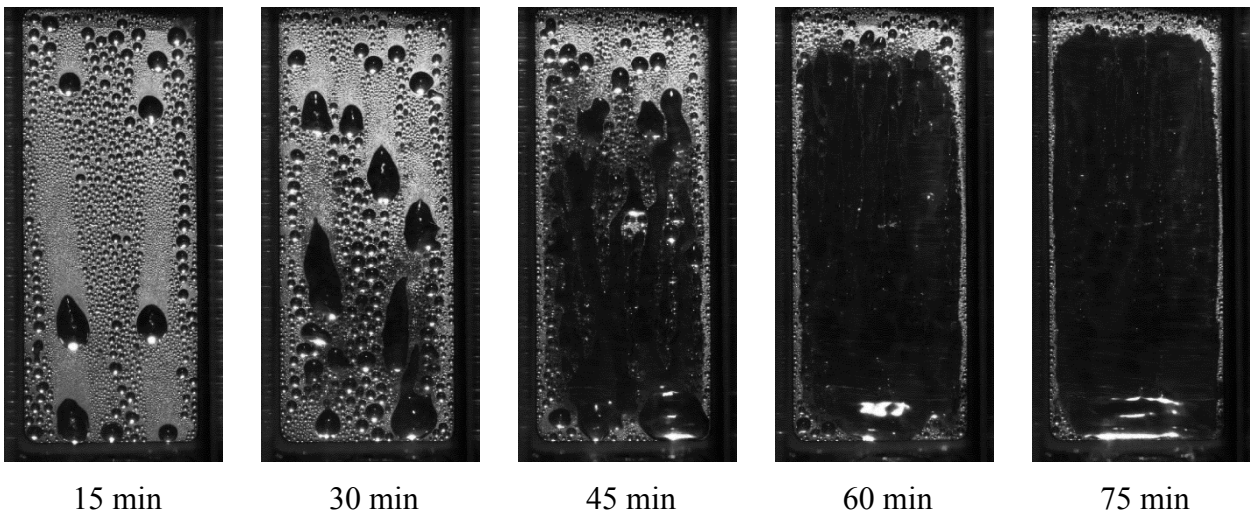
### M5T5\_200

The HTC measured during the pure vapor condensation tests is reported in Figure 5.5, the heat flux is about  $480 \text{ kW m}^{-2}$ . The heat flux is quite constant during all this kind of tests, since it is controlled from the coolant side which is maintained constant on purpose (see Table 5.1).



**Figure 5.5 - HTC versus time for M5T5\_200 coating.**

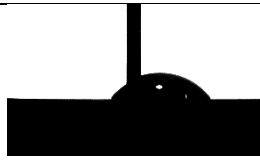

As reported previously, the trend of the coating degradation is monotonic. After a certain time of pure DWC, the droplets start to be elongated due to the increasing of the surface wettability. After this phase, a portion of the surface starts to be flooded showing FWC. The FWC at this point starts to spread all over the surface.



**Figure 5.6 - Time evolution of M5T5\_200 coating.**

Contrary of what expected, the HTC starts to increase with the passing time, reaches a maximum (after about one hour) and then decreases. Moreover, to the maximum value of HTC corresponds a very non-uniform DWC and not a pure DWC as can be seen in Figure 5.6. This behavior has already found by the first authors that studied DWC. With the passing time<sup>243</sup>, the coating deteriorates becoming thinner and thinner, thus decreasing its thermal resistance. Since the coating resistance is very important for the overall HTC (see Chapter 2), even if the thicknesses are very low (200 nm), the HTC tends to be closer to the HTC of the DWC itself. In literature this value is around  $250 \text{ kW m}^{-2} \text{ K}^{-1}$  13,32.

**Table 5.6 - M5T5\_200 surface characterization after condensation tests.**

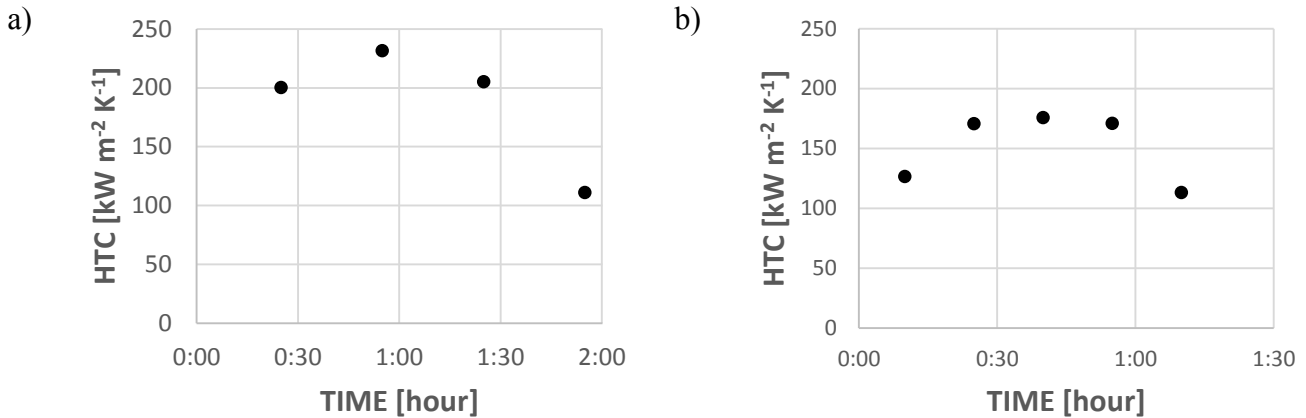
Parameter	Technique	Measurement	Value
$\theta_a$	Sessile drop method		$53^\circ \pm 3^\circ$
$\theta_r$	Sessile drop method		$8^\circ \pm 4^\circ$
Coating thickness	Ellipsometry		$\approx 150 \text{ nm}$

The contact angle measurement confirms the increased wettability expected from the videos, in particular the receding contact angle is very close to  $0^\circ$ . An attempt on measuring the thickness after the condensation test was made with an ellipsometer. The difference between the thickness before and after the condensation test seems to be about 50 nm, thus the coatings seems to be thinner as expected. However, the ellipsometry method is strongly limited if a non-uniform layer is applied due to a high diffusion of the light radiation and the surface after the condensation tests should be ruined. The measurement, then, cannot be considered consistent, it is more a trend.

### **M7T3\_200**

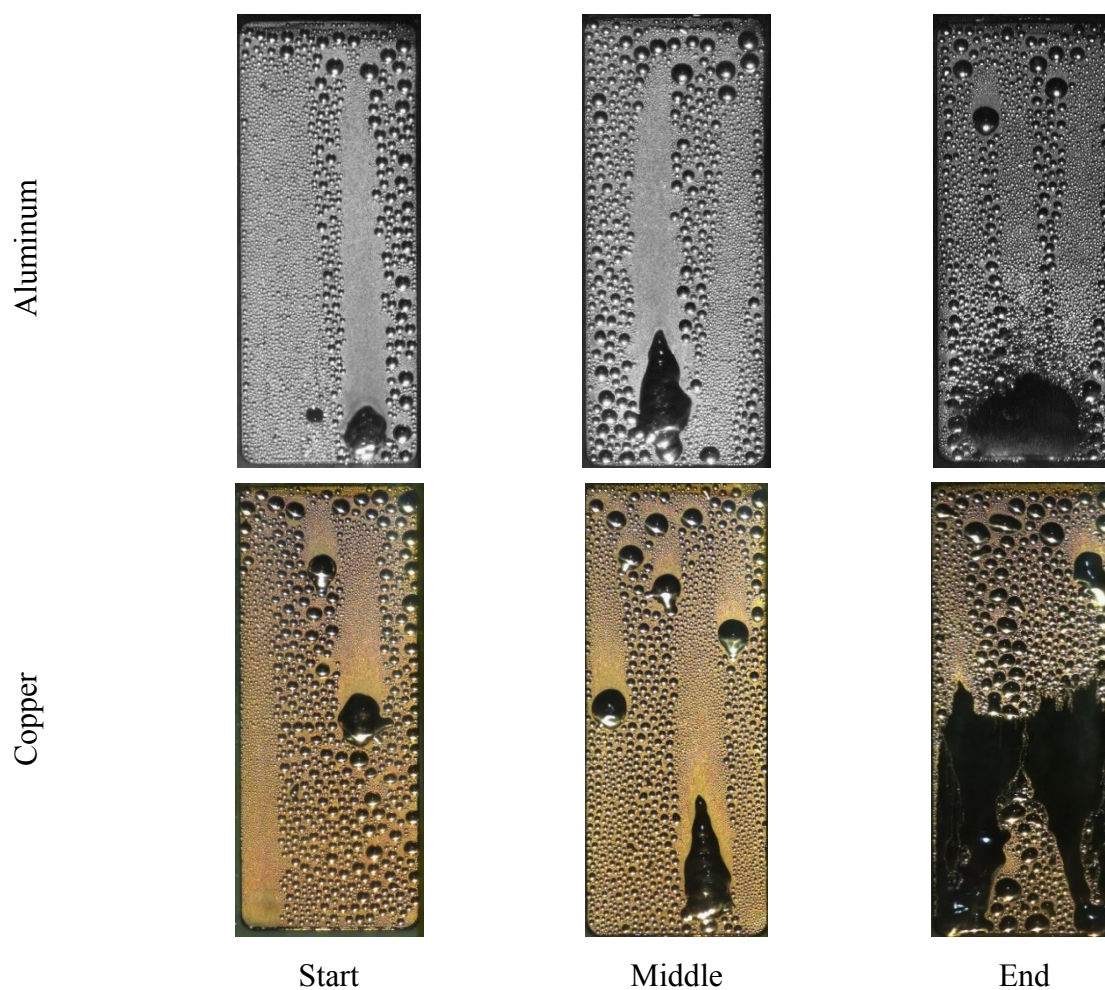
The M7T3\_200 coating has been applied to both copper and aluminum substrate. In Figure 5.7 the HTC trend versus time is presented, the heat flux is about  $400 \text{ kW m}^{-2}$ . Even if the HTC values seem different for the two substrates, the HTC is slightly higher and coating lasts longer on aluminum, the results can be considered similar. In fact, the treatment should interact differently based on the substrate meaning different thicknesses and different bond robustness. In this case, the values reported in Figure 5.7 are too close to appreciate a difference, thus it can be stated that the substrate does not influence the performances of the coating. Furthermore, the degradation looks similar as can be seen in Figure 5.8. DWC images recorded with the high-speed camera are presented and it is possible to

see how the degradation of the surface occurs. It must be underlined that the degradation of the MxTy series presents always the same behavior and characteristics.



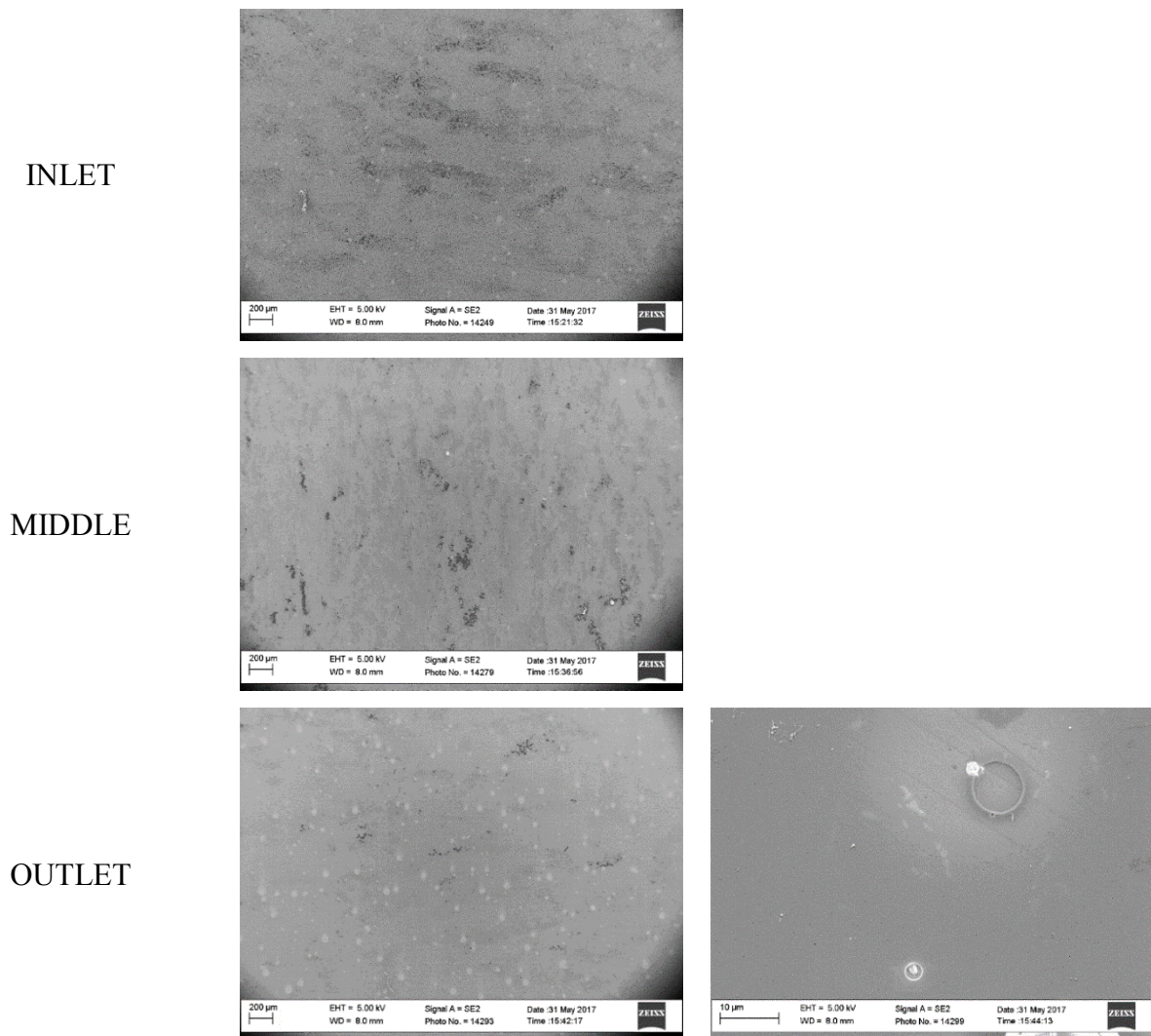
**Figure 5.7 - HTC versus time for M7T3\_200 applied to a) aluminum and b) copper substrate.**

The condensation mode at the beginning is DWC on the entire surface, then there is a gradual transition to FWC: the test stops when about the 10% of the surface is flooded. The droplets' shape changes from a quasi-spherical shape maintained all along the sample to an elongated one about at the middle of the test. At the end of the test, the bottom of the surface is wetted by a continuous layer of condensate. The cause of the degradation could be attributed to the condensate shedding. Since at the outlet the condensate mass flow rate is the highest, the degradation is faster in this position. The flooding of the surface should be an indicator that the surface wettability is changing with the passing time. A proper surface characterization has been done in order to match the thermodynamics measurements with the visualizations.



**Figure 5.8 - Time evolution of M7T3\_200 coating on aluminum and copper.**

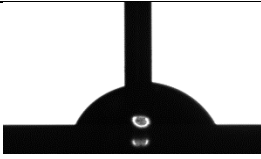
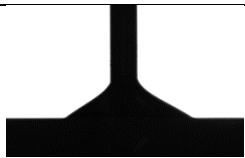
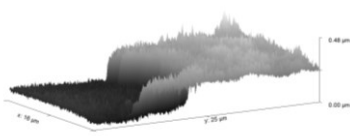
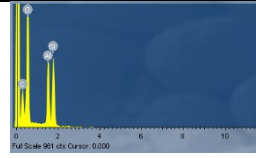
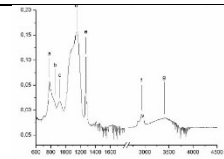
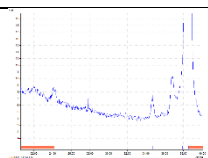
In particular, SEM analysis has been conducted on the aluminum sample. From Figure 5.9 it is possible to notice that while at the inlet and at the middle position the surface does not display significant differences, at the outlet several white spots appear randomly distributed. The zoomed picture focuses one of these features which seems to be a hole on the hydrophobic layer.



**Figure 5.9 - SEM analysis at three different positions along the aluminum substrate: inlet, middle and outlet (for the positioning refer to Chapter 4). Zoomed image of the holes is also showed.**

In fact, at the center of the hole the aluminum substrate shows up; around the hole the coating seems to be thinned since typical characteristics of the aluminum substrate, nano-scratches due to the imperfect polishing, start to be visible. It is also possible to see how growth of globular protuberances may occur inside these holes. The holes were not present before the condensation test (see paragraph 3.2.1.2.1), thus the combination of the vapor shear stress and the condensate flow on the surface causes the breaking of the hydrophobic coating. Once broken, the wettability of the aluminum becomes important increasing the global wettability of the surface. As a result, the contact angles measured after the condensation tests are lower than those measured before (Table 5.7); in particular, at the bottom of the sample where the hole density is higher, the receding contact angle is the lowest (passing from about  $30^\circ$  at the top to  $20^\circ$  at the bottom) and the surface resulted to be flooded by the condensate (Figure 5.8).

**Table 5.7 - M7T3\_200 surface characterization after condensation tests.**

Parameter	Technique	Measurement	Value
$\theta_a$	Sessile drop method		$65^\circ \pm 7^\circ$
$\theta_r$	Sessile drop method		$27^\circ \pm 5^\circ$
Coating thickness	AFM		$\approx 60$ nm
Surface morphology	SEM	\	\
Coating composition	EDX		\
Coating composition	FT-IR		\
Surface composition	XRD		\

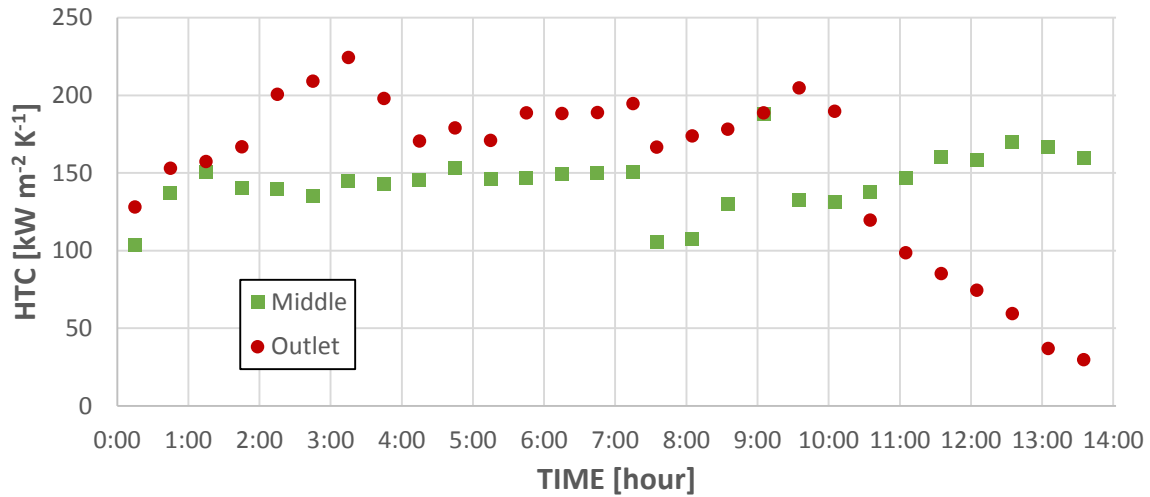
By comparing the absorption spectra obtained from the sample before and after the heat exchange tests, it can be observed that substantially there is no clear variation of the structure due to reactions with water; moreover, the comparison is complicated because, due to the action of the steam, there is a variation in the surface roughness and a partial oxidation of the aluminum underlying the film which influences the absorbance of the substrate. The most important information, however, provided by the IR measurement, is that the presence of methyl groups is confirmed even after the heat exchange test. The coating thickness has been evaluated with AFM, since ellipsometry cannot be applied to the coatings after the condensation tests. The measured value from the top of the layer to the aluminum surface is around 60 nm, way much lower than that measured before the condensation tests (see paragraph 3.2.1.2.1), thus seems that the coating, besides breaking with holes, gets thinner and thinner due to the vapor shear stress/condensate shear. Through EDX measurement (Table 5.8), the concentration of the different atomic species was analyzed between the inlet and the outlet part of the

post-implant sample in order to have a rough estimate of how the film had been removed during the condensation. Considering the constant aluminum value (due to the substrate) and relating it to silicon (mainly deriving from the film Sol-Gel) it was possible to estimate the reduction of the film between the inlet and the outlet. The outlet position resulted to be thinner than the inlet one, as it was expected from the videos, the contact angles measurements and SEM analysis.

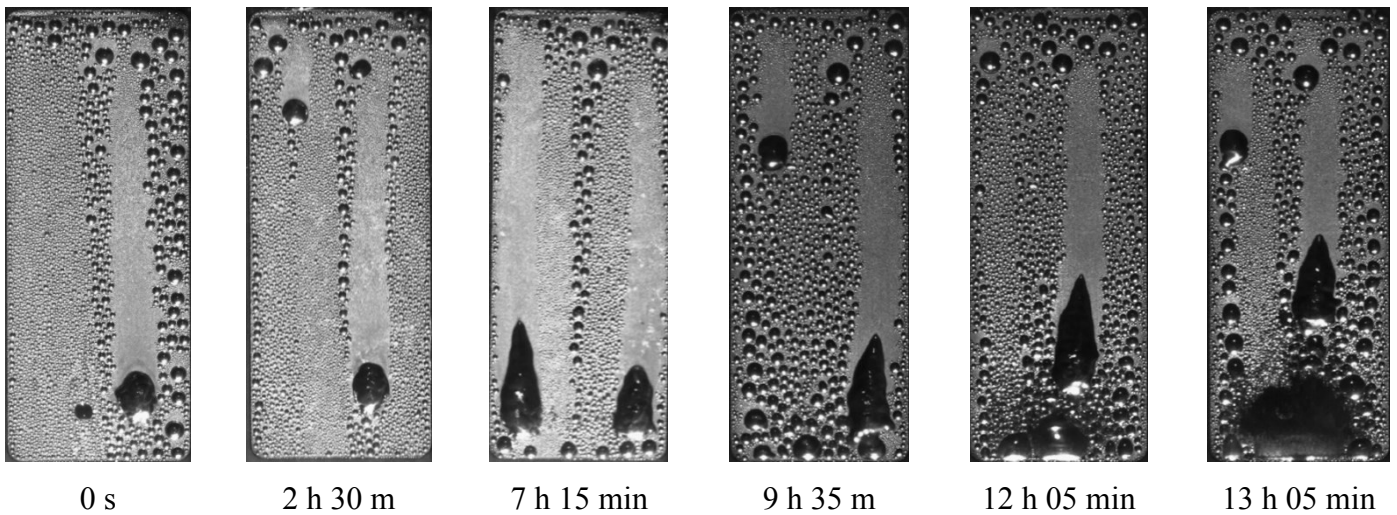
**Table 5.8 - EDX measurement at the inlet and at the outlet position after condensation test on M7T3\_200.**

Element	M7T3_200 inlet		M7T3_200 outlet		Film loss %
	Weight %	Atomic %	Weight %	Atomic %	
Al	22,2	16,3	25,6	19,1	
Si	33,0	23,3	32,1	23,0	15,8

Furthermore, a low-angle XRD measurement was performed to determine the composition and the crystal structure of the complexes that grow from the aluminum substrate after the film has been removed (see Figure 5.9). From the comparison with the database it has been found that the structures grown in the holes of the film are of  $\text{Fe}_3\text{Al}_2(\text{SiO}_4)_3$  (JCPDS Card: 85-2498) that is a compound that incorporates both the elements of the substrate (aluminum with traces of iron and silicon) and of the coating. In Figure 5.10, the HTC trends are reported versus time for two different positions: the middle and the outlet. The tests are performed with a constant heat flux of  $130 \text{ kW m}^{-2}$  and vapor velocity equal to  $2.6 \text{ m s}^{-1}$ . The flooding of the surface is delayed of about 7 times as compared to Figure 5.7, where the heat flux was three times higher. The degradation (Figure 5.11) presents the same behavior of those reported in Figure 5.6 and Figure 5.8: pure DWC, for about 7 hours, DWC with elongated droplets, until 9 hours, and flooding of the outlet position, after about 14 hours. The effect of the flooding of the surface affects the thermodynamic measurements only after 9 hours when the  $\Delta T$  measured at the outlet starts to increase and consequently the respective HTC starts to decrease (Figure 5.10). As reported previously, the two factors that can actually degrade a coating are the shear stress of the vapor and the friction of the condensate flow on the surface: both can interact with the surface mechanically, but also they can interact chemically. All data reported in Figure 5.7 are obtained with a heat flux equal to about  $400 \text{ kW m}^{-2}$ , in Figure 5.10 the tests are performed with a heat flux equal to  $130 \text{ kW m}^{-2}$ ; the vapor velocity is the same ( $2.6 \text{ m s}^{-1}$ ). With such low heat flux, the condensate mass flow rate on the surface will be reduced as it is reduced the amount of the heat exchanged. Seeing an increase of the coating life, it seems that the series MxTy is mostly affected by the friction of the condensate flow instead of the vapor shear stress.



**Figure 5.10 - Time trend of HTC measured at the middle and outlet position. Heat flux exchanged equal to 130 kW m<sup>-2</sup>.**



**Figure 5.11 - Time evolution of M7T3\_200 coating on aluminum. Heat flux exchanged equal to 130 kW m<sup>-2</sup>.**

### M7T3\_300

With this synthesis three samples were made: the first with a single coating layer, the second with two layers in which after the first deposition a heat treatment of 60°C was performed and the third with two layers both treated at 300°C. In Figure 5.12 the HTC evolution over time measured on M7T3\_300 (single layer) is reported for each position (inlet, middle and outlet), calculated as reported in Chapter 4. The trend of the local HTC is different for each position, if for about 30 minutes they are almost constant, after that they diverge with different slopes. The HTC measured at the inlet and at the middle increases over time, the middle reaches a maximum value after 1 hour and 30 minutes from the beginning of the test and then starts to decrease. The outlet, instead, has a decreasing trend for all the 3 hours of the experimental campaign. The heat flux is about 400 kW m<sup>-2</sup>. In Figure 5.13, DWC images recorded with the high-speed camera are shown and it is possible to see how the degradation of the surface occurs.



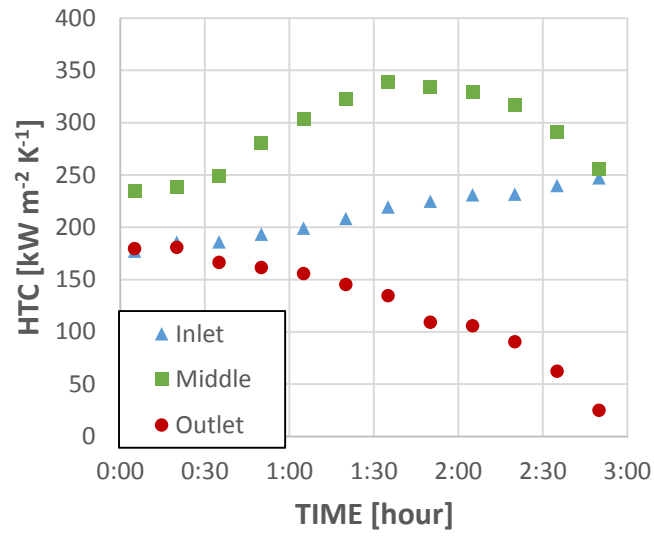


Figure 5.12 - Time trend of HTC measured at the middle and outlet position of M7T3\_300 (single layer).

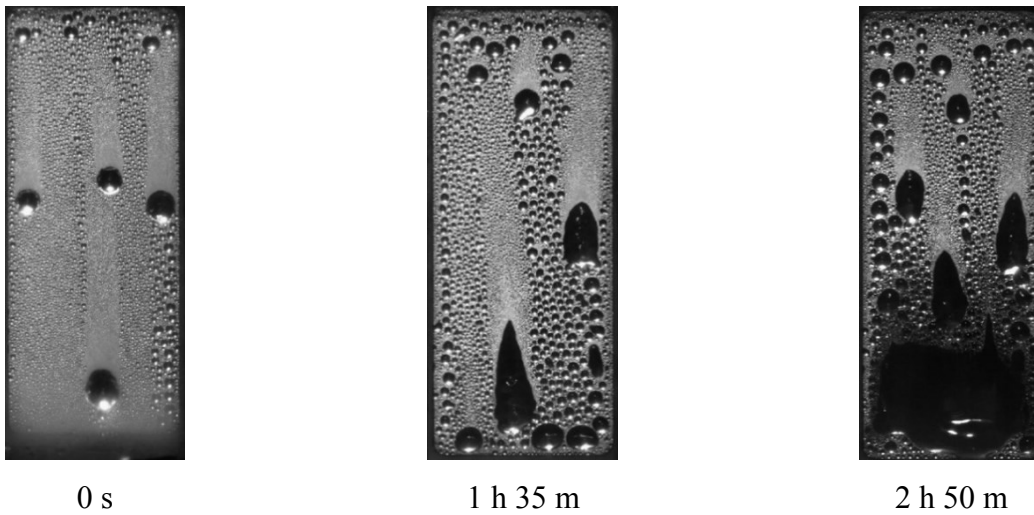


Figure 5.13 - Time evolution of M7T3\_300 coating (single layer) on aluminum.

Table 5.9 - M7T3\_300 (single layer) surface characterization after condensation tests.



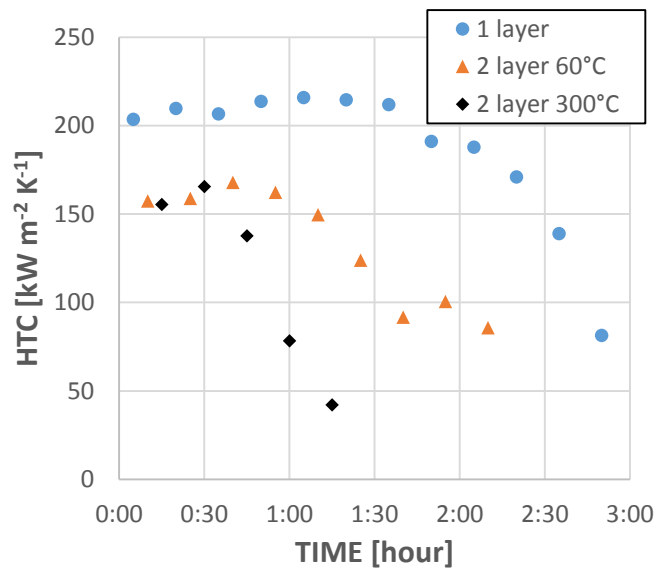
Parameter	Technique	Measurement	Value
$\theta_a$	Sessile drop method		$63^\circ \pm 3^\circ$
$\theta_r$	Sessile drop method		$22^\circ \pm 6^\circ$

Table 5.9 shows the contact angle measurement done on M7T3\_300 and, as for the previous coatings, the receding contact angle is the angle most affected by the condensation test. In Figure 5.13 the HTC measured on the three samples (1 layer, 1 layer 60°+ 1 layer 300°, 2 layer 300°) is reported. The values are very similar, but as regards the duration seems that decrease with the increasing of the layers number. This behavior can be explained by remembering what is explained in Chapter 3 about the baking treatment of sol-gel. When a film is heated up and cooled, tensions are created within it due to the different coefficient of thermal expansion as compared aluminum. These tensions, if they are not properly relaxed, increase as the thickness of the film and the number of layers increases. It is assumed that the intermediate heating processes at 60 ° C and 300 ° C are not enough to relax the residual stresses and this leads to an easier cracking of the film and therefore to a shorter duration during the tests.



**Figure 5.14 - Time trend of HTC measured on M7T3\_300: 1 layer, 1 layer 60°+ 1 layer 300°, 2 layer 300°.**

### M7T3\_400

In Figure 5.15 the time trend of HTC measured on M7T3\_400 is reported. The heat flux is always around 400 kW m<sup>-2</sup> as for the previous coatings. The behavior of such treatment is very similar to those obtained with different baking temperature as can be seen comparing Figure 5.16 and Figure 5.12. A detailed analysis is reported in Chapter 6.

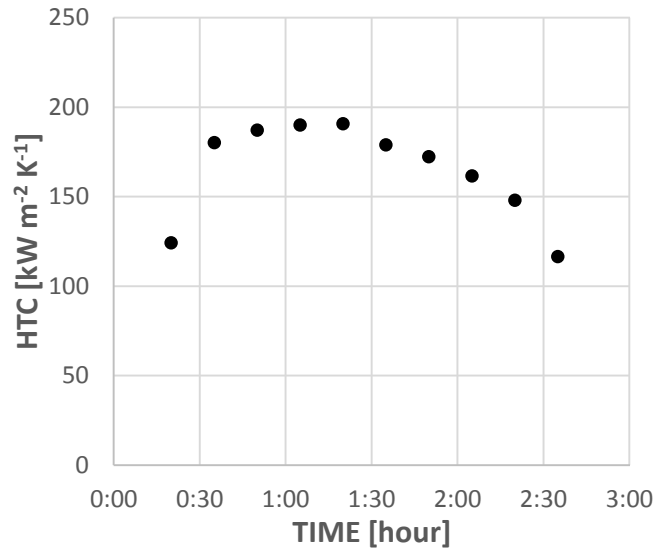
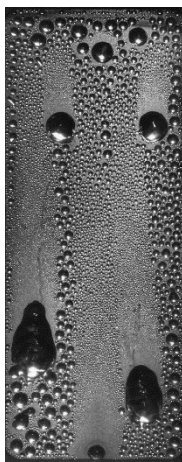
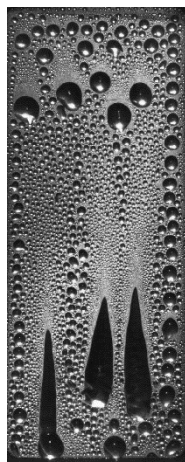


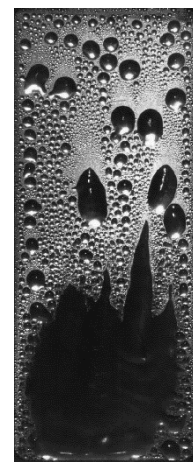
Figure 5.15 - HTC versus time for M7T3\_400 coating.



35 min



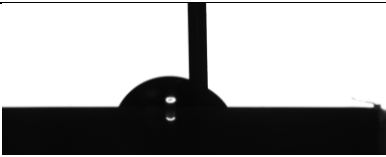
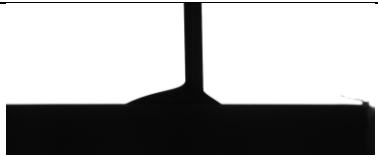
1 hours 35 min



2 hours 35 min

Figure 5.16 - Time evolution of M7T3\_400 coating on aluminum.

Table 5.10 - M7T3\_400 surface characterization after condensation tests.

Parameter	Technique	Measurement	Value
$\theta_a$	Sessile drop method		$51^\circ \pm 7^\circ$
$\theta_r$	Sessile drop method		$16^\circ \pm 3^\circ$

### 5.2.2.3 PxTy series

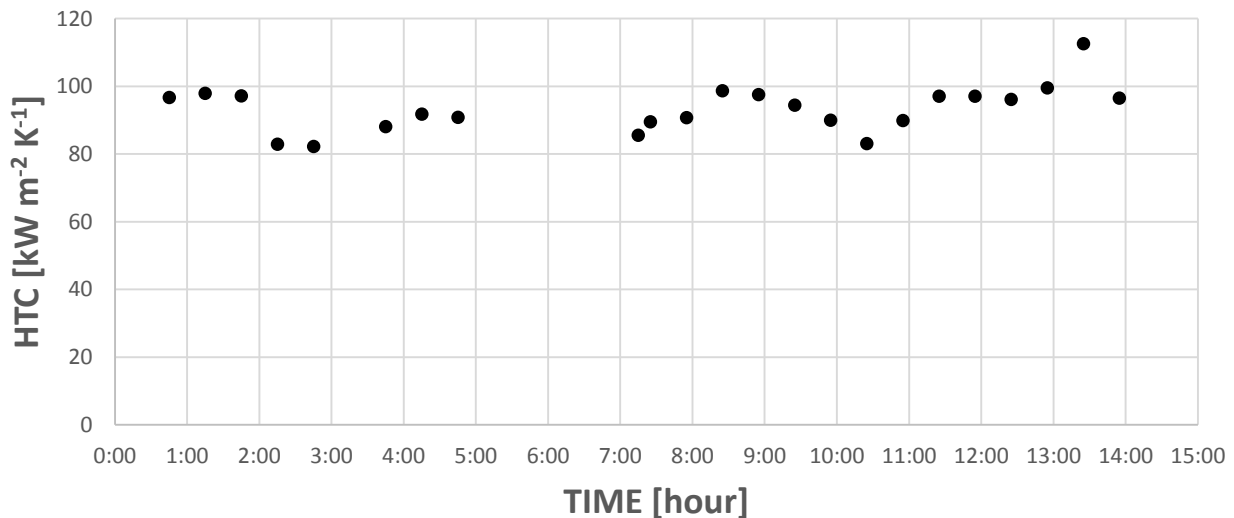
The PxTy series includes different combination of precursors PhTES and TEOS treated at different temperatures. All the combinations are summarized in Table 5.11.

**Table 5.11 - PxTy series.**

Sample	Name	% TEOS	% MTES	% PhTES	Baking Temp.	Dipping Vel.
Al	P7T3_200	30	/	70	200	4,8 cm min <sup>-1</sup>
Al	P7T3_400	30	/	70	400	4,8 cm min <sup>-1</sup>

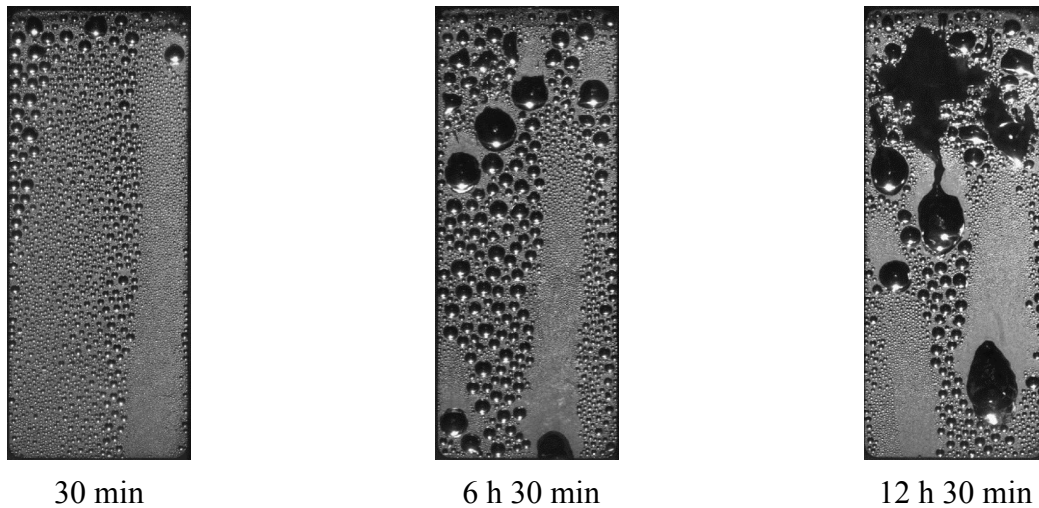
#### P7T3\_200

In Figure 5.17, the HTC versus time is reported for the P7T3\_200 sample. The substitution of MTES with PhTES led to a big extension of the DWC life, from about two hours up to 14 hours. On the other hand, the HTC dropped from 200 kW m<sup>-2</sup> K<sup>-1</sup> to 120 kW m<sup>-2</sup> K<sup>-1</sup>, consistently with the thicknesses measured before the condensation tests for the two sample (see Chapter 3). Looking at the HTC trend in Figure 5.17, even if a small decrease can be noticed with the passing time, there is not a similar performance drop as reported in Figure 5.7 for M7T3\_200. Since after 14 hours about 10% of the surface was flooded (see Figure 5.18), the test had been stopped.

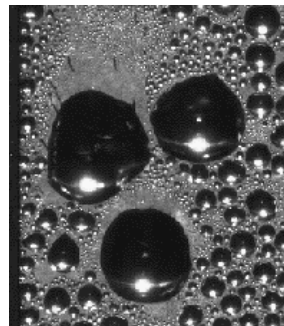


**Figure 5.17 - HTC versus time for P7T3\_200 on aluminum substrate.**

In Figure 5.18, the degradation mode can be appreciated. This type of treatment starts to be ruined from the inlet part and not from the outlet part as happen on the series MxTy. A zoomed images of the surface shows the start of the flooding (Figure 5.19). When a droplet passes through a specific area, instead of leaving everything cleared, it leaves some liquid stripes or channels. With the passing time, the channels increase in size and they become interconnected.



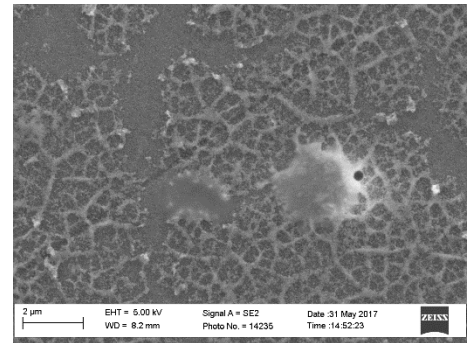
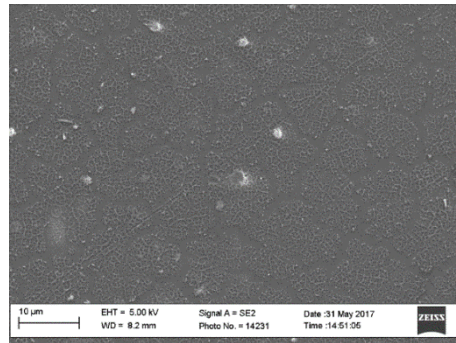
**Figure 5.18 - Time evolution of P7T3\_200 coating on aluminum.**



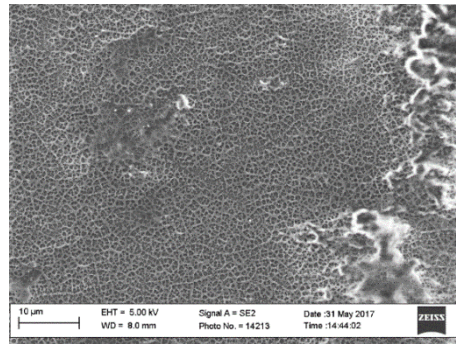
**Figure 5.19 - Zoomed image of the start of degradation of P7T3\_200.**

SEM campaign has been done on the sample after the condensation test in order to get an insight on the degradation development (Figure 5.20). The coating presents a complex porous 3D network all along the surface, more packed at the outlet. In fact, at the inlet position the network is not continuous and homogenous like the other two positions: it is broken randomly with channels. The channels represent the zone where the layer is vanished from the surface and they can be related to the channels seen macroscopically in Figure 5.19. A zoomed image of the coating at the inlet position permits to distinguish a scratch belonging to the aluminum surface partially covered by the coating and partially exposed. As reported in the previous paragraph, the mechanical degradation causes can be due to the vapor shear stress and/or the condensate friction. Since this coating is more ruined in the inlet position, seems that in this case is the vapor shear stress that plays a crucial role in the layer life. The chemical cause, reaction between the hot vapor and the layer, may play a role, but should be homogenous along the sample, since the vapor conditions do not change along the test section.

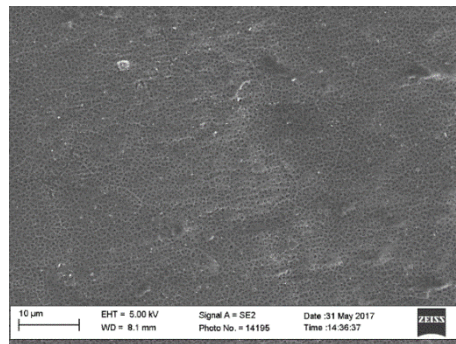
INLET



MIDDLE

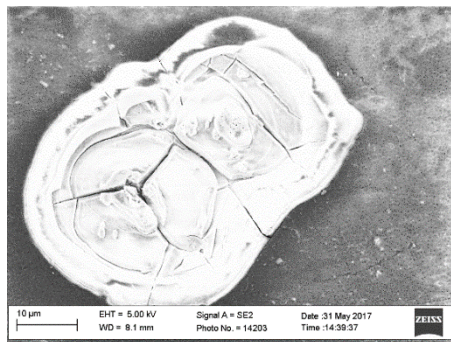


OUTLET





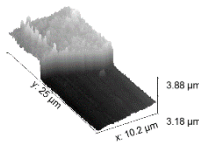
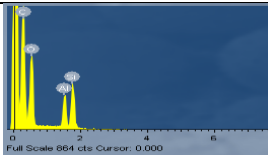
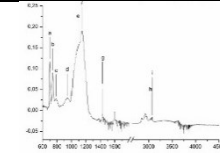
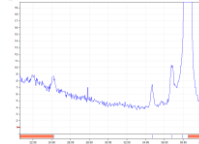
**Figure 5.20 - SEM analysis at three different positions along the aluminum substrate: inlet, middle and outlet (for the positioning refer to Chapter 4). A zoomed image of the surface is also showed.**

In analogy to the previous cases, protuberances with a bulbar form have been observed randomly distributed along the surface (Figure 5.21), the analysis of these structures is done through XRD (Table 5.12). From the measurement it is inferred that the protuberances are composed of aluminum oxide.



**Figure 5.21 - Aluminum oxide formation on the sample.**

**Table 5.12 - P7T3\_200 surface characterization after condensation tests.**

Parameter	Technique	Measurement	Value
$\theta_a$	Sessile drop method		$91^\circ \pm 4^\circ$
$\theta_r$	Sessile drop method		$37^\circ \pm 11^\circ$
Coating thickness	AFM		$\approx 90$ nm
Surface morphology	SEM	\	\
Coating composition	EDX		\
Coating composition	FT-IR		\
Surface composition	XRD		\

The contact angle measurement shows how the dynamic contact angles are changed by the condensation test. Whereas the receding contact angle is decreased, the advancing one is increased. Looking at Figure 5.20, where the SEM analysis shows a very rough surface, and remembering Wenzel equation (see Chapter 2) the phenomenon can be explained. Briefly, the advancing contact angle increases on rough surfaces if the surface wettability does not change and this is the case. As for M7T3\_200, AFM has been used for the measurement of the coating thickness which resulted equal to 90 nm, one third thick of the original coating. Regarding FTIR analysis, there are not substantial differences between before and after tests, proving the stability of such coating from a chemical point of view. The film lost, measured by EDX, between the DWC zone (outlet position) and the FWC zone (inlet position) is around 41 % (Table 5.13). The loss is greater than the loss measured on M7T3\_200 as can be expected from SEM images. The pictures of the two zones (FWC

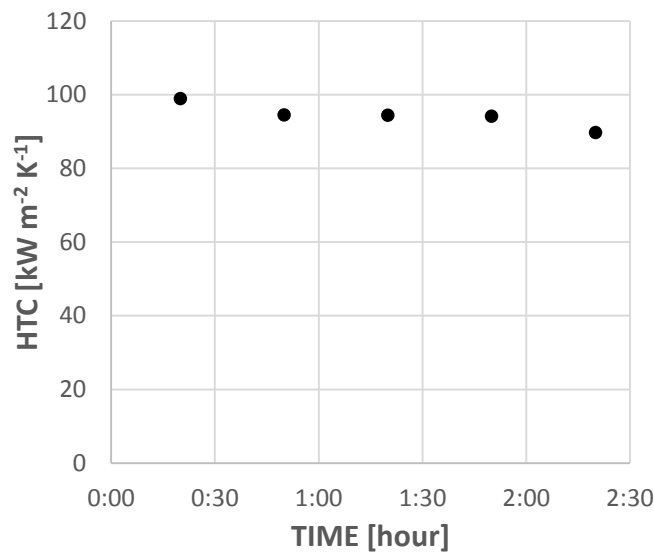
and DWC) in P7T3\_200 display a substantial difference, in the FWC zone the coating barely covers the aluminum substrate.

**Table 5.13 - EDX measurement at the inlet and at the outlet position after condensation test on P7T3\_200.**

Element	P7T3_inlet		P7T3_outlet		Film loss %
	Weight %	Atomic %	Weight %	Atomic %	
Al	19,6	12,2	12,7	7,7	
Si	22,0	13,2	24,0	14,0	40,6

**P7T3\_400**

As for the MxTy series, the higher baking temperature tested is 400°C. The time evolution of HTC and of the coating are displayed in Figure 5.22 and Figure 5.23. The heat exchanged is always around 400 kW m<sup>-2</sup>. In this case, the coating lasted only around 2 hours and half. A lower robustness confirms what was observed in the previous paragraph. To an increase in the heat treatment temperature correspond a marked decrease in the lifetime of the coating. This effect is probably due to the greater rigidity of the silica network due to a greater cross-linking of the coating.



**Figure 5.22 - HTC versus time for P7T3\_400 on aluminum substrate.**

Since the performance of such treatment is much lower than the one treated at 200°C, the influence of the temperature on P7T3 has not been extended.



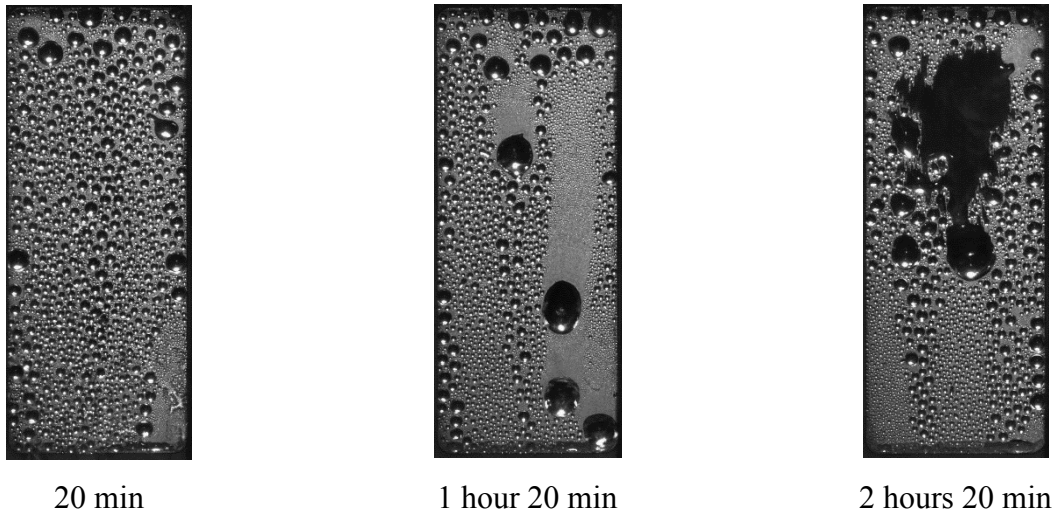
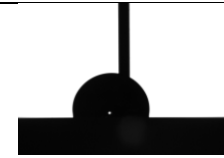



Figure 5.23 - Time evolution of P7T3\_400 coating on aluminum.

Table 5.14 - P7T3\_400 surface characterization after condensation tests.

Parameter	Technique	Measurement	Value
$\theta_a$	Sessile drop method		$51^\circ \pm 7^\circ$
$\theta_r$	Sessile drop method		$16^\circ \pm 3^\circ$

#### 5.2.2.4 PxMy series

The PxMy series includes different combination of precursors PhTES and MTES treated at different temperatures. All the combinations are summarized in Table 5.15.

Table 5.15 - PxMy series.

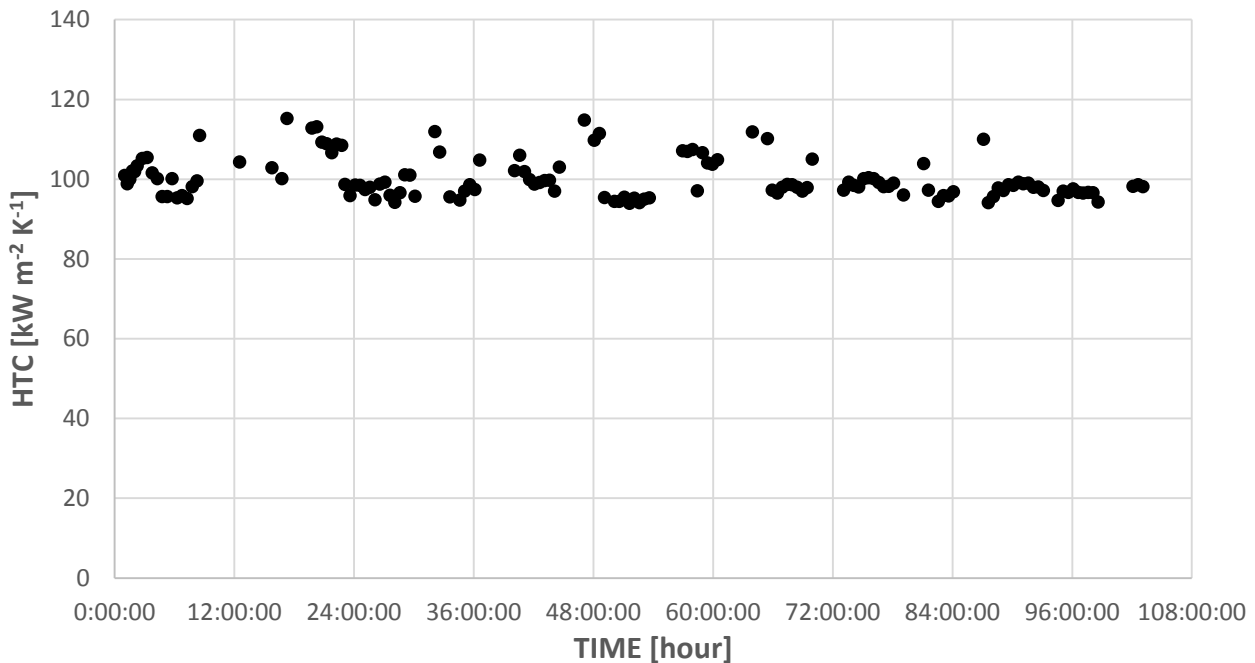
Sample	Name		% TEOS	% MTES	% PhTES	Baking Temp.	Dipping Vel.
Al	P7M3_200		/	30	70	200	4,8 cm min <sup>-1</sup>
Al	M7P3_200		/	70	30	200	4,8 cm min <sup>-1</sup>

As can be seen from the degradation reports done on the series MxTy and PxTy (Figure 5.9 and Figure 5.20 respectively), the coatings degrade in two opposite mode: the first starts to flood at the outlet and the other at the inlet. Even if the causes of the degradation are not clear, more experiments should be done especially on PxTy series, the condensation tests conditions affect the coatings in two

different ways. Combining the properties of PxTy and MxTy should improve the robustness of such coatings, compensating for the shortcomings of one in the other.

### P7M3\_200

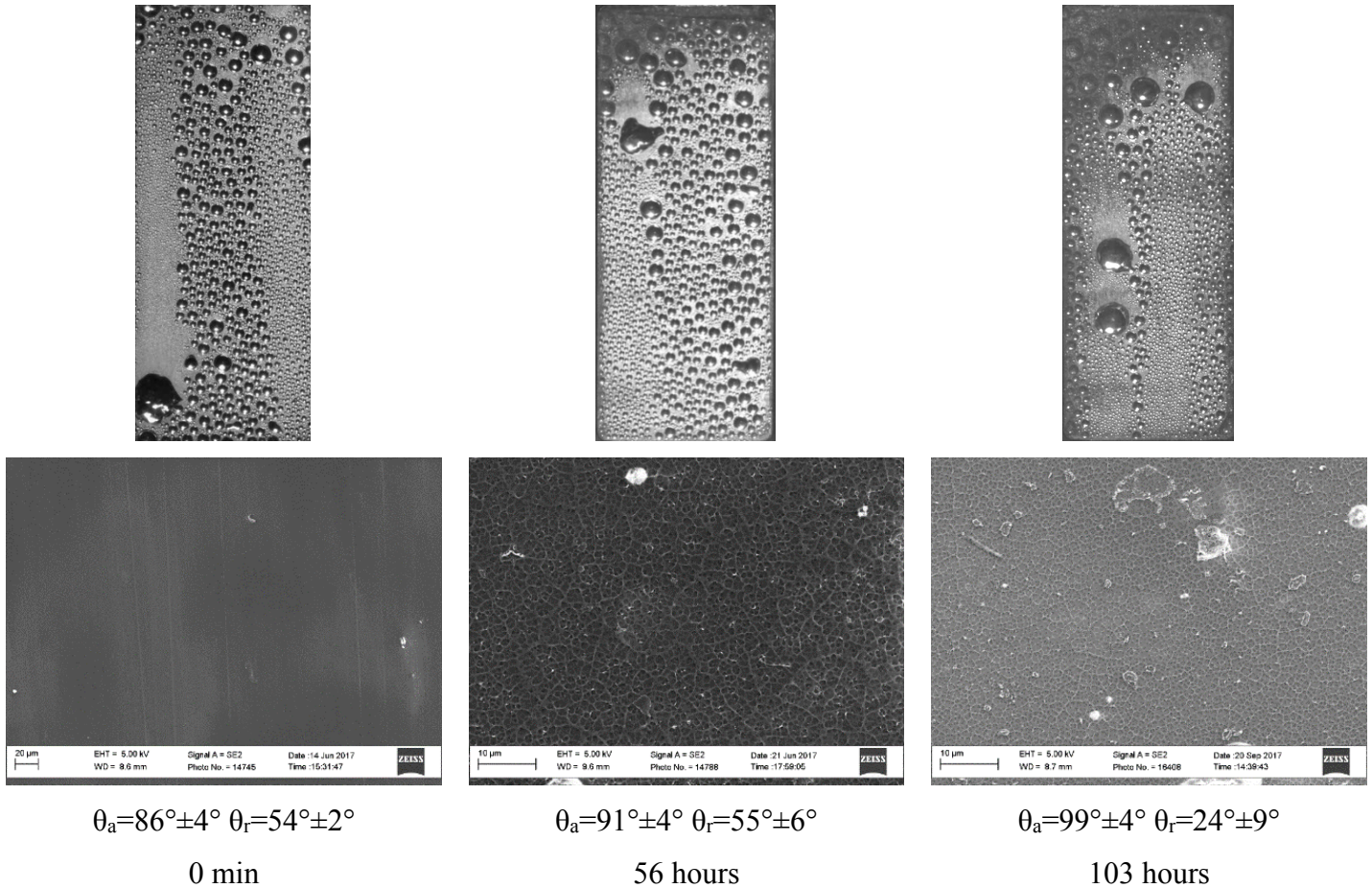
The HTC trend with the passing time is reported in Figure 5.24. The heat exchanged is always around 400 kW m<sup>-2</sup>. The endurance against condensation tests has been deeply improved, exceeding 100 hours of testing. It has to be underlined that the test is not stopped for the flooding of the surface, as shown in Figure 5.25, but for other research needs of the experimental apparatus. The real lifetime of such coatings is not known yet.



**Figure 5.24 - HTC versus time for P7M3\_200 on aluminum substrate.**

In Figure 5.25, the time evolution of P7M3\_200 is reported. The sample was taken off from the test section at the middle (after 56 hours) of the experimental campaign in order to assess the degradation progress on the coating. Both SEM analysis and contact angle measurements have been done on the sample after 56 hours and after 103 hours. SEM images show that the surface changes during vapor condensation, the porous 3D network appeared on the sample is very similar to the one saw in P7T3\_200 (Figure 5.20). Between, 56 and 103 hours there is not a substantial morphological difference, the coating seems to get thinner, since some aluminum features can be observed. The contact angles, instead, whereas remain constant after 56 hours of tests, they start to change after 103 hours. The behavior of the advancing and the receding angles is similar to that found on P7T3\_200. Some characteristic of the coating is changed after 103 hours thus the coating will not endure much more, however the sample should be led to flooding. It is interesting to notice that HTC values measured after couples of hours, 95 kW m<sup>-2</sup> K<sup>-1</sup>, remain after 103 hours, 98 kW m<sup>-2</sup> K<sup>-1</sup>. In Figure

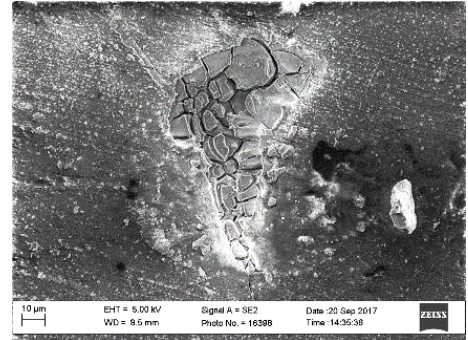
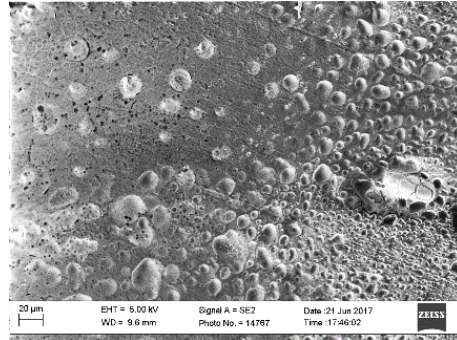
5.26 different SEM magnifications are reported for different zones after 6 and 103 hours. Besides inlet, middle and outlet which are the classical investigated areas, also the upper left corner is reported. As can be seen from Figure 5.25, it seems that a darker area spreads from that corner to the other areas.



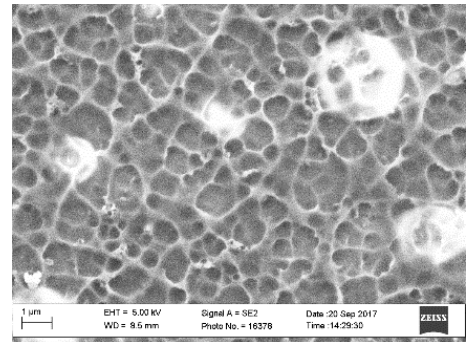
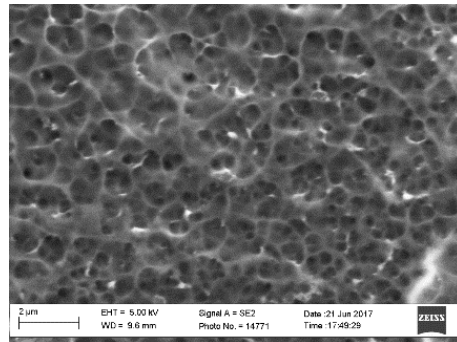
**Figure 5.25 - Time evolution of P7M3\_200 coating on aluminum. SEM images and contact angle measurements are reported for each time-step.**

The sample presented boundary defects before the test session due to the shrinkage of the treatment during the baking process. Those defects gave the start for the degradation as can be seen from Figure 5.25. The SEM shows the surface completely ruined even after 56 hours in the corner, moreover after 103 hours with very big defects of the layer. However, the aluminum surface seems not be exposed to the vapor, since the aluminum oxide features which grow after the exposure are not developed. It is well-known that aluminum reacts with hot steam<sup>102,212,244</sup> as also reported in Figure 5.1. In the other regions, the layer is continuous and homogenous. Looking at the images taken after 56 hours, small differences can be noticed from the inlet to the outlet. The inlet zone seems to be more porous than the outlet, which can be an indicator that the flooding can start from that region as for P7T3\_200. After 103 hours, the coating starts to be more porous all along the sample, showing some white protuberances with a bulbar form in analogy to the previous cases meaning that the coating is enough porous to let the vapor reach the aluminum.

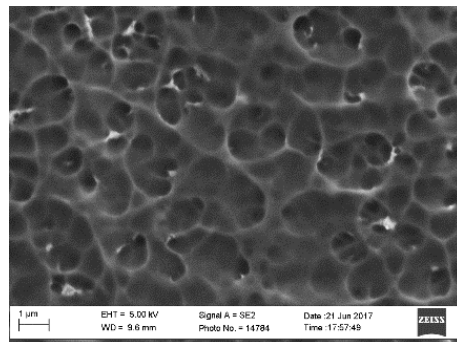
CORNER



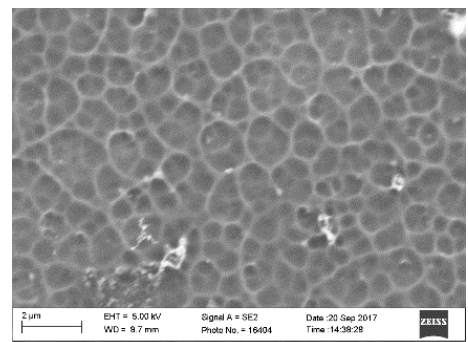
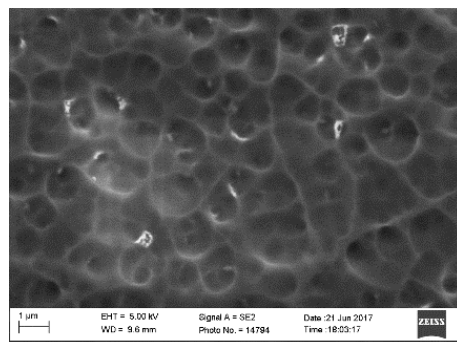
INLET



MIDDLE



OUTLET



56 hours

103 hours

**Figure 5.26 - SEM analysis at four different positions along the aluminum substrate: corner, inlet, middle and outlet (for the positioning refer to Chapter 4). The analysis has been performed after 56 and 103 hours after condensation tests.**

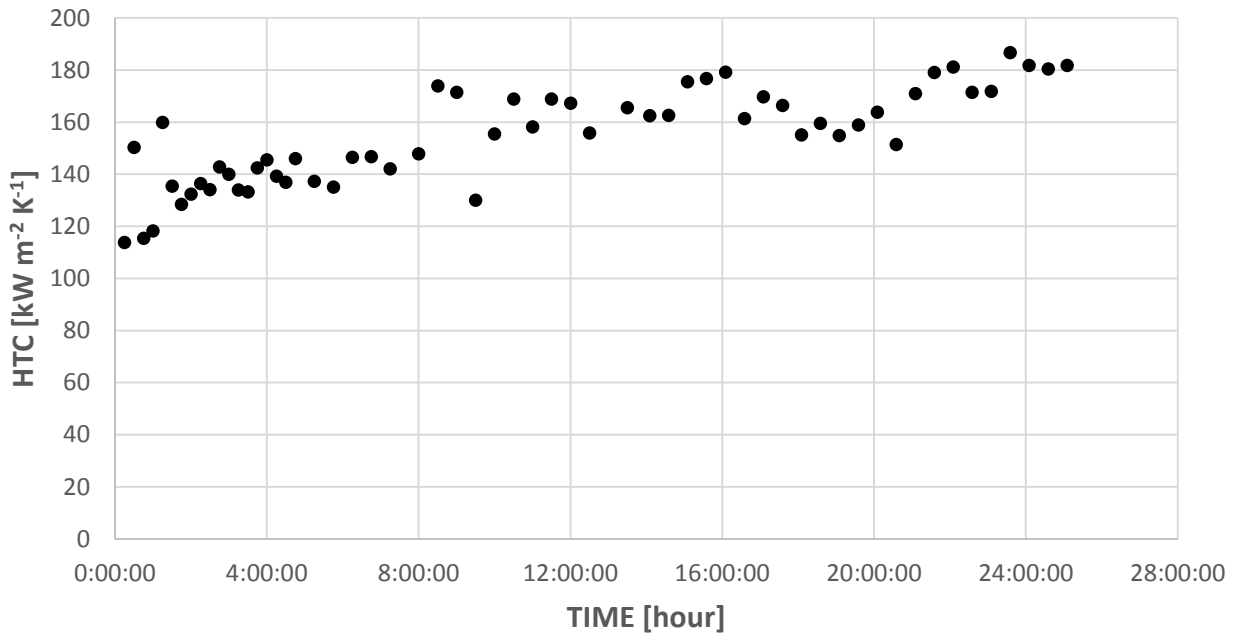
EDX measurement was also performed after 56 hours in order to determine, as in the previous cases, which is the thinner part of the sample. Table 5.16 shows that the inlet part is the most thinner as expected.

**Table 5.16 - EDX measurement at the inlet and at the outlet position after 56 hours of condensation test on P7M3\_200.**

Element	P7M3_inlet		P7M3_outlet		Film loss %
	Weight %	Atomic %	Weight %	Atomic %	
Al	13,4	8,1	9,2	5,4	
Si	23,2	13,5	23,7	13,3	32,4

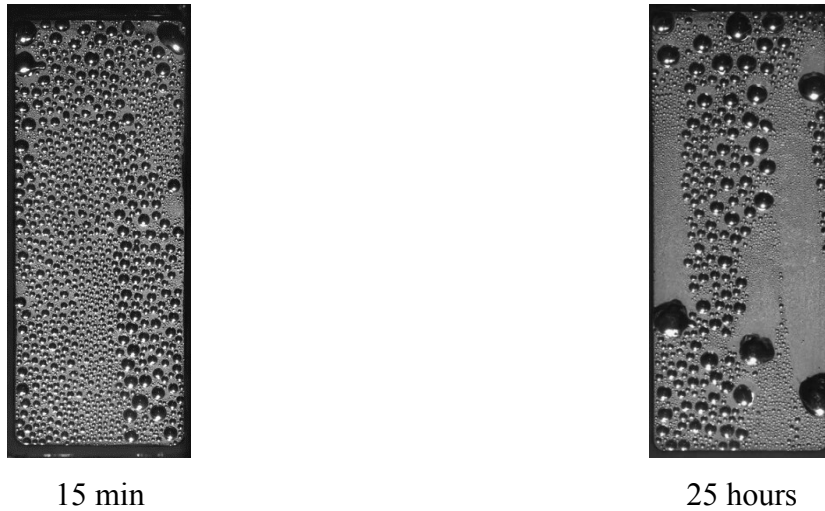
**M7P3\_200**

Here the results obtained on the sample specular to the previous one are presented. In Figure 5.27, the HTC versus time is showed and in Figure 5.28 the images taken at the start and at the end of the condensation test. As for P7M3\_200 the test is not stopped for the flooding of the surface, but for the need of doing other tests. The HTC trend seems to be slightly increasing, but during the first stages of the test is difficult to reach a steady state due to the absence of pumps in the test rig. The first points are affected by the instabilities of the tests. The average HTC is equal to  $160 \text{ kW m}^{-2} \text{ K}^{-1}$  for a heat flux of about  $400 \text{ kW m}^{-2}$ .



**Figure 5.27 - HTC versus time for M7P3\_200 on aluminum substrate.**

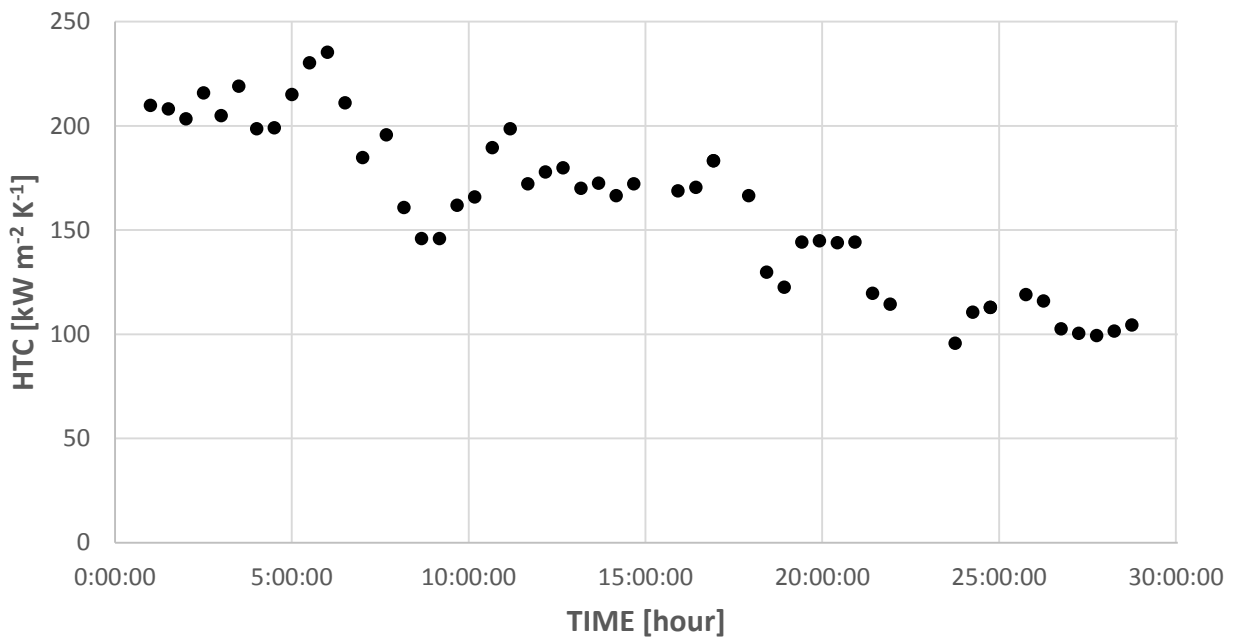
After 25 hours, there are no signs of degradation, meaning that the mixture of MTES and PhTES can be further investigated for achieving very good results in term of durability. This coating is used for the vapor velocity tests, since it is assessed that is not affected by the vapor flow at least for 25 hours.



**Figure 5.28 - Time evolution of M7P3\_200 coating on aluminum.**

#### 5.2.2.5 Graphene coating

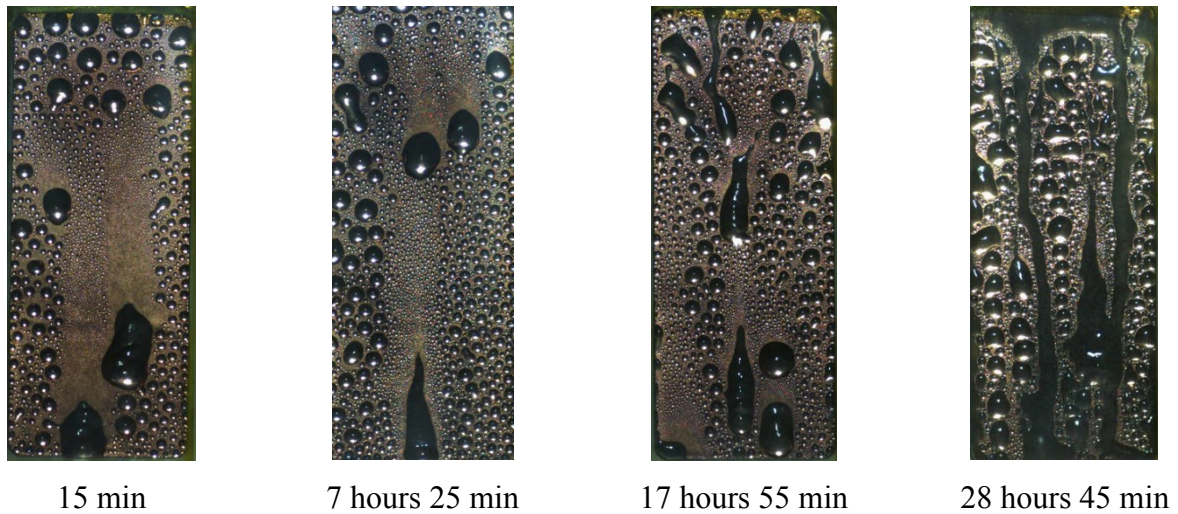
The condensation test on graphene coatings could be done only on copper substrate. The graphene can be deposited and synthesized on aluminum substrate, but the adhesion is too weak to sustain this type of tests. In Figure 5.29 the HTC trend is reported over time for a heat flux equal to  $420 \text{ kW m}^{-2}$ .



**Figure 5.29 - HTC versus time for graphene coating on copper substrate.**

The HTC clearly decreases with the passing time, coherently with the images reported in Figure 5.30. The condensation mode is pure DWC for only few hours, then the droplets start to be elongated (after 7 hours) and, progressively, the surface starts to be partially flooded and with very irregular droplets

(after 28 hours). The graphene layer was not so homogenous even before the condensation test, more efforts are needed in the solution and deposition stage of the process.



**Figure 5.30 - Time evolution of graphene coating on copper.**

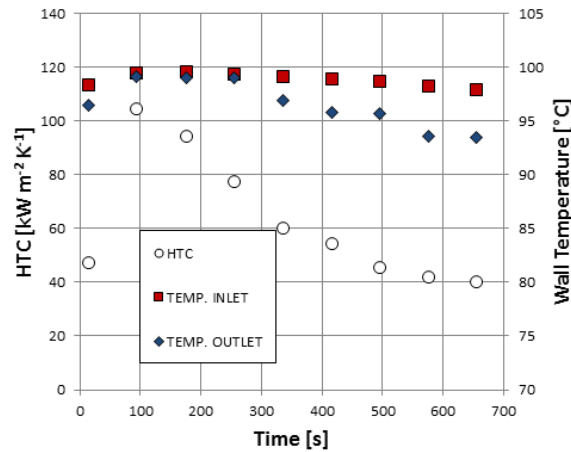
Furthermore, a color variation can be noted. Before the condensation test the surface was the typical color of the mirror-polished copper, after the test it becomes dark orange, as the copper oxide. Probably, during the condensation tests the surface has been slightly degraded, creating defects in the coating. These defects act as privileged zones for the passage of vapor molecules through the coating. The steam, then, interacts with the copper oxidizing it and making it hydrophilic<sup>245-247</sup>. The contact angle measurement leads to  $\theta_a=84^\circ\pm 9^\circ$   $\theta_r\approx 0^\circ$ , where, again, the receding contact angle which is nullified and corresponds to the change in the condensation mode. Such coating, besides the mediocre results, remains an excellent path to follow for a robust coating for a sustained DWC.

#### 5.2.2.6 Superhydrophobic surfaces

In paragraph 3.3 all the superhydrophobic surfaces developed during this work are presented. The surfaces are prepared with two main techniques: the wet chemical etching and aerogel. Since aerogel did not endure in the experimental apparatus, probably because it was not sufficiently anchored to the surface, results obtained on that treatment are not reported in this Section. Please refer to paragraph 3.3.1 for the sample characterization before the condensation test.

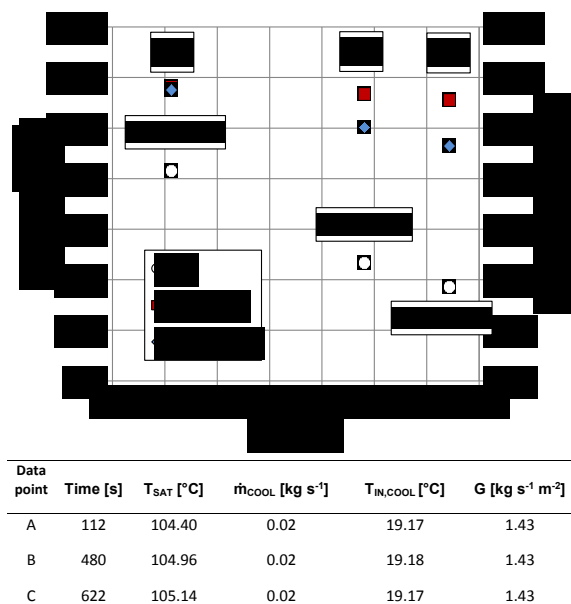
#### Sample #1

In this section, the experimental results acquired over the Sample #1 are reported. In Figure 5.31 the HTC and the wall temperatures measured within the specimen versus time are reported. The two wall temperatures are referred to two different axial positions along the flow of the steam, one closer to the inlet and one closer to the outlet.



**Figure 5.31 - Trend of the heat transfer coefficient and wall temperatures vs. time during pure steam condensation over the Sample #1. Experimental input parameters:  $G=1.4 \text{ kg m}^{-2} \text{ s}^{-1}$ ,  $T_{\text{SAT}}=105^{\circ}\text{C}$ ,  $\dot{m}_{\text{COOL}}=0.02 \text{ kg s}^{-1}$  and  $T_{\text{IN,COOL}}=19.2^{\circ}\text{C}$ .**

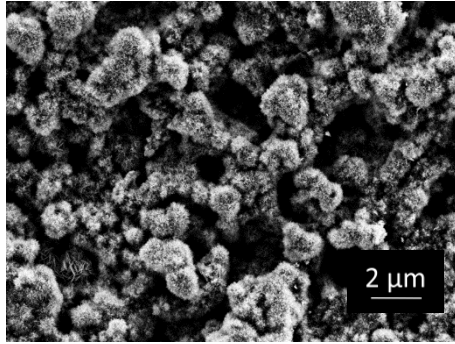
From Figure 5.31 it is clear how the HTC decreases fast over time, during which there may be the transition from a DWC to a FWC. This transition is suggested by the fact that the difference between the two wall temperatures (inlet and the outlet wall temperatures) increases with time. This could be associated with the loss of the superhydrophobic characteristics of the surface, which leads to the formation of a water film along the sample. It is interesting to notice that HTC higher than  $100 \text{ kW m}^{-2} \text{ K}^{-1}$  at  $3.5 \text{ K}$  wall subcooling was measured at  $100 \text{ s}$  and it results about 8 times higher compared to HTC during film condensation on the untreated aluminum sample<sup>44</sup>. In Figure 5.32 the values of HTC,  $T_{\text{WALL}}$  and  $\Delta T$  are reported for three operating conditions (A, B, C). As can be seen in Figure 5.34, condition A corresponds to pure DWC while the two points B and C are referred to hybrid condensation mode.



**Figure 5.32 - HTC and wall temperatures versus time during condensation over the Sample #1. The operating conditions are listed in the table. The point A refers to the images in Figure 5.34a and b, the point B refers to the images in Figure 5.34c and d.**

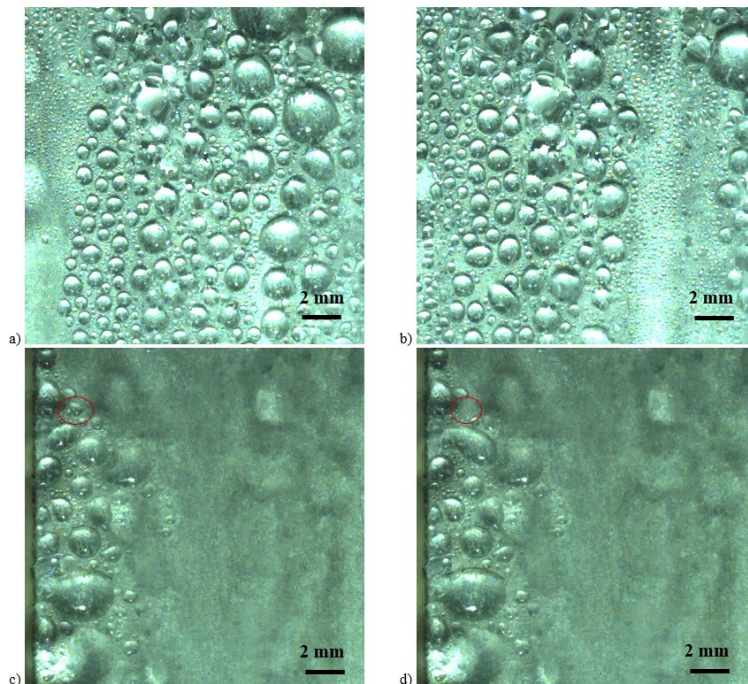


The table of Figure 5.32 reports the main parameters associated to the three points A, B and C. The values reported in the graph for each point are obtained as the average of 40 readings. By comparing the three operating conditions A, B and C, it can be seen from the table that the inlet temperature of the coolant and the saturation temperature do not vary which means that the variation of the surface temperature, and thus the variation of the driving temperature difference  $\Delta T$ , must be explained as the effect of a change in the condensation process itself. As depicted in Figure 5.32, the temperature difference ( $\Delta T$ ) increases from point A to point C. This can be explained by looking at the two temperature measurements at the wall (temperature at inlet and outlet, measured at 1 mm depth). In the case of condition A, the inlet and outlet temperatures display the same value, while for the data points B and C these temperatures differ by more than 10 K. Therefore it can be concluded that, in the conditions B and C, the condensation thermal resistance increases along the steam flow and this is due to the presence of a liquid film that grows from inlet to outlet. The same mechanism of flooding during steam condensation was previously observed by Del Col *et al.*<sup>44</sup> on a hydrophobic surface. Figure 5.34 shows different images taken by the high speed camera during condensation over the Sample #1. In Figure 5.34a and Figure 5.34b it is possible to see the condensation corresponding to the operating condition of point A in Figure 5.32: clearly it corresponds to the mechanism of pure DWC. In this case, the process is a continuous sequence of growth, coalescence and roll-off of droplets. From the images, the shape of the droplets suggest that the contact angle must be lower compared to those measured in open air (Table 3.20) and this may suggest that a Wenzel<sup>33</sup> wetting state is probably occurring here during condensation. After about 5 minutes (Figure 5.34c and Figure 5.34d, corresponding to points B and C of Figure 5.32), some parts of the surface start to be covered by a liquid film and some droplets are absorbed by the liquid film itself. This can be due to the coalescence between the droplet and the film or to the wettability gradient<sup>248</sup>. The images in Figure 5.34c and Figure 5.34d explain that the lower HTC values of points B and C (Figure 5.34) are due to the hybrid condensation occurring in this case. This sample does not exhibit a good durability at the conditions reported in Figure 5.32. A surface characterization has been done also after one hour of continuous vapor condensation. The surface resulted to be completely changed from its initial status (compare Table 3.20 with Figure 5.33).



**Figure 5.33 - SEM image of Sample #1 after one hour of condensation test.**

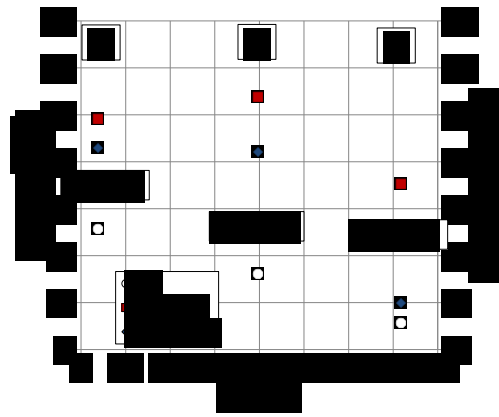
The surface is covered by flower-like features which have been identified as aluminum hydroxides by XRD measurements (see Figure 5.40); aluminum hydroxides are usually formed from the aluminum in contact with boiling water<sup>210</sup>. Furthermore, EDX analysis showed a very low content of fluorine and this is in agreement with the contact angle measurement done after one hour of condensation, displaying very low values of both advancing and receding contact angle ( $< 10^\circ$ ).



**Figure 5.34 - Time-lapse images of DWC over the Sample #1. The images a) and b) correspond to the A point in Figure 5.32; c) and d) refer to the B point in Figure 5.32.**

### *Sample #2*

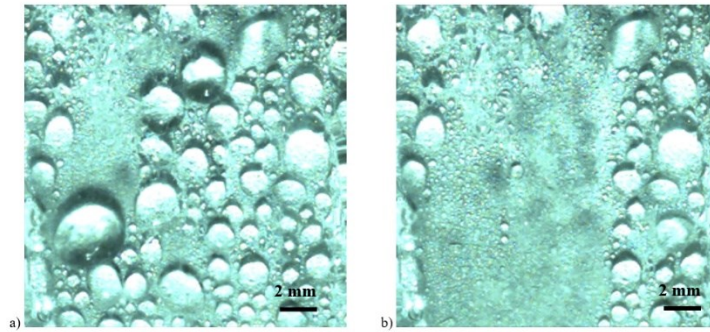
In this section, the experimental data acquired over the Sample #2 is presented. In Figure 5.35 the measured values of HTC,  $T_{\text{wall}}$  and  $\Delta T$  are reported for three operating conditions (A, B and C). Similar to the case of Figure 5.32, the three conditions correspond to pure DWC (point A), and hybrid condensation mode (B and C). This can be inferred from the images of condensation recorded during the tests.



Data point	Time [s]	$T_{SAT}$ [°C]	$\dot{m}_{COOL}$ [kg s <sup>-1</sup> ]	$T_{IN,COOL}$ [°C]	G [kg s <sup>-1</sup> m <sup>-2</sup> ]
A	162	101.77	0.11	24.17	1.41
B	1978	106.66	0.11	24.19	1.41
C	3594	101.19	0.11	24.24	1.47

**Figure 5.35 - Heat transfer coefficient versus time on the Sample #2. The relevant operating conditions are listed in the table.**

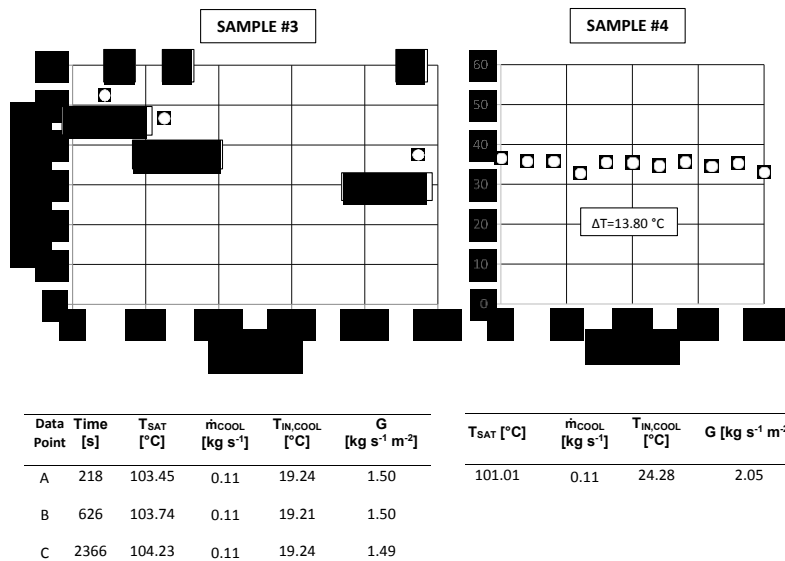
The table in Figure 5.37 reports the characteristic parameters associated to the three operating conditions A, B and C. The values reported for each data point are calculated as the mean of 40 readings, corresponding to 80 seconds of continuous acquisition. The HTC decreases with time and the value measured after 60 minutes (point C) is comparable to the HTC measured over a superhydrophilic surface: this is probably due to the fact that the hydrophobic layer at this point is completely degraded<sup>239</sup>. The wall temperature difference significantly increases from inlet to outlet (Figure 5.37) with the same behavior already observed on Sample #1, indicating the progressive degradation of the substrate. Figure 5.38 shows the condensation occurring over Sample #2 and corresponding to the point A in Figure 5.37. It is a case of pure DWC, where the surface is covered by droplets with variable dimensions: when part of the surface is swept by the falling drop, smaller droplets grow before they reach the dimension to roll off. Moreover, **Figure 5.38** highlights that the shape of the drops does not correspond to the values of contact angle measured in ambient conditions (Sec. 3.1.1). This result is very important for DWC modeling, since contact angles are a fundamental requirements for the implementation of such models<sup>4,26</sup>.



**Figure 5.36 - Time-lapse images of DWC over the Sample #2. The images a) and b) correspond to point A in Figure 5.35.**

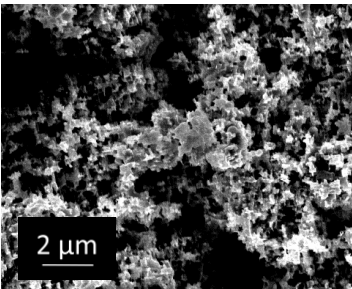
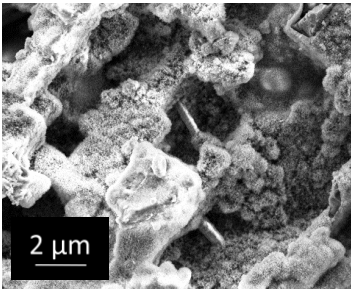
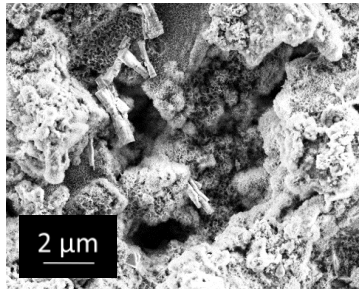
### Sample #3 and #4

The two samples #3 and #4 were obtained with the same etching procedure but different functionalization method. During condensation tests they displayed different condensation modes as expected from the contact angles analysis. Sample #3, which in ambient atmosphere exhibits superhydrophobic characteristics, promoted DWC, whereas only film condensation (FWC) was seen over Sample #4. The low receding contact angle of Sample #4 ( $\theta_r \approx 10^\circ$ ) supports the present result suggesting that the receding contact angle plays a key role in establishing the condensation mode. Here, the receding contact angle of the Sample #4 is too low for promoting DWC, independently from the high advancing contact angle. At the end of the condensation tests, the sample displays advancing contact angle  $\theta_a = 149^\circ \pm 12^\circ$  and a receding contact angle  $\theta_r \approx 0^\circ$  in agreement with measurement performed before the tests. In Figure 5.37, the HTC values measured over Sample #3 and Sample #4 are shown.



**Figure 5.37 - Heat transfer coefficient versus time on Sample #3 and Sample #4. The relevant operating conditions are listed in the table.**

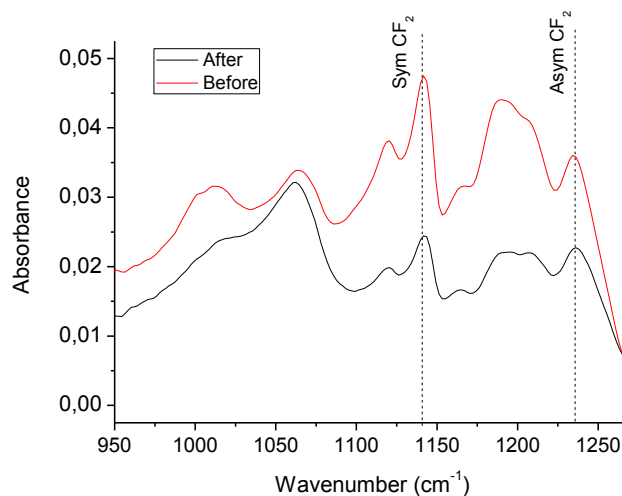
As expected, the HTC measured during FWC is lower than the HTC measured during DWC. Nevertheless, it is interesting to point out that the HTC measured on Sample #4 during FWC is higher than that expected on the untreated sample at the same operating conditions, as already highlighted by Del Col *et al.*<sup>44</sup>. Since Sample #3 promoted dropwise condensation, at least at an initial stage, it was further investigated. Contact angle measurement, SEM images, FTIR analysis and EDX analysis have been done to the sample before, after 1 hour and after 2 hours of testing in order to understand the behaviour of such surface under condensation of high temperature saturated vapor. SEM images and contact angles at different stages are reported in Figure 5.38. The sample promoted dropwise condensation for few minutes then it turns progressively to FWC with a decrease of HTC (Figure 5.37) with a behaviour similar to Sample #1 and Sample #2. The surface before, and even after 1 hour test, displays superhydrophobic characteristics, with advancing contact angle higher than 150° and an hysteresis lower than 10°. Thus, the surface remained superhydrophobic although condensation shifted to filmwise mode. Once the experiment was restarted, the surface did not promote dropwise condensation neither at the initial stage. After another hour of vapor condensation (in total 2 hours of experimental campaign) the surface still displays quite high advancing contact angle but the receding contact angle has significantly decreased ( $\theta_a=143^\circ\pm 33^\circ$  and  $\theta_r=77^\circ\pm 53^\circ$ , as in **Figure 5.38**).

As prepared	Test	After 1 h condensation test	Test	After 2 h condensation test
	DWC to FWC		FWC only	
$\theta_a=158^\circ\pm 1^\circ$ $\theta_r=149^\circ\pm 5^\circ$		$\theta_a=161^\circ\pm 1^\circ$ $\theta_r=151^\circ\pm 5^\circ$		$\theta_a=143^\circ\pm 33^\circ$ $\theta_r=77^\circ\pm 53^\circ$

**Figure 5.38 - SEM images and contact angle measurements taken on Sample #3 at different stages (before tests, after one hour and after two hours tests). Wetting properties and type of condensation are also indicated.**

From the SEM images it is possible to notice that the morphology remains almost the same for the whole campaign, but new structures are created once the specimen is exposed to the condensing steam. These structures are very similar to those found in the Sample #1 once degraded, meaning that the vapor actually modifies the surface. From the XRD analysis it was possible to confirm that those structures are aluminium hydroxides (see Figure 5.40). FTIR measurements confirmed the presence of FOTS on the aluminum substrates both before and after condensation experiments (see Figure 5.39). Figure 5.39 shows the FTIR spectra of Sample #3 before (red line) and after (black line) condensation experiments. The peaks at  $1140\text{ cm}^{-1}$  and  $1240\text{ cm}^{-1}$  can be assigned to the symmetric

and asymmetric stretching frequency of the CF<sub>2</sub> group in the alkyl chain of FOTS. The attribution of the main vibration peaks showed in Figure 5.39 is reported in Table 5.17.

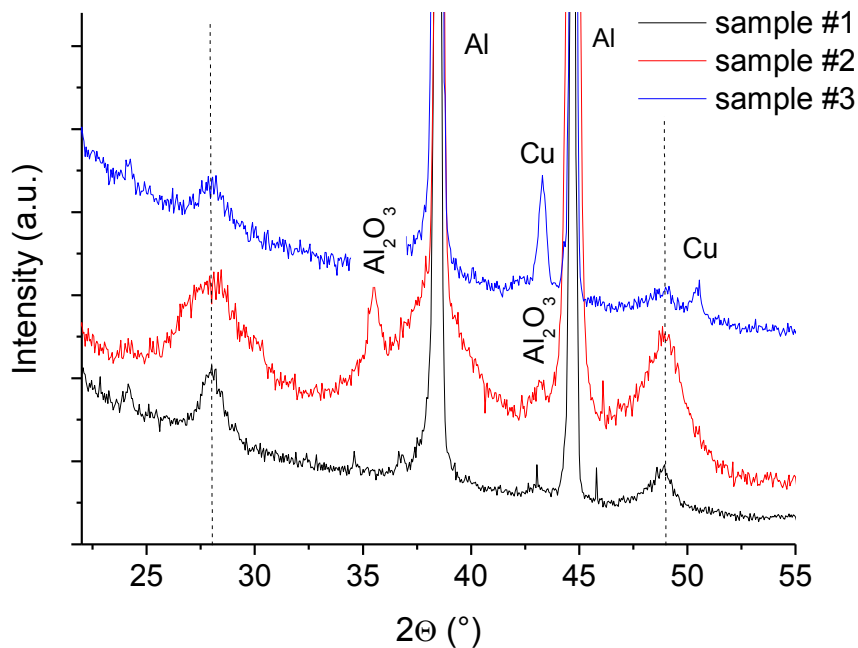


**Figure 5.39 - FTIR spectra of Sample #3 showing the frequency region related to the vibrations of CF<sub>2</sub> groups of FOTS.**

**Table 5.17 - Attribution of the main vibration bands observed in the FTIR spectra reported in Figure 5.39.**

Peak frequency (cm <sup>-1</sup> )	Assignment	Reference
1060	Si-O-Si	1
1120	C-C stretching, C-C-C	1
1140	Symmetric CF <sub>2</sub>	1, 2
1205	C-C-C, C-C	1
1240	Asymmetric CF <sub>2</sub>	1,2

Also EDX analysis showed the presence of similar amount of fluorine before and after the condensation experiments.



**Figure 5.40 - XRD pattern of Sample #1, #2 and #3 after exposure to vapor condensation. The dashed lines indicate the peak position of AlO(OH) (Boehmite IDC #832384), present in all the samples. In Sample #2 it is possible to note also the Al<sub>2</sub>O<sub>3</sub> diffraction peaks (Corundum IDC #750788) and in Sample #3 the Cu diffraction peaks (IDC #782076). The strong diffraction peaks, present in all the samples, are related to the aluminum substrate (IDC #851327).**

### 5.3 Heat flux tests

As reported in Chapter 2, theoretical models predict an increasing HTC with  $\Delta T$  for DWC. Experimentally, looking at small range of  $\Delta T$  (max 5°C due to the apparatus limits) the HTC results to be almost constant. Then, once the HTC is measured for a condition on a specific coating, its value is well-known for a wider range. Besides FWC data, the DWC heat flux tests are performed only on M7T3\_200 and P7T3\_200, for the other coatings HTC values, please refer to the HTC value measured during duration tests reported in the previous paragraph. One parameter that changes with different heat flux is the dynamic behavior of droplets and it will be interesting to match with the thermal results.

#### 5.3.1 FWC tests

FWC is obtained on untreated metal surfaces. The characterization of surfaces is reported in paragraph 5.2.1. Hence the influence of different heat flux and different steam velocities are reported simultaneously for sake of brevity.

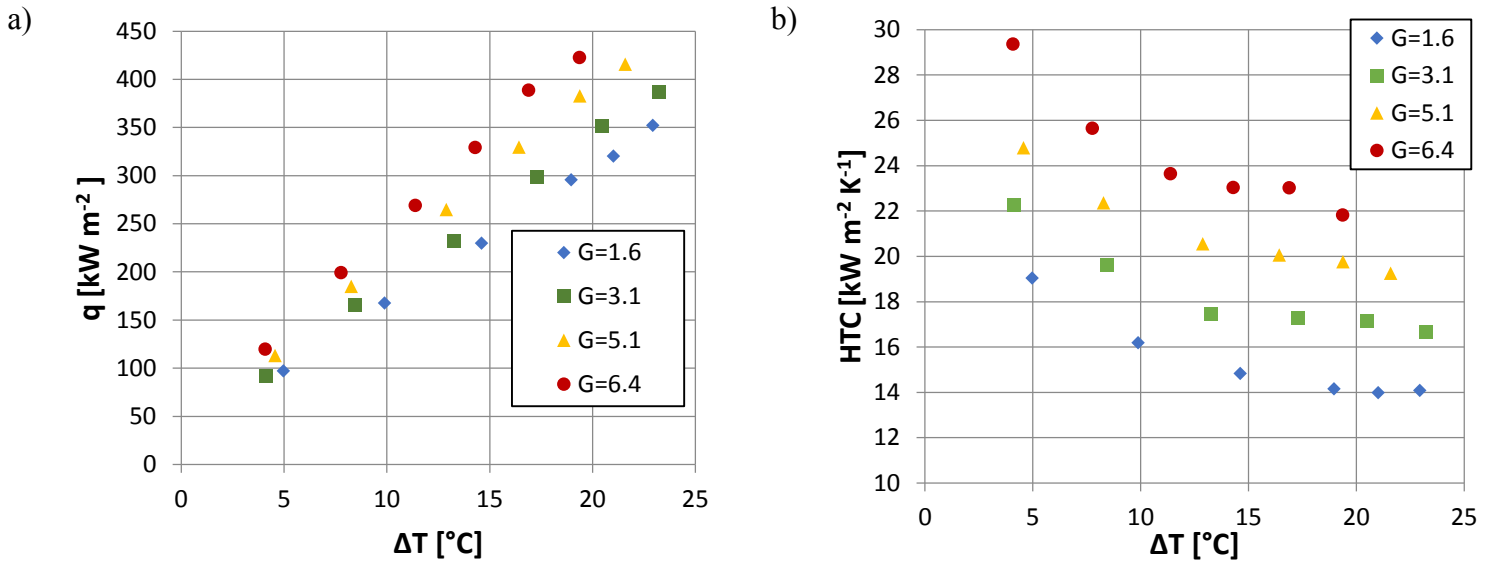
### 5.3.1.1 Aluminum samples

On the aluminum substrate, six different heat fluxes are tested for four different vapor velocities. In Table 5.18 is reported the conversion steam mass flow rate – mean steam velocity.

**Table 5.18 - Steam mass flow rate – mean steam velocity inside test section.**

$G$ [ $\text{kg m}^{-2} \text{s}^{-1}$ ]	$v$ [ $\text{m s}^{-1}$ ]
1.6	2.4
3.1	5.0
5.1	7.2
6.4	9.4

Data are reported in Figure 5.41. The relative experimental uncertainty ranges from 5 % to 12 % as the temperature difference decreases, the vapor velocity has not a significant influence on the uncertainty. For further details please refer to paragraph 4.4.

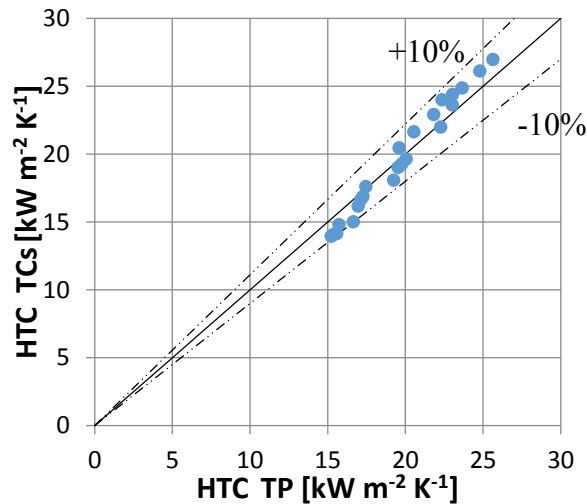


**Figure 5.41 - Heat flux (a) and HTC (b) mean temperature difference between the saturated vapor and the surface during condensation over aluminum untreated sample. The present data refer to variable steam mass velocities  $G$  [ $\text{kg m}^{-2} \text{s}^{-1}$ ].**

Figure 5.41 shows that the heat flux increases when increasing the wall subcooling and the steam mass flow rate. On the other side, the condensation HTC decreases with the increase of the mean temperature difference (especially at high vapor velocity), while it is strongly affected by variations in the steam mass flow rate. The vapor velocity has an important influence on the liquid film thickness and consequently it affects the condensation heat transfer coefficient. In fact, when the mass flux  $G$  increases, the mean velocity of the liquid film increases too, due to the vapor shear stress acting on

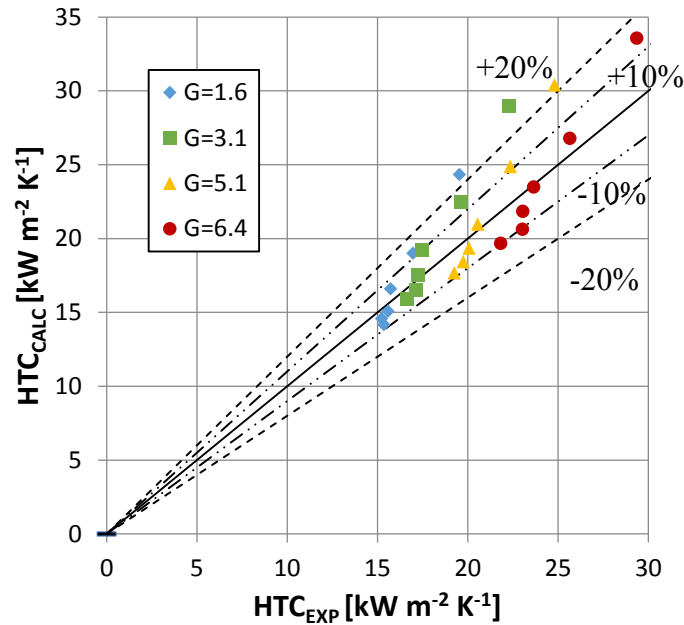


the liquid film. A higher liquid velocity causes a reduction of the liquid film thickness and thus a reduction of the thermal resistance associated with the condensate layer (see Chapter 2). The vapor shear stress is so important that passing from 1.6 to 6.4 kg m<sup>-2</sup> s<sup>-1</sup> the HTC increases by 50% for a fixed  $\Delta T$ . The FWC is useful to verify the different method of calculating the HTC reported in Chapter 4, from the thermal balance of the coolant side and from the thermocouples. As reported in Figure 5.42, the accordance between the two methods is for most of the results in within  $\pm 10\%$ .



**Figure 5.42 - Thermal balance in the test section: comparison between the heat measured on the cooling side (HTC TP) and the one evaluated from the temperature profiles inside the specimen (HTC TCs).**

The data regarding FWC here reported is measured on the aluminum substrate at four different vapor mass flow rate: 1.6, 3.1, 5.1 and 6.4 kg m<sup>-2</sup> s<sup>-1</sup>. The Nusselt theory, which accounts only for the gravity component, is not able to predict the measured HTC<sup>81</sup> and, for this reason, the shear stress part has been added. Figure 5.43 shows the comparison between the calculated and experimental HTC.

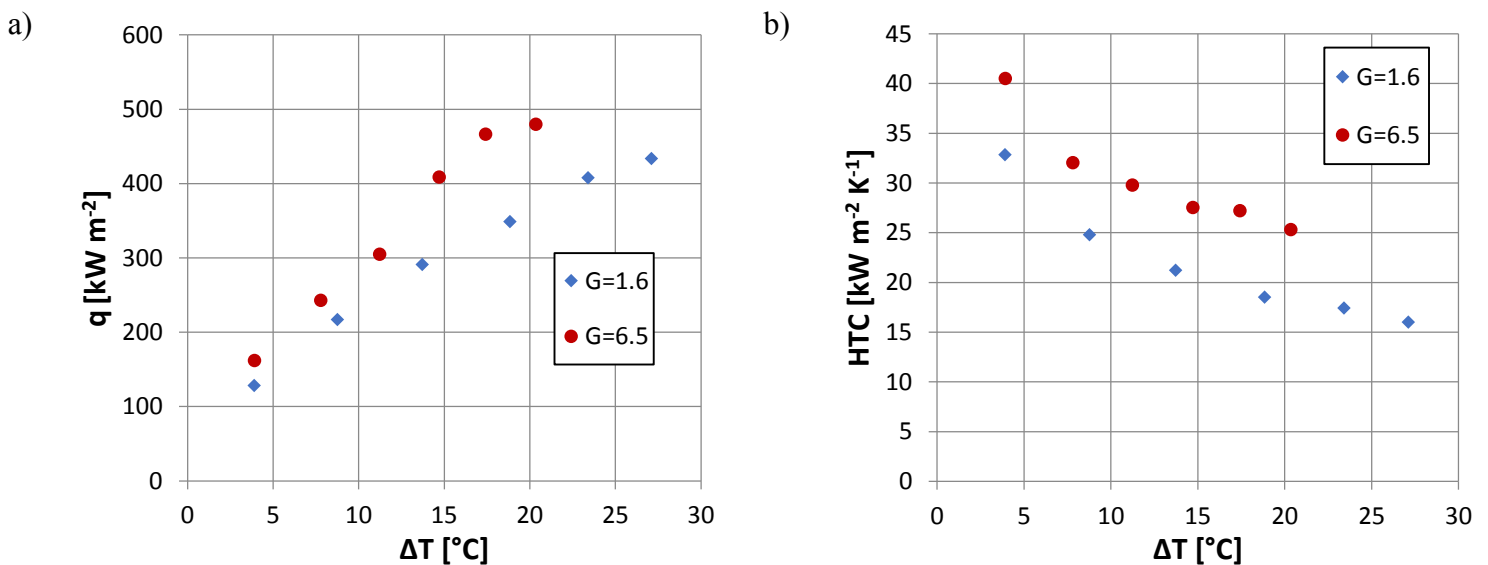


**Figure 5.43 – Comparison between the calculated and experimental HTC during FWC.**

The model reported in Chapter 2, which refers to vertical flat surfaces, presents a good agreement with the experimental data. Most of the points in Figure 5.44 are within  $\pm 10\%$ ; points measured at low  $\Delta T$  for each vapor speed are not well predicted, the model tends to overestimate the experimental data.

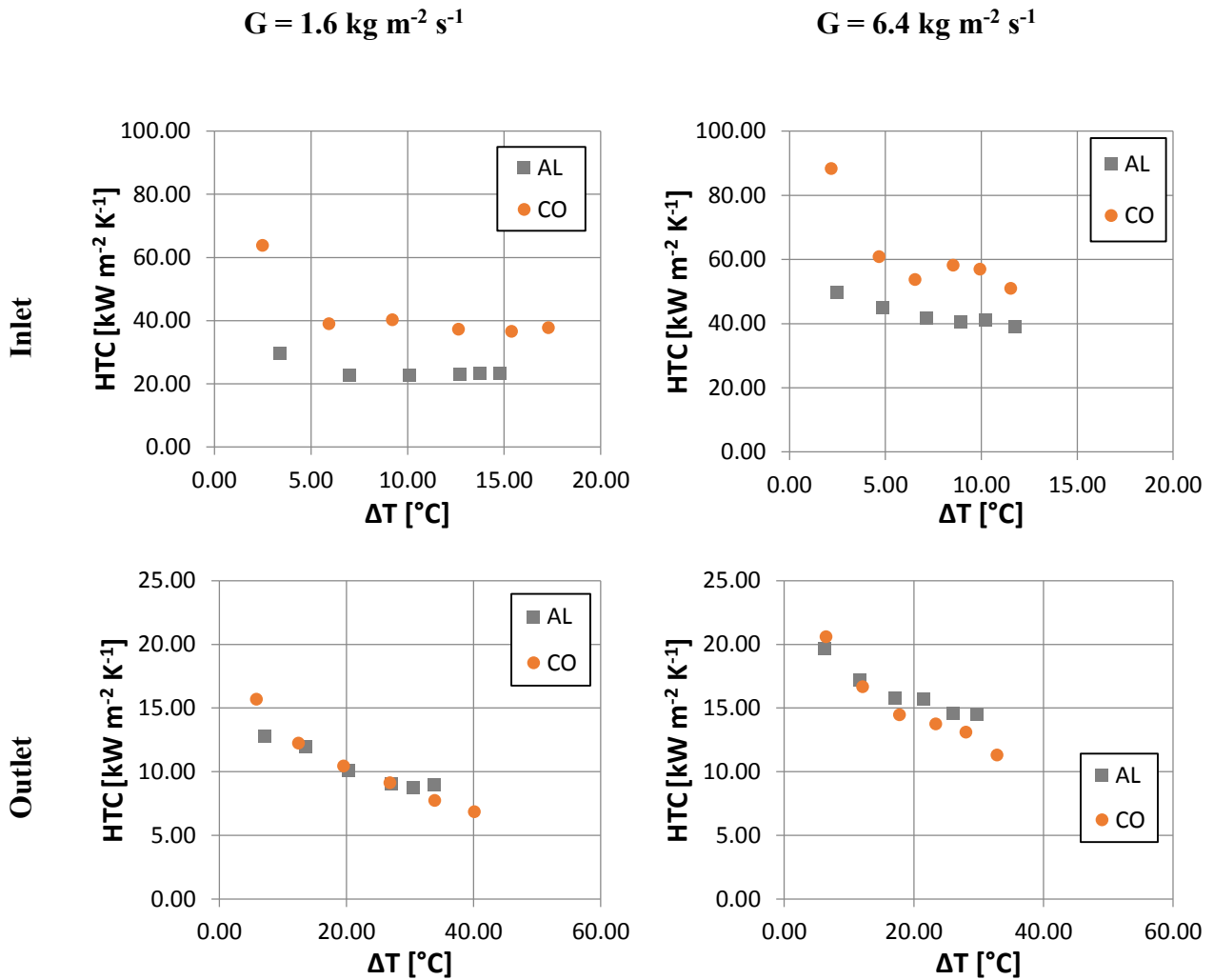
### 5.3.1.2 Copper samples

The same test done on the aluminum substrate is performed on the copper one. The steam mass flow rate tested are the limits of the previous test. The results are summarized in Figure 5.44 and the comparison between the FWC data is held in Chapter 6.



**Figure 5.44 - Heat flux (a) and HTC (b) versus logarithmic mean temperature difference between the saturated vapor and the surface during condensation over copper untreated sample. The present data refer to variable steam mass velocities  $G$  [ $\text{kg m}^{-2} \text{s}^{-1}$ ].**

It is interesting to compare the measurements done during FWC on aluminum and copper substrates. The substrate should not influence the HTC during FWC since the condensate film grows from the vapor inlet to the end of the specimen. In Figure 5.45, the local HTC measured on aluminum and copper for two different vapor mass flow rate are reported.



**Figure 5.45 - Local HTC measured at the inlet and at the outlet of aluminum and copper sample during FWC. The data is referred to two different G.**

As expected, both for aluminum and copper substrate the HTC increases with the increasing of the vapor velocity due to the vapor shear stress which thin the condensate thickness. However, strange results have been measured at the inlet position, exactly where the condensate film appears. In this location, the HTC measured on copper substrate are higher than those measured on the aluminum, whereas at the outlet, where the condensate film is fully developed, the HTC measured is the same for both the materials. The increased local HTC leads to measure higher global HTC on copper as reported in Chapter 5. Although difficult to find some measurement at the very beginning of the film, there is in literature something similar to the present case<sup>221,251</sup>. The different wetting behavior, which is further enhance in the aluminum case at this specific conditions (Figure 5.1), seems to be the reason

of this unexpected phenomenon. The FWC model has not been compared to the points measured during FWC on copper substrate, since it will underestimate those values meaning that some other phenomenon should be taken into account. The Nusselt theory does not consider the relationship between the liquid and the substrate (wetting) and where the condensate film is very thin wettability can be again a factor which influences the condensation phenomenon. Furthermore, it is interesting to notice the wide gap between the HTC measured at the inlet and at the outlet. At a fixed  $\Delta T$ , the increase can be 3 – 4 times between the inlet and the outlet, with the condensate thickness increasing from 10 nm to 100 nm respectively<sup>81</sup>. The idea of take advantage of this very high HTC without coating a surface starts to be studied by researchers, the disadvantages are on assuring that the film does not develop as predicted by the Nusselt theory. Pillars geometry (“American cities”) would be used<sup>252</sup>, thus locally at the top of the pillar very high HTC should be achieved, but how the condensate will be drained from the surface efficiently?

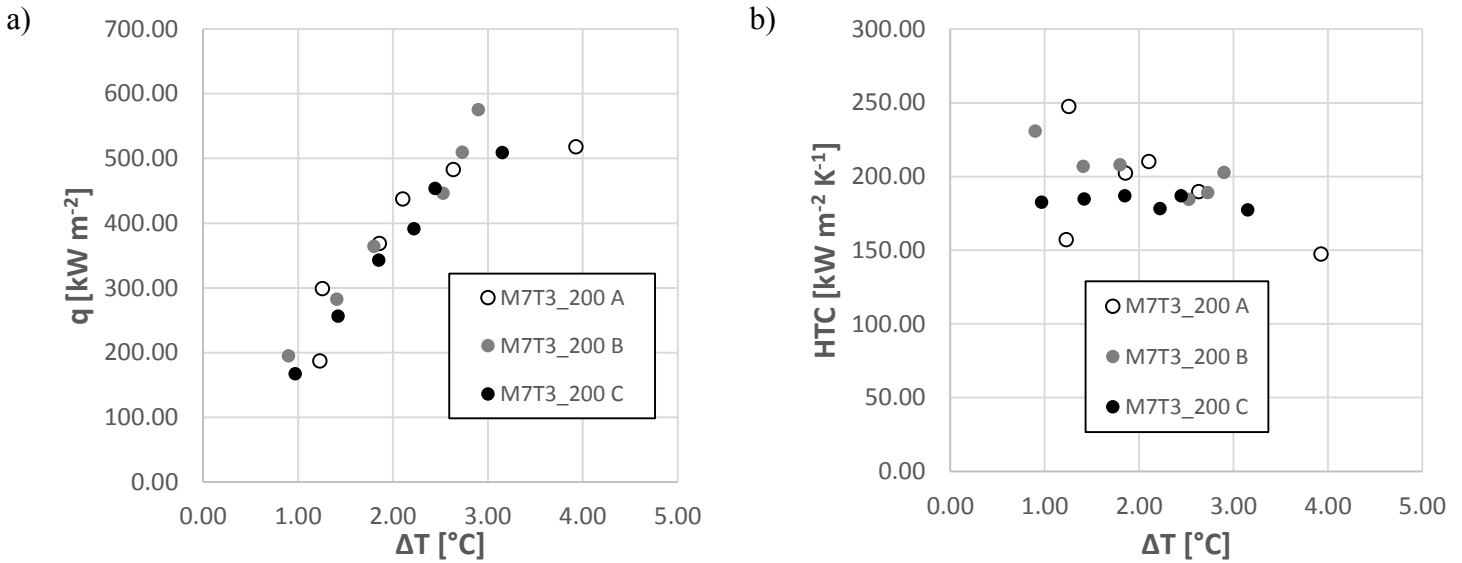
### 5.3.2 DWC tests

Once assessed that the treatment can sustain DWC for a certain amount of time, the heat flux tests can be performed. In particular, two treatments have been chosen for the evaluation of the influence of heat flux on the HTC: M7T3\_200 and P7T3\_200. The two different coatings present different characteristics (see Chapter 3), especially, they have different thicknesses and they showed two different HTCs (see paragraphs 5.2.2.2 and 5.2.2.3). The heat flux tests can be performed within two hours and, whereas P7T3\_200 lasts around 10 hours, M7T3\_200 lasts about two hours. As reported in paragraph 5.2.2.2, a treatment life is also influenced by the heat flux, it increases with the decreasing of the heat flux. Thus, the HTC measured on M7T3\_200 could be considered reliable and without degradation.

#### **5.3.2.1 M7T3\_200**

Even if the robustness of M7T3\_200 is enough to sustain the whole heat flux test, several samples have been treated with the coating and tested in order to ensure the repeatability of the results. Furthermore, the tests have been conducted with different procedure: starting from 10°C of the coolant inlet temperature and rising to 85°C (M7T3\_200 A and C) and vice versa (M7T3\_200 B). Figure 5.46 shows that the repeatability can be confirmed and the mean HTC is constant and equal to about 180 kW m<sup>-2</sup> K<sup>-1</sup> for all the heat fluxes. In order to evaluate the degradation, the contact angle measurement is a good indicator. For example,  $\theta_a=76^\circ\pm 7^\circ$   $\theta_r=34^\circ\pm 4^\circ$  have been measured after the condensation test, which are a little bit lower than those measured before the condensation test (see paragraph 3.2.1.2.1). Even if from a thermal point of view (Figure 5.46) or from a dynamic point of view (Figure 5.47) the vapor flow seems to not affect the coating, at the microscale the surface started

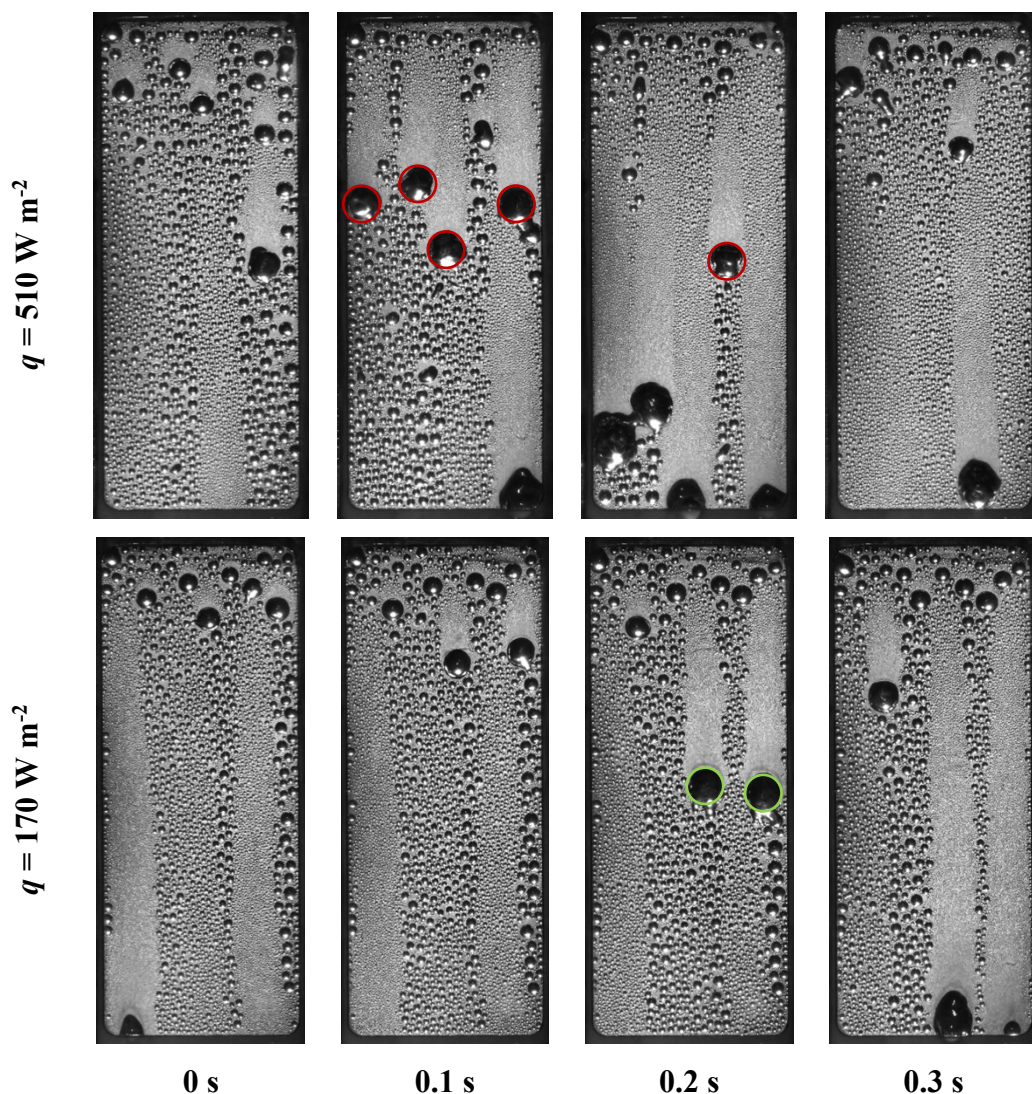
to change. The three samples HTC (M7T3 A B and C) are quite in agreement for the whole test, only the data of M7T3\_A at  $\Delta T=4^\circ\text{C}$  is a little out of the trend probably because the apparatus was not in stable conditions. In this case, degradation should be excluded since that point is the first recorded during that test. The M7T3\_200 C seems to be the most stable during the condensation test, thus it is taken as representative of the M7T3\_200 series henceforward. The relative experimental uncertainty ranges from 11 % to 23 % as the temperature difference decreases, the HTCs have been measured at the middle position. For further details please refer to paragraph 4.4.



**Figure 5.46 - Heat flux (a) and HTC (b) versus mean temperature difference between the saturated vapor and the surface during condensation over M7T3\_200 coating. Three different samples (M7T3\_200 A, B and C) with the same coating are compared.**

Figure 5.47 shows the DWC phenomenon for two operating conditions (heat flux respectively equal to 510 kW m<sup>-2</sup> and 170 kW m<sup>-2</sup>) and with a time step of 0.1 s. The sample is 2 cm wide and 5 cm long and one pixel correspond to 0.045x0.045 mm thus only droplets with radius higher than 0.1 mm are appreciable. The DWC starts at the molecular level, with the formation of small clusters of few molecules on the preferential nucleation sites, which grow by direct steam condensation. Subsequently, due to the proximity of adjacent droplets, the drops come into contact one with each other giving coalescence and they continue to grow. In presence of an external force (e.g. gravity, vapor shear stress...) or surface tension gradient, the droplets begin to slip away when they reach the critical radius. While slipping, the droplets continue to grow by coalescing with other droplets along their path, leaving the surface clean and available for the formation of new nuclei<sup>27,92,101</sup>. In Figure 5.47, only the mechanism of a small part of droplet population during DWC can be observed (see Chapter 2); the droplets grow by both direct vapor condensation and coalescence, until reaching their departing radius, typically at the inlet of the sample, and afterwards the droplets slip down. The process presents some differences depending on the heat flux, but also some analogies. Since the

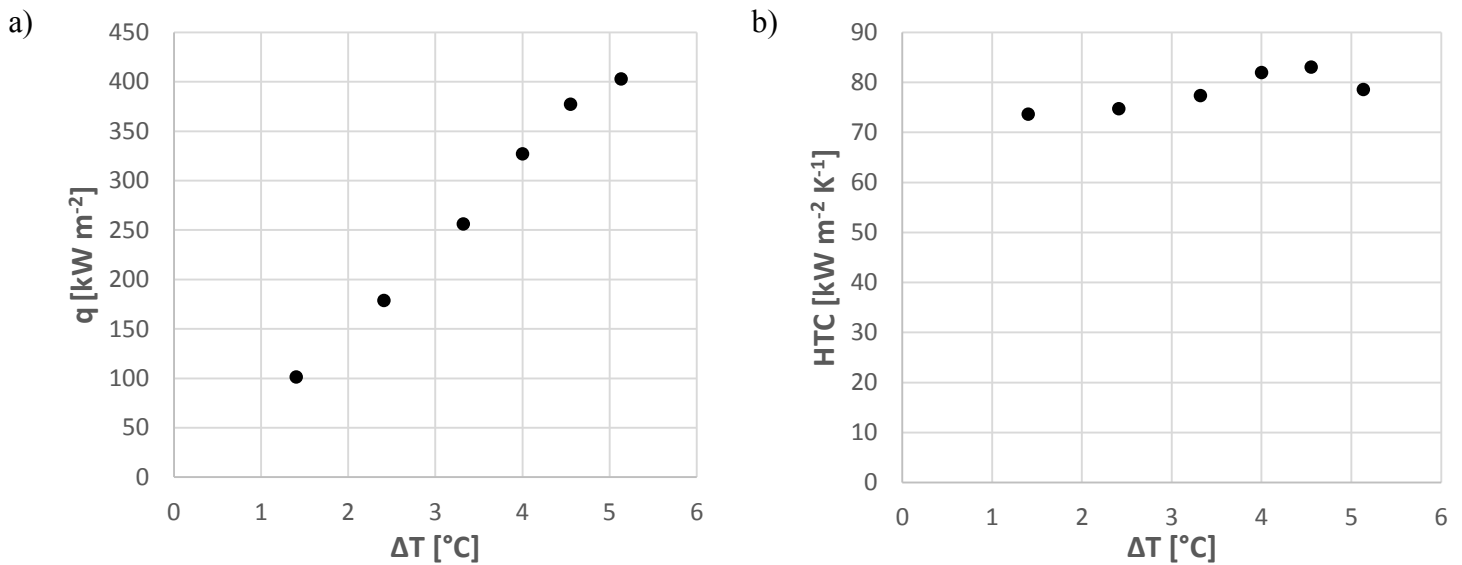
droplet departing radius is a balance between the external forces and the adhesion forces, which allows them to remain attached to the surface, it should be constant regardless the heat flux<sup>26,27</sup>. In both cases presented in Figure 5.47 (which correspond respectively to the highest and lowest heat flux of Figure 5.46a) the measured departing radius is equal to  $1 \text{ mm} \pm 0.1 \text{ mm}$ . Instead, looking at the time needed to reach the departing radius by the droplets, some differences can be appreciated. In the considered interval time, which corresponds to 1000 frames, it is possible to notice that at  $q = 510 \text{ kW m}^{-2}$  the surface is completely renewed in 0.3 s by 5 droplets (highlighted with red circles), whereas at  $q = 170 \text{ kW m}^{-2}$  only 2 droplets sweep the surface in the same 0.3 s time interval (highlighted with green circles).



**Figure 5.47 - Droplets evolution on M7T3\_200 sample at two different heat fluxes ( $q = 510 \text{ kW m}^{-2}$  and  $q = 170 \text{ kW m}^{-2}$ ). At  $510 \text{ kW m}^{-2}$  heat flux, the surface is completely renewed in 0.3 s, as highlighted by the red circles.**

### 5.3.2.2 P7T3\_200

The duration of P7T3\_200 is much higher than the time needed for this type of test. One sample is then reported as a representative of P7T3\_200 series. The data collected are summarized in Figure 5.48, the test conditions are the same applied to the previous coating. The HTC resulted to be constant and equal to about  $80 \text{ kW m}^{-2} \text{ K}^{-1}$  in agreement with the data reported in paragraph 5.2.2.4. The relative experimental uncertainty ranges from 8 % to 18 % as the temperature difference decreases, the HTCs have been measured at the middle position. For further details please refer to paragraph 4.4.



**Figure 5.48 - Heat flux (a) and HTC (b) versus mean temperature difference between the saturated vapor and the surface during condensation over P7T3\_200 coating.**

Contact angles equal to  $\theta_a=83^\circ\pm 4^\circ$   $\theta_r=50^\circ\pm 5^\circ$  have been measured after the condensation test, proving that the degradation does not significantly affect the data. In the following Figure, the droplets behavior for two heat fluxes is reported (please refer to Figure 5.47 for a rough comparison). For the same time interval, the surface is swept by three droplets and one droplet, respectively for  $q = 400 \text{ kW m}^{-2}$  and  $q = 100 \text{ kW m}^{-2}$ . The droplet frequency seems to be fundamental for modeling the heat exchange during DWC, since the droplet population should be the same regardless the heat flux. Similar considerations done on M7T3\_200 can be applied to this case.

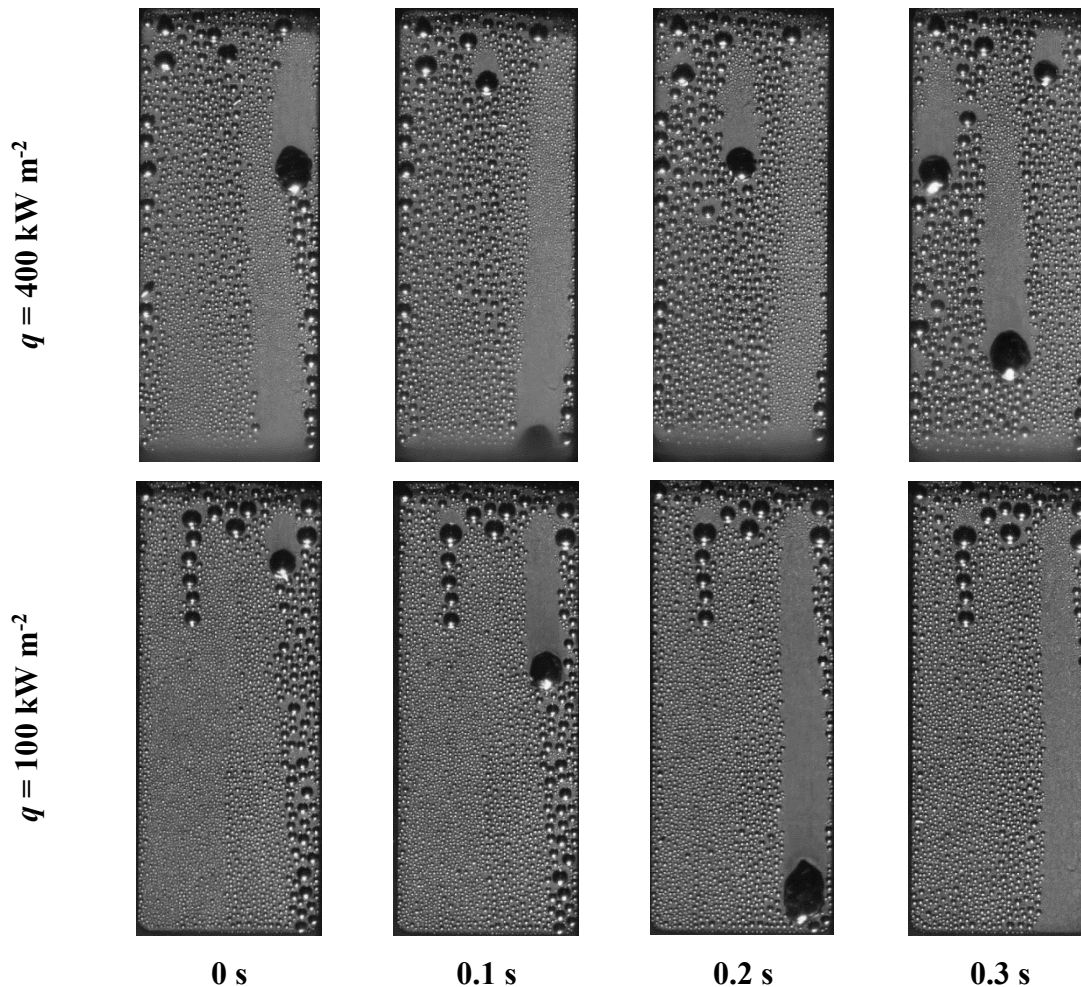


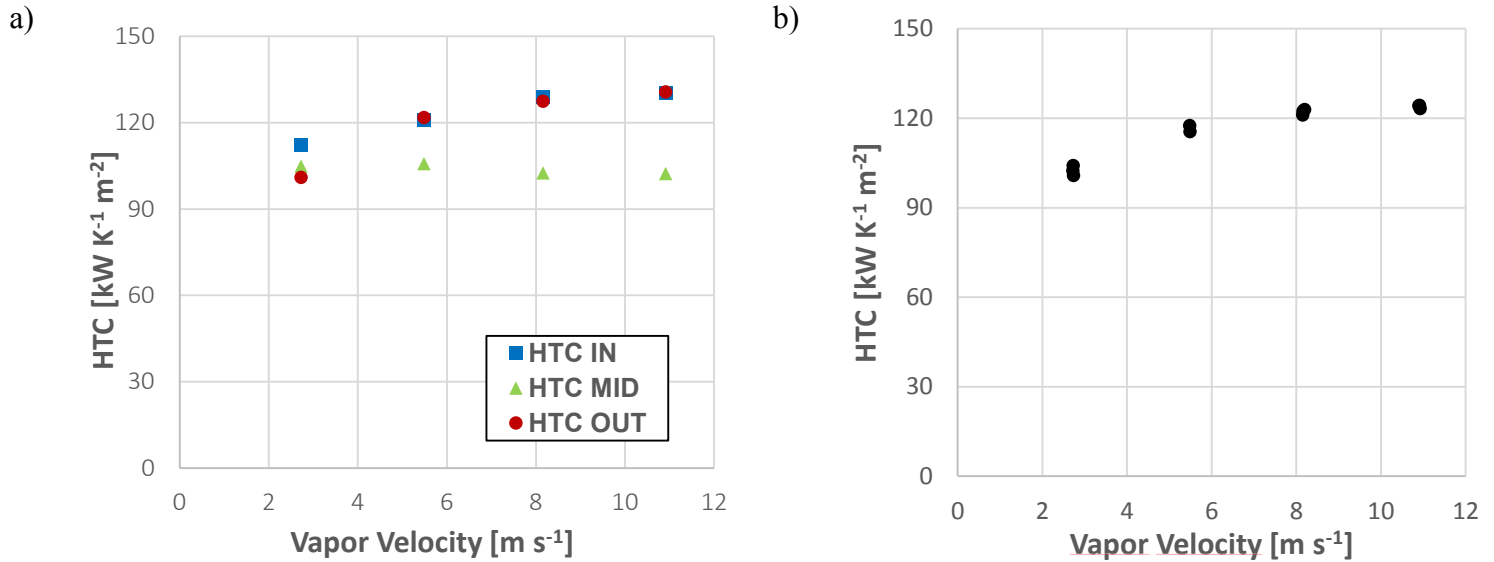
Figure 5.49 - Droplets evolution on P7T3\_200 sample at two different heat fluxes ( $q = 400 \text{ kW m}^{-2}$  and  $q = 100 \text{ kW m}^{-2}$ ).

#### 5.4 Effect of vapor velocity tests

The study of the effect of the steam velocity on the droplet condensation was carried out on M7P3\_200 since the robustness of PxTy series as compared to the others. The speed of the steam is varied playing with the power supplied in the boiling chamber. A variation of the power causes a variation of steam generated and, since the area remains constant, of its speed. Starting from a power of 800 W, the same used for all the previous tests, the power of 3200 W was reached, with steps of 800 W. For each speed condition, three data acquisitions were performed. During the test, the system was adjusted to ensure that the steam velocity was the only variable changing, in particular special care was paid to the saturation temperature. At the end of the experiment, the power was brought back to the initial value for verifying the influence of the treatment degradation on the obtained data. In Figure 5.50, the data measured with this condensation test is reported. The velocities are the same applied to the FWC tests (see paragraphs 5.3.1.1 and 5.3.1.2), whereas the heat flux (Figure 5.51) is maintained constant during the whole procedure. In Figure 5.50, both local and global HTC's have been showed, since it is interesting how only the inlet and the outlet seem affected by the increasing

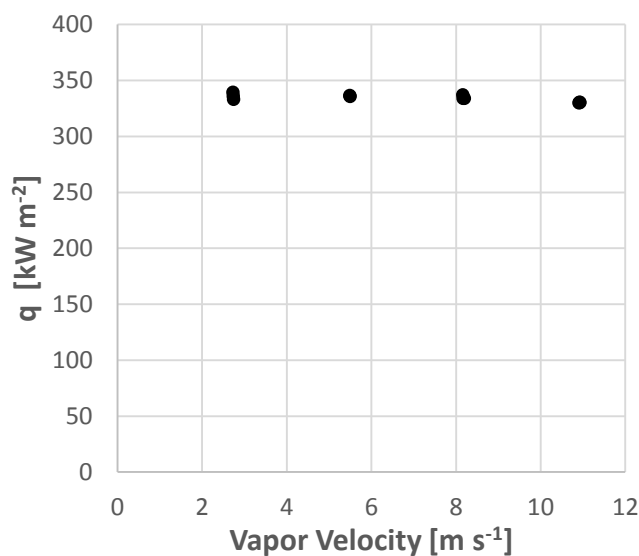


of the vapor shear stress. The HTC measured at the middle position, instead, remain constant for the whole test. However, considerations are made on the global HTC which slightly increases with the increasing of the vapor speed. In fact, by increasing the speed from  $2.7 \text{ m s}^{-1}$  to  $11 \text{ m s}^{-1}$ , a modest increase in heat transfer coefficient is obtained, which goes from  $107 \text{ kW K}^{-1} \text{ m}^{-2}$  to  $120 \text{ kW K}^{-1} \text{ m}^{-2}$ . A possible explanation is provided in the next Chapter where the data are analyzed.



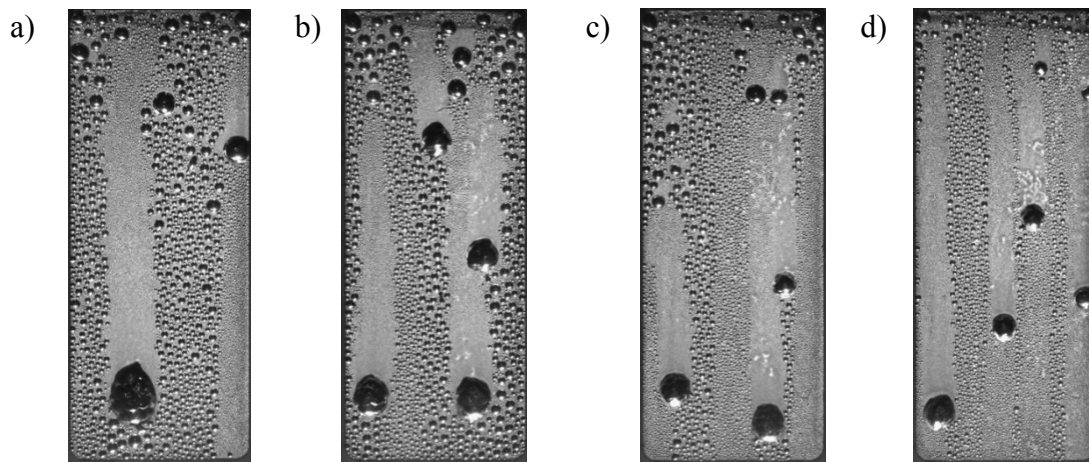
**Figure 5.50 - a) local and b) global HTC versus vapor velocity. The present data is obtained on M7P3\_200.**

Figure 5.51 reports the measured heat flux during the condensation test which remains constant during the whole campaign. This is because the two-phase heat transfer coefficient is much higher than the convective one on the cooling side, thus the main thermal resistance is located on the back side of the sample.



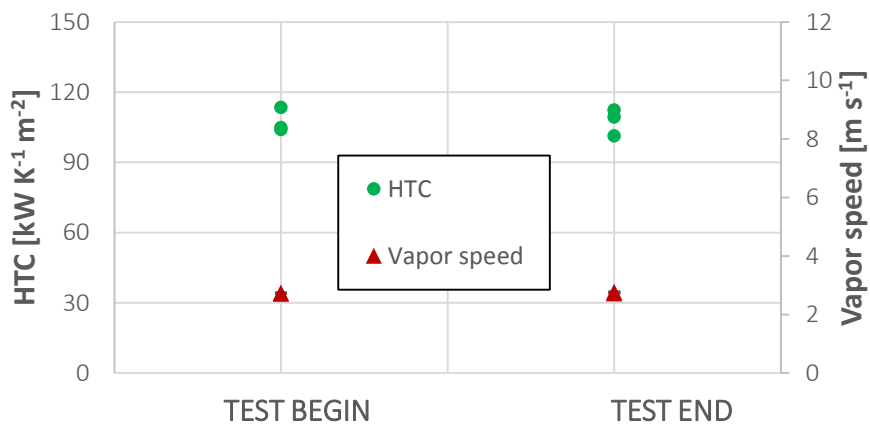
**Figure 5.51 - Heat flux versus vapor velocity. The present data is obtained on M7P3\_200.**

From the visual point of view, the speed of the steam has a strong impact on the characteristics of the drops. In fact, as the speed increases, there is a progressive decrease in the average size of the departing drops, which sweep more frequently the sample surface (Figure 5.52).



**Figure 5.52 - DWC on M7P3\_200 with different vapor velocities: a) 2.7 m s<sup>-1</sup>, b) 5.5 m s<sup>-1</sup>, c) 8.2 m s<sup>-1</sup> and d) 11 m s<sup>-1</sup>**

The data reported in Figure 5.53 have been taken at the beginning and at the end of the test at the same conditions in order to verify that the results obtained are not affected by the degradation of the treatment.



**Figure 5.53 - heat transfer coefficient of the sample M7P3\_200 at the beginning and at the end of the test for the same speed of the steam**

The HTC seems to be not affected by the tests. Further evidence of the absence of degradation is proved by the analysis of contact angles displayed in Table 5.19. The comparison of contact angles verifies that there are no major changes before and after the test.

**Table 5.19 - Contact angle measurements performed before and after condensation test on M7P3\_200 with different vapor velocities.**

	$\theta_a$	$\theta_r$
Before test	$93 \pm 5$	$72 \pm 8$
After test	$82 \pm 2$	$55 \pm 5$



# Chapter 6 - Data analysis of DWC

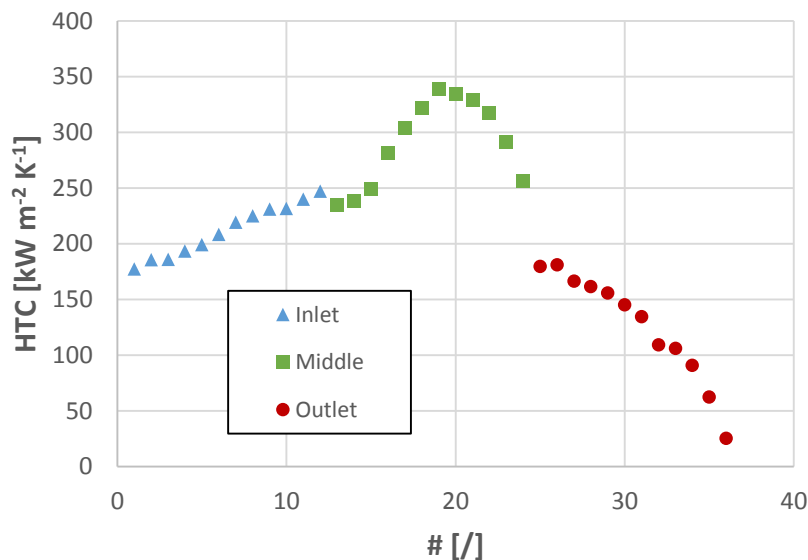
In this last Chapter, the experimental results are summarized and compared to the theory.

## 6.1 Heat transfer measurement analysis

The thermal measurements done during DWC are analyzed from a critical point of view. These analyses should stimulate a deeper knowledge of the phenomenon.

### 6.1.1 On the coating life

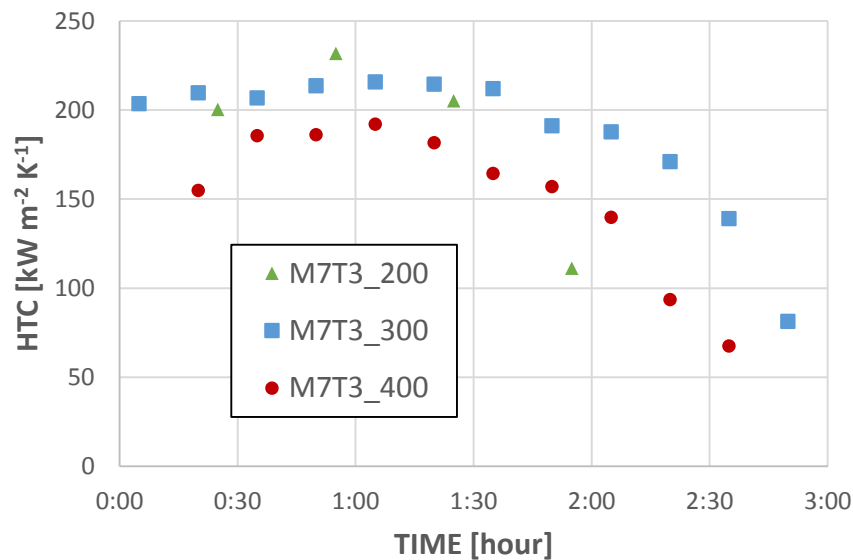
The coating duration is the essential topic when DWC data are discussed. In Chapter 5 the degradation of coatings is widely discussed and described with SEM analysis, contact angle measurements, etc., but from a thermal point of view there is something else which can be noticed. In Figure 6.1 the data reported in Figure 5.13 is reported in a different way. The data is measured on M7T3\_300 and at the three different locations where thermocouples are embedded. Instead of report the HTC versus time, the HTC measured at the inlet, middle and outlet position are plotted in series, respectively.



**Figure 6.1 - HTC measured at the inlet, middle and outlet position during DWC on M7T3\_300. The data is plotted in series.**

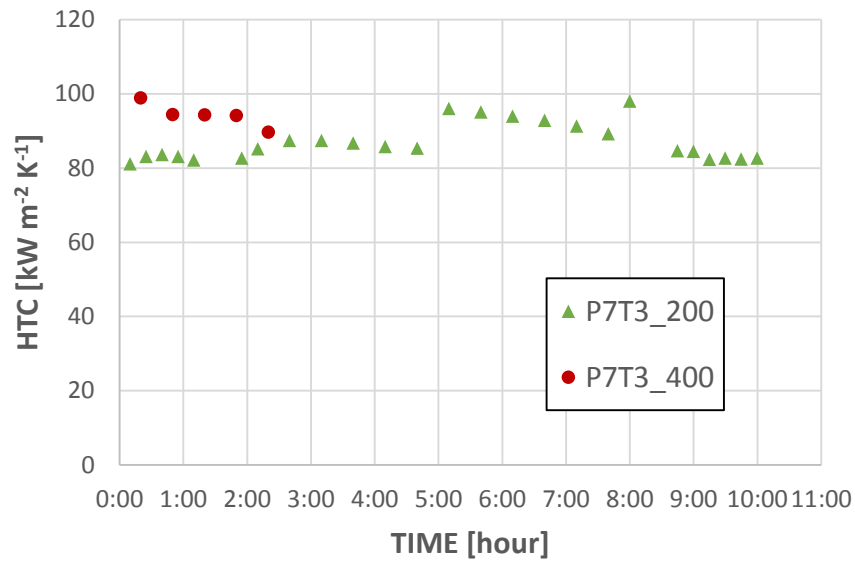
The HTC starts from around  $170 \text{ kW m}^{-2} \text{ K}^{-1}$  reaches a peak at  $350 \text{ kW m}^{-2} \text{ K}^{-1}$  and then starts to decrease until  $25 \text{ kW m}^{-2} \text{ K}^{-1}$ . The M7T3 series starts to degrade at the outlet position, where it is flooded at the end of the test and where the lowest HTC are measured. Figure 6.1 shows exactly the evolution of the degradation of the coating not only with the passing time, but also in the space

dimension. Putting together the three positions in series, the total evolution of HTC in a randomly point of the surface for that coating can be appreciate. Actually, in very old paper<sup>61,97,241</sup>, when also degradation was used to be described, a similar trend is presented for HTC. The trend is probably related to the coating which gets thinner and thinner due to the condensation processes. As reported in Chapter 2, the coating resistance strongly influences the HTC value. In the following, a comparison of the M7T3 series is shown.



**Figure 6.2 - HTC versus time measured on M7T3\_200, M7T3\_300 and M7T3\_400 during DWC.**

Although the M7T3\_300 resulted to be the most robust coating with a total life of 2 hours and 50 minutes, the difference is very fragile. Several samples have been tested for each treatments thus the duration is sufficiently confirmed, however all the treatment can be used indifferently. The lower baking temperature seems to be not enough to crystalize the coating, it presents a sharper parabolic degradation trend, whereas 300°C and 400°C allow a smoother HTC decrease. In the following Figure, the HTCs obtained on P7T3 series are reported.



**Figure 6.3 - HTC versus time measured on P7T3\_200 and P7T3\_400 during DWC.**

In this case, the duration is not discussed. The higher baking temperature seems to make the coating more fragile. In Chapter 5, also the PxMy series is presented and it resulted to be the most robust among the sol-gel coatings, hence it is underlined that both P7M3\_200, lasted more than 100 hours, and M7P3\_200, lasted more than 25hours, are not tested until the flooding of the surface.

### 6.1.2 On the coating performance

The performances of the various coating is hereby discussed. In Figure 6.4 and Figure 6.5, heat flux and HTC measured on graphene, M7T3\_200, M7P3\_200, P7M3\_200, P7T3\_200 and on untreated aluminum surface are summarized.

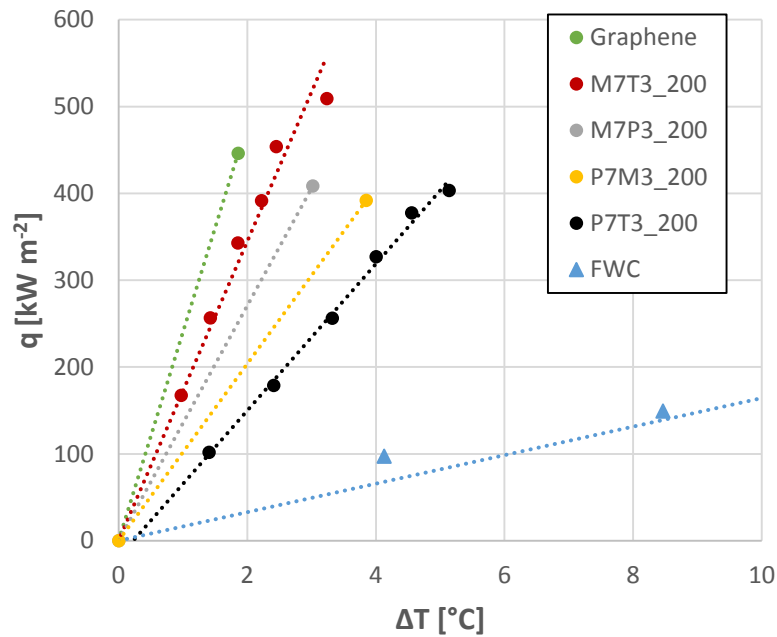


Figure 6.4 - Heat flux measured on graphene, M7T3\_200, M7P3\_200, P7M3\_200, P7T3\_200 and on untreated aluminum surface.

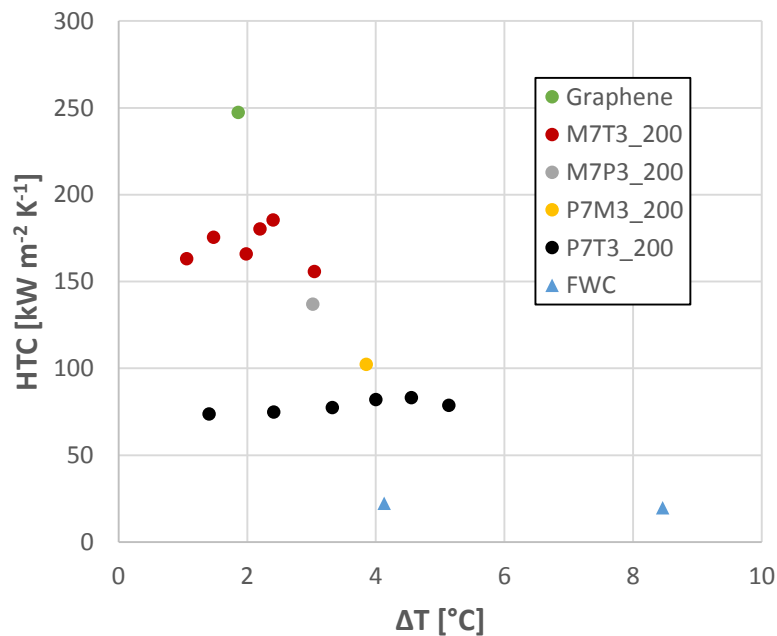


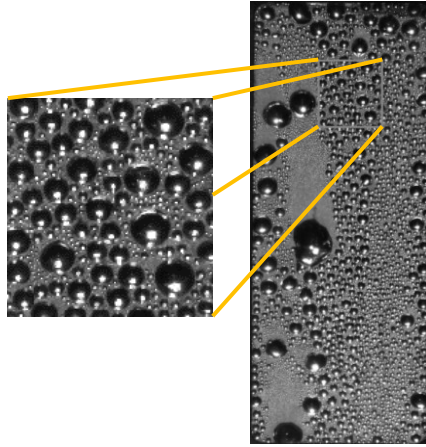
Figure 6.5 - HTC measured on graphene, M7T3\_200, M7P3\_200, P7M3\_200, P7T3\_200 and on untreated aluminum surface.

In Figure 6.4 the slopes of the heat flux are highlighted even for sample where only one condition has been tested (graphene, P7M3\_200, M7P3\_200). In that case a line between that point and the origin has been plotted. The slope of the heat flux is related to the HTC, higher the slope higher the HTC (Figure 6.5). The highest HTC is measured on graphene coatings as expected having thicknesses of few nanometers and high thermal conductivity, that value is around the value associated to the pure DWC HTC<sup>32,80</sup>. After graphene, M7T3\_200, M7P3\_200, P7M3\_200 and P7T3\_200 are found in order. The order is closely related to the coating thickness. Even if the thermal conductivity could not be measured, it should be very similar to all the sol-gel coatings. Some further clarifications must be added. The sample M7T3\_200, as already reported, lasts around the time of carrying the performance tests and it cannot be reasonable to think that the thickness is the same measured before the condensation test (200 nm). After the duration test a coating thickness of around 60 nm has been measured, then it can be assessed that a thickness around 100 nm can be related to the HTC reported in Figure 6.5. Combining the duration with the performances, the graphene coating seems to be the most promising solution in order to maximize the two factors. In Figure 6.5 HTC measured during FWC are plotted for a HTC comparison, the graphene coating presents an augmentation of more than 10 times. By looking at the dynamic contact angle measured after the condensation tests, some interesting information can be gathered on the FWC-DWC boundary. The advancing contact angle is around 65° both for the untreated sample and M7T3\_200 (or other treated surfaces), whereas the receding tends to be 0° during FWC. The measured receding contact angle on surfaces which promoted DWC is always higher than 0°. It seems that this parameter can be used as threshold between the two condensation modes.

### 6.1.3 Heat flux from video analysis

The heat exchanged is related to the condensate mass flow rate on the surface, thus knowing the condensate mass flow rate is possible to measure the heat flux. Monitoring the growing process of the condensing droplets, which increase in size until the droplet departing diameter, the volume of condensate is easily obtained. The only variable which must be hypothesized is the angle with which the droplets grow during DWC and in literature the advancing contact angle is the chosen one. In Figure 6.6, an image taken during DWC is shown with a highlighted area, the area where this analysis has been conducted.





**Figure 6.6 - Image taken during DWC. The area highlighted is the area where the heat flux has been measured.**

Briefly, different frames have been analyzed taking care of not having droplets which fall down due to gravity or important droplets which exit from the area of analysis due to coalescence. The droplets have been identified with circle for each frame, from the diameter the volume is found. The volume can be transformed to a mass through the density and the increasing mass due to the passing time is the mass flow rate. The analysis has been conducted on P7T3\_200 (at the beginning of the test) and on M7T3\_200 at the beginning and at the end of the test, the heat flux measured with this method has been compared to the heat flux measured with the thermocouples in that position. The results are summarized in the following Table.

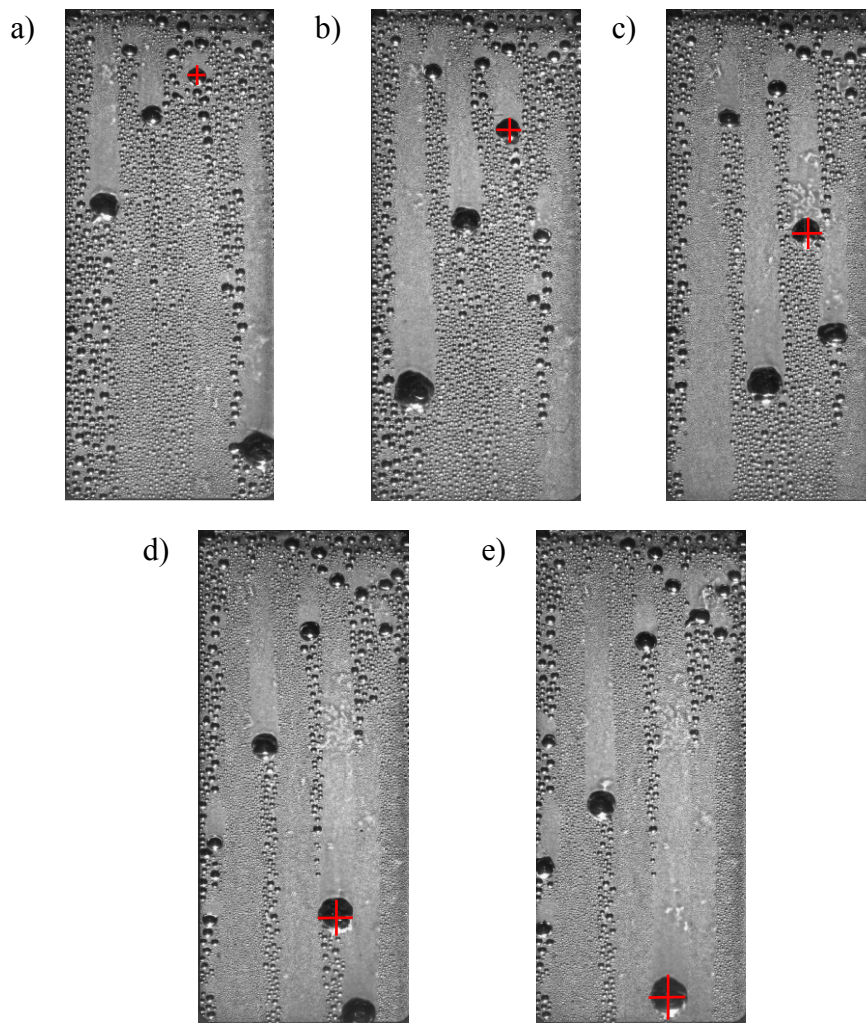
**Table 6.1 - Heat flux measured from video analysis.**

<b>Video</b>	<b>P7T3_200_I</b>	<b>M7T3_200_II</b>	<b>M7T3_200_XXVI</b>
<b>Location on Test Sample</b>	Inlet	Middle	Inlet
<b>Experimental Heat Flux</b> $(\frac{kW}{m^2})$	352.00	134.06	126.79
<b>Heat Flux Assuming 90°</b> $(\frac{kW}{m^2})$	714.78	261.88	483.52
<b>Calculated Contact Angle (°)</b>	61	63	37
<b>Advancing Contact Angle (°)</b>	84	82	59
<b>Receding Contact Angle (°)</b>	58	63	35

Table 6.1 shows the big error (around 200%) if the advancing contact angle is considered as growing contact angle. Imposing a high contact angle,  $90^\circ$ , implies higher condensate volumes, then this angle should be decreased. Furthermore, the images recorded permit to measure only very big droplets, big if compared to the total population of droplets which is supposed to be during DWC. Again, considering only a “small” part of droplet population should strongly underestimate the heat flux, instead with  $90^\circ$  the heat flux is totally overestimated. Imposing an angle which is very close to the receding contact angle measured in ambient conditions, the heat flux measured from the video perfectly correspond to the heat flux measured by thermocouples. Intuitively, a droplet grows with the advancing contact angle, but, if the definitions of advancing and receding contact angle are considered, this idea can be changed. The receding contact angle is the angle assumed by the liquid moving toward a wet surface and this is exactly what is happening during saturated vapor condensation. A big droplet, droplet with higher radius than the effective radius, is growing on other smaller droplets, then is growing on a wetted surface. The angle assumed by this droplets must be a weighted average between the advancing and the receding contact angle with respect if a infinitesimal portion of contact line is advancing on a wetted (droplets) or dry area. Since most of the contact line is growing on droplets, this angle is very close to the receding contact angle. However, to confirm this theory a side view of droplets growing on wetted area should be implemented. More information about this analysis can be found in personal documents.

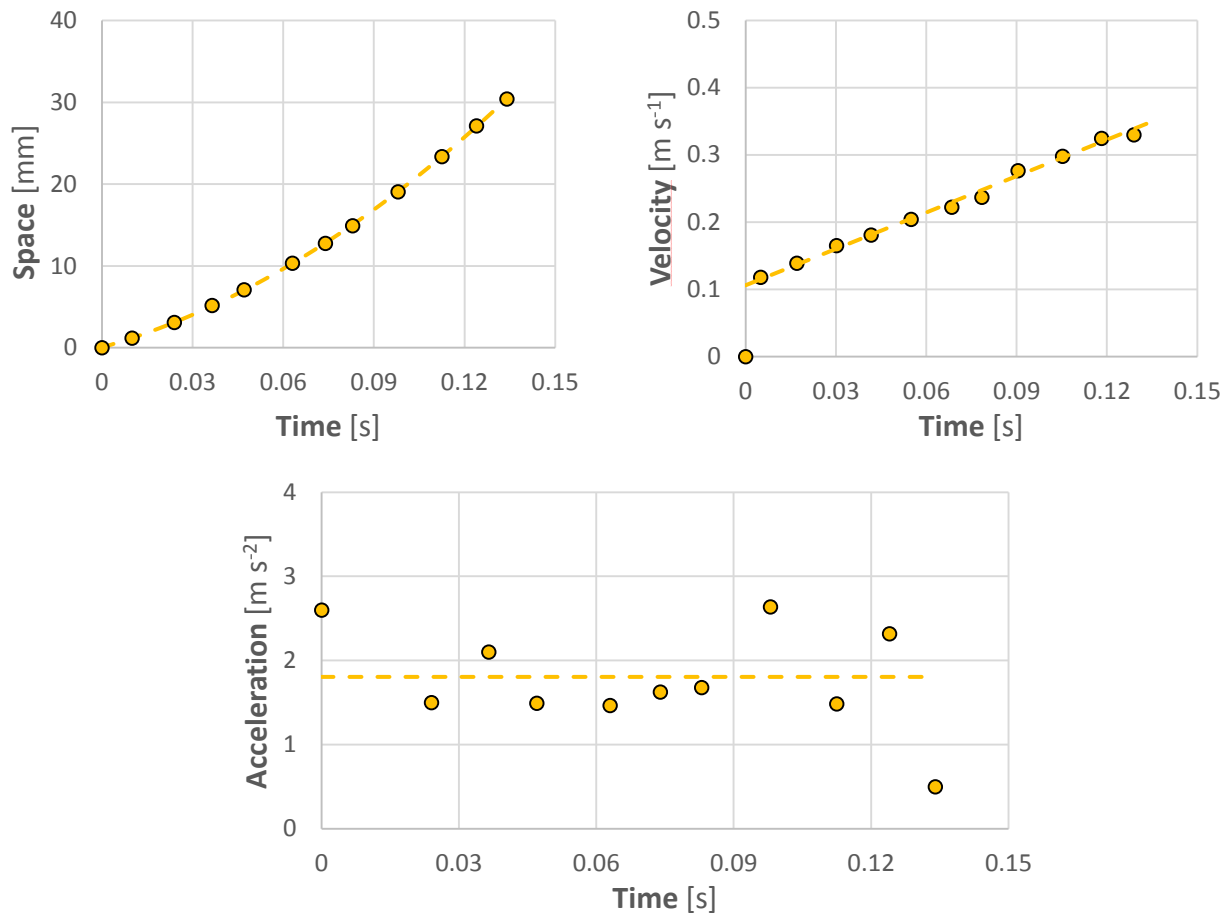
#### 6.1.4 Droplets dynamic at different vapor velocities

In Chapter 5, thermal measurements with four different vapor mass velocities are described from a thermodynamic point of view, here some video analyses are reported. As already reported the vapor velocity should influence the maximum droplet diameter and then the acceleration with which droplets fall along the vertical surface. An example of droplet tracking is reported in Figure 6.7.



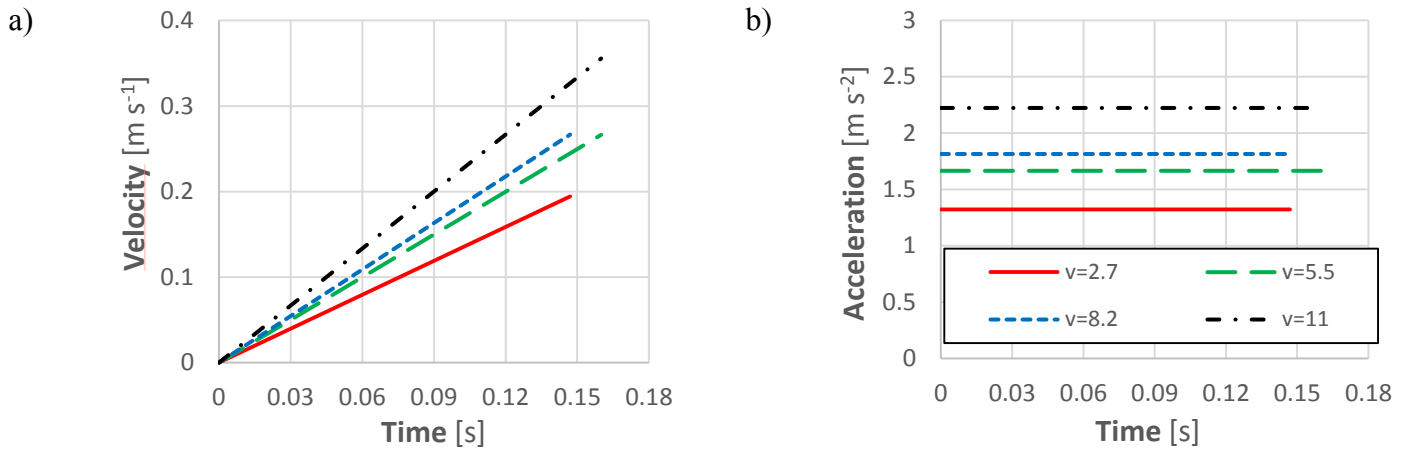
**Figure 6.7 - Tracking example of a falling drop.**

For each velocity a video has been recorded. In each video, at least five comparable droplets have been tracked and analyzed in terms of position, velocity and acceleration. An example is reported in the following Figure.



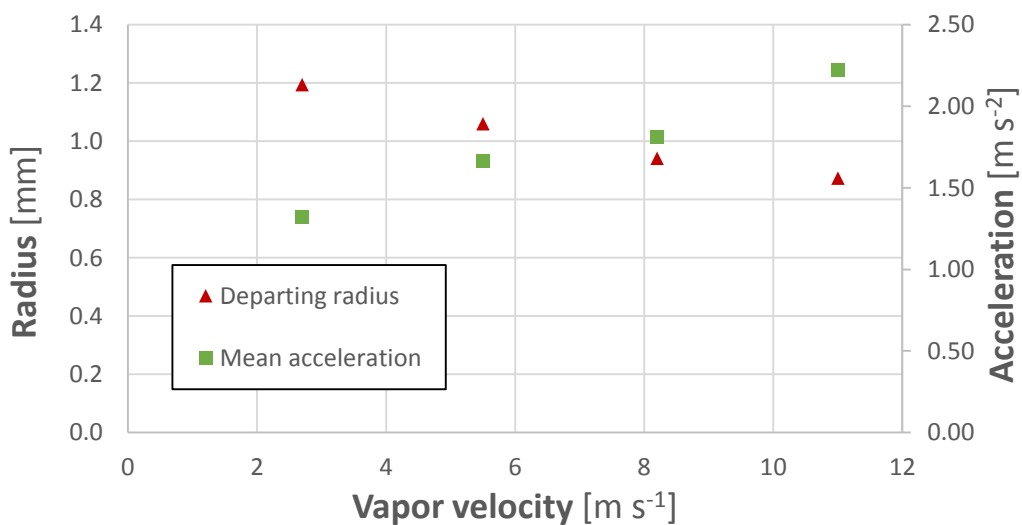
**Figure 6.8 - Example of single droplet dynamic analysis. Vapor velocity equal to 8.2 m s<sup>-1</sup>.**

The example reported in Figure 6.8 shows the typical result of a droplet falling down the surface. The droplet during its fall encounters other droplets in its path and, depending on the droplets dimensions, it will be decelerate non uniformly. This is the explanation for the high scattering in the acceleration graph in Figure 6.8. Averaging at least five droplets, a good estimation of the acceleration undergone by droplets can be reached. The results for the entire test campaign are summarized in Figure 6.9 in terms of velocity and acceleration. The tested vapor velocities are 2.7 m s<sup>-1</sup>, 5.5 m s<sup>-1</sup>, 8.2 m s<sup>-1</sup> and 11 m s<sup>-1</sup>. It has to be underlined that the declared velocity is the velocity which came from a balance in the boiling chamber, but, furthermore, it is a mean velocity. The real shear stress insisting on a droplet is related to a different value of vapor speed, lower than the declared one.



**Figure 6.9 - Measured a) velocities and b) accelerations of droplets with the passing time for four different vapor speed. The vapor velocities are expressed in m s<sup>-1</sup>.**

Increasing the vapor shear stress implies the increasing of droplets acceleration as expected, although the increasing magnitude is not maintained. Even if the vapor speed is increased by four times, the acceleration is increased by a factor 1.7. The main result, instead, is that the droplet maintains a constant acceleration during its path and the motion can be considered uniformly accelerated which is not obvious. Figure 6.10 summarizes the value of droplet acceleration adding a measure of droplet departing diameter.



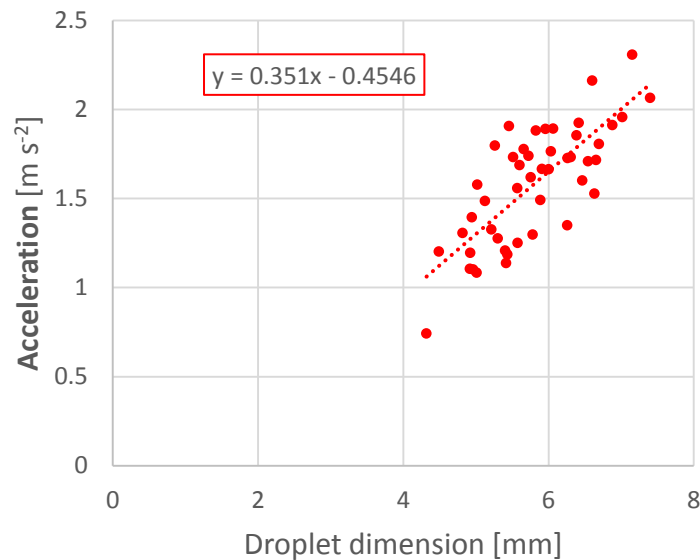
**Figure 6.10 - Departing radius and droplet acceleration versus vapor speed.**

Increasing the vapor speed the droplet departing diameter decreases as reported in Chapter 2. The main results are summarized in Table 6.2.

**Table 6.2 - Main results of droplet dynamic with different vapor speed.**

Power	Vapor velocity	Departing radius	Final velocity	Acceleration
[W]	[m s <sup>-1</sup> ]	[mm]	[m s <sup>-1</sup> ]	[m s <sup>-2</sup> ]
800	2.7	1.19	0.31	1.3
1600	5.5	1.06	0.35	1.7
2400	8.2	0.94	0.37	1.8
3200	11	0.87	0.43	2.2

From the droplet departing diameter to its acceleration, adhesion force, gravity force and vapor shear stress play a crucial role. The force balance determines the motion of droplet, further experiments are needed for separate each component in order to develop a proper formulation for the phenomenon. A wider analysis has been conducted on droplet with a vapor speed of 2.7 m s<sup>-1</sup> which is the velocity most used during the present work, the resume is shown in Figure 6.11.



**Figure 6.11 - Droplet acceleration versus droplet dimension (at the outlet) measured on different coatings.**

There is a clear correlation between the droplet dimension, measured at the outlet of the sample, and the acceleration since, for example, gravity force is applied to the volume of the drop. In order to avoid this phenomenon, in the previous analysis droplets with same final dimension are chosen. Droplets can easily vary their dimension during the falling, depending on how much condensate encounters in their path. Moreover, the increased acceleration with the increased droplet dimension should be linked to the area exposed to the vapor speed which should increase the shear stress. For further aspects and the detailed description of this analysis please refer to Tancon *et al.*<sup>237</sup>.

## 6.2 Experimental data compared to the theory

Models fully described in Chapter 2 are here applied to the experimental data. For further analyses please refer to my other work<sup>103,104</sup>.

### 6.2.1 Droplet departing radius

Droplet departing radius, as reported in Chapter 2, is the result of a force balance of gravity, adhesion and vapor shear stress and it is independent from the heat flux. This first statement is proved considering DWC performance tests on M7T3\_200 and P7T3\_200 (reported in Chapter 5). Even though the heat flux ranges from 100 kW m<sup>-2</sup> to 500 kW m<sup>-2</sup>, the droplet departing radius remains constant equal to 1 and 1.3 mm, respectively. DWC does not change its droplet dimensions in function of the heat exchanged, but it changes its frequency; the droplet departing diameter will be reached faster. The models reported in Chapter 2 use two different expressions for  $r_{max}$ :

$$r_{max} = K_3 \left[ \frac{\sigma}{\rho_l g} \right]^{\frac{1}{2}}$$

and

$$r_{max} = \sqrt{\frac{6(\cos(\vartheta_r) - \cos(\vartheta_a)) \sin(\vartheta)}{\pi(2 - 3 \cos(\vartheta) + \cos^2(\vartheta))} \frac{\gamma}{\rho_l g}}$$

where the second one is recently developed<sup>27</sup>. In Table 6.3, the results from the Equations and the droplet departing radius have been reported.

**Table 6.3 - Comparison between calculated and experimental droplet departing radius.**

Model	$r_{max}$ [mm]	$\theta_a$ [°]	$\theta_r$ [°]	$\Delta\theta$ [°]
Le Frevre and Rose	1.0	\	\	\
Kim <i>et al.</i>	1.4-1.6	\	\	\
M7T3_200	1.0	83	64	19
P7T3_200	1.3	83	57	26
M7P3_200	1.2	89	61	28
P7M3_200	1.3	86	54	32

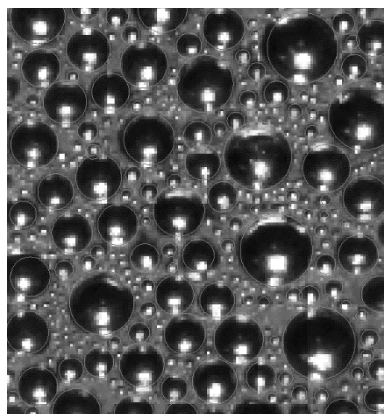
The empirical formula proposed by Rose tends to underestimate the measured values, whereas the model proposed by Kim and co-workers tends to overestimate the data. Kim *et al.* formula, while takes into account the surface wettability, does not consider the vapor shear stress which tends to decrease  $r_{max}$ . As reported in Chapter 2, the models are applied from the measured  $r_{max}$  in order to avoid other misleading results. However, in Table 6.3 the advancing, receding and contact angle hysteresis are reported. It is interesting to analyze what is the parameter which much influence the departing radius. If the hysteresis is considered and sorted in ascending order, the departing radii do not follow an ascending order and the same happens proceeding with  $\theta_a$ . If  $\theta_r$  is taken as parameter instead, the droplet departing radius matches a reasonable order, decreasing the receding contact angle the adhesion force increases then the departing radius increases. As reported in paragraph 6.1.3.4, a proper formulation for  $r_{max}$  should be developed.

### 6.2.2 Droplet population

The total heat flux can be calculated if the number of droplets divided per radius are known. The formulation proposed by Le Fevre and Rose

$$N(r) = \frac{1}{3\pi r^2} \left( \frac{r}{r_{max}} \right)^{-\frac{2}{3}}$$

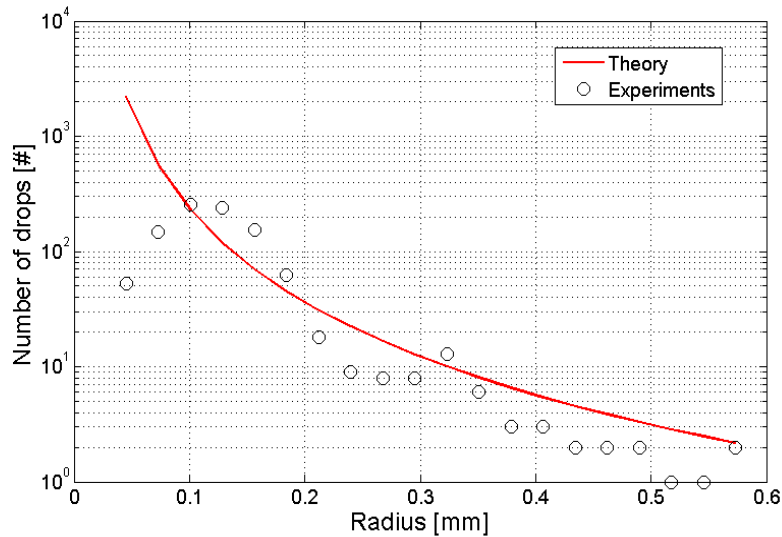
is typically associated to the “big” droplet population. The threshold between the “small” and “big” droplet population should be related to the nucleation site density and even imposing a low value for  $N_s$  ( $10^{10}$ ) the effective radius is around 1  $\mu\text{m}$ . From the videos taken, the minimum radius which can be analyzed is around 100  $\mu\text{m}$ , definitely a small portion of the entire droplet population. An example of the analysis is displayed in Figure 6.12.



**Figure 6.12 - Image taken during DWC. The droplets are fitted with circles.**

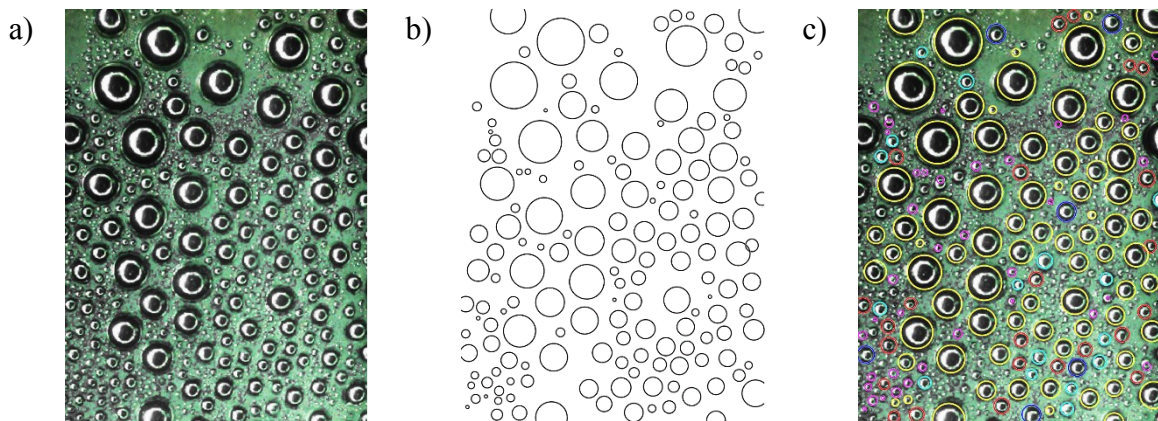


The illumination system did not allow to develop an automatic procedure for the droplet counts, the analysis is reduced to small areas and few images, but Equation 2.67 still was confirmed as can be seen in Figure 6.13. For further details please see Parin *et al.*<sup>103,104</sup>.



**Figure 6.13 - Comparison between model and experiment for droplet population.**

Recently, new effort was put in developing an automatic approach for the droplets count. A toroidal led has been built in order to improve the illumination of the condensing surface. The aim is to form a uniform illumination inside droplets and a high contrast between droplets and background. The difficulty is related on creating a clear limit for the droplets boundary. An example of the recent develop is presented in the following Figure.



**Figure 6.14 - Image processing of DWC phenomenon with a toroidal home-made illumination system.**

### 6.2.3 Model comparison

The model described in Chapter 2 for DWC are here compared with the experimental data. The input parameter for the models are, where possible, taken from experiments. In particular, saturation temperature, the coating thickness, droplet contact angles and droplet departing diameter. The coating conductivity is supposed equal to  $0.2 \text{ W m}^{-2} \text{ K}^{-1}$ , value usually reported for such coatings in models. As discussed in Chapter 2, probably the main resistance is related to the contact resistance between the substrate and the coating, then the nature of coatings becomes less important. The nucleation site density is related to the minimum droplet radius as suggested by Rose<sup>95</sup>. Models with these input parameters are applied to the sol-gel coatings: M7T3\_200, P7T3\_200, M7P3\_200 and P7M3\_200. For the last two, only one point is reported since only duration tests have been performed. The results are listed in Figure 6.15. The Lefevre and Rose model can be applicable only on M7T3\_200 where the measured HTC are very close to the HTC related to the pure DWC<sup>13</sup>, thus where the coating resistance is really low (please refer to paragraph 6.1.3.2). The Abu-Orabi model, as already discussed in Chapter 2, probably has a mistake in its formulation and for this reason it overestimates the HTC. The Chavan and co-workers model tends also to overestimate the HTC as can be expected from model comparison in Chapter 2. The other models fit the all the experimental data within  $\pm 20\%$ . As discussed previously, only the thermal conductivity is supposed by the author, the models are then able to predict quite efficiently the HTC on different substrates with different characteristics. The other big open question is the relationship between the nucleation site density and the minimum radius, i.e. with the heat flux. The present author is sure that a relation exists, but probably not in the terms presented by Rose<sup>95</sup>. The relation should incorporate the wettability of the surface for instance. Supposing the relation wrong and imposing a fixed  $N_s = 10^{11}$  to Chavan *et al.* model, Figure 6.16 is obtained.

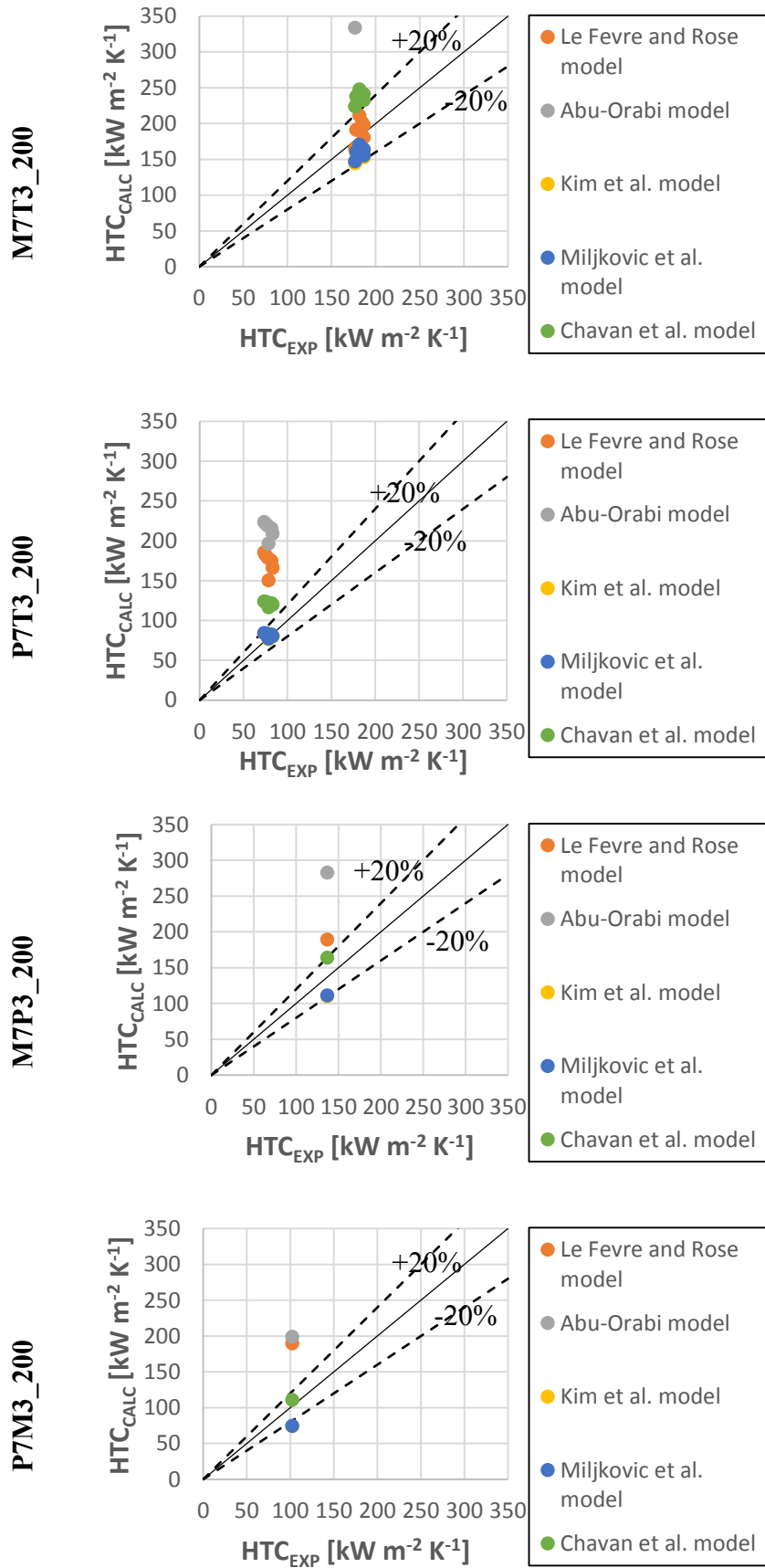
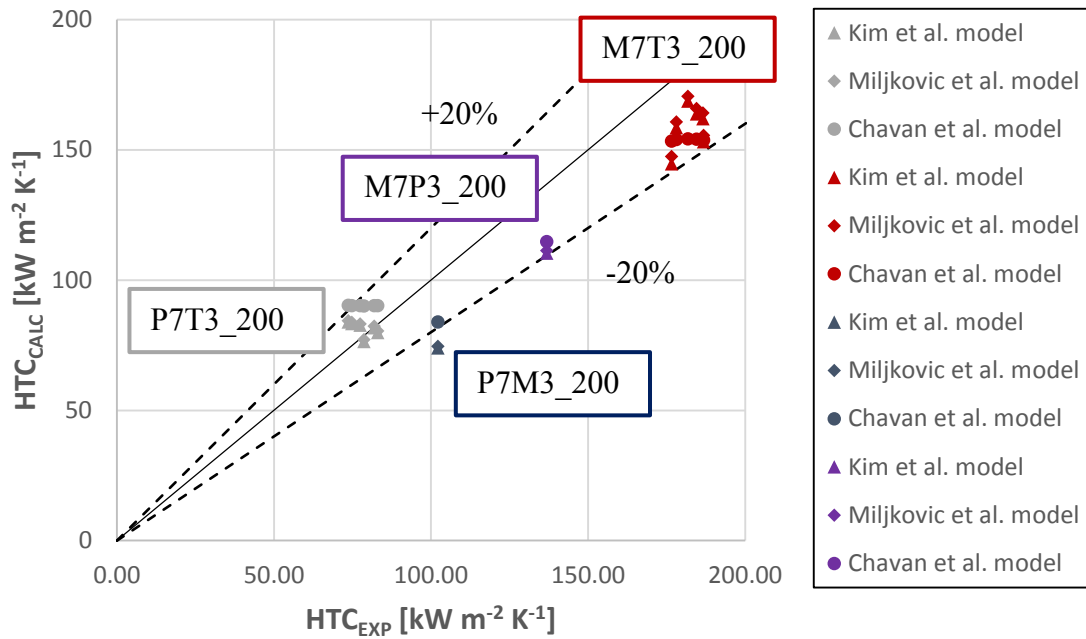
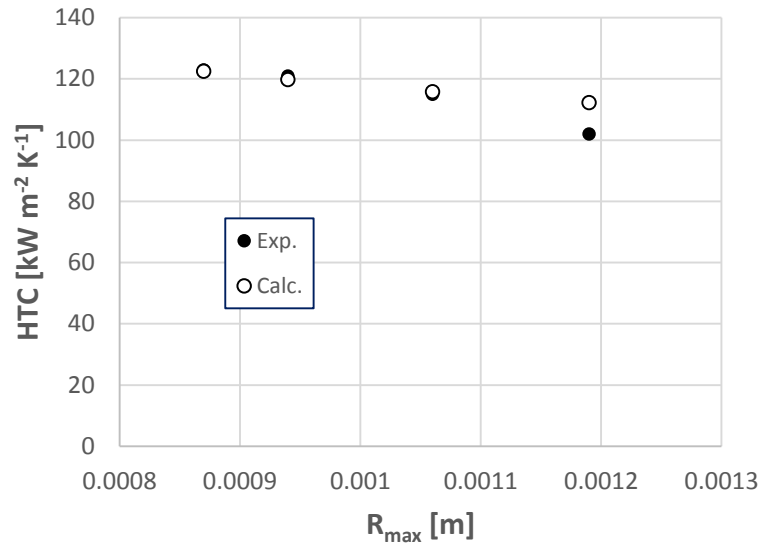


Figure 6.15 - Comparison between calculated and measured HTC during DWC for M7T3\_200, P7T3\_200, M7P3\_200 and P7M3\_200



**Figure 6.16 - Comparison between calculated and measured HTC during DWC for M7T3\_200, P7T3\_200, M7P3\_200 and P7M3\_200. For Chavan *et al.* a fixed  $N_s = 10^{11}$  has been imposed.**

With the new value for Chavan *et al.* the experimental data are better predicted: The value is the same value used in the model comparison in Chapter 2 with which the results predicted by Chavan *et al.* were the same predicted by Kim *et al.* and Miljkovic *et al.*. The issue is if the numerical simulation performed by Chavan and co-workers is right or if the relation for  $N_s$  proposed by Rose and the droplet thermal resistance proposed by Kim *et al.* are right. Probably, upgrading the  $N_s$  formula and using the output of numerical simulation will be the best choice. The model proposed by Miljkovic *et al.* has been used also for predict the HTC at different vapor velocities. The model does not consider any kind of vapor speed influence, however the droplet departing radius can be imposed which should be the only parameter influenced by the vapor shear stress. Results are shown in Figure 6.17.



**Figure 6.17 - Comparison between predicted and measured HTC for different vapor speed. The vapor speed is related to the departing diameter as reported in Figure 6.10.**

Surprisingly, the model underestimates the measured HTC at the minimum vapor speed by around 10 % and fit perfectly the data at higher velocities. The HTC increasing due to the increased shear stress is confirmed by models, confirming that the HTC cannot be increased significantly by working on the vapor speed. The most efficient parameter for the HTC augmentation has been confirmed to be the coating thickness.

# Conclusions

The present work focused on the study of the dropwise condensation phenomenon of pure steam on engineered surfaces. The research started from some preliminary studies and it achieved important results in terms of coating stability, heat transfer measurements and knowledge of the DWC phenomenon.

The initial goal was to develop a chemical treatment to impart hydrophobicity on metal surfaces for DWC promotion. The sol-gel method was chosen since it forms a continuous and long-standing film over the metal surface and, thus, several solutions, with different hydrophobic reagents (FOTS, Graphene, MTES, PhTES, TEOS, ecc...), were applied over aluminium and copper surfaces. The treatments were obtained by varying several parameters of the solution preparation (reagents concentration, dipping velocity, temperature) and the results on the condensation performance have been studied. Two main research branches were identified as hydrophobic coatings (silane-based coatings and graphene coatings), whereas wet-chemical process and aerogel coatings have been applied on substrates obtaining superhydrophobicity. A special effort was spent to characterize properly the surface before and after the condensation tests with the following analyses:

- Sessile drop analysis for static\dynamic contact angles measurements;
- Ellipsometry for the coating thickness measurement;
- Etching method for the coating thickness measurement;
- SEM for the coating morphology identification;
- AFM or 2D-profilometry for the surface roughness measurements;
- FTIR for the chemical bonds identification over the surface;
- Sessile drop method with water and diiodomethane for the surface free energy measurements;
- Raman spectroscopy and Raman map for assessing the graphene presence (where suitable).

The measurements have been performed at the Material Science Engineering laboratory. Several mixtures have been investigated for the dropwise condensation promotion. The mixture between MTES and TEOS with molar ratios of 50 – 50 and 70 – 30 has been heated to three different temperatures 200°C, 300°C and 400°C. The mixture between PhTES and TEOS with molar ratio 70 - 30 has been treated at 200°C and 400°C. The comparison of the characterizations obtained before and after the condensation tests was fundamental to detect the surface characteristics which may

affect the two-phase heat transfer performances. The information collected led to the optimization of the treatments robustness. In particular, the mixture of PhTES and MTES has been developed with two different molar ratios 70 - 30 and 30 - 70 and heated to 200 °C. The treatments presented hydrophobic behaviour, having  $\theta_a = 90^\circ \pm 5^\circ$  and  $\theta_r = 65^\circ \pm 5^\circ$ . The thickness of such coatings varied between 200 nm and 400 nm. Furthermore, graphene coatings have been successfully applied to copper substrate and treated at 500°C. The graphene coatings present a wettability very similar to the wettability of the previous treatments but with much lower thicknesses (estimated at around tens of nm).

Furthermore, some preliminary studies were conducted on treated surfaces in order to further characterize such coatings as frost formation delayers. Bouncing tests of water droplets were performed on five different surfaces with different wetting characteristics from different highs. The aerogel treatment has been identified as the best surface for repel impacting water droplets. The hydrophobic surface resulted to be the best solution for retain water since it does not show droplet fragmentation.

A main objective of the present research was the measurement of the heat transfer coefficient during dropwise condensation on water-repellent surfaces and its enhancement with respect to filmwise mode. The existing experimental apparatus at the Two Phase Heat Transfer Lab of the University of Padova, which allows simultaneously the performance measurement and the visualization of the phenomenon in saturated conditions and with a non-negligible steam velocity, has been used. All the treatments developed during the present research have been tested in this facility. Superhydrophobic surfaces did not sustain DWC for an acceptable amount of time, then only results on hydrophobic coating are discussed. Different types of condensation tests were performed on each treatment:

- Endurance tests: the test conditions are maintained constant for the entire test. The life of a treatment is limited, in fact even if dropwise condensation (DWC) is initially promoted, after a certain period filmwise condensation (FWC) appears, meaning that the layer degrades.
- Performance tests: the operating conditions are varied during the test. Typically, the heat transfer coefficient (HTC) is a function of the difference between the vapor and the surface temperature. With this test, this relationship is assessed.
- Velocity tests: the steam velocity is varied in order to measure the influence of the vapor shear stress on the HTC and on the droplets dynamic.

All the data gathered has been analyzed and evaluated considering the proper uncertainty. Thermodynamic results and high-speed videos have been acquired and analyzed. A wide campaign on untreated surfaces was carried out on the existing experimental apparatus to measure the filmwise condensation heat transfer coefficients with different vapor mass flow rate. The results were compared with filmwise condensation model founded in the literature. Later, the hydrophobic surfaces were tested and the dropwise condensation was observed on the aforementioned coatings. The main thermodynamic results are summarized in the following.

- DWC has been achieved on treated metal surfaces and compared against FWC finding a staggering increase which ranges between 4 and 10 times in terms of HTC. The highest HTC was measured on graphene coatings with  $250 \text{ kW m}^{-2} \text{ K}^{-1}$ .
- Starting from treatments life of minutes, the coating lifetime reached more than 100 hours. The best results in terms of durability were shown by the mixture of PhTES and MTES with a molar ratio of 70 – 30 and heated to  $200^\circ\text{C}$ .
- The vapor velocity influence on the HTC during DWC and on droplets dynamic have been assessed. The steam speed has a strong impact on the characteristics of the drops; as the speed increases, there is a progressive decrease in the average size of the departing drops, which sweep more frequently the sample surface. However, the HTC augmentation is very limited (around 20%)

Other important interesting results obtained during DWC test are:

- The lifetime of a treatment is affected by the heat flux. In particular, the mixture MTES – TEOS (70 – 30 molar ratio,  $200^\circ\text{C}$  baking temperature) has been tested with two different imposed heat fluxes:  $400 \text{ kW m}^{-2}$  and  $130 \text{ kW m}^{-2}$ . At the lowest heat flux, the coating lifetime increased by 10 times as compared to the highest heat flux.
- The lifetime of a treatment is not affected by the substrate. The same coating deposited on aluminium and copper substrate showed the same behaviour in terms of performance and durability.
- The coating thickness strongly influence the heat transfer coefficient during dropwise condensation. Doubling the coating thickness entails a heat transfer coefficient drop of 50 %. The phenomenon is confirmed both theoretically and experimentally.
- The receding contact angle has a crucial role in the DWC promotion. From videos analysis for the estimation of the heat flux, the receding contact angle seems to be the growing contact



angle in saturated conditions. It plays also a crucial role in the transition between filmwise and dropwise condensation mode. Wettability characterization of untreated, which promoted filmwise condensation, and treated surfaces, which promoted dropwise condensation, after condensation tests showed similar advancing contact angle but different receding contact angle. However, further analyses are needed for the confirmation of the phenomenon, such as direct wettability measurement during condensation tests.

Several videos of dropwise condensation at different operating conditions were recorded by means of high speed camera, which were useful to analyze the relationship between the measured heat transfer coefficient and the surface wettability. Other fundamental parameters of DWC were measured, e.g. droplet departing diameter, droplet population and sweeping period. From measurement of the droplet population at different time-steps it was possible to develop a new method for determining the condensate mass flow rate during DWC.

The amount of data collected during the experimental campaign was the basis for understanding the dropwise condensation phenomena and it was compared to available models found in literature: Le Fevre and Rose model (1966), Abu-Orabi model (1998), Kim *et al.* model (2011), Miljkovic *et al.* model (2013) and Chavan *et al.* model (2016).

The more recent models showed a good agreement ( $\pm 20\%$ ) with the experimental data obtained on different coating. Furthermore, a theoretical study of conduction inside nanolayer has been conducted strengthening the theoretical knowledge about DWC model. Since Fourier's law cannot be applicable on such thin coatings, other models should be applied for the estimation of the coating thermal resistance. The contact resistance between the substrate and the coating seemed to be the biggest obstacle on the thermal exchange at the nanoscale.

The research on dropwise condensation still need further analyses and experimental data, though. Besides finding new endurance solutions in terms of coating stability maintaining high heat transfer coefficients over time, several other aspects should be investigated or assessed. The missing fundamental characterization is the measure of coatings thermal resistance, which should verify its strong influence on the HTC during DWC of saturated steam. A considerable amount of videos have been collected which should be systematically analyzed in order to confirm the formulation of "big" droplets population and its independence by the heat flux and coating composition. Using special camera lens and a proper illumination the visible droplets size should decrease; this approach is

important for the verification of the formulation at the microscale. The vapor shear stress influence analysis is still in a beginning phase, the relationship between external forces and droplet departing radius is not enough understood. At the end, it will be interesting to investigate the surfaces developed and tested during these years in different test conditions, e.g. during humid air condensation and frost formation, which should reveal, in my opinion, interesting results in terms of life duration.



# Nomenclature

$A$  = area, m<sup>2</sup>

$A_1, A_2, A_3$  = coefficients, -

$A_c$  = droplet lateral area, m<sup>2</sup>

$A_{ls}$  = droplet wet area, m<sup>2</sup>

$B_1, B_2$  = coefficients, -

$Bi$  = Biot Number, -

$C$  = integral constant, -

$C_d$  = drag coefficient, -

$c_p$  = specific heat capacity, J kg<sup>-1</sup> K<sup>-1</sup>

$d$  = pillar diameter, m

$D_h$  = hydraulic diameter, m

$\frac{d}{dy}$  = gradient along  $y$  axis, m<sup>-1</sup>

$\frac{d}{dz}$  = gradient along  $z$  axis, m<sup>-1</sup>

$dz$  = derivate of length along  $z$  axis, m

$\left(\frac{dp}{dz}\right)_F$  = two-phase frictional pressure gradient, Pa m<sup>-1</sup>

$E$  = coefficient, -

$F$  = coefficient, -

$F_A$  = droplet moving adhesive force, N

$F_{adhesive}$  = droplet static adhesive force, N

$F_{cohesive}$  = droplet static cohesive force, N

$F_D$  = drag force, N

$F_G$  = gravity force, N

$F_R$  = droplet static resulting force, N

$Fr$  = Froude number, -

$f_1, f_2$  = area fraction of component 1,2, -

$f_r$  = the roughness factor, -

$f$  = fraction of surface area covered by drops, -

$G$  = moisture specific mass flow rate, kg s<sup>-1</sup>

$G$  = droplet growth rate,  $\text{m s}^{-1}$   
 $H$  = coefficient, -  
 $h$  = latent heat,  $\text{J kg}^{-1}$   
 $h$  = pillar height, m  
 $HTC$  = heat transfer coefficient, W or kW  $\text{m}^{-2} \text{K}^{-1}$   
 $g$  = gravity acceleration,  $\text{m s}^{-2}$   
 $k$  = non-circular perimeter factor, -  
 $k$  = uncertainty cover factor, -  
 $K_1$  = factor, -  
 $K_2$  = factor, -  
 $K_3$  = factor, -  
 $L$  = length, m  
 $l$  = pillar center-to-center spacing, m  
 $l_c$  = average condensing droplet spacing, m  
 $\dot{m}$  = mass flux,  $\text{kg s}^{-1}$   
 $N$  = droplet “big” population,  $\text{m}^{-3}$   
 $n$  = droplet “small” population,  $\text{m}^{-3}$   
 $N_s$  = nucleation site density,  $\text{m}^{-2}$   
 $Nu$  = Nusselt number, -  
 $P$  = perimeter, m  
 $p$  = pressure, Pa  
 $Pr$  = Prandtl number, -  
 $P_w$  = droplet wet perimeter, m  
 $\dot{q}$  = heat flux,  $\text{W m}^{-2}$   
 $q_b$  = heat flux through the base of a hemispherical drop,  $\text{W m}^{-2}$   
 $R$  = gas constant,  $\text{J K}^{-1} \text{mol}^{-1}$   
 $r'$  = latent heat of vaporization,  $\text{J kg}^{-1}$   
 $r$  = droplet radius, m  
 $r$  = roughness degree, -  
 $r_{min}$  = droplet minimum radius, m  
 $r_{var}$  = droplet variable radius, m  
 $Re$  = Reynolds number, -  
 $S$  = cross section,  $\text{m}^2$   
 $T$  = temperature, K

$u$  = velocity,  $\text{m s}^{-1}$   
 $u_a, u_b$  = type A and B uncertainty, -  
 $u_c$  = combined uncertainty, -  
 $\bar{u}$  = mean velocity,  $\text{m s}^{-1}$   
 $V$  = droplet volume,  $\text{m}^3$   
 $v$  = specific volume,  $\text{m}^3 \text{kg}^{-1}$   
 $x$  = vapor quality, -  
 $y$  = perpendicular axis, m  
 $W_a$  = adhesive energy, J  
 $w_a$  = specific adhesive energy,  $\text{N m}^{-1}$   
 $w_c$  = specific cohesive energy,  $\text{N m}^{-1}$   
 $We$  = Weber number, -  
 $z$  = longitudinal axis, m

*Greek symbols:*

$\alpha$  = heat transfer coefficient,  $\text{W m}^{-2} \text{K}^{-1}$   
 $\bar{\alpha}$  = mean heat transfer coefficient,  $\text{W m}^{-2} \text{K}^{-1}$   
 $\gamma$  = specific heat capacity ratio, -  
 $\gamma_{sg}$  = superficial tension between solid and gas,  $\text{N m}^{-1}$   
 $\gamma_{lg}$  = superficial tension between liquid and gas,  $\text{N m}^{-1}$   
 $\gamma_{ls}$  = superficial tension between solid and liquid,  $\text{N m}^{-1}$   
 $\delta$  = thickness, m  
 $\Delta\theta$  = contact angle hysteresis,  $^\circ$   
 $\Delta T_{ml}$  = logarithmic mean temperature difference, K,  $^\circ\text{C}$   
 $\zeta$  = ratio of the principal specific heat capacities, -  
 $\Phi^2$  = two-phase multiplier, -  
 $\varepsilon'$  = turbulent flow diffusivity,  $\text{m}^3 \text{s}^{-1}$   
 $\theta$  = Young\equilibrium contact angle,  $^\circ$   
 $\theta_a$  = advancing contact angle,  $^\circ$   
 $\theta_c$  = Cassie – Baxter contact angle,  $^\circ$   
 $\theta_r$  = receding contact angle,  $^\circ$   
 $\theta_w$  = Wenzel contact angle,  $^\circ$   
 $\lambda$  = thermal conductivity,  $\text{W m}^{-1} \text{K}^{-1}$   
 $\mu$  = dynamic viscosity, Pa s

$\rho$  = density, kg m<sup>-3</sup>

$\sigma$  = surface tension, N m<sup>-1</sup>

$\tau$  = droplet sweeping period, s<sup>-1</sup>

$\tau$  = shear stress, Pa

$\tau_i$  = shear stress at the liquid-vapor interface, Pa

$\tau_0$  = shear stress at the solid-liquid interface, Pa

$\Gamma$  = condensate mass flux per unit width, kg s<sup>-1</sup>

*Subscripts:*

*b* = base

*BC* = boiling chamber

*coat* = coating

*cool* = coolant

*d* = droplet

*E* = equilibrium

*e* = effective

*l* = liquid

*LO* = liquid only

*F* = friction

*GRAV* = gravitational

*g* = gas

*H* = homogenous

*in* = inlet

*max* = maximum

*mid* = middle

*min* = minimum

*Nu* = Nusselt

*out* = outlet

*S* = slip

*s* = solid

*SAT* = saturation

*SS* = shear stress

*TP* = thermopile

*WALL* = surface

*v* = vapor





# Bibliography

1. Molly Maupin, Joan Kenny, Susan Hutson, John Lovelace, Nancy Barber, K. L. *Estimated Use of Water in the United States in 2010*. US Geological Survey. **1405**, (2010).
2. Khawaji, A. D., Kutubkhanah, I. K. & Wie, J. M. Advances in seawater desalination technologies. *Desalination* **221**, 47–69 (2008).
3. Tomaszewicz, M., Abou Najm, M., Beysens, D., Alameddine, I. & El-Fadel, M. Dew as a sustainable non-conventional water resource: A critical review. *Environ. Rev.* **23**, (2015).
4. Enright, R., Miljkovic, N., Alvarado, J. L., Kim, K. & Rose, J. W. Dropwise Condensation on Micro- and Nanostructured Surfaces. *Nanoscale Microscale Thermophys. Eng.* **18**, 223–250 (2014).
5. Parin, R., Del Col, D., Bortolin, S. & Martucci, A. Dropwise condensation over superhydrophobic aluminium surfaces. *J. Phys. Conf. Ser.* **745**, 032134 (2016).
6. Torresin, D., Tiwari, M. K., Del Col, D. & Poulikakos, D. Flow condensation on copper-based nanotextured superhydrophobic surfaces. *Langmuir* **29**, 840–848 (2013).
7. Rykaczewski, K. *et al.* Dropwise condensation of low surface tension fluids on omniphobic surfaces. *Sci. Rep.* **4**, 4158/1-4158/8 (2014).
8. Lafuma, A. & Quéré, D. Superhydrophobic states. *Nat. Mater.* **2**, 457–60 (2003).
9. Gao, L. & McCarthy, T. J. How Wenzel and Cassie were wrong. *Langmuir* **23**, 3762–3765 (2007).
10. Quéré, D. Non-sticking drops. *Reports Prog. Phys.* **68**, 2495–2532 (2005).
11. Bhushan, B. & Jung, Y. C. Natural and biomimetic artificial surfaces for superhydrophobicity, self-cleaning, low adhesion, and drag reduction. *Prog. Mater. Sci.* **56**, 1–108 (2011).
12. de Gennes, P. G., Brochard-Wyart, F. & Quere, D. *Capillarity and Wetting Phenomena: Drops, Bubbles, Pearls, Waves*. (Springer New York, 2003).
13. Rose, J. W. Dropwise condensation theory and experiment: a review. *Proc. Inst. Mech. Eng. Part A J. Power Energy* **216**, 115–128 (2002).
14. Bani Kananeh, a., Rausch, M. H., Fröba, a. P. & Leipertz, a. Experimental study of dropwise condensation on plasma-ion implanted stainless steel tubes. *Int. J. Heat Mass Transf.* **49**, 5018–5026 (2006).
15. Choi, W. T., Oh, K., Singh, P. M., Breedveld, V. & Hess, D. W. Wettability control of stainless steel surfaces via evolution of intrinsic grain structures. *J. Mater. Sci.* **51**, 5196–5206 (2016).
16. Kananeh, A. B., Rausch, M. H., Leipertz, A. & Fröba, A. P. Dropwise Condensation Heat Transfer on Plasma-Ion-Implanted Small Horizontal Tube Bundles. *Heat Transf. Eng.* **31**,

821–828 (2010).

17. Watanabe, N. & Aritomi, M. Correlative relationship between geometric arrangement of drops in dropwise condensation and heat transfer coefficient. *Int. J. Heat Mass Transf.* **105**, 597–609 (2017).
18. Enright, R., Miljkovic, N., Dou, N., Nam, Y. & Wang, E. N. Condensation on Superhydrophobic Copper Oxide Nanostructures. *J. Heat Transfer* **135**, 091304 (2013).
19. Roudgar, M. & De Coninck, J. Condensation heat transfer coefficient versus wettability. *Appl. Surf. Sci.* **338**, 15–21 (2015).
20. Schrader, M. E. Wettability of clean metal surfaces. *J. Colloid Interface Sci.* **100**, 372–380 (1984).
21. Vemuri, S., Kim, K. J., Wood, B. D., Govindaraju, S. & Bell, T. W. Long term testing for dropwise condensation using self-assembled monolayer coatings of n-octadecyl mercaptan. *Appl. Therm. Eng.* **26**, 421–429 (2006).
22. Preston, D. J., Mafra, D. L., Miljkovic, N., Kong, J. & Wang, E. N. Scalable Graphene Coatings for Enhanced Condensation Heat Transfer. *Nano Lett.* **15**, 2902–2909 (2015).
23. Paxson, A. T., Yagüe, J. L., Gleason, K. K. & Varanasi, K. K. Stable dropwise condensation for enhancing heat transfer via the initiated chemical vapor deposition (iCVD) of grafted polymer films. *Adv. Mater.* **26**, 418–423 (2014).
24. Rausch, M. H., Fröba, a. P. & Leipertz, a. Dropwise condensation heat transfer on ion implanted aluminum surfaces. *Int. J. Heat Mass Transf.* **51**, 1061–1070 (2008).
25. June, B., Kuok, C., Jin, K., Hwang, T. & Yoon, H. International Journal of Heat and Mass Transfer Dropwise steam condensation on various hydrophobic surfaces: Polyphenylene sulfide ( PPS ), polytetrafluoroethylene ( PTFE ), and self-assembled micro / nano silver ( SAMS ). *Int. J. Heat Mass Transf.* **89**, 353–358 (2015).
26. Miljkovic, N., Enright, R. & Wang, E. N. Modeling and Optimization of Superhydrophobic Condensation. *J. Heat Transfer* **135**, 111004 (2013).
27. Kim, S. & Kim, K. J. Dropwise Condensation Modeling Suitable for Superhydrophobic Surfaces. *J. Heat Transfer* **133**, 081502 (2011).
28. Tsuchiya, H. *et al.* Improvement of heat transfer by promoting dropwise condensation using electrospun polytetrafluoroethylene thin films. *New J. Chem.* **41**, 982–991 (2017).
29. Tsuchiya, H. *et al.* Liquid-Infused Smooth Surface for Improved Condensation Heat Transfer. *Langmuir* **33**, 8950–8960 (2017).
30. Mahapatra, P. S., Ghosh, A., Ganguly, R. & Megaridis, C. M. Key design and operating parameters for enhancing dropwise condensation through wettability patterning. *Int. J. Heat*

- Mass Transf.* **92**, 877–883 (2016).
31. Hwang, K. W. *et al.* Effects of heat flux on dropwise condensation on a superhydrophobic surface. *J. Mech. Sci. Technol.* **30**, 2141–2149 (2016).
  32. Shigeo, H. & Hiroaki, T. Dropwise condensation of steam at low pressures. *Int. J. Heat Mass Transf.* **30**, 497–507 (1987).
  33. Wenzel, R. Resistance of solid surfaces to wetting by water. *Ind. Eng. Chem.* **28**, 988–994 (1936).
  34. Cassie, A. B. D. & Baxter, S. Wettability of porous surfaces. *Trans. Faraday Soc.* **40**, 546–551 (1944).
  35. Gao, L. & McCarthy, T. J. Contact angle hysteresis explained. *Langmuir* **22**, 6234–6237 (2006).
  36. Lam, C. N. C., Wu, R., Li, D., Hair, M. L. & Neumann, a W. Study of the advancing and receding contact angles: liquid sorption as a cause of contact angle hysteresis. *Adv. Colloid Interface Sci.* **96**, 169–91 (2002).
  37. Fernandez-Toledano, J. C., Blake, T. D., Lambert, P. & De Coninck, J. On the cohesion of fluids and their adhesion to solids: Young’s equation at the atomic scale. *Adv. Colloid Interface Sci.* **245**, 102–107 (2017).
  38. Nosonovsky, M. & Bhushan, B. Roughness-induced superhydrophobicity: a way to design non-adhesive surfaces. *J. Phys. Condens. Matter* **20**, 225009 (2008).
  39. Nosonovsky, M. & Bhushan, B. Hierarchical roughness optimization for biomimetic superhydrophobic surfaces. *Ultramicroscopy* **107**, 969–979 (2007).
  40. Öner, D. & McCarthy, T. J. Ultrahydrophobic surfaces. Effects of topography length scales on wettability. *Langmuir* **16**, 7777–7782 (2000).
  41. Jagdheesh, R., Pathiraj, B., Karatay, E., Römer, G. R. B. E. & Huis In’T Veld, a. J. Laser-induced nanoscale superhydrophobic structures on metal surfaces. *Langmuir* **27**, 8464–8469 (2011).
  42. Miljkovic, N. *et al.* Jumping-droplet-enhanced condensation on scalable superhydrophobic nanostructured surfaces. *Nano Lett.* **13**, 179–187 (2013).
  43. Enright, R., Miljkovic, N., Al-Obeidi, A., Thompson, C. V & Wang, E. N. Condensation on superhydrophobic surfaces: the role of local energy barriers and structure length scale. *Langmuir* **28**, 14424–32 (2012).
  44. Del Col, D., Parin, R., Bisetto, A., Bortolin, S. & Martucci, A. Film condensation of steam flowing on a hydrophobic surface. *Int. J. Heat Mass Transf.* **107**, 307–318 (2017).
  45. Zhong, L., Xuehu, M., Sifang, W., Mingzhe, W. & Xiaonan, L. Effects of surface free energy

- and nanostructures on dropwise condensation. *Chem. Eng. J.* **156**, 546–552 (2010).
46. Qu, X. *et al.* Self-propelled sweeping removal of dropwise condensate. *Appl. Phys. Lett.* **106**, 1–5 (2015).
  47. Chen, X. *et al.* Nanograssed micropyrnidal architectures for continuous dropwise condensation. *Adv. Funct. Mater.* **21**, 4617–4623 (2011).
  48. Traipattanakul, B., Tso, C. Y. & Chao, C. Y. H. Study of jumping water droplets on superhydrophobic surfaces with electric fields. *Int. J. Heat Mass Transf.* **115**, 672–681 (2017).
  49. Golovin, K. *et al.* Designing durable icephobic surfaces. (2016).
  50. Khedir, K. R., Kannarpady, G. K., Ryerson, C. & Biris, A. S. An outlook on tunable superhydrophobic nanostructural surfaces and their possible impact on ice mitigation. *Prog. Org. Coatings* **112**, 304–318 (2017).
  51. Momen, G., Jafari, R. & Farzaneh, M. Ice repellency behaviour of superhydrophobic surfaces : Effects of atmospheric icing conditions and surface roughness. *Appl. Surf. Sci.* **349**, 211–218 (2015).
  52. Bharathidasan, T., Kumar, S. V., Bobji, M. S., Chakradhar, R. P. S. & Basu, B. J. Effect of wettability and surface roughness on ice-adhesion strength of hydrophilic , hydrophobic and superhydrophobic surfaces. *Appl. Surf. Sci.* **314**, 241–250 (2014).
  53. Kim, M., Kim, H., Lee, K. & Kim, D. R. Frosting characteristics on hydrophobic and superhydrophobic surfaces : A review. *Energy Convers. Manag.* **138**, 1–11 (2017).
  54. Amer, M. & Wang, C. Review of defrosting methods. *Renew. Sustain. Energy Rev.* **73**, 53–74 (2017).
  55. Maitra, T. *et al.* Hierarchically nanotextured surfaces maintaining superhydrophobicity under severely adverse conditions. *Nanoscale* **6**, 8710–8719 (2014).
  56. Bernagozzi, I., Antonini, C., Villa, F. & Marengo, M. Fabricating superhydrophobic aluminum: An optimized one-step wet synthesis using fluoroalkyl silane. *Colloids Surfaces A Physicochem. Eng. Asp.* **441**, 919–924 (2014).
  57. Song, J. *et al.* Ultrafast fabrication of rough structures required by superhydrophobic surfaces on Al substrates using an immersion method. *Chem. Eng. J.* **211–212**, 143–152 (2012).
  58. Schmidt, E., Schurig, W. & Sellschopp, W. Versuche über die kondensation von wasserdampf in film- und tropfenform. *Forsch. im Ingenieurwes.* **12**, 53–63 (1930).
  59. Parin, R., Del Col, D., Bortolin, S. & Martucci, A. Dropwise condensation over superhydrophobic aluminium surfaces. *J. Phys. Conf. Ser.* **745**, (2016).
  60. Davies, G. A., Mojtehed, W. & Ponter, A. B. Measurement of contact angles under condensation conditions. The prediction of dropwise-filmwise transition. *Int. J. Heat Mass*

- Transf.* **14**, 709–713 (1971).
61. Neumann, A. w., Abdelmessih, A. h. & Hameed, a. The role of contact angles and contact angle hysteresis in dropwise condensation heat transfer. *Int. J. Heat Mass Transf.* **21**, 947–953 (1978).
  62. Fernandez-Toledano, J. C., Blake, T. D. & De Coninck, J. Young's Equation for a Two-Liquid System on the Nanometer Scale. *Langmuir* **33**, 2929–2938 (2017).
  63. Van Oss, C., Good, R., Chaudhury, M. & Oss, C. Additive and nonadditive surface tension components and the interpretation of contact angles. *Langmuir* **4**, 884–891 (1988).
  64. Law, B. M. *et al.* Line tension and its influence on droplets and particles at surfaces. *Prog. Surf. Sci.* **92**, 1–39 (2017).
  65. Padday, J. F. & Uffindell, N. D. The calculation of cohesive and adhesive energies from intermolecular forces at a surface. *J. Phys. Chem.* **76**, 1407–1414 (1968).
  66. Lauga, E., Brenner, M. P. & Stone, H. A. *Microfluidics: The No-Slip Boundary Condition.* (2007).
  67. Young, T. III. An essay on the cohesion of fluids. *Philos. Trans. R. Soc. London* **95**, 65–87 (1805).
  68. Chibowski, E. On some relations between advancing, receding and Young's contact angles. *Adv. Colloid Interface Sci.* **133**, 51–59 (2007).
  69. Wenzel, R. N. Resistance of solid surfaces to wetting by water. *J. Ind. Eng. Chem. (Washington, D. C.)* **28**, 988–994 (1936).
  70. Bico, J., Tordeux, C. & Quéré, D. Rough wetting. *Europhys. Lett.* **55**, 214–220 (2001).
  71. Milne, A. J. B. & Amirfazli, A. The Cassie equation: How it is meant to be used. *Adv. Colloid Interface Sci.* **170**, 48–55 (2012).
  72. Weisensee, P. B., Neelakantan, N. K., Suslick, K. S., Jacobi, A. M. & King, W. P. Impact of air and water vapor environments on the hydrophobicity of surfaces. *J. Colloid Interface Sci.* **453**, 177–185 (2015).
  73. Fowkes, F. M. *Contact Angle, Wettability, and Adhesion.* (AMERICAN CHEMICAL SOCIETY, 1964). doi:10.1021/ba-1964-0043
  74. Bico, J., Thiele, U. & Quéré, D. Wetting of textured surfaces. *Colloids Surfaces A Physicochem. Eng. Asp.* **206**, 41–46 (2002).
  75. Conti, J., De Coninck, J. & Ghazzal, M. N. Design of water-repellant coating using dual scale size of hybrid silica nanoparticles on polymer surface. *Appl. Surf. Sci.* **436**, 234–241 (2018).
  76. De Coninck, J., Dunlop, F. & Huillet, T. Wetting in 1 + 1 dimensions with two-scale roughness. *Phys. A Stat. Mech. its Appl.* **438**, 398–415 (2015).

77. Cheng, J., Vandadi, A. & Chen, C.-L. Condensation heat transfer on two-tier superhydrophobic surfaces. *Appl. Phys. Lett.* **101**, 131909 (2012).
78. Wang, S. & Jiang, L. Definition of superhydrophobic states. *Adv. Mater.* **19**, 3423–3424 (2007).
79. Law, K.-Y. Definitions for Hydrophilicity, Hydrophobicity, and Superhydrophobicity: Getting the Basics Right. *J. Phys. Chem. Lett.* **5**, 686–688 (2014).
80. Rose, J. W. Dropwise condensation theory and experiment: A review. *Proc. Inst. Mech. Eng. Part A J. Power Energy* **216**, 115–128 (2002).
81. Parin, R., Del Col, D. & Bisetto, A. Experimental and theoretical analysis of condensation over nanoengineered surfaces. (2015).
82. Nusselt, W. Die Oberflächenkondensation des Wasserdampfes. *Z. Verein. Deutsch. Ing.* **60**, 541–546, 569–575 (1916).
83. Rose, J. W. Condensation Heat Transfer Fundamentals. *Chem. Eng. Res. Des.* **76**, 143–152 (1998).
84. Baehr, H. D., Stephan, K. Wärme- und Stoffübertragung. *Springer-Verlag* (2004).
85. Chen, M. M. An Analytical Study of Laminar Film Condensation: Part 1—Flat Plates. *J. Heat Transfer* **83**, 48–54 (1961).
86. Depew, C. A. & Reisbig, R. L. Vapor condensation on a horizontal tube using teflon to promote dropwise condensation. *Ind. Eng. Chem. Process Des. Dev.* **3**, 365–369 (1964).
87. Mayhew, Y. R., Griffiths, D. J. & Phillips, J. W. Effect of Vapour Drag on Laminar Film Condensation on a Vertical Surface. *Proc. Inst. Mech. Eng. Conf. Proc.* **180**, 280–287 (1965).
88. Carpenter, E. F. & Colburn, A. P. The effect of vapour velocity on condensation inside tubes. in *ASME, General Discussion on Heat Transfer* (1951).
89. Friedel, L. Improved friction pressure drop correlations for horizontal and vertical two-phase pipe flow. in *Proceedings of the European Two-phase Group Meeting, Ispra, Italy, Paper E2* (1979).
90. Churchill, S. W. Comprehensive Correlating Equations for Heat, Mass and Momentum Transfer in Fully Developed Flow in Smooth Tubes. *Ind. Eng. Chem. Fundam.* **16**, 109–116 (1977).
91. Butterworth, D. in *Heat Exchanger Design Handbook* (1983).
92. Khandekar, S. & Muralidhar, K. *Dropwise Condensation on Inclined Textured Surfaces*. (Springer, 2014).
93. Schmidt, E., Schurig, W., Sellschopp, W. Versuche über die kondensation von wasserdampf in film- und tropfenform. *Forsch. im Ingenieurwes.* **1**, 53–63 (1930).

94. E. J. Le Fevre, J. W. R. Heat-Transfer Measurements During Condensation of Steam. *Sci. York* 272–273 (1963).
95. Rose, J. W. Further aspects of dropwise condensation theory. *Int. J. Heat Mass Transf.* **19**, 1363–1370 (1976).
96. Stylianou, S. A. & Rose, J. W. Dropwise Condensation of Surfaces Having Different Thermal Conductivities. *Am. Soc. Mech. Eng. Appl. Mech. Div. AMD* **102**, 69–77 (1979).
97. Citakoglu, E. & Rose, J. W. Dropwise condensation-some factors influencing the validity of heat-transfer measurements. *Int. J. Heat Mass Transf.* **11**, 523–537 (1968).
98. Rose, J. W. On the mechanism of dropwise condensation. *Int. J. Heat Mass Transf.* **10**, 755–762 (1967).
99. Rose, J. W. Personal reflections on fifty years of condensation heat transfer research. *J. Enhanc. Heat Transf.* **22**, 89–120 (2015).
100. Rose, J. W. Dropwise condensation theory. *Int. J. Heat Mass Transf.* **24**, 191–194 (1981).
101. Abu-Orabi, M. Modeling of heat transfer in dropwise condensation. *Int. J. Heat Mass Transf.* **41**, 81–87 (1998).
102. Chavan, S. *et al.* Heat Transfer through a Condensate Droplet on Hydrophobic and Nanostructured Superhydrophobic Surfaces. *Langmuir* **32**, 7774–7787 (2016).
103. Parin, R., Penazzato, A., Bortolin, S. & Col, D. Del. Modeling of Dropwise Condensation on Flat Surfaces. *13th Int. Conf. Heat Transf. Fluid Mech. Thermodyn. Portorož, 17-19 July* (2017).
104. Penazzato, A., Parin, R. & Del Col, D. Studio della condensazione a gocce attraverso i modelli e le immagini. (2017).
105. Sameer, K. & Krishnamurthy, M. *Dropwise Condensation on Inclined Textured Surfaces.* (2014).
106. Bonner, R. W. Correlation for dropwise condensation heat transfer: Water, organic fluids, and inclination. *Int. J. Heat Mass Transf.* **61**, 245–253 (2013).
107. Wen, H. W. & Jer, R. M. On the heat transfer in dropwise condensation. *Chem. Eng. J.* **12**, 225–231 (1976).
108. Lee, S. *et al.* A dropwise condensation model using a nano-scale, pin structured surface. *Int. J. Heat Mass Transf.* **60**, 664–671 (2013).
109. Oh, J. *et al.* Jumping-droplet electronics hot-spot cooling. *Appl. Phys. Lett.* **110**, 1–6 (2017).
110. Miljkovic, N., Preston, D. J., Enright, R. & Wang, E. N. Electric-field-enhanced condensation on superhydrophobic nanostructured surfaces. *ACS Nano* **7**, 11043–11054 (2013).
111. Fatica, N. & Katz, D. L. Dropwise condensation. *Chem. Eng. Prog.* **45**, 661–674 (1949).



112. Gose, E. E., Mucciardi, A. N. & Baer, E. Model for dropwise condensation on randomly distributed sites. *Int. J. Heat Mass Transf.* **10**, 15–22 (1967).
113. Rose, J. W. & Glicksman, L. R. Dropwise condensation—The distribution of drop sizes. *Int. J. Heat Mass Transf.* **16**, 411–425 (1973).
114. Maa, J. R. Drop size distribution and heat flux of dropwise condensation. *Chem. Eng. J.* **16**, 171–176 (1978).
115. Tianqing, L., Chunfeng, M., Xiangyu, S. & Songbai, X. Mechanism study on formation of initial condensate droplets. *AIChE J.* **53**, 1050–1055 (2007).
116. Yongji, S., Dunqi, X., Jifang, L. & Siexong, T. A study on the mechanism of dropwise condensation. *Int. J. Heat Mass Transf.* **34**, 2827–2831 (1991).
117. Kaviany, M. *Essentials of heat transfer*. (2011).
118. Liu, X. & Cheng, P. Lattice Boltzmann simulation for dropwise condensation of vapor along vertical hydrophobic flat plates. *Int. J. Heat Mass Transf.* **64**, 1041–1052 (2013).
119. Wu, W. H. & Maa, J. R. A mechanism for dropwise condensation and nucleation. *Chem. Eng. J.* **11**, 143–146 (1976).
120. Burnside, B. M. & Hadi, H. A. Digital computer simulation of dropwise condensation from equilibrium droplet to detectable size. *Int. J. Heat Mass Transf.* **42**, 3137–3146 (1999).
121. Qi, B., Wei, J., Zhang, L. & Xu, H. A fractal dropwise condensation heat transfer model including the effects of contact angle and drop size distribution. *Int. J. Heat Mass Transf.* **83**, 259–272 (2015).
122. Liu, X. & Cheng, P. Dropwise condensation theory revisited: Part I. Droplet nucleation radius. *Int. J. Heat Mass Transf.* **83**, 833–841 (2015).
123. Liu, X. & Cheng, P. Dropwise condensation theory revisited Part II. Droplet nucleation density and condensation heat flux. *Int. J. Heat Mass Transf.* **83**, 842–849 (2015).
124. Graham, C. & Griffith, P. Drop size distributions and heat transfer in dropwise condensation. *Int. J. Heat Mass Transf.* **16**, 337–346 (1973).
125. Mu, C., Pang, J., Lu, Q. & Liu, T. Effects of surface topography of material on nucleation site density of dropwise condensation. *Chem. Eng. Sci.* **63**, 874–880 (2008).
126. Dimitrakopoulos, P. & Higdon, J. J. L. On the displacement of three-dimensional fluid droplets from solid surfaces in low-Reynolds-number shear flows. *J. Fluid Mech.* **377**, 189–222 (1998).
127. Parin, R., Bortolin, S., Martucci, A. & Col, D. Del. Dropwise condensation of flowing saturated steam: experimental results and modeling. in *10th International Conference on Boiling and Condensation Heat Transfer, 12th-15th March 2018 in Nagasaki, Japan* (2018).
128. Tanaka, H. A Theoretical Study of Dropwise Condensation. *J. Heat Transfer* **97**, 72–78 (1975).

129. Schrage, R. A theoretical study of interphase mass transfer. (1953).
130. Umur, A. & Griffith, P. Mechanism of Dropwise Condensation. *J. Heat Transfer* **87**, 275–282 (1965).
131. Cai, S. Q. & Bhunia, A. Dropwise Condensation on/in High Roughness Structures. *J. Heat Transfer* **139**, 041501 (2017).
132. Scarratt, L. R. J., Steiner, U. & Neto, C. A review on the mechanical and thermodynamic robustness of superhydrophobic surfaces. *Adv. Colloid Interface Sci.* **246**, 133–152 (2017).
133. Miljkovic, N., Enright, R. & Wang, E. N. Effect of Droplet Morphology on Growth Dynamics and Heat Transfer during Condensation on Superhydrophobic Nanostructured Surfaces. 1776–1785 (2012).
134. Choi, W., Tuteja, A., Mabry, J. M., Cohen, R. E. & McKinley, G. H. A modified Cassie–Baxter relationship to explain contact angle hysteresis and anisotropy on non-wetting textured surfaces. *J. Colloid Interface Sci.* **339**, 208–216 (2009).
135. Anand, S. & Son, S. Y. Sub-micrometer dropwise condensation under superheated and rarefied vapor condition. *Langmuir* **26**, 17100–17110 (2010).
136. Dietz, C., Rykaczewski, K., Fedorov, a. G. & Joshi, Y. Visualization of droplet departure on a superhydrophobic surface and implications to heat transfer enhancement during dropwise condensation. *Appl. Phys. Lett.* **97**, 97–100 (2010).
137. Rykaczewski, K. & Scott, J. H. J. Methodology for imaging nano-to-microscale water condensation dynamics on complex nanostructures. *ACS Nano* **5**, 5962–5968 (2011).
138. Miljkovic, N. & Wang, E. N. Condensation heat transfer on superhydrophobic surfaces. *MRS Bull.* **38**, 397–406 (2013).
139. Sadhal, S. S. & Martin, W. W. Heat transfer through drop condensate using differential inequalities. *Int. J. Heat Mass Transf.* **20**, 1401–1407 (1977).
140. Hurst, C. J. & Olson, D. R. Conduction through Droplets during Dropwise Condensation. *J. Heat Transfer* **95**, 12–19 (1973).
141. Da Re, M., Del Col, D. & Parin, R. Analysis of superhydrophobic thin films for heat exchange and droplet bouncing.
142. Kittel, C. *Kittel's Introduction to Solid State Physics*. (Wiley, 2018).
143. Chen, G. *Nanoscale Energy Transport and Conversion*. (Oxford, 2005).
144. Majumdar, A. Microscale Heat Conduction in Dielectric Thin Films. *J. Heat Transfer* **115**, 7–16 (1993).
145. Cahill, D. G., Goodson, K. & Majumdar, A. Thermometry and Thermal Transport in Micro/Nanoscale Solid-State Devices and Structures. *J. Heat Transfer* **124**, 223 (2002).

146. Dong, Y. *Dynamical analysis of non-fourier heat conduction and its application in nanosystems. Dynamical Analysis of Non-Fourier Heat Conduction and Its Application in Nanosystems* (2015). doi:10.1007/9783662484852
147. Alvarez, F. X. & Jou, D. Memory and nonlocal effects in heat transport: From diffusive to ballistic regimes. *Appl. Phys. Lett.* **90**, 83109 (2007).
148. Griffin, A. J., Brotzen, F. R. & Loos, P. J. Effect of thickness on the transverse thermal conductivity of thin dielectric films. *J. Appl. Phys.* **75**, 3761–3764 (1994).
149. Khvesyuk, V. I. & Skryabin, A. S. Heat Conduction in Nanostructures. *High Temp.* **55**, 428–450 (2017).
150. Liu, W. & Asheghi, M. Phonon-boundary scattering in ultrathin single-crystal silicon layers. *Appl. Phys. Lett.* **84**, 3819–3821 (2004).
151. Ju, Y. S. & Goodson, K. E. Phonon scattering in silicon films with thickness of order 100 nm. *Appl. Phys. Lett.* **74**, 3005–3007 (1999).
152. Lambropoulos, J. C. *et al.* Thermal conductivity of dielectric thin films. *J. Appl. Phys.* **66**, 4230–4242 (1989).
153. Swartz, E. T. & Pohl, R. O. Thermal boundary resistance. *Rev. Mod. Phys.* **61**, 605–668 (1989).
154. Zago, L., Martucci, A. & Parin, R. Superfici metalliche superidrofobiche per condensazione a gocce. (2017).
155. Rigon, M., Martucci, A., Sturaro, M. & Parin, R. Rivestimenti a bagnabilità controllata su superfici metalliche per condensazione a gocce metalliche. (2017).
156. Cushing, B. L., Kolesnichenko, V. L. & O'Connor, C. J. Recent advances in the liquid-phase syntheses of inorganic nanoparticles. *Chem. Rev.* **104**, 3893–3946 (2004).
157. Hench, L. L. & West, J. K. The Sol-Gel Process. *Chem. Rev.* **90**, 33–72 (1990).
158. Lee, M., Kim, T., Bae, C., Shin, H. & Kim, J. Fabrication and applications of metal-oxide nanotubes. *Jom* **62**, 44–49 (2010).
159. Schubert, U., Hiising, N. & Lorenz, A. Hybrid Inorganic-Organic Materials by Sol-Gel Processing of Organofunctional Metal Alkoxides. *Chem. Mater.* **7**, 2010–2027 (1995).
160. S. A. Khan, E. M. Rabinovich, R. K. Prud'homme, M. J. S. and N. J. K. Rheological monitoring of gelation kinetics of silica sols. *Mater. Res. Soc. Symp. Proc.* **121**, 73 (1988).
161. Wang, D. & Bierwagen, G. P. Sol-gel coatings on metals for corrosion protection. *Prog. Org. Coatings* **64**, 327–338 (2009).
162. Rustom, R. Gel Route to Homogeneous Glass Preparation. *J. Am. Ceram. Soc.* **52**, 344
163. Amiri, S. & Rahimi, A. Hybrid nanocomposite coating by sol – gel method : a review. *Iran. Polym. J.* **25**, 559–577 (2016).

164. Purcar, V. *et al.* Fabrication of hydrophobic and antireflective coatings based on hybrid silica films by sol-gel process. *Surf. Coatings Technol.* **206**, 4449–4454 (2012).
165. Huang, S. I., Shen, Y. J. & Chen, H. Study on the hydrophobic surfaces prepared by two-step sol-gel process. *Appl. Surf. Sci.* **255**, 7040–7046 (2009).
166. Sheen, Y. C. *et al.* Non-fluorinated superamphiphobic surfaces through sol-gel processing of methyltriethoxysilane and tetraethoxysilane. *Mater. Chem. Phys.* **114**, 63–68 (2009).
167. Kheshgi, H. S., Kistler, S. F. & Scriven, L. E. Rising and falling film flows: Viewed from a first-order approximation. *Chem. Eng. Sci.* **47**, 683–694 (1992).
168. Wilson, S. D. R. The drag-out problem in film coating theory. *J. Eng. Math.* **16**, 209–221 (1982).
169. Landau, L. & Levich, B. in *Dynamics of Curved Fronts* (ed. Pelcé, P.) 141–153 (Academic Press, 1988). doi:<https://doi.org/10.1016/B978-0-08-092523-3.50016-2>
170. Ahmed, A., Clowes, R., Willneff, E., Myers, P. & Zhang, H. Porous silica spheres in macroporous structures and on nanofibres. *Philos. Trans. R. Soc. A Math. Phys. Eng. Sci.* **368**, 4351–4370 (2010).
171. Stöber, W., Fink, A. & Bohn, E. Controlled growth of monodisperse silica spheres in the micron size range. *J. Colloid Interface Sci.* **26**, 62–69 (1968).
172. Liberman, A., Mendez, N., Trogler, W. C. & Kummel, A. C. Synthesis and surface functionalization of silica nanoparticles for nanomedicine. *Surf. Sci. Rep.* **69**, 132–158 (2014).
173. Rao, A. V. *et al.* Water repellent porous silica films by sol-gel dip coating method. *J. Colloid Interface Sci.* **352**, 30–35 (2010).
174. Green, D. L. *et al.* Size, volume fraction, and nucleation of Stober silica nanoparticles. *J. Colloid Interface Sci.* **266**, 346–358 (2003).
175. Liu, J. *et al.* Extension of the stöber method to the preparation of monodisperse resorcinol-formaldehyde resin polymer and carbon spheres. *Angew. Chemie - Int. Ed.* **50**, 5947–5951 (2011).
176. Rao, A. V., Latthe, S. S., Mahadik, S. A. & Kappenstein, C. Mechanically stable and corrosion resistant superhydrophobic sol-gel coatings on copper substrate. *Appl. Surf. Sci.* **257**, 5772–5776 (2011).
177. Kozuka, H. Stress evolution on gel-to-ceramic thin film conversion. *J. Sol-Gel Sci. Technol.* **40**, 287–297 (2006).
178. Klein, L., Aparicio, M. & Jitianu, A. *Handbook of Sol-Gel Science and Technology.* (2017). doi:10.1007/978-3-319-19454-7
179. Innocenzi, P., Abdirashid, M. O. & Guglielmi, M. Structure and Properties of Sol-Gel Coatings

- from Methyltriethoxysilane and Tetraethoxysilane. *J. Sol-Gel Sci. Technol.* **3**, 47–55 (1994).
180. Bateau, J. *et al.* Large and Stable Refractive Index Change in Photochromic Hybrid Materials. *Chem. Mater.* **10**, 1945–1950 (1998).
  181. Zampieri, G., Del Col, D. & Parin, R. Analisi sperimentale dello scambio termico in condensazione a gocce su superfici idrofobiche. (2017).
  182. Duran, A., Serna, C., Fornes, V. & Navarro, J. M. F. Structural considerations about SiO<sub>2</sub> glasses prepared by sol-gel. *J. Non. Cryst. Solids* **82**, 69–77 (1986).
  183. Almeida, R. M. & Pantano, C. G. Structural investigation of silica gel films by infrared spectroscopy. *J. Appl. Phys.* **68**, 4225–4232 (1990).
  184. Abe, Y., Hatano, H. & Gunji, T. Preparation and properties of flexible thin films by acid-catalyzed hydrolytic polycondensation of methyltrimethoxysilane. *J. Polym. Sci. Part A Polym. Chem.* **33**, 751–754 (1995).
  185. Vorotilov, K. A., Vasiljev, V. A., Sobolevsky, M. V & Afanasyeva, N. I. Structure, properties and applications of phenyl-modified silicate films. *Thin Solid Films* **288**, 57–63 (1996).
  186. Sheffer, M., Groysman, A. & Mandler, D. Electrodeposition of sol-gel films on Al for corrosion protection. *Corros. Sci.* **45**, 2893–2904 (2003).
  187. Wang, D. & Bierwagen, G. P. Sol-gel coatings on metals for corrosion protection. *Prog. Org. Coatings* **64**, 327–338 (2009).
  188. Novoselov, K. S. *et al.* Two-dimensional gas of massless Dirac fermions in graphene. **438**, 197–200 (2005).
  189. Geim, A. K. & Novoselov, K. S. The rise of graphene. *Nat. Mater.* **6**, 183 (2007).
  190. Rafiee, J. *et al.* Wetting transparency of graphene. *Nat. Mater.* **11**, 217–222 (2012).
  191. Balandin, A. A. *et al.* Superior Thermal Conductivity of Single-Layer Graphene. *Nano Lett.* **8**, 902–907 (2008).
  192. Stankovich, S. *et al.* Graphene-based composite materials. *Nature* **442**, 282 (2006).
  193. Renteria, J. D. *et al.* Strongly Anisotropic Thermal Conductivity of Free-Standing Reduced Graphene Oxide Films Annealed at High Temperature. *Adv. Funct. Mater.* **25**, 4664–4672 (2015).
  194. Preston, D. J., Mafra, D. L., Miljkovic, N., Kong, J. & Wang, E. N. Scalable graphene coatings for enhanced condensation heat transfer. *Nano Lett.* **15**, 2902–2909 (2015).
  195. Han, J. T., Kim, S. Y., Woo, J. S. & Lee, G. W. Transparent, conductive, and superhydrophobic films from stabilized carbon nanotube/silane sol mixture solution. *Adv. Mater.* **20**, 3724–3727 (2008).
  196. Pei, S. & Cheng, H. M. The reduction of graphene oxide. *Carbon N. Y.* **50**, 3210–3228 (2012).

197. Chua, C. K. & Pumera, M. Chemical reduction of graphene oxide: a synthetic chemistry viewpoint. *Chem. Soc. Rev.* **43**, 291–312 (2014).
198. Marcano, D. C. *et al.* Improved Synthesis of Graphene Oxide. *ACS Nano* **4**, 4806–4814 (2010).
199. Hummers, W. S. & Offeman, R. E. Preparation of Graphitic Oxide. *J. Am. Chem. Soc.* **80**, 1339 (1958).
200. Zhu, Y. *et al.* Graphene and graphene oxide: Synthesis, properties, and applications. *Adv. Mater.* **22**, 3906–3924 (2010).
201. Stankovich, S. *et al.* Synthesis of graphene-based nanosheets via chemical reduction of exfoliated graphite oxide. **45**, 1558–1565 (2007).
202. Akhavan, O. The effect of heat treatment on formation of graphene thin films from graphene oxide nanosheets. *Carbon N. Y.* **48**, 509–519 (2009).
203. Childres, I., Jauregui, L. A., Park, W., Cao, H. & Chen, Y. P. *Raman spectroscopy of graphene and related materials.*
204. Malard, L. M., Pimenta, M. A., Dresselhaus, G. & Dresselhaus, M. S. Raman spectroscopy in graphene. *Phys. Rep.* **473**, 51–87 (2009).
205. Maitra, T. *et al.* Hierarchically nanotextured surfaces maintaining superhydrophobicity under severely adverse conditions. *Nanoscale* **6**, 8710–8719 (2014).
206. Lu, S., Chen, Y., Xu, W. & Liu, W. Controlled growth of superhydrophobic films by sol-gel method on aluminum substrate. *Appl. Surf. Sci.* **256**, 6072–6075 (2010).
207. Sarkar, D. K., Farzaneh, M. & Paynter, R. W. Superhydrophobic properties of ultrathin rf-sputtered Teflon films coated etched aluminum surfaces. *Mater. Lett.* **62**, 1226–1229 (2008).
208. Sarkar, D. K., Farzaneh, M. & Paynter, R. W. Wetting and superhydrophobic properties of PECVD grown hydrocarbon and fluorinated-hydrocarbon coatings. *Appl. Surf. Sci.* **256**, 3698–3701 (2010).
209. Saleema, N., Sarkar, D. K., Paynter, R. W. & Chen, X. G. Superhydrophobic aluminum alloy surfaces by a novel one-step process. *ACS Appl. Mater. Interfaces* **2**, 2500–2502 (2010).
210. Jafari, R. & Farzaneh, M. Fabrication of superhydrophobic nanostructured surface on aluminum alloy. *Appl. Phys. A Mater. Sci. Process.* **102**, 195–199 (2011).
211. Zuo, Z. *et al.* Fabrication and anti-icing property of coral-like superhydrophobic aluminum surface. *Appl. Surf. Sci.* **331**, 132–139 (2015).
212. Liu, L., Zhao, J., Zhang, Y., Zhao, F. & Zhang, Y. Fabrication of superhydrophobic surface by hierarchical growth of lotus-leaf-like boehmite on aluminum foil. *J. Colloid Interface Sci.* **358**, 277–283 (2011).
213. Xu, W., Lan, Z., Peng, B. L., Wen, R. F. & Ma, X. H. Effect of surface free energies on the

- heterogeneous nucleation of water droplet: A molecular dynamics simulation approach. *J. Chem. Phys.* **142**, 054701 (2015).
214. Fürstner, R., Barthlott, W., Neinhuis, C. & Walzel, P. Wetting and self-cleaning properties of artificial superhydrophobic surfaces. *Langmuir* **21**, 956–961 (2005).
  215. Lee, D. K., Cho, Y. H., Lee, J. W. & Park, M. S. Wettability of microstructured Pyrex glass with hydrophobic and hydrophilic properties. *Surf. Coatings Technol.* **319**, 213–218 (2017).
  216. Qi, B., Zhou, J., Wei, J. & Li, X. Study on the wettability and condensation heat transfer of sine-shaped micro-grooved surfaces. *Exp. Therm. Fluid Sci.* **90**, 28–36 (2018).
  217. Li, C. *et al.* Reversible switching of water-droplet mobility on a superhydrophobic surface based on a phase transition of a side-chain liquid-crystal polymer. *Adv. Mater.* **21**, 4254–4258 (2009).
  218. Chen, C. H. *et al.* Dropwise condensation on superhydrophobic surfaces with two-tier roughness. *Appl. Phys. Lett.* **90**, 1–4 (2007).
  219. Wier, K. A. & McCarthy, T. J. Condensation on ultrahydrophobic surfaces and its effect on droplet mobility: Ultrahydrophobic surfaces are not always water repellent. *Langmuir* **22**, 2433–2436 (2006).
  220. Orejon, D. *et al.* Simultaneous dropwise and filmwise condensation on hydrophilic microstructured surfaces. *Int. J. Heat Mass Transf.* **114**, 187–197 (2017).
  221. Torresin, D., Tiwari, M. K., Del Col, D. & Poulikakos, D. Flow condensation on copper-based nanotextured superhydrophobic surfaces. *Langmuir* **29**, 840–848 (2013).
  222. Flores-Vivian, I., Hejazi, V., Kozhukhova, M. I., Nosonovsky, M. & Sobolev, K. Self-assembling particle-siloxane coatings for superhydrophobic concrete. *ACS Appl. Mater. Interfaces* **5**, 13284–13294 (2013).
  223. Bisetto, A., Stamatopoulos, C., Tiwari, M. K., Del Col, D. & Poulikakos, D. Robust superhydrophobic aluminium based surfaces for two-phase heat transfer applications. in *Eurotherm Seminar 101 - Transport Phenomena in Multiphase Systems – Krakow - Poland* (2014).
  224. Parin, R. *et al.* Nano-structured aluminum surfaces for dropwise condensation. *Surf. Coatings Technol.* **348**, 1–12 (2018).
  225. Kocon, L., Despetis, F. & Phalippou, J. Ultralow density silica aerogels by alcohol supercritical drying. 96–100 (1998).
  226. Hrubesh, L. W. Aerogel applications. (1998).
  227. Gurav, J. L., Jung, I.-K., Park, H.-H., Kang, E. S. & Nadargi, D. Y. Silica Aerogel: Synthesis and Applications. *J. Nanomater.* **2010**, 1–11 (2010).

228. Schmidt, M. & Schwertfeger, F. Applications for silica aerogel products. 364–368 (1998).
229. Schwertfeger, F., Frank, D. & Schmidt, M. Hydrophobic waterglass based aerogels without solvent exchange or supercritical drying. 24–29 (1998).
230. Soleimani Dorcheh, A. & Abbasi, M. H. Silica aerogel; synthesis, properties and characterization. *J. Mater. Process. Technol.* **199**, 10–26 (2008).
231. Rao, A. P., Rao, A. V. & Bangi, U. K. H. Low thermalconductive, transparent and hydrophobic ambient pressure dried silica aerogels with various preparation conditions using sodium silicate solutions. *J. Sol-Gel Sci. Technol.* **47**, 85–94 (2008).
232. Bhagat, S. D., Kim, Y. H., Moon, M. J., Ahn, Y. S. & Yeo, J. G. A cost-effective and fast synthesis of nanoporous SiO<sub>2</sub> aerogel powders using water-glass via ambient pressure drying route. *Solid State Sci.* **9**, 628–635 (2007).
233. Shewale, P. M., Rao, A. V. & Rao, A. P. Effect of different trimethyl silylating agents on the hydrophobic and physical properties of silica aerogels. *Appl. Surf. Sci.* **254**, 6902–6907 (2008).
234. Bhagat, S. D. *et al.* Superhydrophobic silica aerogel powders with simultaneous surface modification, solvent exchange and sodium ion removal from hydrogels. *Microporous Mesoporous Mater.* **112**, 504–509 (2008).
235. Liu, T. Q., Sun, W., Sun, X. Y. & Ai, H. R. Effect of hierarchical architecture of superhydrophobic surface on the condensed drop's final state. *Wuli Huaxue Xuebao/ Acta Phys. - Chim. Sin.* **26**, 2989–2996 (2010).
236. Del Col, D., Parin, R., Bisetto, A., Bortolin, S. & Martucci, A. Film condensation of steam flowing on a hydrophobic surface. *Int. J. Heat Mass Transf.* **107**, (2017).
237. Tancon, M., Del Col, D. & Parin, R. Indagine sperimentale della condensazione a gocce di vapor d'acqua. (2018).
238. Tosatto, G., Del Col, D. & Parin, R. Analisi di scambio termico in condensazione a gocce su superfici idrofobiche. (2016).
239. Bisetto, A., Bortolin, S. & Del Col, D. Experimental analysis of steam condensation over conventional and superhydrophilic vertical surfaces. *Exp. Therm. Fluid Sci.* **68**, 216–227 (2015).
240. *ISO Guide to the expression of uncertainty in measurement.* (1995).
241. Tanner, D. W., Potter, C. J., Pope, D. & West, D. HEAT TRANSFER IN DROPWISE CONDENSATION-PART I The effects of heat flux, steam velocity and non-condensable gas concentration. *Int. J. Heat Mass Transf.* **8**, 419–426 (1965).
242. Zhang, B. J., Kuok, C., Kim, K. J., Hwang, T. & Yoon, H. Dropwise steam condensation on various hydrophobic surfaces: Polyphenylene sulfide (PPS), polytetrafluoroethylene (PTFE),



- and self-assembled micro/nano silver (SAMS). *Int. J. Heat Mass Transf.* (2015). doi:10.1016/j.ijheatmasstransfer.2015.05.060
243. Tanner, D. W., Pope, D., Potter, C. J. & West, D. HEAT TRANSFER IN DROPWISE CONDENSATION-PART II Surface Chemistry. *Int. J. Heat Mass Transf.* **8**, 427–436 (1965).
244. Weisensee, P. B. *et al.* Condensate droplet size distribution on lubricant-infused surfaces. *Int. J. Heat Mass Transf.* **109**, 187–199 (2017).
245. Cohen-tanugi, D., Grossman, J. C., Cohen-tanugi, D. & Grossman, J. C. Water permeability of nanoporous graphene at realistic pressures for reverse osmosis desalination Water permeability of nanoporous graphene at realistic pressures for reverse osmosis desalination. **074704**, (2016).
246. Meng Miao, Marco Buongiorno Nardelli, Q. W. and Y. L. First principles study of the permeability of graphene to hydrogen atoms. *Phys. Chem. Chem. Phys.* **15**, 16132–16137 (2013).
247. Settnes, M., Power, S. R. & Lin, J. About a permeability of graphene pores. doi:10.1088/1757-899X/87/1/012111
248. Ghosh, A., Beaini, S., Zhang, B. J., Ganguly, R. & Megaridis, C. M. Enhancing Dropwise Condensation through Bioinspired Wettability Patterning. *Langmuir* **30**, 13103–13115 (2014).
249. Devaprakasam, D., Sampath, S. & Biswas, S. K. Thermal Stability of Perfluoroalkyl Silane Self-Assembled on a Polycrystalline Aluminum Surface. *Langmuir* **20**, 1329–1334 (2004).
250. Karim, M. R. & Islam, M. S. Thermal behavior with mechanical property of fluorinated silane functionalized superhydrophobic pullulan/poly(vinyl alcohol) blends by electrospinning method. *J. Nanomater.* **2011**, (2011).
251. Yaghoubian, S. & Ward, C. A. Initiation of wetting, filmwise condensation and condensate drainage from a surface in a gravity field. *Phys. Chem. Chem. Phys.* **19**, 20808–20817 (2017).
252. Aili, A., Ge, Q. & Zhang, T. Effect of Mini/Micro/Nanostructures on Filmwise Condensation of Low-Surface-Tension Fluids. *J. Heat Transfer* **140**, 102402 (2018).
253. Antonini, C., Villa, F., Bernagozzi, I., Amirfazli, A. & Marengo, M. Drop rebound after impact: The role of the receding contact angle. *Langmuir* **29**, 16045–16050 (2013).
254. Gauthier, A., Symon, S., Clanet, C. & Quéré, D. Water impacting on superhydrophobic macrottextures. *Nat. Commun.* **6**, 8001 (2015).
255. Tuteja, A., Choi, W., McKinley, G. H., Cohen, R. E. & Rubner, M. F. Design parameters for superhydrophobicity and superoleophobicity. *MRS Bull.* **33**, 752–758 (2008).